COPY 5

A thesis

entitled

"ELECTROMIGRATION IN THIN FILMS OF ALUMINIUM"

by

Stephen Roberts B.Sc., A.R.C.S.

Submitted for the

Degree of Doctor of Philosophy

of the

University of London

Imperial College of Science and Technology

London

1982

ABSTRACT

Electromigration is a common cause of failure of the aluminium thin film metallizations used in many microelectronic devices and circuits. The objective of the present work was to draw correlations between processing parameters, microstructure and susceptibility to electromigration failure of vacuum-evaporated aluminium films on amorphous SiO_2.

The chemical composition of the Al - SiO_2 interface was examined using x-ray photoelectron spectroscopy, Auger electron spectroscopy and transmission electron microscopy and diffraction. The effects of substrate surface preparation and temperature on Al - SiO_2 interfacial reaction were investigated. Reduction of the SiO_2 by the aluminium, resulting in the production of polycrystalline silicon and η - alumina, was found to occur under the conditions prevalent in many industrial metallization processes. The implications of Al-SiO_2 reaction for device reliability are discussed.

A range of techniques, including transmission and scanning electron microscopy and grazing incidence x-ray diffraction, were used to characterize the grain size, preferred orientation and surface topography of aluminium films deposited onto SiO_2 under various conditions. 1 μm thick aluminium films were found to have a $\langle 111 \rangle$ fibre texture and the mean grain size ranged from less than 0.5 μm for deposition at 300 K, to $\sim$ 5 μm, for deposition at 675 K. Some thinner films were also examined, and trends in grain size and orientation with thickness were established. "Growth hillocks", "annealing hillocks" and other surface features were observed in certain films.

Photolithography was used to prepare 10 μm wide tracks from 1 μm thick aluminium films, and these were tested for electromigration failure under accelerated conditions. The median time to failure was found to increase with grain size in the range 2 μm to 5 μm, and an "activation energy" for electromigration failure of

$0.6 \pm .05$ eV was measured in the 433 K to 473 K temperature range. Films having a 1 μm mean grain size, prepared at lower temperature, gave an "activation energy" of 0.38 eV, suggesting a different failure mode. Examination of failed films using optical and scanning electron microscopy revealed the presence of the voids, hillocks and whiskers known to be associated with electromigration in polycrystalline thin films.

The results are interpreted in terms of the various models for electromigration damage proposed in the literature, and the possible importance of the Al - SiO_2 interface is also discussed.

CONTENTS

Page

Page

Page

CHAPTER 1

INTRODUCTION

Electromigration (the motion of atoms in a conductor due to the flow of an electric current) was discovered in 1861 by Gerardin. In most practical situations, the effects of electromigration are not apparent, because of the relatively low values of current density and temperature. Consequently, for 100 years the phenomenon remained a subject of mainly academic interest.

With the advances in semiconductor device technology in the 1960's, however, electromigration became a problem of technological importance. The thin film contact metallizations of the new silicon planar devices were required to carry current densities in excess of 10^8 A m^{-2}. Under these conditions electromigration posed a serious threat to reliability by causing open circuit failure of the metallization tracks. Further reductions in the scale of device geometries over the following years aggravated the problem, and a considerable amount of research was undertaken with the aim of reducing electromigration damage in real metallizations.

Some progress has been made in this area with the use of alloy films and passivation layers, but due to the large number of variables in the deposition process, and their effect on the film properties, apparently similar experiments by different workers have often yielded conflicting results. It was therefore decided to make a careful study of electromigration failure in thin films of pure aluminium (the basic material of most metallization systems), in order to evaluate the effects of deposition conditions and film microstructure. As well as grain size and orientation effects, which have been investigated by some other workers, the role of the Al - SiO_2 interface in electromigration and other failure modes was studied.

The thesis may be divided into three main sections. Chapters 2 to 5 comprise a study of the Al - SiO_2 interface. Previous work is reviewed in Chapter 2 and the

present experiments, in which the Al - Si O_2 interface was analysed by x-ray photoelectron spectroscopy and transmission electron microscopy, are described in Chapters 3 and 4. The significance of the results in the context of device reliability is discussed in Chapter 5.

The second section of work, namely the effect of deposition conditions and annealing treatments on the microstructure of aluminium thin films, is covered in Chapters 6 and 7. Chapter 6 is a review of experimental and theoretical work in the field of thin film deposition, and Chapter 7 contains a description of the present electron microscopy experiments in this area.

Electromigration is treated in Chapters 8 and 9, which form the third main section of the thesis. Chapter 8 contains a brief historical introduction and a discussion of the theory of electromigration, followed by a review of recent developments in the field of electromigration failure in microelectronic devices. The present experiments, comprising an investigation of electromigration failure in thin aluminium films using accelerated life testing, are discussed in Chapter 9.

Finally, the main results of the three sections are summarized in Chapter 10.

CHAPTER 2

REVIEW OF EXPERIMENTAL WORK ON THE Al - SiO_2 INTERFACE

2.1 Introduction

With the advent of silicon planar devices using thermally grown SiO_2 insulation and aluminium contact metallization, the Al - SiO_2 interface has become a subject of considerable importance in the semiconductor device industry. The performance and reliability of devices may be affected by the properties of the Al - SiO_2 interface in several ways.

Firstly, chemical reaction between the aluminium and the native oxide on the silicon is necessary in order to establish good ohmic contact. This is the basis of the "sintering" step in device processing.

Secondly, Al - SiO_2 reaction is responsible for the adhesion of the metallization to the SiO_2 insulator. The relatively good adhesion of aluminium to SiO_2 is one reason why it is used as a metallization, rather than gold, for example. However, Al - SiO_2 adhesion can be poor under certain conditions (e.g. when aluminium is vacuum-evaporated onto SiO_2 at temperatures less than ~450 K; d'Heurle et al 1968). Poor adhesion causes detachment of the metallization from the device, particularly at the bond pads during ultrasonic wedge bonding of aluminium wires. The problem can be alleviated to some extent by the use of thermocompression gold ball bonding, which causes less disruption of the metallization. These bonds, however, suffer from other failure mechanisms associated with the interdiffusion of gold and aluminium (English and Melliar-Smith 1978). Bonding techniques such as aluminium thermocompression ball bonding may prove more reliable (Taylor 1980), but ultimately the bond strength must be limited by the metallization to substrate adhesion.

Severe non-adhesion reduces the thermal contact between the metallization

and the device, resulting in excessive temperature rise of the conductor due to Joule heating. This in turn accelerates void formation by electromigration and impairs reliability (Rosenberg and Berenbaum 1968).

Thirdly, the Al - SiO_2 interface is a possible path for electromigration, this being particularly important in narrow ($\lesssim$1 μm) metallizations having a "bamboo" grain structure. The flux of aluminium atoms migrating via the interface will depend on the chemical and crystallographic structure which determine the activation energy for interface diffusion. Devices passivated with a film of SiO_2 also have an Al - SiO_2 interface at the upper surface of the metallization. The structure of this interface may be different from that of the lower interface, since in general the conditions under which the interfaces are formed are different. For example, the lower interface is usually formed by the evaporation or sputter-deposition of aluminium onto thermally grown SiO_2. The upper interface may be formed by sputter-depositing SiO_2 onto aluminium, which may have a native oxide on its surface.

Fourthly, the performance of metal-oxide-silicon (MOS) devices is critically dependent on the electronic properties of the metal - SiO_2 interface. Changes in the barrier height at the Al - SiO_2 interface (Hickmott 1980) and the breakdown potential of MOS capacitors (Chou and Eldridge 1970) on annealing have been attributed to chemical changes that have taken place at the interface.

As a result of its technological importance, the Al - SiO_2 interface has received a considerable amount of attention over the past 15 years. However, experiments to determine the chemical and crystalline nature of the interface by electron spectroscopies and diffraction techniques are few in number. Section 2.2 is a review of the indirect experimental evidence for chemical reaction at the Al - SiO_2 interface, while direct observations of reaction products are discussed in section 2.3.

2.2 Indirect Evidence for Reaction at the Al - SiO_2 Interface

Some of the earliest evidence for chemical reaction at the Al - SiO_2 interface came from the experiments of Lehman (1964), in which the effects of annealing on the channel conduction of n-channel enhancement-mode MOSFETs were investigated. Various gate metallizations were used, these being evaporated onto the 800 nm thick thermally grown gate oxide at room temperature. The channel current with the gate floating was measured for each device. The gate voltage required to give a channel current of 10 μA, with a source-drain voltage of 25 V, was also determined. The devices were then annealed in nitrogen for successive 15 minute periods at increasing temperatures and the channel conduction was measured after each anneal. All of the devices had a low initial channel conductance, which was found to increase after annealing between 673 K and 873 K. The effect was greatest for devices with aluminium and magnesium gate metallizations and least for those with copper and gold. Lehman noted a correlation of the magnitude of the effect of annealing with the free energy of oxide formation of the metal, and suggested an interfacial reaction of the type

$$M + SiO_2 \longrightarrow MO_x + Si\,O_{2-x}$$

MOSFET structures without any gate metallization were subjected to similar annealing treatments in atmospheres of oxygen, nitrogen and forming gas (10% H_2, 90% N_2). Significant increase in the channel conductance was observed only when forming gas was used, thus supporting the hypothesis that reduction of the SiO_2 was the cause.

These results are in agreement with the model proposed by Thomas and Young (1964) in which the removal of oxygen ions from the surface of SiO_2 (for example, by reaction with aluminium) creates oxygen ion vacancies in the SiO_2. These vacancies, bearing a positive charge, migrate to the Si - SiO_2 interface, where they cause an n-type inversion layer in the p-type silicon under the gate electrode, thus enhancing

the channel conduction. The presence of phosphorous pentoxide in the SiO_2 layer acts as an oxygen source, inhibiting the formation of oxygen vacancies and reducing positive space charge effects (Kerr et al 1964).

Osburn and Weitzman (1972) measured the leakage current - voltage characteristics of MOS capacitors. They found that post-metallization annealing at 773 K in dry nitrogen for 5 minutes lowered the current resulting from a fixed applied voltage by 2 to 3 orders of magnitude, for electron injection from both the aluminium and the silicon interfaces. The temperature and field dependence of both conduction modes in the range 300 K to 500 K indicated that conduction was due to Fowler-Nordheim tunnelling of the $Al - SiO_2$ and $Si - SiO_2$ interface barriers. The effect of annealing was an apparent increase of 1.5 eV in the barrier height. Two models were proposed to explain this phenomenon. The first involves the removal, on annealing, of trap levels 1.5 eV below the conduction band edge in SiO_2. In the second model, annealing removes bulk charge trapped in the SiO_2, thus changing the shape of the tunnelling barrier. No detailed mechanisms were proposed for either model, but chemical changes at the $Al - SiO_2$ interface may be involved.

Hartstein et al (1978) measured the barrier height for electron injection between 10 nm Al films and thermally grown SiO_2. They used a photon-assisted tunnelling technique, with photon energies in the range 0.1 eV to 0.4 eV. Annealing at 1273 K in nitrogen prior to aluminium deposition had little effect on the barrier height, as did annealing at 673 K for 20 minutes in forming gas. However, the same treatment in forming gas after metallization increased the barrier height from 3.05 eV to 3.25 eV.

This result is supported by the work of Hickmott (1980). He made capacitance - voltage (C - V) measurements on $Al - SiO_2 - Si$ capacitors to determine the effective barrier height at the $Al - SiO_2$ interface. The specimens consisted of 0.7 mm square aluminium capacitors, produced by photolithography, on thermally grown SiO_2 of

various thicknesses in the range 65 nm to 350 nm. All specimens were annealed for 20 minutes at 673 K in forming gas to reduce the surface state density and surface charge before aluminium was deposited from a tantalum boat or B_5N_3 crucible. Some specimens were given various post-metallization anneals in nitrogen or forming gas.

C-V measurements were taken to find the flat-band voltage for each oxide thickness. At the flat-band condition, there is no charge induced in the silicon and the flat-band voltage V_{fb} is given by

$$V_{FB} = \Phi_{eff} - \frac{Q_{ss}}{C_o} + \Phi_F \qquad (2.1)$$

where Φ_{eff} is the effective barrier height, Φ_F is the Fermi potential of the semiconductor measured from the mid-gap, Q_{ss} is the surface-charge density at the $Si-SiO_2$ interface and C_o is the capacitance per unit area due to the SiO_2,

$$\text{i.e.} \quad C_o = \frac{\varepsilon_{ox}\varepsilon_o}{t_{ox}} \qquad (2.2)$$

where ε_{ox} is the relative permittivity of the oxide and t_{ox} is its thickness.

Hence, if V_{fb} is plotted against t_{ox}, a straight line is obtained, the slope of which gives Q_{ss} and the intercept Φ_{eff}.

Specimens annealed at 673 K for 20 minutes in forming gas after metallization were found to suffer an increase in Φ_{eff} of between 0.12 eV and 0.30 eV, depending on whether the substrate was n-type or p-type {111} or {100} silicon. Specimens given a similar anneal in nitrogen showed an increase in Φ_{eff} of between 0.10 eV and 0.15 eV (see figure 2.1). The linearity of V_{fb} versus t_{ox} indicates that there is no bulk charge in the SiO_2. The surface charge at the $Si-SiO_2$ interface is positive and is not affected by annealing, as all the curves are parallel. Therefore, any aluminium entering the SiO_2 as a result of annealing must have done so in an uncharged form.

In order to show that the observed changes in Φ_{eff} were due to changes at the

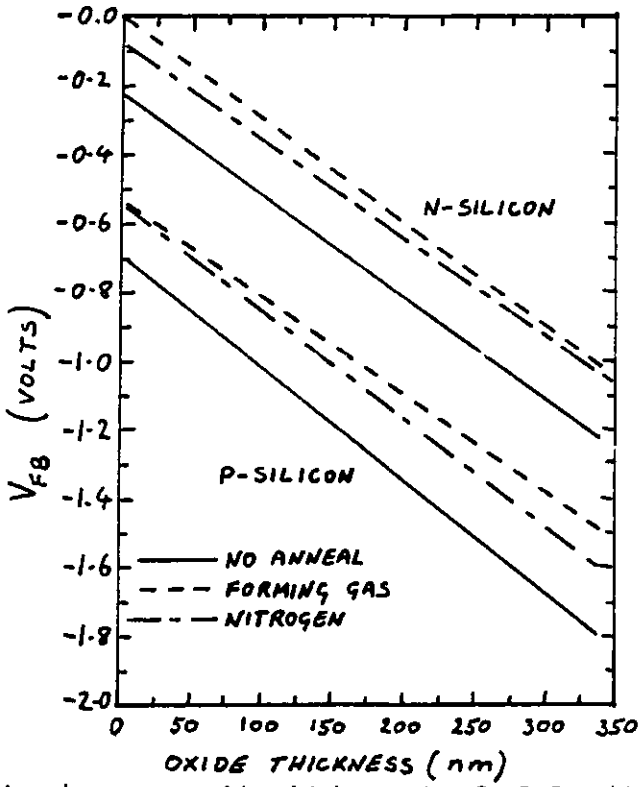

Flat-band voltage vs oxide thickness for Si-SiO_2-Al capacitors annealed under different conditions. {100} silicon. (From Hickmott 1980)

FIGURE 2.1

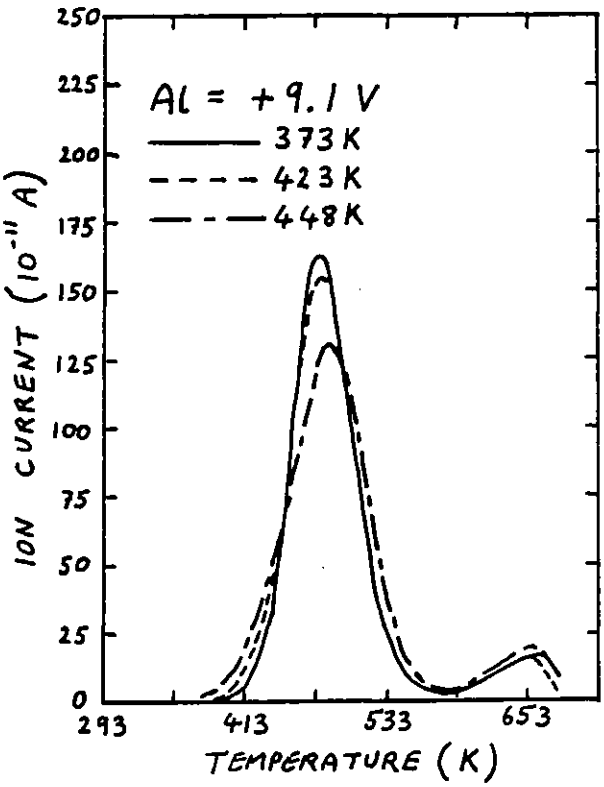

Effect of annealing for 5 min without bias on initial TSIC curves for Al-SiO_2-Si samples. 3.3 10^{17} Na /m^2. 400 nm SiO_2. (From Hickmott 1980).

FIGURE 2.2

Al - SiO_2 interface, Hickmott used the technique of thermally stimulated ionic conductivity (TSIC) measurement on Al - SiO_2 - Si capacitors. 500 nm films of SiO_2 were grown by steam-oxidation on p-type {100} silicon at 1373 K. Sodium chloride was deposited on the oxide surface by evaporation from a tantalum boat and the aluminium metallization was immediately deposited on top of the NaCl film. TSIC measurements were performed by heating the specimen in dry nitrogen at a controlled rate from 300 K to 700 K with a fixed applied bias of approximately 10 volts across the capacitor. As the temperature increased, Na^+ ions were released from traps at one interface and moved to the other interface under the influence of the electric field. Therefore, with the aluminium electrode positive, the ion current contained information on sodium traps at the Al - SiO_2 interface. (The motion of Cl^- ions was taken to be negligible in the temperature range investigated). The TSIC curves obtained by Hickmott are shown in figure 2.2. The effect of annealing without bias prior to taking TSIC measurements was a shift and broadening of the ion current versus temperature peak, indicating the presence of traps which released sodium at lower temperatures. Annealing for 5 minutes at only 373 K produced changes in the peak. TSIC measurement is therefore a very sensitive technique, although the heating involved in taking the measurements must produce artefacts. Also, the presence of NaCl at the Al - SiO_2 interface must affect any reaction occurring.

To summarize, reaction at the Al - SiO_2 interface is thought to be responsible for the formation of an inversion layer in p-type silicon at its interface with SiO_2 in a MOS structure. Lehman (1964) has suggested that this is due to migration of positive charge through the SiO_2 layer. This conflicts with Hickmott's C-V measurements which show that no charge enters the SiO_2 as a result of annealing MOS capacitors. Increases in the effective barrier height for electron injection from Al to SiO_2 in annealed MOS structures have been reported by Osburn and Weitzman (1972), Hartstein

et al (1978) and Hickmott (1980). In addition, TSIC measurements have shown that changes in the trap levels at the Al - SiO_2 interface occur at temperatures as low as 373 K. However, the precise nature of these changes cannot be ascertained by experiments of this kind.

2.3 Direct Observations of Chemical Reaction at the Al - SiO_2 Interface

Reaction products at the Al - SiO_2 interface have been identified by a number of workers using a variety of techniques. X-ray photoelectron spectroscopy (XPS) and Auger electron spectroscopy (AES) are capable of detecting small quantities of atoms and are ideally suited to interface studies. In addition, these techniques give information on the chemical bonding state of atoms and can distinguish between aluminium in Al_2O_3 and metallic Al, for example. Electron diffraction (transmission and reflection) and x-ray diffraction have been used to elucidate the crystalline structure of the interface.

The reaction between silica and molten aluminium has been known for some time, one of the earliest reports being due to Brondyke (1953), who observed the penetration of molten aluminium into alumina-silica refractory materials. Silicon released by the reaction was picked up by the molten aluminium, but no alumina-like reaction products were detected because of the high initial alumina content of the refractory (up to 99%). The reaction was slow below 980 K but the rate increased rapidly above 1030 K. Brondyke proposed that the reaction occurring was :-

$$4\,Al + 3\,SiO_2 \longrightarrow 2\,Al_2O_3 + 3\,Si$$

This reaction is to be expected on thermodynamic grounds. The formation of SiO_2 and Al_2O_3 are both exothermic, releasing 804 kJ mol^{-1} and 1575 kJ mol^{-1} respectively. The difference between the free energies of formation produces the driving force for the reduction of SiO_2 by aluminium, which is expected to release 737 kJ for every 4 moles of aluminium oxidized. This is equivalent to 1.9 eV per

aluminium atom.

Brondyke's work was followed up by Standage and Gani (1967) who studied the reaction between pure vitreous silica rods and molten aluminium. Using x-ray diffraction and electron microprobe analysis, they identified the η, θ and α phases of alumina as well as elemental silicon in the reacted specimens. These authors reported an induction time of several minutes before reaction commenced. However, Prabriputaloong and Piggott (1973a) demonstrated that this effect was due to the adventitious oxide on the surface of the aluminium when the experiment was performed in air at atmospheric pressure. As the silica rod was immersed in the molten aluminium, the oxide film was drawn down around the rod and formed a barrier to penetration by the aluminium. When the reaction was carried out under vacuum no induction time was observed.

Cratchley and Baker (1967) noted that the tensile strength of silica fibre reinforced aluminium was greatly reduced after annealing for 160 hours at temperatures in the range 673 K to 833 K. Microexamination of specimens annealed at 773 K showed that interdiffusion between the silica fibres and aluminium matrix had occurred. At 838 K a slightly exothermic reaction was seen to occur and was attributed to the formation of a liquid aluminium-silicon eutectic. (The aluminium-silicon eutectic temperature is 850 K). At 913 K a rapid exothermic reaction occurred which caused complete degradation of the material.

The reaction of vacuum-evaporated aluminium films on SiO_2 was studied by Silverman (1968). The specimens consisted of 200 nm thick aluminium films on fused silica, dry oxygen-grown SiO_2 on silicon and steam-grown SiO_2 on silicon. These were annealed at temperatures between 673 K and 898 K in atmospheres of argon, air, hydrogen, nitrogen and oxygen and in a vacuum of 10^{-6} m bar. The electrical resistance of the films was measured by a four point probe technique and was used as

an indicator of the extent of reaction. No reaction was detected in samples annealed for 1 hour at temperatures less than 848 K in any ambient. At 873 K the extent of reaction increased significantly with the moisture content of the atmosphere, as determined by dew point measurements of the various gases. Reaction in vacuum was found to be extremely slow, even at 898 K. There was little difference in the reaction rates for the 3 different substrate materials, although reaction was slightly faster for steam-grown SiO_2. This was attributed to its higher water content. Visual observations of the reacted specimens revealed darkening of the aluminium surface and x-ray diffraction showed the presence of silicon in cases where large increases in resistance had been recorded. No crystalline alumina was detected. Silverman proposed that water, either in the ambient or in the silica, promoted the reduction of SiO_2 by aluminium. However, it seems likely that the main effect of moisture in the ambient was to oxidize the surface of the aluminium film, giving an amorphous oxide not easily detected by x-ray diffraction. The presence of silicon in some annealed specimens confirms that $Al - SiO_2$ reaction must nevertheless have occurred, and it is not clear why crystalline alumina from this reaction was not also detected.

While conducting experiments on the effects of processing variations on the dielectric breakdown of SiO_2 layers in MOS structures, Chou and Eldridge (1970) observed that prolonged annealing of aluminium metallized specimens caused a complete short circuit of the SiO_2. For specimens with 100 nm thick oxides, shorting occurred after one hour at 773 K in nitrogen. Oriented defects were seen at the periphery of the aluminium metallization, their shapes being triangular or rectangular, depending on whether the silicon had a $\{111\}$ or $\{100\}$ orientation. The residual aluminium films were removed in dilute hydrochloric acid and collodion replicas were made of the SiO_2 surface. The replicas showed that roughening of the surface had occurred and that the oriented defects were pits 1 μm to 2 μm deep and 1 μm to 10 μm across. A black film

seen to line the pits was removed with the replicas and identified as γ - Al_2O_3 by transmission electron diffraction. Electron microprobe analysis of unetched specimens revealed the pits to be filled with aluminium, while the surrounding areas were depleted of aluminium. In some cases plateaux about 500 nm high were observed adjacent to the pits. The authors suggested that rapid mass transfer occurred during annealing, with silicon atoms diffusing away from the $\{111\}$ facets of the pits to form raised areas under the aluminium, while aluminium filled the γ - Al_2O_3-lined pits. Some specimens were implanted with 75 keV oxygen ions before metallization, and were found to suffer shorting and pit formation after annealing for 1 hour at only 573 K. It is thought that the presence of ion-implantation damage in the SiO_2 accelerated the diffusion of aluminium into the substrate and subsequent reaction.

Prabriputaloong and Piggott (1974) investigated the reaction of 100 nm thick vacuum-evaporated aluminium films with vitreous silica and quartz single crystal substrates. Aluminium was deposited either at the reaction temperature, which ranged from 673 K to 823 K, or at room temperature. The substrates were heated to 1073 K for 10 minutes under vacuum prior to metallization, to desorb water from the surface. The specimens were reacted in air or under vacuum (10^{-6} m bar), then examined by reflection high energy electron diffraction (RHEED), optical microscopy and transmission electron microscopy replica techniques. RHEED patterns from reacted specimens comprised continuous rings, which were interpreted as arising from polycrystalline silicon and a mixture of θ-and α-alumina. X-ray diffraction from the crushed reaction products confirmed this result. The annealing time required before the reaction products first appeared depended on the temperature, and varied from 10 minutes at 800 K to 6 hours at 673 K (see figure 2.3). Very little difference in reaction rate was noted between films deposited onto hot and cold substrates and between specimens reacted under vacuum and in air. However, reaction was more rapid on vitreous silica substrates

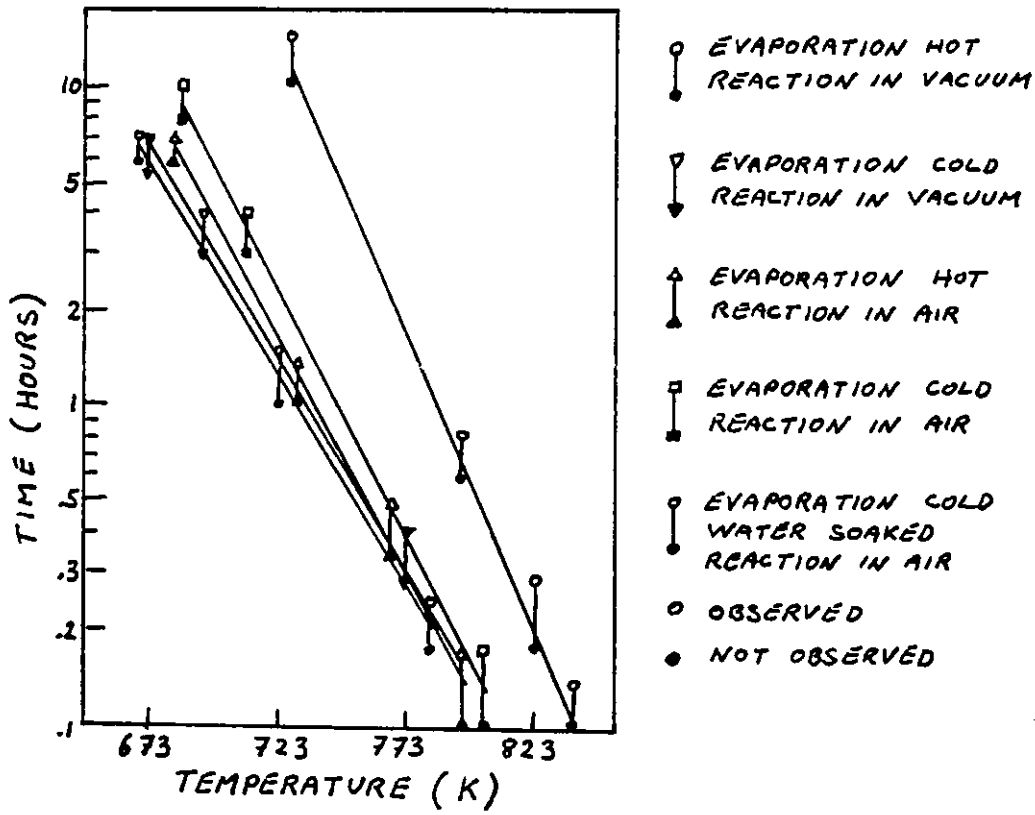

Curves showing time to first appearance of reaction products in thin-film Al-SiO_2 reaction under different conditions. (From Prabriputaloong and Piggott 1974)

FIGURE 2.3

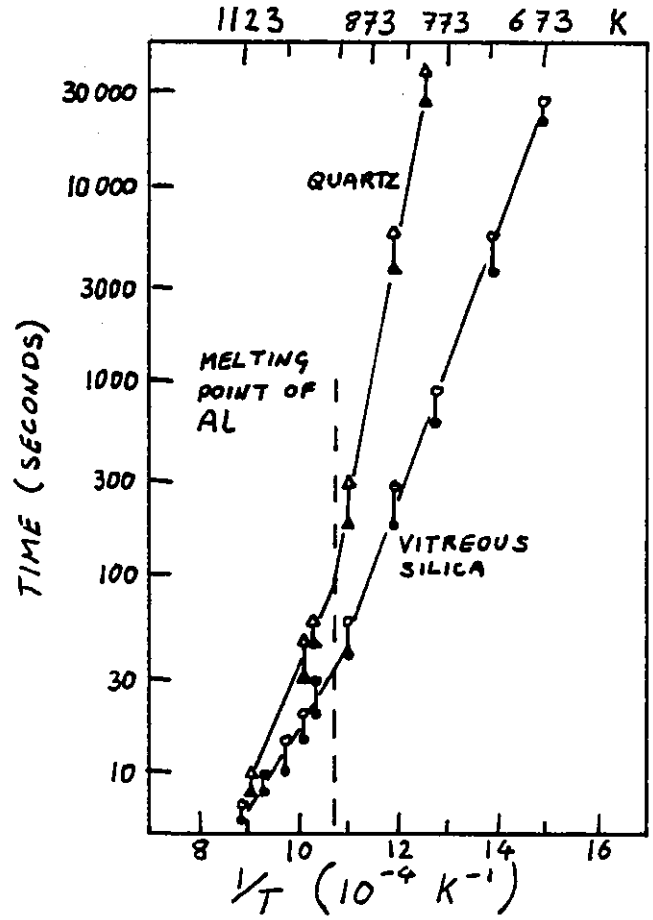

Arrhenius plots of reactions between Al and quartz and vitreous silica at temperatures both above and below the melting point of Al.
(From prabriputaloong and Piggott 1974)

FIGURE 2.4

than on quartz single crystals.

The effect of water-soaking substrates before aluminium deposition was also investigated and was found to reduce the reaction rate and cause disruption of the films. This result is opposed to that of Silverman (1968) which showed increased reaction rates when water was present. The results of Prabriputaloong and Piggott also conflict with those of Silverman in that the latter failed to observe any reaction below 823 K and did not detect crystalline alumina in any specimen. It may be concluded that x-ray diffraction is not always sensitive enough to detect the small amounts of reaction products present.

Prabriputaloong and Piggott performed a control experiment in which they deposited aluminium onto rocksalt and heated it in air to produce a surface layer of aluminium oxide. The Al - Al_2O_3 films were floated off the substrates in water and examined by transmission electron diffraction. No polycrystalline Al_2O_3 was detected, but the aluminium diffraction features were seen to become more diffuse after air-oxidation. This was attributed to the presence of amorphous Al_2O_3. It was therefore concluded that the polycrystalline alumina detected in the aluminium on silica specimens was indeed formed by Al - SiO_2 reaction.

Further experiments were performed in which aluminium films on SiO_2 were annealed under vacuum at temperatures above the melting point of aluminium (Prabriputaloong and Piggott 1974 and 1973b). The only solid reaction product was silicon. The authors suggested that volatile Al_2O was also formed, although it was not detected by the mass spectrometer. Activation energies for reaction were found to differ for quartz and fused silica substrates and for reaction above and below the melting point of aluminium (933 K). (See figure 2.4). It is interesting to note that the change in reaction kinetics occurred at 933 K and not at the Al - Si eutectic temperature (850 K), as suggested by Cratchley and Baker.

Auger sputter profiling was used by Strausser et al (1978) and Strausser and Majumder (1978) to examine the interfaces formed when aluminium was deposited onto SiO_2 by dc sputtering and electron-beam evaporation. The substrates consisted of 100 nm of dry oxygen-grown SiO_2 on n-type {111} silicon wafers. The surface was cleaned by etching in aqueous hydrofluoric acid, rinsing in deionized water and drying in nitrogen before aluminium deposition. Sputter-deposition was carried out in a Sloan d.c. sputtering system at an argon pressure of 7×10^{-3} m bar, which gave a deposition rate of 50 nm per minute. After 50 nm of aluminium had been deposited onto two thirds of the surface, the specimen was exposed to air so that a thin ($\sim$ 2 nm) oxide layer would form on the aluminium surface. A second 50 nm aluminium film was then deposited over half of the first film to give the structure shown in figure 2.5. This specimen configuration, with a thin layer of Al_2O_3 at a known distance beneath the surface, allowed the sputter-etching rate to be determined experimentally.

Profiling was performed using a 1 keV argon ion beam of current density 30 - 75 $\mu A\ cm^{-2}$. The beam was rastered over the specimen to ensure uniformity of etching. The Auger analyser was a CMA with 0.25% energy resolution. The primary electron beam (4.5 keV, 1 μA) was rastered over a 200 μm square to reduce the possibility of electron beam induced desorption of oxygen from the specimen surface. The Auger transitions monitored during profiling are listed in table 2.1, along with the mean free paths of the Auger electrons. (The mean free path determines the ultimate depth resolution attainable). The resulting profile (figure 2.6) shows the presence of Al_2O_3 and free silicon, distributed over a 30 nm thick interface layer.

The authors explained the large observed interface width by assuming that mixing and reaction of aluminium and SiO_2 occurred within a "liquid like" layer, formed by the relatively energetic aluminium atoms arriving from the sputter-deposition source. The aluminium atoms had kinetic energies in the range 10 eV to 20 eV. As the sputtering

Auger Electron Energy (eV)	Transition		Electron m.f.p. (nm)
52	Al in Al_2O_3	LVV	0·4
67	Al	LVV	0·4
78	Si in SiO_2	LVV	0·4
92	Si	LVV	0·4
503	O	$KL_{2,3}L_{2,3}$	1·2
1389	Al in Al_2O_3	$KL_{2,3}L_{2,3}$	2·5
1396	Al	$KL_{2,3}L_{2,3}$	2·5
1611	Si in SiO_2	$KL_{2,3}L_{2,3}$	2·9
1618	Si	$KL_{2,3}L_{2,3}$	2·9

Peaks Monitored through the Al-SiO_2 Interface.

(from Strausser et al 1978)

TABLE 2.1

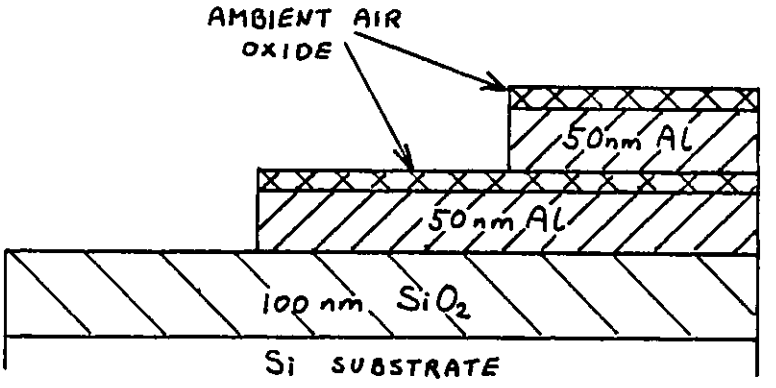

Cross-sectional diagram of the samples used by Strausser et al (1978)

FIGURE 2.5

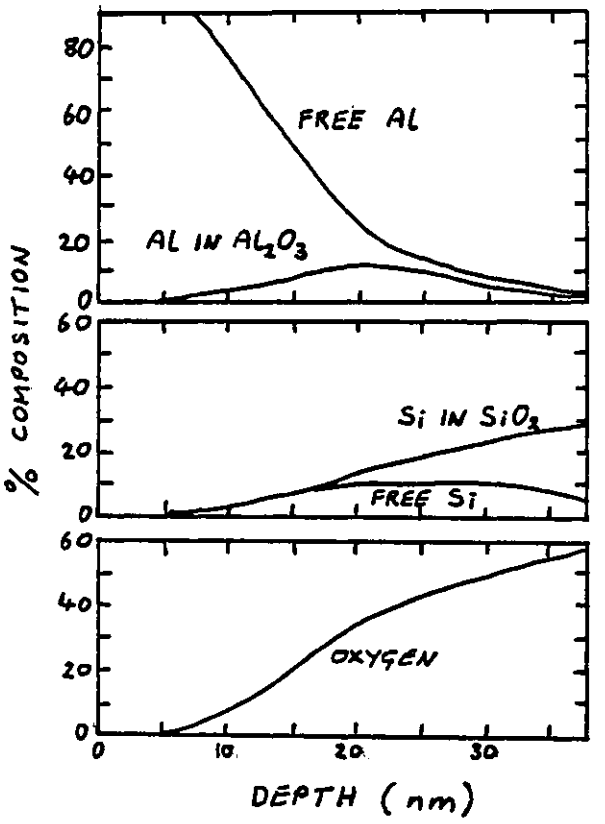

Atomic percentage composition of the two states of aluminium the two states of silicon and of oxygen as a function of distance through the Al-SiO_2 interface. (From Strausser et al 1978).

FIGURE 2.6

threshold of SiO_2 by aluminium atoms is thought to be 30 eV to 35 eV, there would have been considerable molecular motion at the surface but not enough for sputtering of SiO_2 to occur. On the basis of this model, the degree of intermixing, and hence the interface width, is expected to be smaller in the case of e-beam evaporated aluminium, as the kinetic energy of the incident atoms is only around 0.5 eV. The temperature of the top few atomic layers should therefore be lower and the rate of interdiffusion and reaction reduced. For example, the mean diffusion velocity of silicon in aluminium is 1300 nm s^{-1} at 773 K but only 16 nm s^{-1} at 473 K and the solubility of silicon in aluminium falls from 0.75% to 0.006% over the same temperature range (Van Gurp 1973).

However, the interface profiles for e-beam deposited aluminium films as determined by Strausser and Majumder are almost identical to those for sputter-deposited films. The authors suggested that the degree of intermixing may be controlled by the energy released by the reaction itself, rather than the kinetic energy of the incident aluminium atoms. This seems unlikely, however, since the energy released by the reduction reaction is only 1.9 eV per aluminium atom, which is small compared to the 20 eV kinetic energy of sputter-deposited aluminium atoms.

It is felt, therefore, that the authors' interpretation of the data is unsatisfactory and that the large interface widths observed were artefacts of the profiling process. Several types of sputter-induced damage have been observed during profiling experiments. For example, Grunthaner et al (1979) compared depth profiles of the $Si - SiO_2$ interface obtained by wet etching and ion etching techniques. Their results, obtained using high resolution XPS, showed that a 500 eV argon ion beam produced chemical changes at the interface, which the authors attributed to "knock-on" effects followed by reaction between the displaced atoms and the previously existing oxide phase at the interface. Cook et al (1980) observed roughening of the surface of amorphous SiO_2 during sputter-

profiling. A correlation between initial roughness and interface broadening was discovered by Hofmann et al (1977), who performed Auger sputter profiling on Ni-Cr multilayer sandwich structures using a 1 keV argon ion beam. Severe degradation of the interfaces was observed in some specimens, to the extent that 11.5 nm layers of nickel and chromium could hardly be resolved. The authors suggested re-deposition and re-sputtering as the cause of the broadening.

The initial stages of reaction at the Al - SiO_2 interface were studied by Bachrach and Bauer (1979) and Bauer et al (1980), using XPS under ultra high vacuum conditions. A {111} cleavage face of silicon was prepared in-situ at a pressure of 3×10^{-10} m bar (Bauer et al 1978) and oxidized by dosing with pulses of molecular oxygen. The oxide formed by this process has been characterized using XPS (Bauer et al 1979) and shown to consist of stoichiometric SiO_2, except at the interface region which extends over only one bond length. Aluminium was deposited from a water-cooled boron nitride molecular beam source onto the specimen at room temperature. The vacuum during deposition was better than 5×10^{-10} m bar. High resolution XPS was performed using 140 eV synchrotron radiation and a double-pass cylindrical mirror analyser.

Figure 2.7 shows a comparison of the time-evolution of the Al 2p core level spectra taken from two aluminium overlayers of different thicknesses on SiO_2. 40 minutes after deposition of the 0.15 nm overlayer, the aluminium had formed an intermediate chemical state, characterized by a chemical shift of 1.8 eV of the Al 2p binding energy. (The authors suggested that this state was similar to that obtained after 50L to 100L oxygen exposure of an aluminium film prepared in uhv conditions; Flodstrom et al 1976). After six or seven hours at room temperature, a chemical shift of 2.7 eV was observed, indicating the formation of Al_2O_3. The elemental silicon 2p peak was also detected, showing that reduction of the SiO_2 had occurred.

The XPS spectra from a 6 nm thick aluminium film did not change significantly

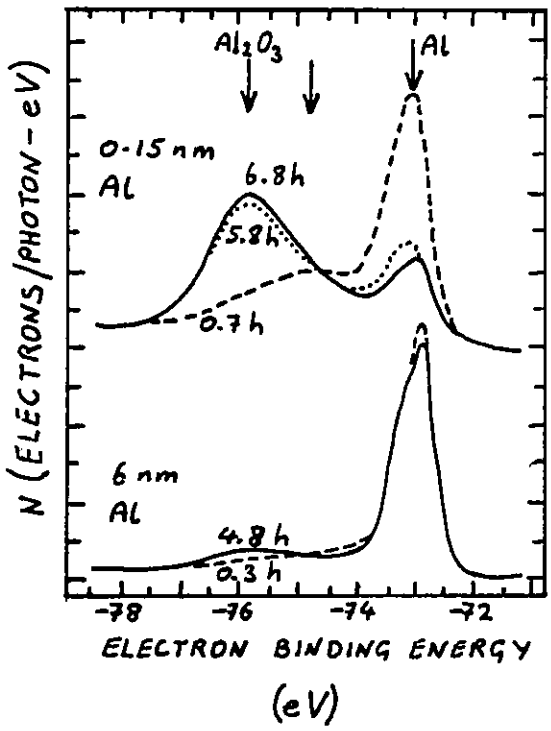

Time evolution of Al 2p core levels for two thicknesses of films deposited and measured at room temperature on oxidized silicon. (From Bachrach and Bauer 1979).

FIGURE 2.7

with time. It was therefore concluded that the chemical shifts observed in the spectrum of the 0.15 nm film were entirely due to interfacial reaction between aluminium and SiO_2.

The authors proposed the following model for the reaction. The intermediate oxidation state of the aluminium is thought to correspond to a geometry of oxygen within or above an aluminium {111} layer, the oxygen atoms occupying the sites between 3 close packed aluminium atoms. The initial stage of formation of the Al - SiO_2 interface is thus visualised as groups of three aluminium atoms clustered around oxygen atoms of SiO_2. Oxygen is then removed from the SiO_2, forming the thermodynamically more stable Al_2O_3 and liberating silicon. The interface then consists of a layer of elemental silicon residing between oxidized regions of silicon and aluminium.

To summarize, reaction at the Al- SiO_2 interface has been shown to produce Al_2O_3 and free silicon under certain conditions. The reaction proceeds at room temperature in clean uhv conditions (Bauer et al 1980). Under less ideal conditions, higher temperatures appear to be necessary for reaction to occur, but the results of different experimenters vary widely. Disparity also exists between the phases of alumina found at the interface. γ -alumina was identified by Chou and Eldridge (1970), while Prabriputaloong and Piggott (1974) observed the θ and α phases. Silverman (1968) observed silicon but could not detect any crystalline alumina.

CHAPTER 3

A STUDY OF THE Al - SiO_2 INTERFACE

USING X-RAY PHOTOELECTRON SPECTROSCOPY

3.1 Introduction

The aim of the experiments described in this chapter was to determine the chemical nature of the Al - SiO_2 interface using x-ray photoelectron spectroscopy (XPS). Thin (~1 monolayer) films of aluminium were deposited by in-situ evaporation onto thermally oxidized silicon in ultra high vacuum (uhv) conditions. The effects of temperature and surface contamination on the Al - SiO_2 reaction rate were investigated.

XPS (also known as electron spectroscopy for chemical analysis - or ESCA) is ideally suited to such an application, by virtue of its sensitivity to the chemical bonding or oxidation state of atoms, and its ability to "see through" a thin adsorbed layer and probe both the substrate and adsorbate. "Chemical shifts" of the 2p and 2s electron binding energies of silicon and aluminium were measured, enabling the chemical composition of the interface to be determined. Originally it was intended that Auger electron spectroscopy (AES) should also be employed, but because of electrostatic charging problems this technique was of limited use.

Al - SiO_2 reaction was detected at room temperature, the products being Al_2O_3 and elemental silicon. At higher temperatures complete oxidation of the aluminium overlayer was observed. The reaction was much slower for "as prepared" SiO_2, which had some surface contamination, than for ion bombarded SiO_2.

It is hoped that this study forms a useful extension to the work of Bauer et al (1980), the present results being directly relevant to Al - SiO_2 reactions in semiconductor devices.

3.2 XPS and AES as Techniques for Surface and Interface Analysis

There are many reviews of XPS and AES in the literature (e.g. Cardona and Ley 1978 and Chang 1971). The following descriptions are therefore brief and concentrate on particular aspects of the techniques pertaining to the system under investigation and the apparatus used.

3.2.1 Basic Principles of XPS

When a photon of energy $h\nu$ is incident on the surface of a solid containing atoms of type A, photoionization can occur :

$$A + h\nu \longrightarrow A^{+*} + e^{-}$$

The photoelectron may be ejected from the valence band (as in ultraviolet photoelectron spectroscopy - UPS) or from a core level, if the photon has sufficient energy. The ejection of core level electrons by x-ray photons is the basis of XPS. The photoelectrons emerge with one or more discrete values of kinetic energy, which are dependent upon the levels from which the electrons were ejected. Hence, energy analysis of the photoelectrons enables the atom of origin to be identified.

The energy level diagram for XPS is given in figure 3.1. The energy of the incident photon, $h\nu$, is imparted to a core level electron of binding energy E_b. This is the energy which is required to raise the electron to the Fermi level, and an additional amount of energy ϕ_s (the work function) is needed to promote the electron to the vacuum level. To conserve momentum, a small fraction of the electron energy is taken up by the recoil of the atom. (The recoil energy, E_r, is negligible for atoms heavier than lithium when Mg Kα incident radiation is being used). The remaining portion of the incident photon energy appears as the kinetic energy, E_k, of the emitted electron.

The spherical sector analyser (see section 3.4) transmits only electrons of energy P (the "pass energy" of the analyser). Electrons from the specimen, however, are

retarded by an energy R before they enter the spherical sector, and the work function, ϕ_a, of the analyser must also be taken into account. From figure 3.1 it can be seen that

$$E_b = h\nu - R - P - \phi_a - E_r \qquad (3.1)$$

If absolute binding energies are to be determined, all of the quantities on the right of equation 3.1 must be accurately known. In addition, any electrostatic charging of the specimen, due to electron emission, must be compensated for. For the purposes of the present study, however, we are concerned mainly with relative binding energies. (The XPS peaks of interest are readily identifiable, even though they may be shifted in energy by a few eV due to charging).

In addition to the true XPS peaks, photoelectron spectra may contain several other types of features. Photon-induced Auger transitions produce peaks which are independent of the photon energy (see section 3.2.4) and are therefore readily identifiable. Energy loss peaks due to bulk and surface plasmon excitation appear at well defined energies on the low kinetic energy side of the photoelectron peak with which they are associated. "Shake-up" satellite peaks may also occur if the incident photon causes excitation of a second electron, instead of imparting its full quantum of energy to the photoelectron. Shake-up satellites are usually of low intensity relative to the main XPS peak and appear at lower kinetic energies. X-ray satellite peaks are also seen in spectra recorded using non-monochromatic x-rays. These features are caused by photoemission of electrons by photons of various discrete energies present in the line spectrum of the incident radiation. The magnitude and energy of these satellites therefore depends on the target material of the x-ray source.

3.2.2 Chemical Shifts in XPS

"Chemical shift" is the term applied to the change in binding energy of a core

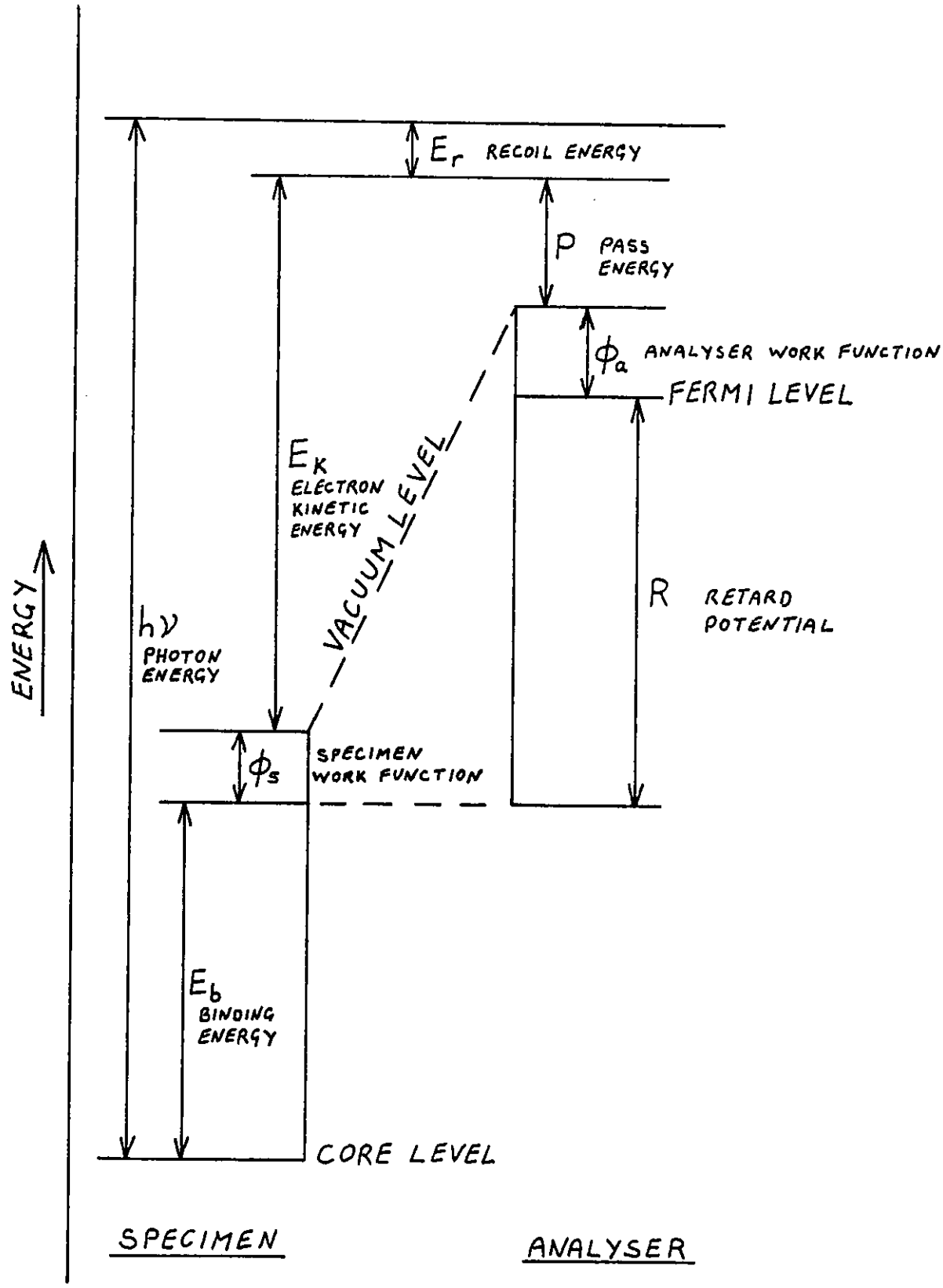

$$h\nu = E_b + R + \phi_a + P + E_r$$

Energy level diagram for XPS

FIGURE 3.1

electron resulting from a change in the chemical environment of the atom. A core electron experiences an attractive force due to the positive charge on the atomic nucleus. The nuclear charge, however, is screened to some extent by the valence electrons of the atom. The resulting force gives the binding energy, E_b, of the core electron. Removal of one or more of the valence electrons (as occurs, for example, in a metal during ionic bonding) reduces the screening charge and hence increases the core electron binding energy.

The effect is similar for the oxidation of a metallic solid, but here the process involved is not the complete removal of valence electrons from an individual atom, but the transfer of conduction electrons from the vicinity of the metal ion core to the oxide anion. It has been observed (Johnson 1975) that the chemical shifts observed on the formation of ionic oxides are roughly proportional to the number of electrons transferred. On average, a chemical shift of 1 eV occurs for each electron donated by the metal ion.

The binding energies of the XPS peaks made use of in the present study are listed in table 3.1, along with the chemical shifts (where appropriate).

3.2.3 Surface Sensitivity and Quantitative XPS

The incident x-rays penetrate far into the specimen, so the sampling depth is determined solely by the inelastic mean free paths of the ejected electrons and the angles at which they emerge from the surface. In the present experiments, the specimen was arranged such that electrons travelling normal to the surface were detected by the analyser. This condition is taken to apply in the following calculations. The inelastic mean free path of an electron is dependent upon its kinetic energy and the material through which it is travelling. The mean free paths of electrons used in the present work, when ejected by Mg Kα radiation, were determined from data compiled by Seah and Dench (1979). The values, listed in table 3.1, are in the range 1.5 nm to 2.0 nm. Therefore, the depth of material sampled in XPS is of the order of several

Element	Chemical State	Level	Binding Energy (eV)	Mean Free Path (nm)	Relative Analyser Trans--mission Function	Sub-shell Photo--ionization X-section
Silicon	Free Si	$2p_{3/2}$	99	2.0	0.8	} 0.232
		$2p_{1/2}$	100	2.0	0.8	
		2s	149	2.0	0.8	0.199
Silicon	SiO_2	2p	103.5	2.0	0.8	0.232
		2s	154.6	2.0	0.8	0.199
Aluminium	Al metal	$2p_{3/2}$	73	2.0	0.8	} 0.156
		$2p_{1/2}$	74	2.0	0.8	
		2s	118	2.0	0.8	0.171
Aluminium	Al_2O_3	2p	75.8	2.0	0.8	0.156
Oxygen	Free	1s	532	1.5	1.0	0.55
Carbon	Free	1s	284	1.7	0.85	0.222

XPS data used in the present study.

TABLE 3.1

Element	Auger Transition	Kinetic Energy (eV)	Mean Free Path (nm)
Silicon	KLL	1605	2.5
	LVV	92	0.4
Aluminium	KLL	1388	2.3
	LVV	67	0.4
Oxygen	KLL	516	1.0
Carbon	KLL	268	0.8
Argon	LMM	215	0.8

AES data used in the present study.

TABLE 3.2

nanometres.

The area under an XPS peak of a given binding energy is proportional to the number of electrons of that binding energy detected by the analyser. Therefore, XPS peak areas can be used as a measure of the electron signal from any type of atom, provided the transmission function of the analyser is taken into consideration. For the spherical sector analyser, the transmission function varies inversely as the square root of the electron kinetic energy (Hughes and Phillips 1982).

Consider a monolayer of atoms of type A on the surface of a thick substrate of unit area containing atoms of type B. The surface is uniformly irradiated by a beam of monochromatic x-rays of flux .

The number of electrons of binding energy E_b^A (and kinetic energy E_k^A) ejected from the monolayer per unit time is given by

$$J_o^A = \Phi \sigma(E_b^A) n^A \qquad (3.2)$$

where n^A is the number of A atoms in the monolayer and $\sigma(E_b^A)$ is the photoionization cross section of the energy level of binding energy E_b^A.

The electron signal, I_o^A, detected by the analyser is some fraction f T (E_k^A) of J_o^A, where f is the fraction of the electrons leaving the specimen which enter the analyser and T (E_k^A) is the transmission function for electrons of kinetic energy E_k^A.

Hence, $$I_o^A = f\ T(E_k^A)\ \Phi \sigma(E_b^A) n^A \qquad (3.3)$$

Now consider the signal I_o^B from the first layer of B atoms in the substrate. The incident x-radiation flux can be taken to be the same at all points in the specimen as the x-rays are only weakly absorbed. The number of electrons ejected from this layer per unit time is

$$J_o^B = \Phi \sigma(E_b^B) n^B \qquad (3.4)$$

where $\sigma(E_b^B)$ is the photoionization cross section for the energy level E_b^B and n^B is the number of B atoms in a monolayer of unit area. The signal detected by the analyser is therefore given by

$$I_o^B = f\,T(E_K^B)\,\Phi\,\sigma(E_b^B)\,n^B\,\exp\left[-z^A/\lambda^A(E_K^B)\right] \tag{3.5}$$

where $\lambda^A(E_k^B)$ is the inelastic mean free path in material A of electrons of kinetic energy E_k^B, $T(E_k^B)$ is the analyser transmission function for these electrons and z^A is the thickness of the overlayer (which, in this instance, is the thickness of one monolayer of A atoms).

The total signal, I_∞^B, from the substrate is therefore given by

$$I_\infty^B = \int_o^\infty f\,T(E_K^B)\,\Phi\,\sigma(E_b^B)\,N^B\exp\left[-z^A/\lambda^A(E_K^B)\right]\exp\left[-z/\lambda^B(E_K^B)\right]dz \tag{3.6}$$

where $\lambda_B(E_k^B)$ is the mean free path of electrons of kinetic energy E_k^B in material B and N^B is the number of B atoms per unit volume. (The integral can be taken to infinity since the substrate thickness and x-ray penetration depth are very large compared with the electron mean free paths).

Therefore

$$I_\infty^B = f\,T(E_K^B)\,\Phi\,\sigma(E_b^B)\,N^B\lambda^B(E_K^B)\exp\left[-z/\lambda^A(E_K^B)\right] \tag{3.7}$$

For the case where the adsorbate is in the form of a layer of uniform thickness z^A (which is now equal to several monolayer thicknesses), the signal intensity from the adsorbate is given by

$$I_{z^A}^A = \int_o^{z^A} f\,T(E_K^A)\,\Phi\,\sigma(E_b^A)\,N^A\exp\left[-z/\lambda^A(E_K^A)\right]dz \tag{3.8}$$

i.e.

$$I_{z^A}^A = f\,T(E_K^A)\,\Phi\,\sigma(E_b^A)\,N^A\lambda^A(E_K^A)\left\{1-\exp\left[-z^A/\lambda^A(E_K^A)\right]\right\} \tag{3.9}$$

where N^A is the number of A atoms per unit volume.

The signal from the substrate is still given by equation 3.7.

For an adsorbate consisting of islands of monolayer thickness covering a fraction X of the substrate surface, the expressions for the electron signals become

$$I^A = X f T(E_k^A) \Phi \sigma(E_b^A) n^A \qquad (3.10)$$

and

$$I_\infty^B = f T(E_k^B) \Phi \sigma(E_b^B) N^B \lambda^B(E_k^B) \{1 - X + X \exp[-z^A/\lambda^A(E_k^B)]\} \qquad (3.11)$$

Hence, the fractional coverage is given by

$$X = \frac{T(E_k^B)\,\sigma(E_b^B)\,N^B\lambda^B(E_k^B)}{(I_\infty^B/I_x^A)\,T(E_k^A)\,\sigma(E_b^A)\,n^A + T(E_k^B)\,\sigma(E_b^B)\,N^B\lambda^B(E_k^B)\{1 - \exp[-z^A/\lambda^A(E_k^B)]\}} \qquad (3.12)$$

The transmission function and subshell photoionization cross sections (from Evans et al 1978) for photoelectrons observed in the present study are given in table 3.1.

3.2.4 Basic Principles of AES

In section 3.2.1 the ionization of an atom by an incident photon was considered. Ionization may also be caused by electron bombardment :

$$A + e_1^- \longrightarrow A^{+}* + e_1^- + e_2^-$$

The resulting excited ion may relax either by x-ray fluorescence :

$$A^{+}* \longrightarrow A^{+} + h\nu$$

or by Auger electron emission :

$$A^{+}* \longrightarrow A^{++} + e^-$$

The two competing processes occur with different probabilities, depending on the element and the energy levels involved. The x-ray fluorescence yield decreases

for elements of low atomic number, Z. The Auger process tends to become less efficient for higher Z elements, but the Auger yield can be kept fairly constant with Z if low energy transitions are chosen.

The energy level diagram for a $KL_1L_{2,3}$ Auger transition in silicon is shown in figure 3.2 (taken from Chang 1974). The energy, E, of the Auger electron can be estimated, assuming the energy level diagram to be approximately valid during the transition.

The primary electron creates a hole in the K shell core level. This hole is filled by an L_1 electron with the release of an amount of energy $(E_K - E_{L_1})$. This energy is imparted to the Auger electron, which is ejected from the $L_{2,3}$ level. The Auger electron must expend an energy $(E'_{L_{2,3}} + \phi)$ to escape from the atom, where ϕ is the work function. Now $E'_{L_{2,3}}$ is not equal to $E_{L_{2,3}}$ because of the extra positive charge on the atom. Instead, $E'_{L_{2,3}}$ will be approximately equal to $E_{L_{2,3}}$ of the next heavier atom, which has an extra positive charge on the nucleus,

i.e. $$E'_{L_{2,3}}(Z) \simeq E_{L_{2,3}}(Z+1) \qquad (3.13)$$

Hence, the Auger electron energy is given by :

$$E(Z) \simeq E_K(Z) - E_{L_1}(Z) - E_{L_{2,3}}(Z+1) - \phi \qquad (3.14)$$

Or, for any Auger transition WXY :

$$E_{WXY}(Z) \simeq E_W(Z) - E_X(Z) - E_Y(Z+1) - \phi \qquad (3.15)$$

An even better approximation (due to Chung and Jenkins 1970) is :

$$E_{WXY}(Z) \simeq E_W(Z) - \tfrac{1}{2}\left[E_X(Z) + E_Y(Z) + E_X(Z+1) + E_Y(Z+1)\right] - \phi \qquad (3.16)$$

The Auger electron energy is thus independent of the energy of the primary electron (or incident photon) and is characteristic of the element of origin. The energies of the Auger electrons detected in the present work, and their mean free paths, are listed

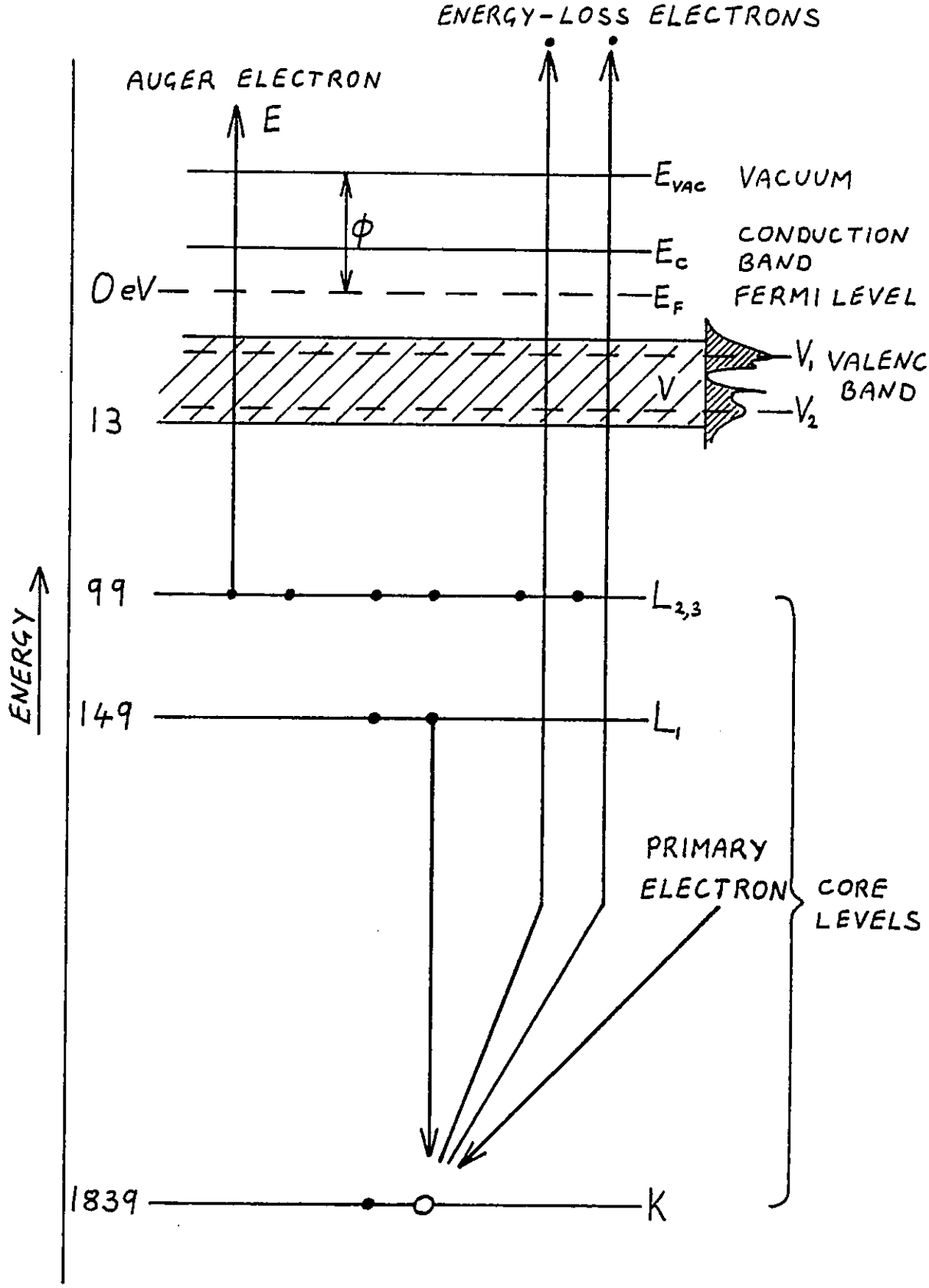

KL L Auger process in silicon, after primary electron ionization

FIGURE 3.2

in table 3.2. The primary electron beam of energy 3 keV has a mean free path of around 3 nm, but the short ($\sim$ 0.5 nm) escape depths of the Auger electrons make AES a highly surface sensitive technique.

The energy of an Auger electron is sensitive to the chemical environment of the atom, particularly when the transition involves the valence band. Therefore, AES can yield information on chemical bonding. In the present study, however, AES was used merely as a "fingerprint" technique to identify contaminants etc. present on surfaces.

The signal, I(E) detected by the spherical sector analyser is dependent upon the number of electrons, N(E), of kinetic energy E ejected from the specimen per unit time, and the "energy window", ΔE, of the analyser. (See section 3.4).

i.e. $$I(E) \propto \Delta E \, N(E) \qquad (3.17)$$

The Auger peaks are small but relatively sharp features superposed on the slowly varying background of secondary electron intensity. Hence, the Auger peaks are more easily detected if $N'(E)$ $\left[= d\,N(E)/dE\right]$ is plotted rather than N(E). In practice, this is achieved electronically by applying a small modulating voltage $k \sin \omega t$ to the analyser. The first harmonic of the output current is detected, using a lock-in amplifier, to give a signal proportional to $N'(E)$ plus some error terms dependent upon the exact modulation-detection scheme employed.

3.3 Apparatus

The experiments were performed in a V-G Scientific ESCALAB 5 Spectrometer, shown schematically in figure 3.3. The instrument comprised two vacuum chambers, one used for specimen preparation, and the other for analysis by XPS and AES. Specimens were transferred between the two chambers on a carriage operated by a rotary motion feedthrough. The chambers could be isolated from one another by a gate valve and each chamber was individually pumped.

FIGURE 3.3

The ESCALAB 5

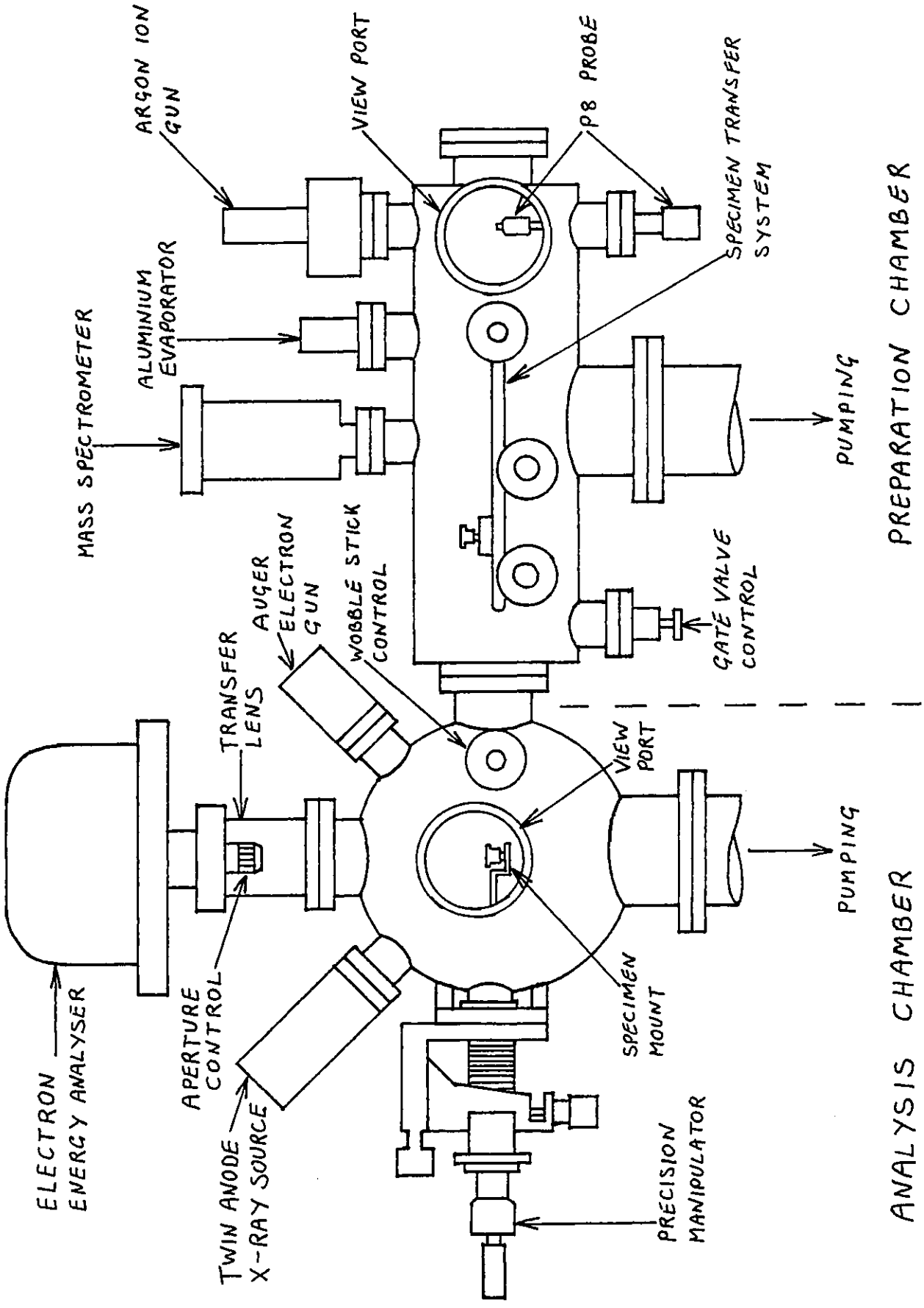

Each pumping system consisted of a 4-inch diffusion pump, charged with "Santovac 5" polyphenyl ether pumping fluid, backed by a 2-stage rotary pump through a zeolite filter. A liquid nitrogen cold trap was used to improve the pumping efficiency for water vapour and prevent backstreaming of oil vapour. Additional pumping was provided by titanium getters which were activated for 2 minutes every 4 hours. The system could be baked at 450 K to outgas the internal surfaces and thus improve the vacuum. The pressure was measured by an ionization gauge in each chamber. The vacuum after bakeout was better than 3×10^{-11} m bar.

The preparation chamber was fitted with an AG2 sputter ion gun for specimen surface preparation. Research grade argon was fed into the gun via an MD5 leak valve and the high tension (up to 10 kV) was supplied by an AGS2 unstabilized power supply. A P8 specimen heater probe allowed temperatures of up to $\sim$ 850 K to be obtained, as measured by a chromel-alumel thermocouple incorporated in the probe. The P8 probe also allowed rotation of the specimen, for example during argon ion bombardment. A liquid nitrogen-cooled evaporator, a shutter and a quartz crystal film thickness monitor were also installed in the preparation chamber. (For details of the film thickness monitor see section 4.2.2 and Appendix B). A V-G QX 200 quadrupole mass spectrometer was available for residual gas analysis in the preparation chamber.

The analysis chamber was constructed from mu-metal in order to provide magnetic shielding. It contained an LEG61 electron gun for AES and a dual anode (magnesium and aluminium) x-ray source for XPS. The x-ray source was isolated from the main chamber by a thin aluminium foil window and was pumped by a small ion pump. This arrangement prevented outgassing of the x-ray source from adversely affecting the pressure in the analysis chamber. The specimen was mounted on a high precision manipulator during analysis by XPS and AES. Specimens were transferred between the

manipulator and the carriage by means of a "wobble stick" fitted with a fork which engaged with the specimen mounting stud. The 150° spherical sector analyser was mounted above the analysis chamber in a mu-metal housing.

The electronics, manufactured by Vacuum Generators, comprised power supplies for the spectrometer, electron gun and x-ray sources, and detection circuitry for measuring the analyser output signal in XPS and AES modes. Spectra were plotted on a Bryans 26000 X-Y recorder and a digital voltmeter gave direct readout of kinetic energy (AES mode) or binding energy (XPS mode).

3.4 Operating Principles of the Spectrometer

The spherical sector analyser is central to the operation of the ESCALAB, being used for both XPS and AES. The analyser, shown schematically in figure 3.4, functions as a band-pass filter for electrons whose energies lie in a narrow band, Δ E, around the pass energy of the spherical sector. The pass energy is determined by the physical dimensions of the analyser and by the potential difference applied between the inner and outer hemispheres. Both the energy resolution and the sensitivity of the analyser are dependent upon the pass energy, sensitivity increasing and resolution decreasing as the pass energy is increased. The resolution is also controlled by the size of the entrance and exit slits of the analyser.

Electrons from the specimen pass through an electrostatic lens where they are retarded before they enter the spherical sector. An XPS spectrum is obtained by sweeping the retard voltage on the lens, the pass energy being kept constant. In this way the energy resolution remains constant over the scan. For the present experiments a pass energy of 20 eV and 4 mm entrance and exit slits were used. The energy resolution claimed by the manufacturers for these operating conditions is 1.2 eV. The largest contribution to this is from the 0.8 eV line width of Mg $K\alpha_{1,2}$ radiation.

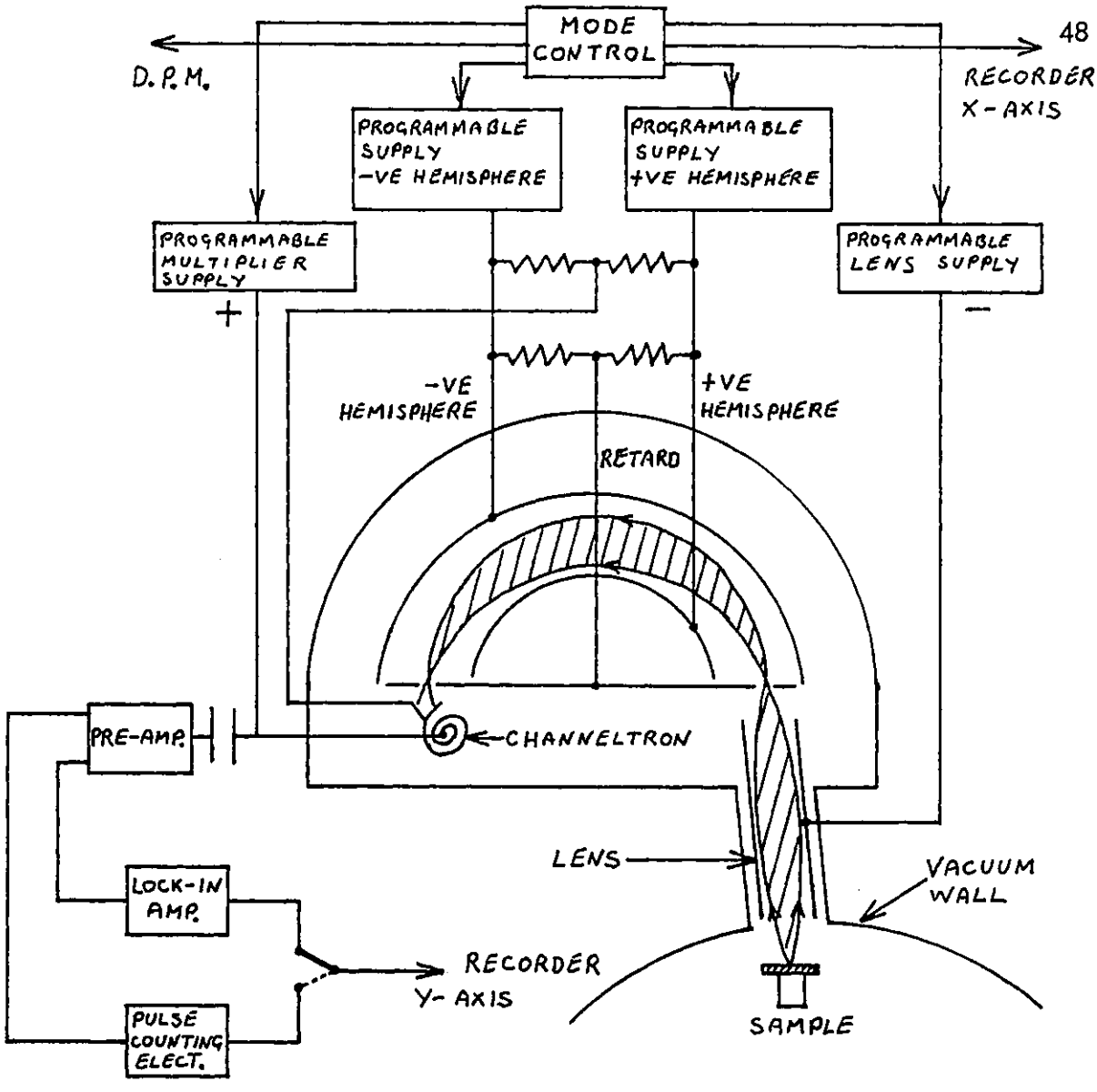

The ESCALAB analyser and control electronics

FIGURE 3.4

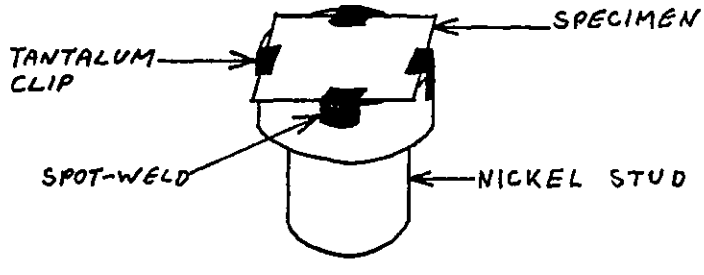

Method of specimen mounting

FIGURE 3.5

The number of electrons entering the analyser at low kinetic energies rises steeply because of the large number of slow secondary electrons emitted by the specimen. In the "constant analyser energy" (CAE) mode of operation described above, this leads to a very large signal being produced at low energies. For XPS this is generally unimportant, since most of the interesting XPS peaks lie close to the incident photon energy at around 1250 eV.

In AES, however, many of the features of interest occur at low kinetic energies. The problem of secondary electron background is overcome by operating the analyser in the "constant retard ratio" (CRR) mode, in which the ratio of kinetic energy to pass energy is kept constant. This has the desired effect of reducing the sensitivity at low energies. However, the energy resolution is no longer constant over a spectrum, being best at low kinetic energies.

Having passed through the spherical sector, electrons of the selected energy are incident on a channel electron multiplier (channeltron) which amplifies the electron current. In XPS, the current leaving the exit slit of the analyser is typically 10^{-16}amps to 10^{-14}amps. The channeltron is operated at a gain of around 10^{8}, and pulse counting techniques are used to measure the signal. In AES, where the currents are larger, the channeltron is operated at reduced gain and synchronous detection is employed.

3.5 Experimental Method

The SiO_2 substrate material consisted of a 1 μm layer of steam-grown oxide on a polished, n-type, $\{111\}$ -oriented silicon wafer. (See Appendix A for details of oxide growth). The wafer was scribed and broken into 1 cm squares, using a diamond scriber. Three such substrates were mounted on nickel specimen studs using tantalum clips (see figure 3.5). Two clean n-type $\{111\}$ silicon substrates were prepared in a similar way.

The tungsten helical coil of the liquid nitrogen-cooled evaporator was outgassed by flashing at white heat in vacuo and was loaded with 99.995% purity aluminium wire. The evaporator was fitted to the preparation chamber, the substrates were inserted, and the system was evacuated. When the pressure in the analysis and preparation chambers had fallen to 5×10^{-8} m bar, the evaporator and the titanium sublimation pumps were outgassed. The system was then baked at 450 K for 24 hours. After allowing time to cool and filling the liquid nitrogen traps, the pressure was less than 10^{-10} m bar in each chamber. The titanium sublimation pumps were outgassed again and then activated, reducing the pressure to 3×10^{-11} m bar. The aluminium evaporator and specimen heater probe were outgassed to less than 10^{-10} m bar before experiments were started.

Ion bombardment was performed using a partial pressure of 5×10^{-6} m bar of argon in the preparation chamber. (The pressure in the ion gun was greater than this as the gas was admitted through the gun). The chamber was pumped by the diffusion pump during ion bombardment to maintain cleanliness. The ion current, measured at the specimen, was 20 μA for an ion energy of 3 keV. Higher energies were not used as the ions tended to become trapped in the substrate surface. Substrates were rotated on the P8 probe during ion bombardment to achieve maximum uniformity of sputtering. Ion bombardment for 200 seconds removed all traces of carbon contamination from SiO_2 and carbon and oxygen from silicon, as detected by XPS and AES.

Two of the three SiO_2 substrates were argon ion bombarded immediately before aluminium deposition. The third was used in the "as prepared" condition. Both silicon substrates were ion bombarded before use.

To deposit aluminium, the substrate was positioned under the evaporator on the specimen transfer carriage. (The other substrates were removed to the analysis chamber and the isolation valve closed to prevent contamination). The cooling jacket of the evaporator was filled with liquid nitrogen and the evaporator current was increased

until the desired deposition rate was indicated by the quartz crystal monitor. The shutter was then opened until a film of the desired thickness had been deposited. Deposition rates ranged from 0.05 nm s^{-1} to 0.2 nm s^{-1} and mean film thicknesses from 0.2 nm to 0.4 nm. The spread in values arose from errors in the monitor due to heating of the quartz crystal by the evaporator. Substrates were not purposely heated during deposition, but the evaporator caused a small temperature rise. The pressure in the preparation chamber remained below 7×10^{-10} m bar during evaporation and recovered to 3×10^{-11} m bar within several minutes. Only then was the isolation valve opened, so that the analysis chamber pressure never rose above 3×10^{-11} m bar.

The aluminium on SiO_2 or aluminium on silicon specimen was transferred to the analysis chamber and examined by XPS (and in some cases AES). XPS was performed using Mg $K\alpha$ radiation (1253.6 eV) and Al $K\alpha$ radiation (1486.6 eV). The Mg $K\alpha$ line is sharper, giving better energy resolution, and was used to produce the majority of the spectra. Al $K\alpha$ radiation was used to check the presence of "artefacts" (e.g. $K\alpha_3$ x-ray satellites and x-ray-induced Auger peaks) in the spectra, as these shift relative to the true photoelectron peaks when radiation of a different wavelength is used. The x-ray source was operated at an anode voltage of 15 kV and an emission current of 20 mA. The analyser was operated in CAE mode when taking XPS spectra. The specimen was positioned so as to maximize the Si 2p peak and minimize signals from the tantalum and nickel components of the specimen mount. Good signal-to-noise ratio ($\sim$50 : 1) was obtained by taking 10 minutes to scan each spectrum so that a long time constant (typically 3 seconds) could be employed in the detection circuitry.

XPS spectra were repeated after successive intervals of several hours, the specimen being maintained at room temperature. Changes in the shapes and relative positions of peaks were noted. When no further changes occurred, the specimen was transferred to the P8 probe for annealing treatment. After being allowed to cool to

room temperature, the specimen was replaced on the manipulator and the XPS spectrum again recorded. The procedure was repeated using various annealing times and temperatures and changes in the spectra were noted. Care was taken to locate the specimen in the same position each time the XPS spectrum was recorded, so that the same area of the specimen was analysed. The high precision manipulator was essential for this purpose.

3.6 Results

The results for argon ion bombarded SiO_2, "as prepared" SiO_2 and clean silicon substrates will be discussed individually in sections 3.6.1 to 3.6.3.

For all SiO_2 substrates, it was impossible to obtain an Auger spectrum after aluminium had been deposited, although Auger spectra were readily obtained from aluminium on silicon specimens. The effect is attributed to electrostatic charging of small islands of aluminium on an insulating layer of SiO_2, as a result of secondary electron emission by the primary electron beam. When clean n-type silicon (resistivity 3 Ω cm) was the substrate, charging did not occur. Auger spectra were also obtainable from SiO_2 substrates before aluminium was deposited, presumably because the secondary electron yield of SiO_2 is small compared to that of aluminium. No charging problems were encountered in obtaining XPS spectra.

3.6.1 Aluminium on Argon Ion Bombarded SiO_2

The XPS spectrum from an argon ion bombarded SiO_2 substrate is shown in figure 3.6. The Ta 4f peak at 25 eV binding energy and Ta $4d_{3/2}$ and $4d_{5/2}$ at 242 eV and 230 eV originate from the tantalum clips used to mount the specimen. Using relative peak areas (see section 3.2.3) it was calculated that the area of tantalum "seen" by the analyser was approximately 1/70 of the area of SiO_2. It was later found possible to reduce the tantalum signals even further, by careful positioning of the specimen.

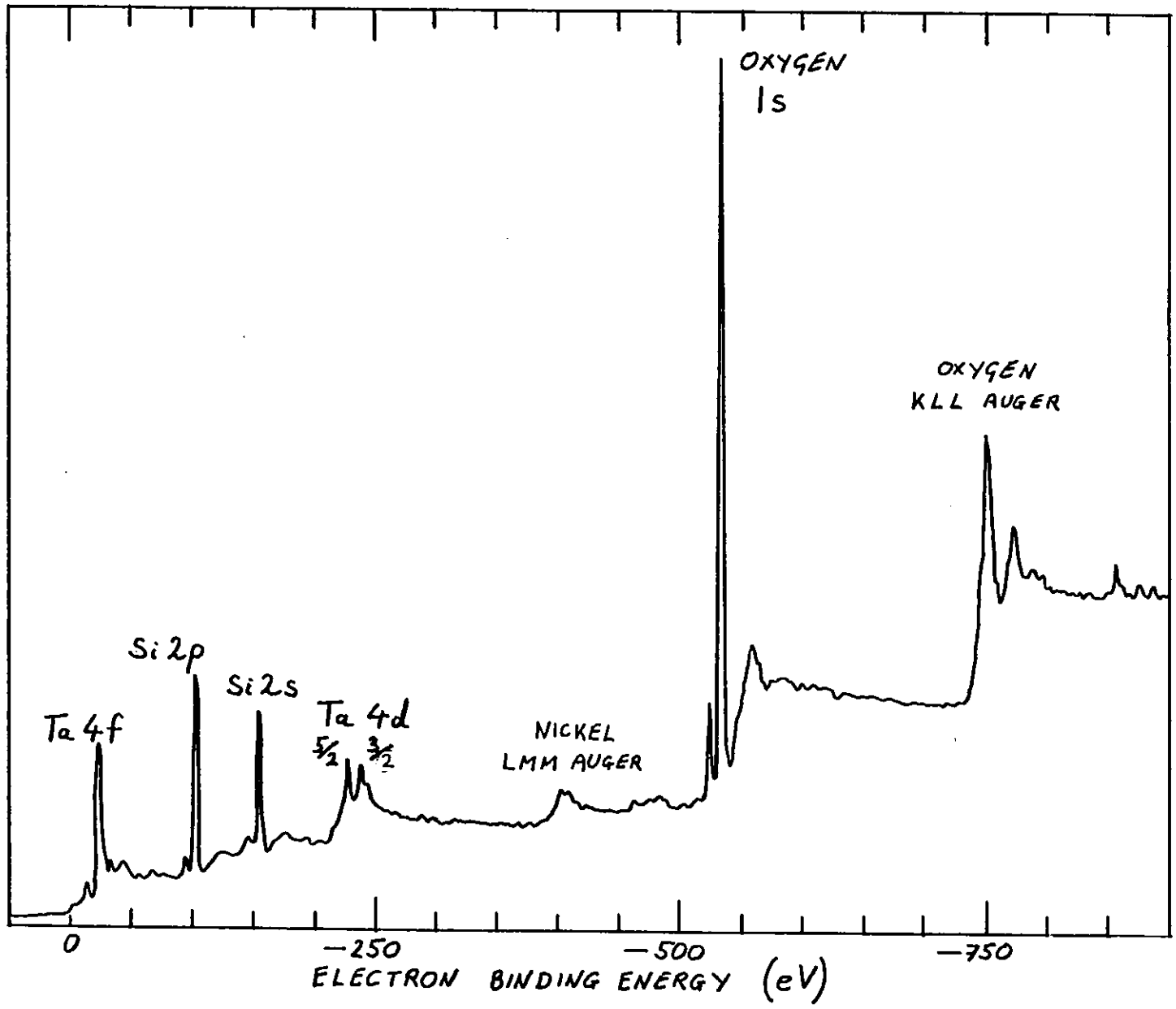

XPS spectrum from ion-bombarded SiO_2

FIGURE 3.6

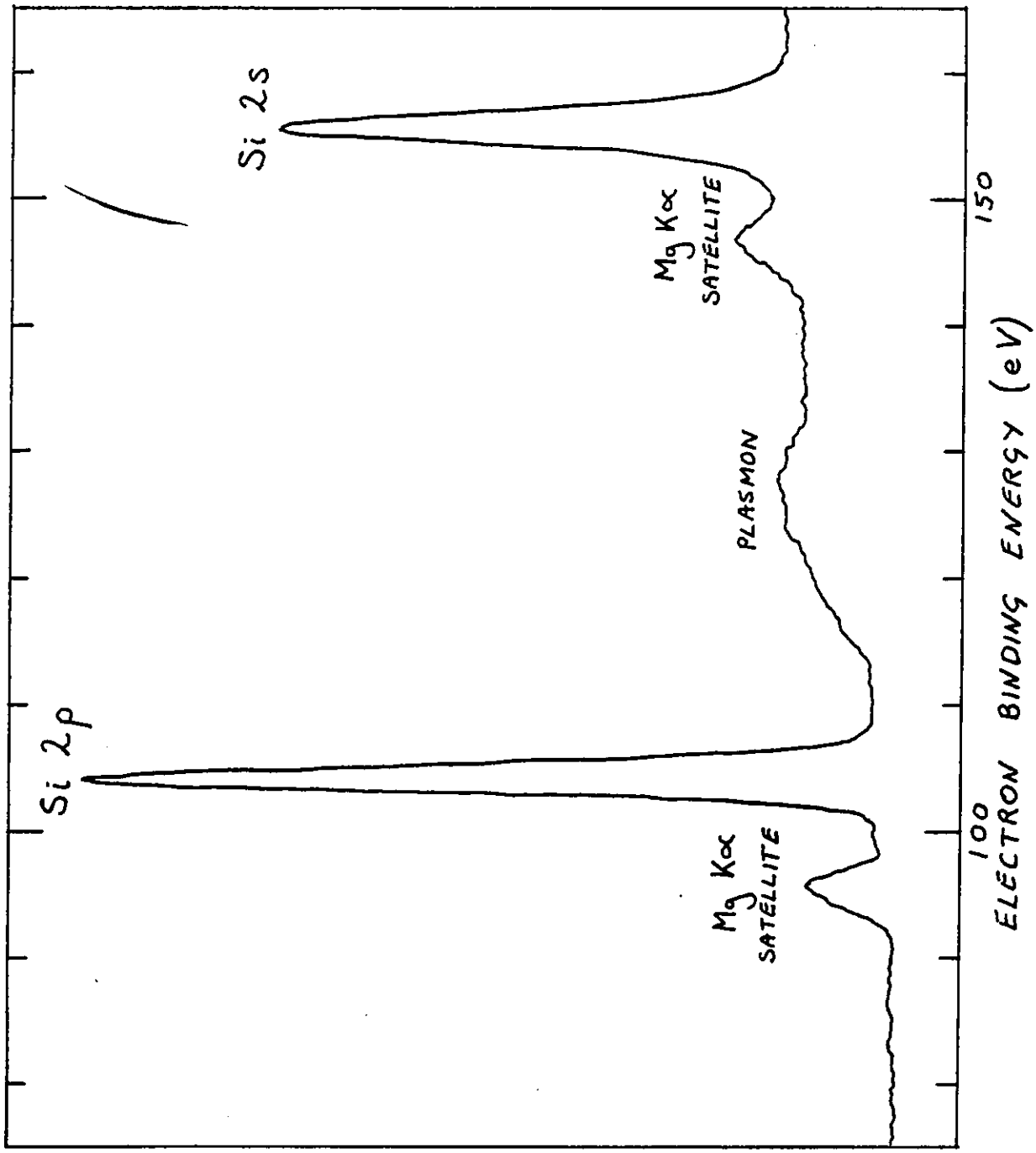

Silicon 2s and 2p spectra from ion-bombarded SiO_2

FIGURE 3.7

Nickel XPS peaks were totally absent from the spectrum, again because of specimen positioning.

The silicon 2s and 2p peaks are shown in greater detail in figure 3.7. These peaks are situated at 154.6 eV and 103.1 eV respectively and therefore exhibit the 3.8 eV chemical shift corresponding to SiO_2 (Siegbahn 1972). Elemental silicon peaks at 150.8 eV and 99.2 eV are totally absent from the spectrum. The peaks at approximately 146 eV and 95 eV are x-ray satellites due to Mg $K\alpha_3$ radiation (1262 eV) in the spectrum from the x-ray source. The broad features around 125 eV and 175 eV are plasmon loss peaks associated with the Si 2p and 2s peaks respectively.

The XPS spectrum after the deposition of 0.5 nm of aluminium is shown by curve A of figure 3.8. In addition to the Al 2p and Al 2s peaks at 73 eV and 118 eV respectively, a small elemental silicon 2p peak is visible at around 99.2 eV and the Si 2s peak at 154.6 eV has developed a shoulder on the low binding energy side, also indicating the presence of free silicon. Comparison with curve A of figure 3.15, taken from an ion bombarded thick aluminium film, shows the Al 2p and 2s peaks to be slightly broader than those of pure aluminium. The broadening is attributed to the presence of an oxide of aluminium, the chemically shifted peaks of which are not resolvable from the pure aluminium peaks.

Curves B to D (figure 3.8) show how the spectrum changed with time, the specimen being maintained at room temperature in a vacuum of 3×10^{-11} mbar. An increase in the broadening of the Al 2p peak is seen in curve B (taken after 19 hours). After 42 hours (curve C) the Al 2p peak has developed a high energy shoulder. This feature finally splits off to form a subsidiary peak at around 75.5 eV after 91 hours (curve D). This peak is thought to be due to Al_2O_3 as it has a chemical shift of approximately 2.5 eV.

The effects of subsequent heating of the specimen are shown in curves E to I.

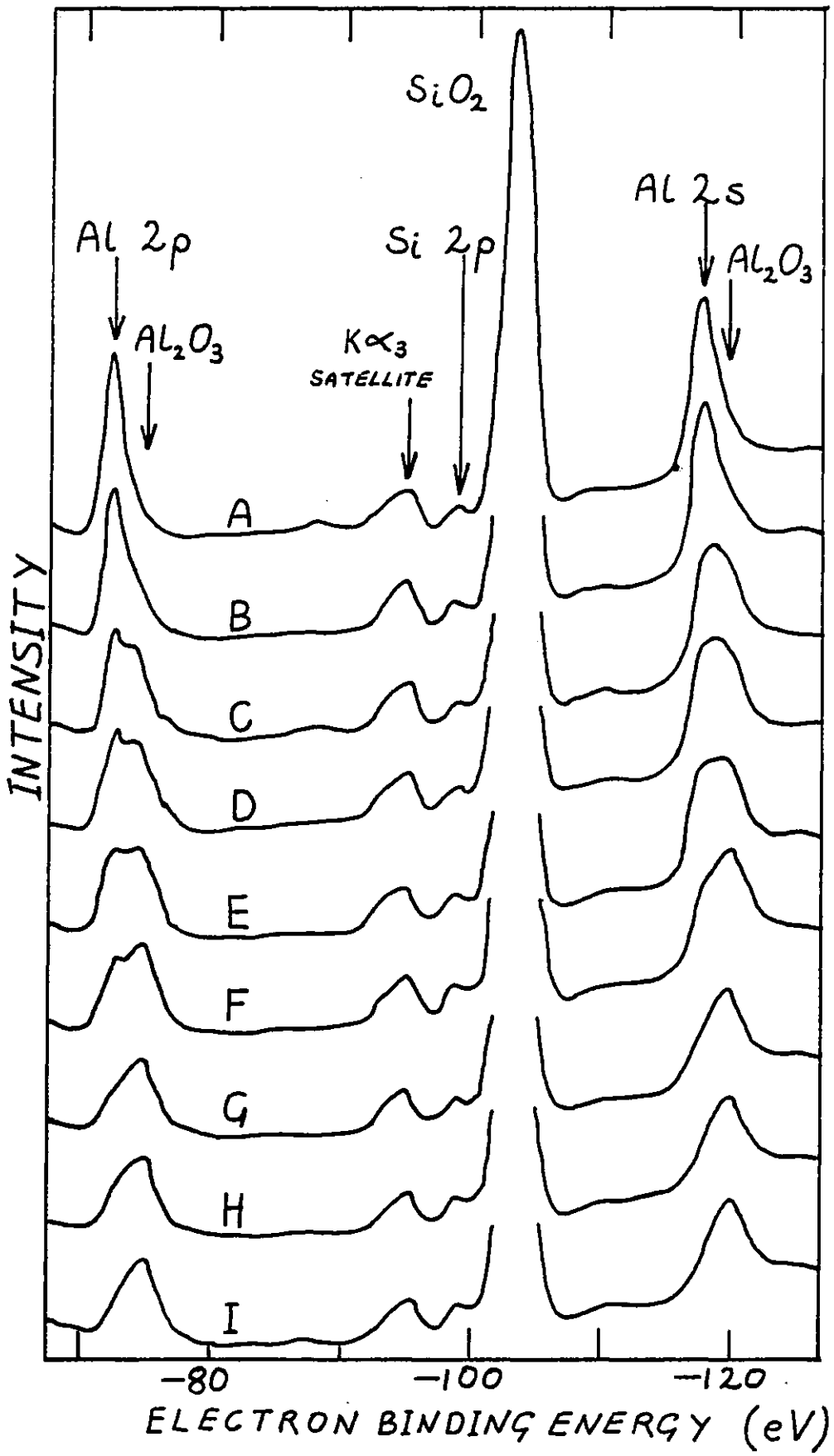

XPS spectra recorded at various times after the deposition of 0.5nm of Al onto ion-bombarded SiO_2 at room temperature.

A,30 min; B,19 h; C,42 h; D,91 h at room temperature.

E,30 min at 525 K; F,16 h at 525K; G,30 min at 575K; H,30 min at 650K; I,30 min at 750K.

FIGURE 3.8

After heating at 525 K for 30 minutes, the Al_2O_3 peak has grown to the same height as the pure aluminium peak (curve E) and after 16 hours at this temperature the Al_2O_3 feature is dominant. Curves G to I, recorded after heating for 30 minutes at 575 K, 650 K and 750 K respectively, show the disappearance of the elemental aluminium 2p peak and the growth of the chemically shifted Al_2O_3 peak.

It should be noted that aluminium must also have been deposited onto the tantalum clips and exposed areas of the nickel stud. This aluminium would not undergo interfacial reaction, but remain as metallic aluminium, thus increasing the unshifted Al 2p signal. However, as the areas of tantalum and nickel seen by the analyser were small ($\lesssim 1/70$) compared to the area of SiO_2, the error in the recorded aluminium signals is negligible.

The Al 2s peak was also seen to undergo changes of shape during the course of reaction. The effects were not so pronounced as for the Al 2p peak, however, because the superposition of the Si 2p plasmon loss peak on the Al 2s peak distorted the shape of the latter. The small elemental silicon 2p peak was seen to increase only slightly as the reaction proceeded.

The results from a second experiment, in which 0.2 nm of aluminium was deposited onto ion bombarded SiO_2, are shown in figure 3.9. Since the mean thickness of the deposit was smaller, the aluminium peak shapes were more sensitive to small amounts of aluminium oxide formed at the interface. Hence, a significant broadening of the Al 2p peak was evident even in the initial stages of reaction (curve A). The changes in the shape of the peaks observed during reaction at room temperature (curves A to E) and on heating (curves F to G) occurred over a similar time scale to those seen for the 0.5 nm aluminium deposit. The final chemical shift of the Al 2p peak was again 2.5 eV.

3.6.2 Aluminium on "As Prepared" SiO_2

The SiO_2 substrate in the "as prepared" condition gave the XPS spectrum shown

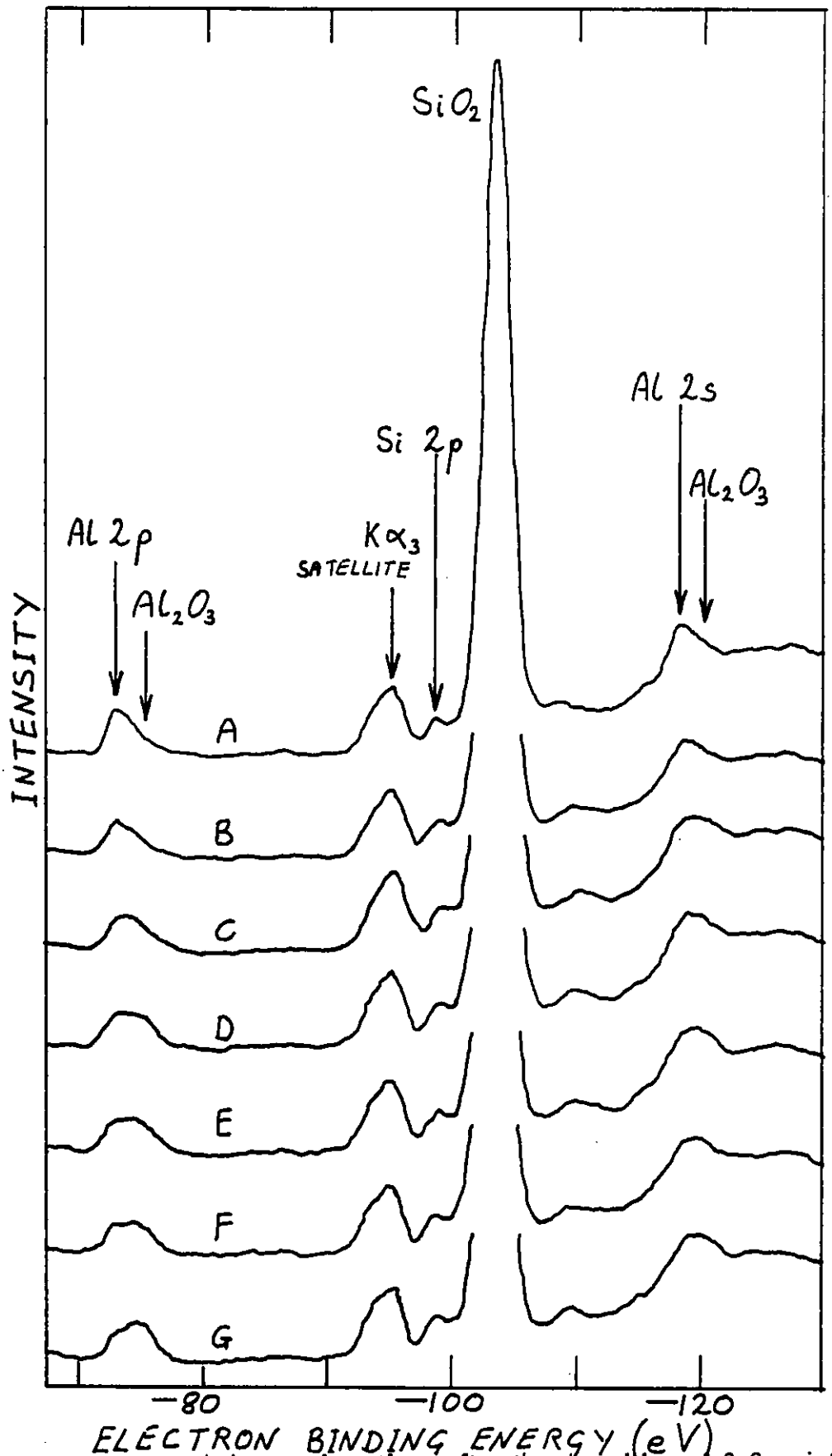

XPS spectra recorded at various times after the deposition of 0.2 nm of Al onto ion-bombarded SiO_2 at room temperature.

A, 15 min; B, 4 h; C, 19 h; D, 44 h; E, 68 h at room temperature.

F, 30 min at 650 K; G, 30 min at 850 K.

FIGURE 3.9

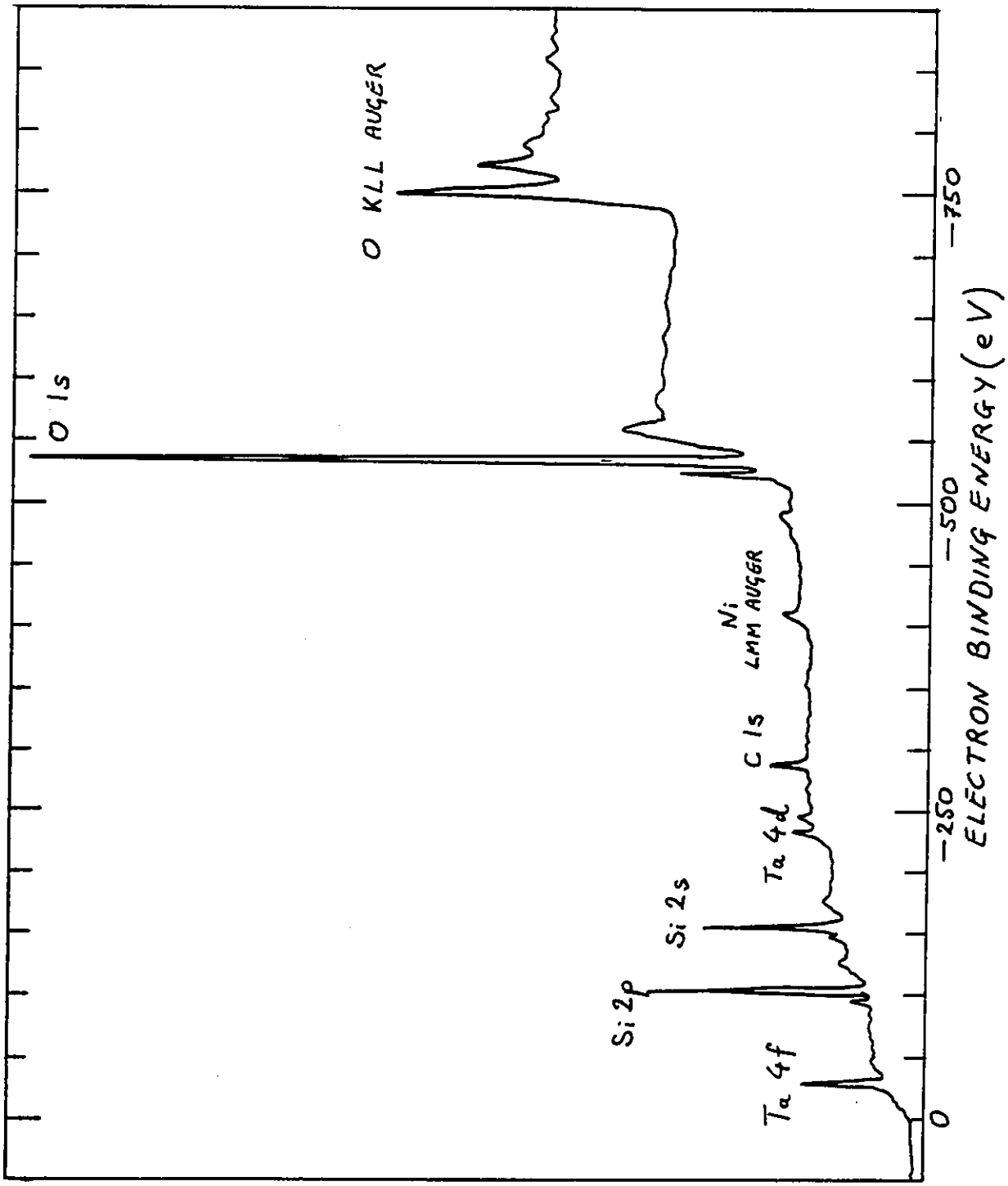

XPS spectrum from "as prepared" SiO_2

FIGURE 3.10

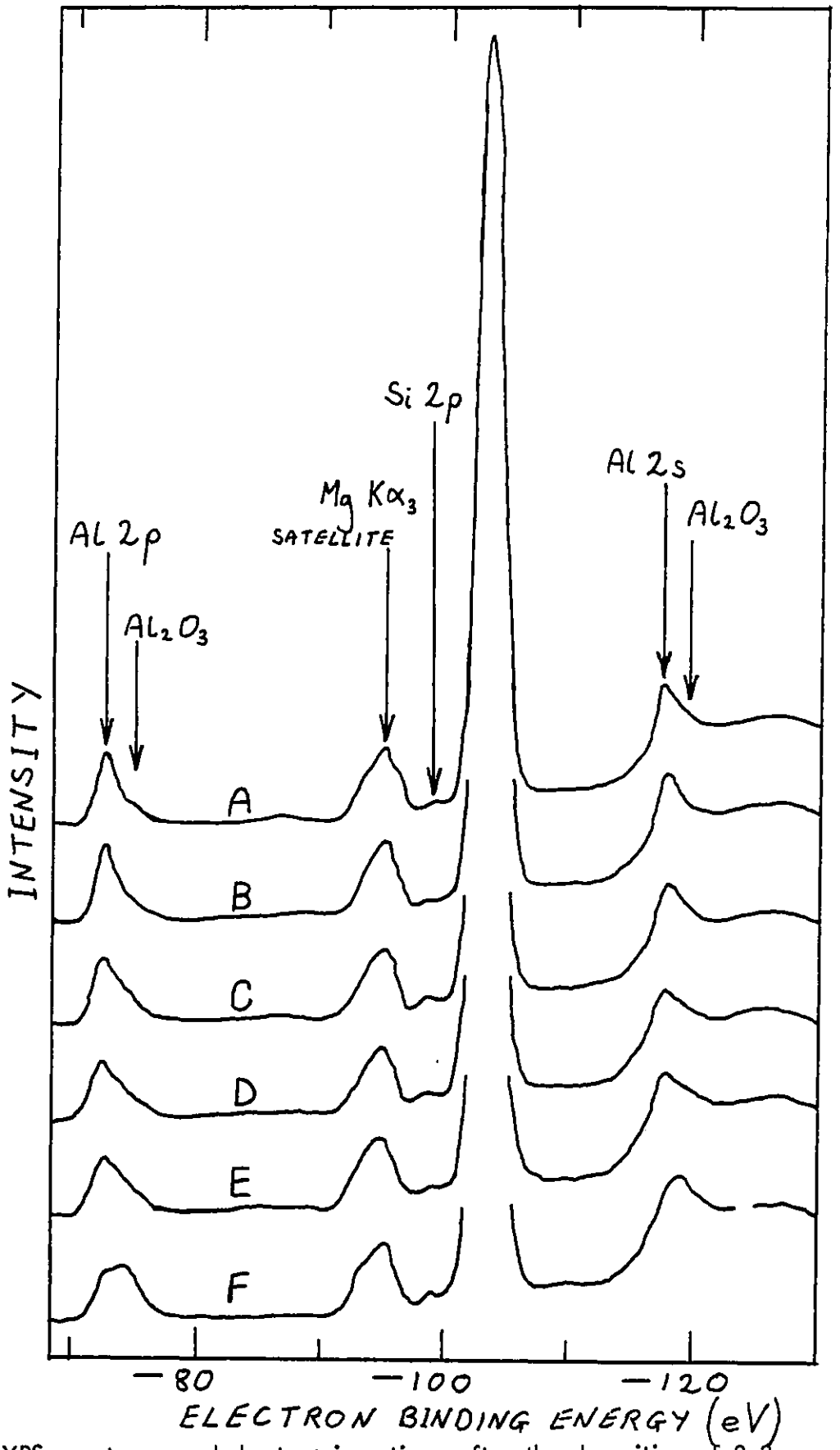

XPS spectra recorded at various times after the deposition of 0.3 nm of Al onto "as prepared" SiO_2 at room temperature.

A, 15 min; B, 5 h; C, 21 h; D, 44 h; at room temperature.

E, 30 min at 650 K; F, 30 min at 750 K.

FIGURE 3.11

in figure 3.10. The carbon 1s peak was estimated to correspond to approximately 20% of a monolayer coverage, by the application of equation 3.12. This amount of carbon contamination is thought to be typical for substrates exposed to the atmosphere. No other surface contaminants were detected by XPS or AES.

The XPS spectrum after the deposition of 0.3 nm of aluminium is shown in figure 3.11. In curve A (taken 15 minutes after deposition), the Al 2p peak is only slightly broadened. Also, the elemental silicon 2p peak is much smaller than that of curve A of figure 3.9, which was taken from a similar thickness of aluminium on ion bombarded SiO_2.

Curves B to D (figure 3.11) show the spectra after leaving the specimen at room temperature for 5 hours, 21 hours and 44 hours respectively. The shape of the Al 2p peak and the size of the free silicon 2p peak in curve D indicate the formation of less Al_2O_3 and silicon than do curve C of figure 3.8 and curve D of figure 3.9 (taken after similar reaction times for aluminium on ion bombarded SiO_2).

Heating the specimen at 650 K for 30 minutes produced some change in the Al 2p peak and heating at 750 K for 30 minutes gave rise to a broad peak with a chemical shift of $\sim$ 2.5 eV (curves E and F, figure 3.11). Compare this, however, with the almost complete conversion of aluminium to Al_2O_3 seen after a similar treatment of the aluminium on ion bombarded SiO_2 (curve I, figure 3.8).

3.6.3 Aluminium on Ion Bombarded Silicon

The XPS spectrum of the $\{111\}$ silicon substrate after argon ion bombardment is shown in figure 3.12. The Si 2s and Si 2p peaks at 150.8 and 99.2 eV are seen to have both single and double bulk plasmon peaks associated with them, at 17 eV and 34 eV from the main peaks. Mg Kα_3 satellite peaks are also evident.

Curve A of figure 3.13 is the spectrum after 0.4 nm of aluminium had been deposited. The Al 2s and Al 2p peaks are sharp, showing that negligible oxidation

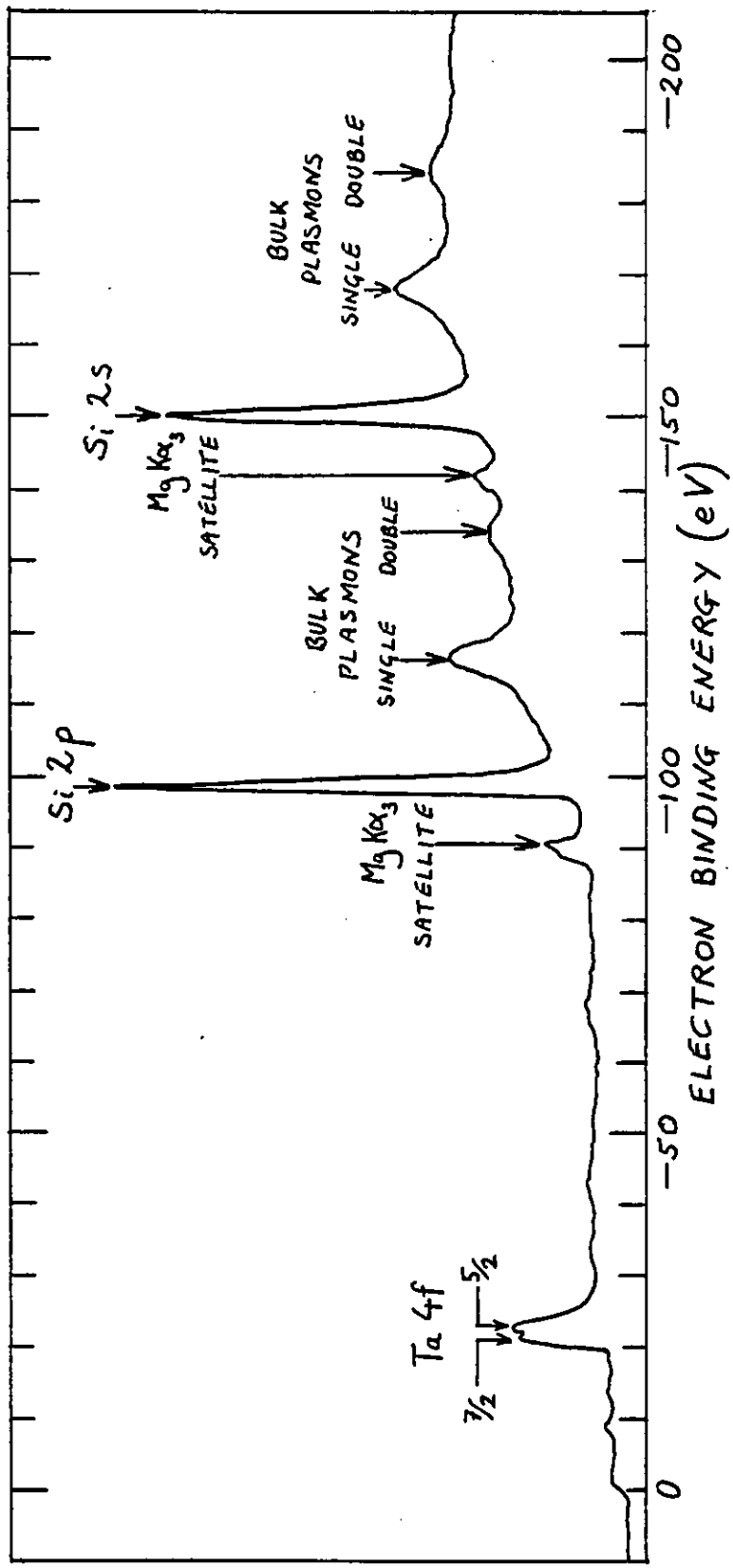

XPS spectrum from ion-bombarded silicon.

FIGURE 3.12

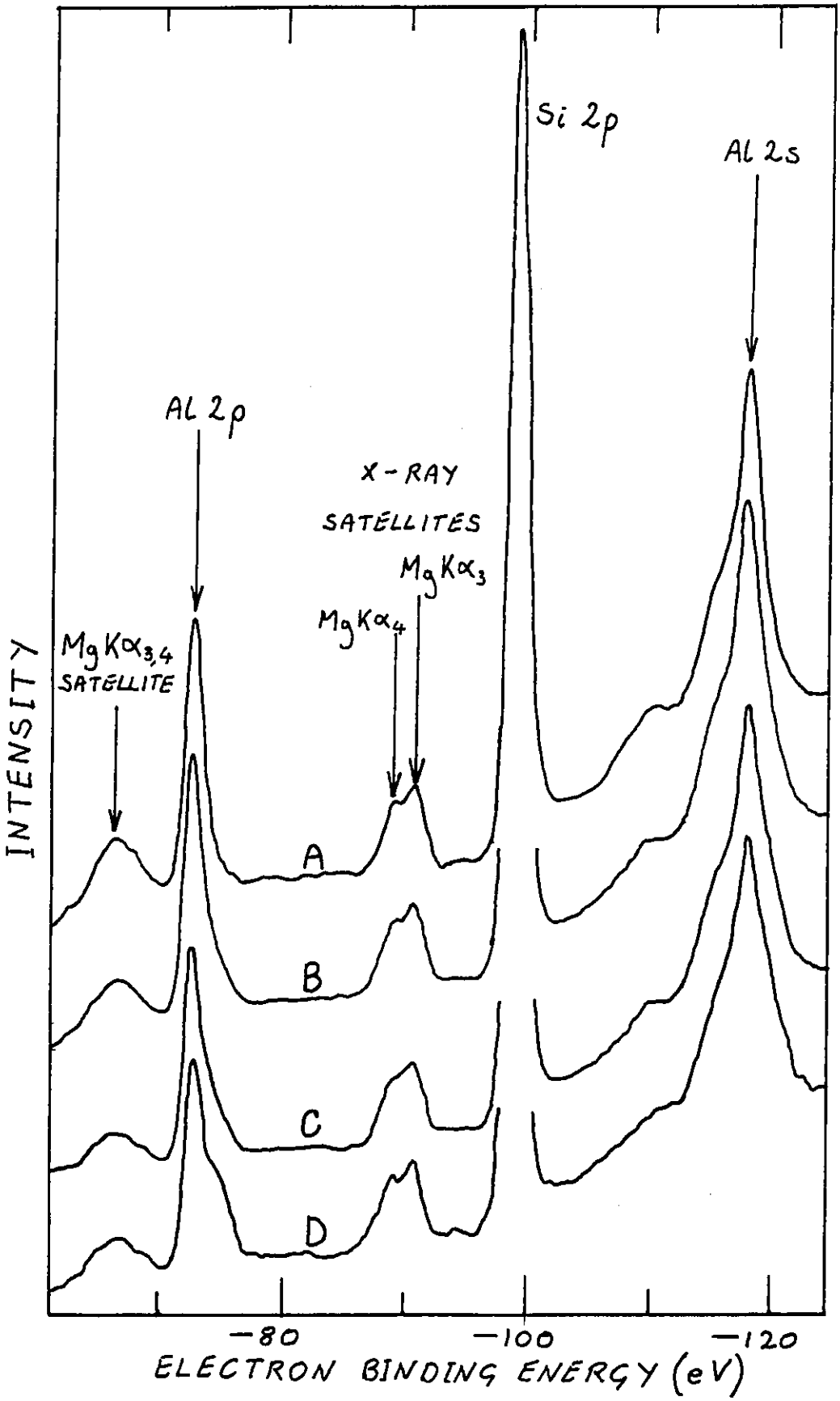

XPS spectra recorded at various times after the deposition of 0.4 nm of Al onto ion-bombarded silicon.

A, 15 min; B, 38 h; C, 62 h; D, 163 h at room temperature.

E, 30 min at 750 K.

FIGURE 3.13

of the aluminium has occurred. Curves B and C, recorded after leaving for 62 hours and 163 hours respectively in a vacuum of 3×10^{-11} mbar, show little change. Even heating at 750 K for 30 minutes (curve D) had only a small effect on the peak shapes.

It is concluded that oxidation of the aluminium surface by oxygen-containing gases in the ambient was negligible under the experimental conditions used. Therefore, the Al_2O_3 detected in the aluminium on SiO_2 experiments (sections 3.6.1 and 3.6.2) must have been formed by reaction at the Al - SiO_2 interface.

3.7 Discussion

The present results from aluminium on ion bombarded, steam-grown SiO_2 differ slightly from those obtained by Bauer et al (1980) using SiO_2 grown in-situ (see section 2.3). Whereas the latter saw the oxidation of the aluminium deposit proceed to virtual completion in about 7 hours at room temperature, in the present experiments heating was necessary to bring about complete reaction. This difference in reaction rate is thought to be a consequence of the different ways in which the SiO_2 substrates were prepared. The SiO_2 used by Bauer et al was grown in uhv conditions and so was extremely clean and free from water. The steam-grown SiO_2 used in the present work must have contained some water (in the form of OH^- or H_3O^+) which became incorporated in the oxide during growth (Wolters 1979). Water contamination could not be detected by XPS, even if present in reasonably large quantities. The hydrogen would not be seen because of its extremely small photoionization cross section (Scofield 1976) and oxygen present in water could not be distinguished from oxygen in SiO_2.

Nevertheless, the present results show that considerable reaction between steam-grown SiO_2 and vapour-deposited aluminium does occur at room temperature, with the formation of Al_2O_3 and elemental silicon. Furthermore, elemental silicon appears to be liberated during or shortly after aluminium deposition, while the conversion of the

aluminium deposit to Al_2O_3 proceeds slowly. The formation of Al_2O_3 appears to saturate after approximately 90 hours, at which point less than half of a 0.5 nm aluminium deposit has been oxidized to Al_2O_3. The elemental silicon 2p peak was seen to increase only slightly during this period and the subsequent high-temperature treatment. This result may be explicable in terms of the reaction model proposed by Bauer et al (1980) in which an intermediate oxidation state of aluminium is first formed. It is possible that the initial oxidation state gave rise to a chemical shift of the Al 2p peak which was too small to be clearly detected by the ESCALAB spectrometer, which had an energy resolution of approximately 1.2 eV. Such an intermediate oxidation state could have caused the slight broadening of the Al 2p peak observed in the initial stages of reaction. Clearly, the use of a high resolution spectrometer and an x-ray monochromator is essential if the reaction is to be observed in greater detail.

The results for aluminium on "as prepared" SiO_2 demonstrate the importance of surface preparation in controlling the reaction rate. The ion bombarded surfaces were clean (and probably damaged to some extent), and were therefore highly reactive. The "as prepared" substrates were contaminated with carbon and probably also absorbed and adsorbed water from the atmosphere. (Water adsorption is discussed in section 4.3.5). Some reaction occurred with these substrates at room temperature, as evidenced by the change of shape of the Al 2p peak, indicating oxide formation. However, the small size of the elemental silicon 2p peak shows that extensive reduction of the SiO_2 did not occur. It is therefore suggested that the aluminium overlayer reacted mainly with water on the surface of the SiO_2, to form aluminium oxide.

The results reported by Strausser et al (1978), which show Al_2O_3 and silicon to be distributed over a 30 nm thick interface layer, cannot be reconciled with the present findings. It therefore seems likely that the large interface width measured by Strausser et al is an artefact of the depth profiling process, as discussed in section 2.3.

The implications of the present results to Al - SiO_2 reactions in semiconductor devices are discussed in section 5.2.

3.8 Subsidiary Experiment : XPS and AES Sputter-Profiling of Thick Aluminium Films

3.8.1 Introduction

The aim of the experiment was to characterize the impurities present in thick, vacuum evaporated aluminium films as a function of distance below the surface. The films were prepared under conditions similar to those in an industrial evaporation plant, and the resulting impurities are thought to be typical of those found in aluminium device metallizations.

3.8.2 Experimental Method

Two 1 μm thick aluminium films were deposited onto 1 cm square, steam-oxidized silicon substrates at rates of 1 nm s^{-1} and 10 nm s^{-1}. In each case the substrates were at room temperature during deposition and the base pressure in the chamber was 2×10^{-7} m bar. (The evaporation plant is described in detail in sections 4.2 and 6.2). The specimens were stored at room temperature and atmospheric pressure for 4 weeks then loaded into the ESCALAB in the usual way and the system evacuated. However, bakeout was not performed because heating the specimens to 450 K may have caused changes in their structure or chemical composition.

XPS and AES spectra were taken from each specimen, then argon ion bombardment was carried out and the spectra taken again. The procedure was repeated until no further changes in the spectra were seen.

3.8.3 Results and Discussion

The XPS spectra taken before ion bombardment were very similar for both specimens. Figure 3.14 shows the spectrum from the film deposited at 10 nm s^{-1}, which reveals the presence of aluminium, oxygen and carbon, as well as tantalum from the

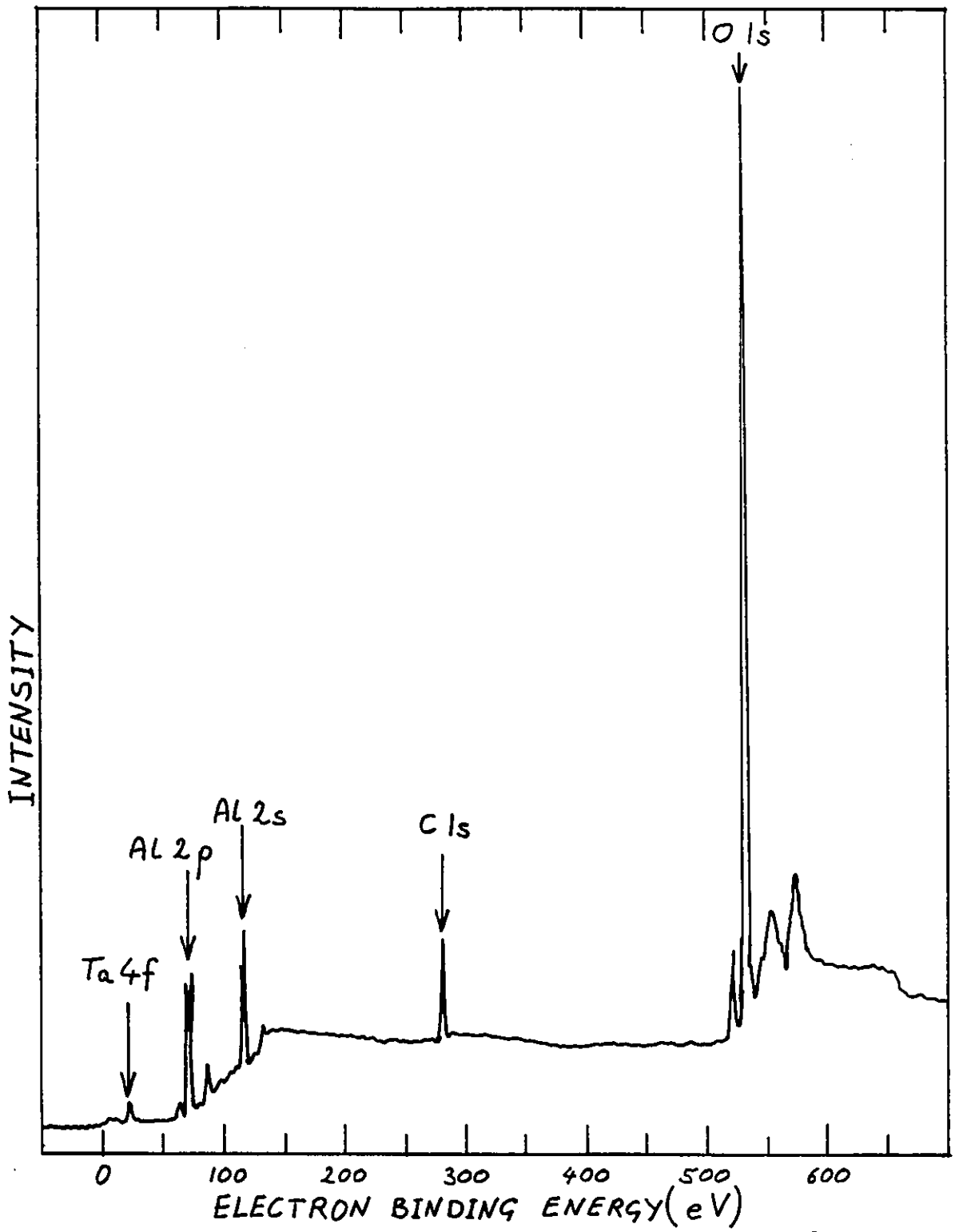

XPS spectrum from air-exposed 1 μm Al film deposited at 10 nm s^{-1} onto SiO_2 at room temperature.

FIGURE 3.14

specimen mount. Curve A of figure 3.15 shows the Al 2s and Al 2p features in greater detail. Each of these features is split into two distinct peaks with a separation of 2.5 eV, showing that aluminium is present both as metallic Al and as Al_2O_3. Bulk plasmon peaks are also visible in the spectrum.

Curve B shows the same region of the spectrum after the specimen was ion bombarded for 10 minutes using a 100 μA beam of 7 keV argon ions. The Al 2s and Al 2p features are now seen to be narrow single peaks of binding energies 118 eV and 73 eV respectively, corresponding to aluminium metal. The plasmon spectra are now very prominent. The peaks separated from the Al 2s and Al 2p peaks by approximately 15 eV, 30 eV and 45 eV are due to single, double and triple excitation of the aluminium bulk plasmon of energy 15.3 eV (Ritchie 1957). Surface plasmon peaks are also visible, at approximately 11 eV from the 2s and 2p peaks. The carbon and oxygen peaks had almost vanished after ion bombardment, indicating that the aluminium oxide and carbon were surface contaminants.

Measurement of the relative peak areas in curve A of figure 3.15 enabled the amounts of surface Al_2O_3 and carbon to be estimated. It was assumed that the Al_2O_3 existed as a layer of uniform thickness on the surface of the aluminium, and that the carbon resided in a monolayer of fractional coverage on top of the Al_2O_3. The equations of section 3.2.3 were then applied to find the fractional coverage of the carbon layer and the thickness of the aluminium oxide film. Hence, the Al_2O_3 was estimated to be 2 nm thick and the carbon monolayer had a coverage of approximately 50%.

The aluminium film deposited at 1 nm s^{-1} was examined by XPS and AES after successive short periods of argon ion bombardment. The resulting Al 2s and Al 2p XPS peaks and the corresponding oxygen 1s peaks are shown in figures 3.16 and 3.17. The corresponding Auger spectra (figure 3.18) show the decrease in magnitude of the oxygen KLL and carbon KLL signals with progressive ion bombardment. The argon LMM signal

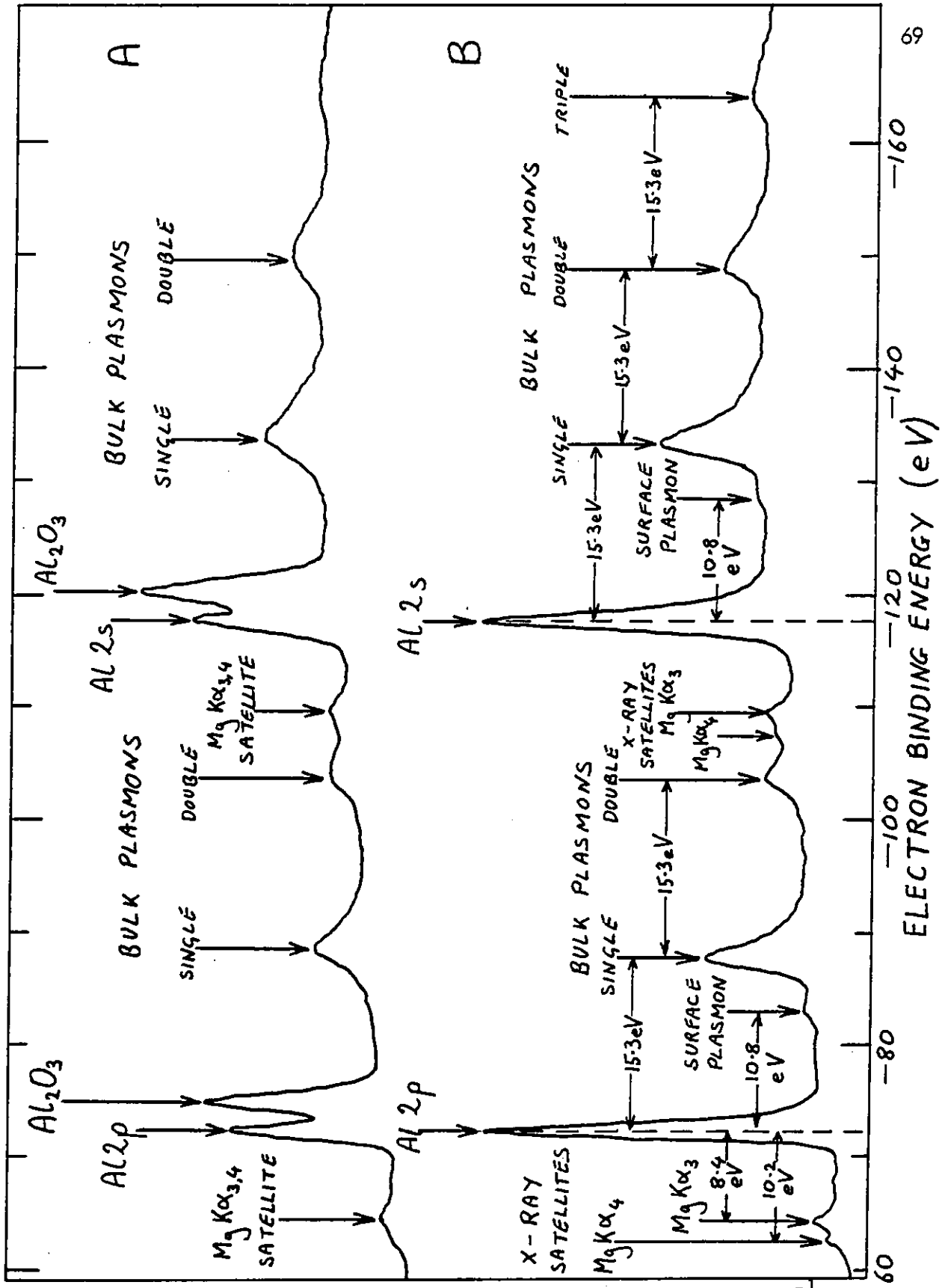

Al 2s and 2p spectra from air-exposed 1 um Al film deposited at 10 nm s^{-1}
A, as prepared; B, after argon ion bombardment at 100 uA for 10 minutes.

FIGURE 3.15

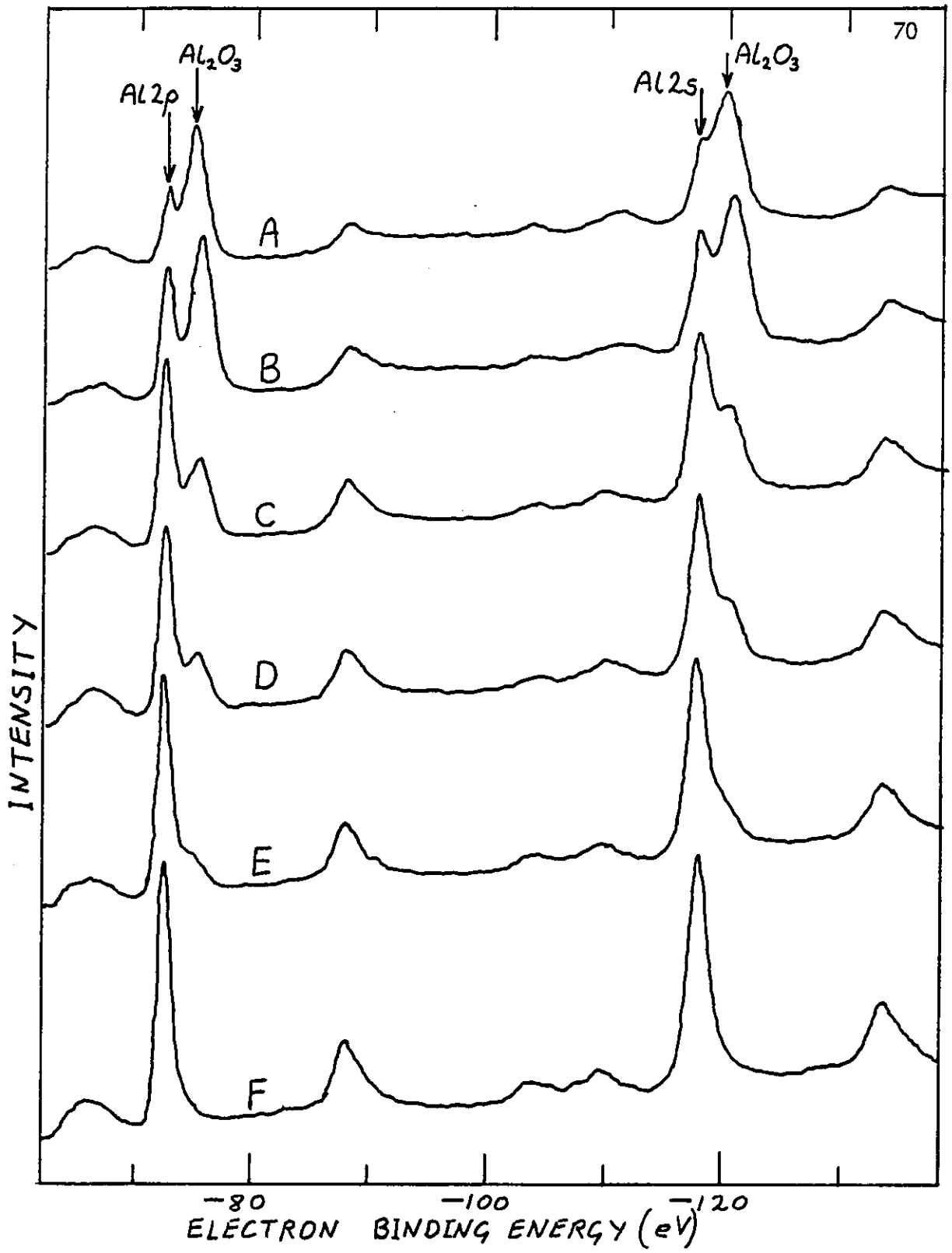

Al 2 p and 2 s spectra from 1 μm Al film deposited at 1 nm s^{-1}, after various periods of ion bombardment using a 100 uA beam of 3 keV argon ions. A, "as prepared"; B, 6 s; C, 24 s; D, 36 s; E, 78 s; F, 10 min.

FIGURE 3.16

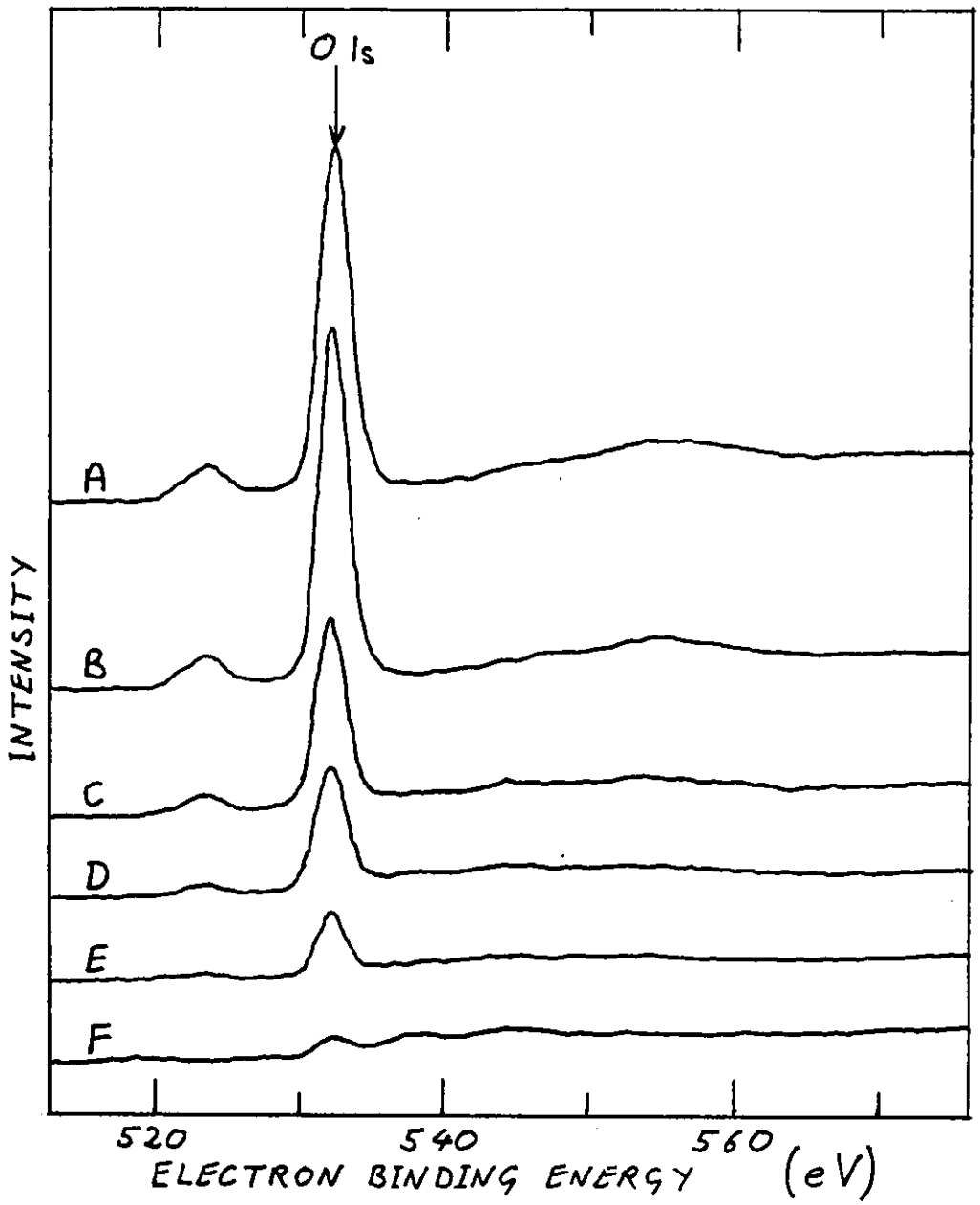

Oxygen 1s spectra corresponding to the Al 2p and 2s spectra in figure 3.16.

FIGURE 3.17

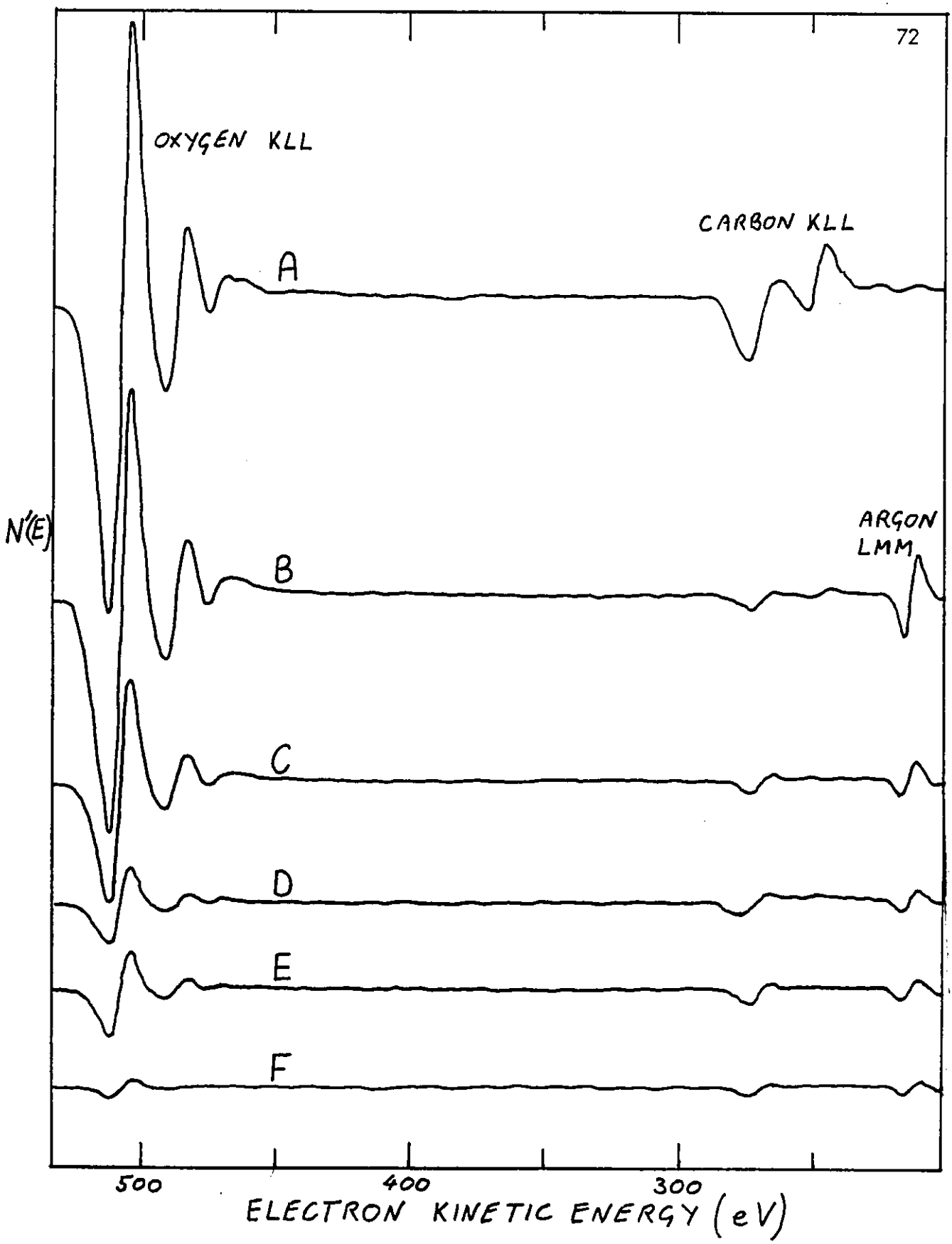

Oxygen and carbon KLL Auger electron spectra corresponding to the XPS spectra in figures 3.16 and 3.17.

FIGURE 3.18

is seen to grow as a result of argon ions becoming trapped in the aluminium surface.

It must be emphasized that these series of spectra do not enable a true depth profile to be constructed. The ion beam was not rastered, so the sputtering rate was not uniform over the surface. Instead, a crater was formed, owing to the non-uniform current density of the ion beam. Therefore spectra recorded at any instant consisted of the sum of signals originating from all points on the surface of the crater, and hence from different depths below the original surface of the film.

The final Al 2s and Al 2p line shapes, after prolonged ion bombardment, were very similar for both specimens. (The differences in magnitude between the peaks in curve B of figure 3.15 and curve F of figure 3.16 are due to differences in the areas of the two specimens). The final peak shapes were taken to be representative of pure metallic aluminium and were used as reference for the spectra obtained in the Al- SiO_2 interface experiments (sections 3.6.1 to 3.6.3).

The difference in deposition rate between the two films did not appreciably affect their bulk purity. The surface oxide and carbon contamination are attributed to atmospheric exposure during specimen transfer from the evaporation plant to the ESCALAB. As the specimens were stored in the laboratory for 4 weeks at atmospheric pressure before they were examined in the ESCALAB, the 2 nm thickness of the Al_2O_3 film is thought to be the limiting thickness for the native oxide at room temperature.

CHAPTER 4

A STUDY OF THE Al - SiO_2 INTERFACE USING TRANSMISSION ELECTRON MICROSCOPY

4.1 Introduction

The experiments discussed in this chapter were conducted in order to identify the crystalline phases of Al_2O_3 and silicon produced by Al - SiO_2 interfacial reaction and to establish the conditions necessary for reaction to occur. Alumina may exist in any of 14 crystal phases (Wefers and Bell 1972). The phase present at the Al - SiO_2 interface may have consequences regarding the reliability of aluminium thin film metallizations, especially from the point of view of interface electromigration.

The experiments fall into two main categories. The first series of experiments (sections 4.2.1 to 4.2.7) entailed the deposition of aluminium films onto steam-grown SiO_2 in a conventional evaporation plant. Chemical thinning was then carried out to enable the specimens to be examined in the transmission electron microscope (TEM).

In the second series of experiments (sections 4.3.1 to 4.3.5) aluminium was deposited onto steam-grown SiO_2 in the specimen chamber of the TEM and various annealing treatments were performed in situ. In addition, several similar experiments were performed using evaporated films of silicon monoxide as the substrates.

Reaction between aluminium and "as prepared" SiO_2 was found to occur at temperatures of 575 K and above. The reaction products were identified as polycrystalline silicon and η - Al_2O_3. Water contamination of the SiO_2 surface was found to be effective in preventing Al - SiO_2 reaction at temperatures much below the melting point of aluminium. With SiO substrates, reaction occurred under similar conditions, but the γ- rather than the η - phase of alumina was formed.

4.2 The Evaporator Experiments

4.2.1 The Substrate Material

So that the results of this study might be directly relevant to the problems associated with aluminium metallization on silicon devices, steam-grown SiO_2 was used as the substrate material. However, in order to use transmission electron microscopy and diffraction to examine the films, specimens had to be sufficiently thin (not more than ~100 nm thick to obtain a good diffraction pattern using 80 keV electrons). Therefore, 50 nm SiO_2 layers were used, instead of the 1 μm layers normally employed as the insulator in silicon planar technology. After aluminium had been deposited, the silicon was removed from the back of the specimen to leave the aluminium supported on a 50 nm film of SiO_2 (see section 4.2.3).

4.2.2 The Evaporation Plant

The evaporation chamber was a 12-inch glass bell jar. This was evacuated by a 4-inch diffusion pump charged with "Santovac 5" pumping fluid. A liquid nitrogen cold trap was used to reduce backstreaming of oil vapour and improve the pumping efficiency for water vapour. A rotary pump, fitted with a zeolite trap, was used to back the diffusion pump and to rough-pump the chamber. The ultimate chamber pressure was 2×10^{-7} m bar, as measured by a Penning gauge. A Centronics AIG 50 quadrupole mass spectrometer was used for residual gas analysis. A typical mass spectrum is shown in figure 4.1.

The layout of the chamber is shown in figure 4.2. Evaporation was carried out from a 5 mm diameter helical coil, comprising 10 turns of triple-stranded 0.5 mm diameter tungsten wire. The use of multi-stranded wire reduces the rate at which alloying occurs between the tungsten and molten aluminium, and hence prolongs evaporator life (Holland 1956). The evaporator was positioned 150 mm above the substrate, and when loaded with four 30 mm lengths of 1 mm diameter aluminium wire, permitted films of up

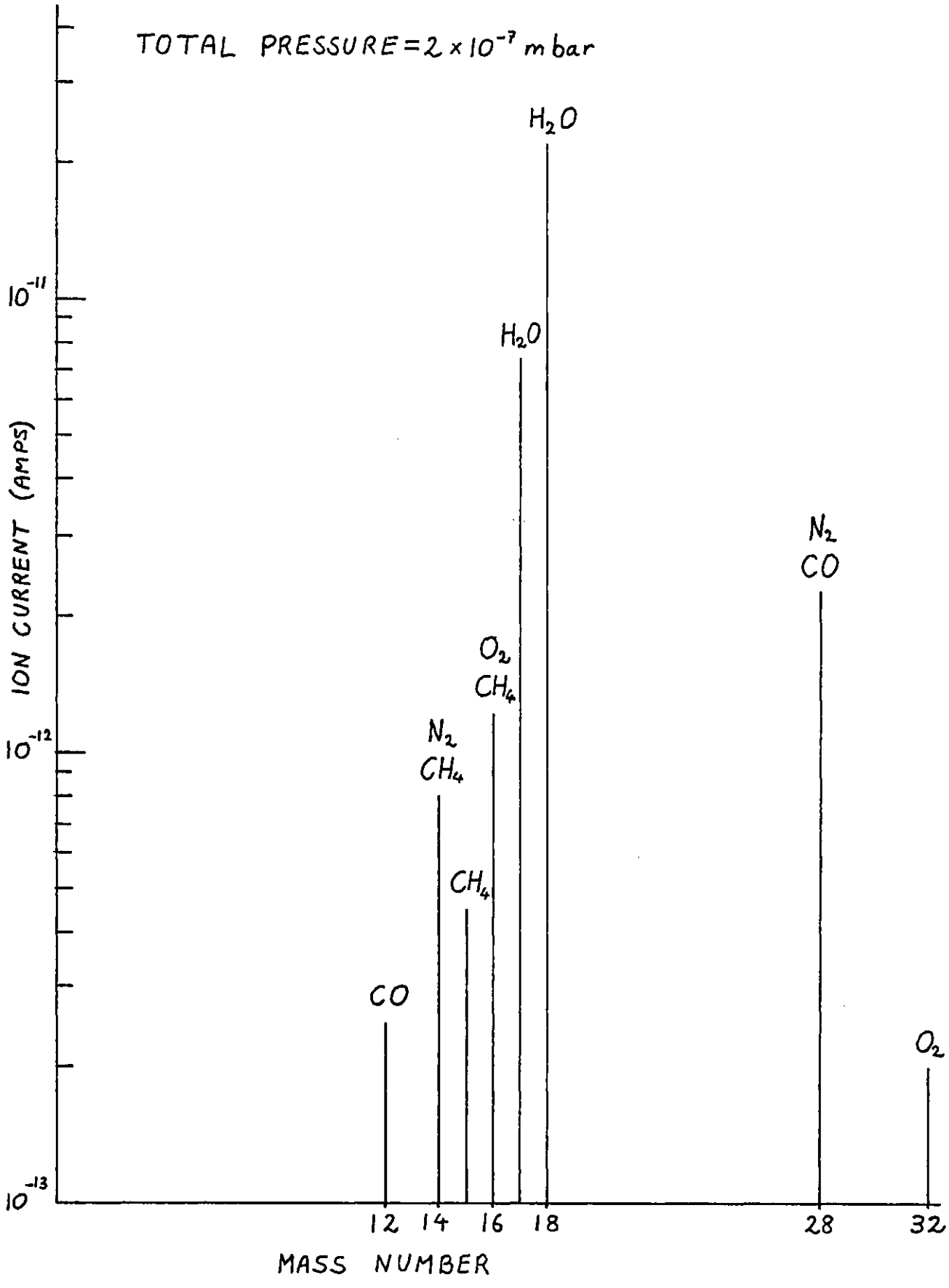

Residual gas spectrum from the aluminium evaporation system with liquid nitrogen trap in operation.

FIGURE 4.1

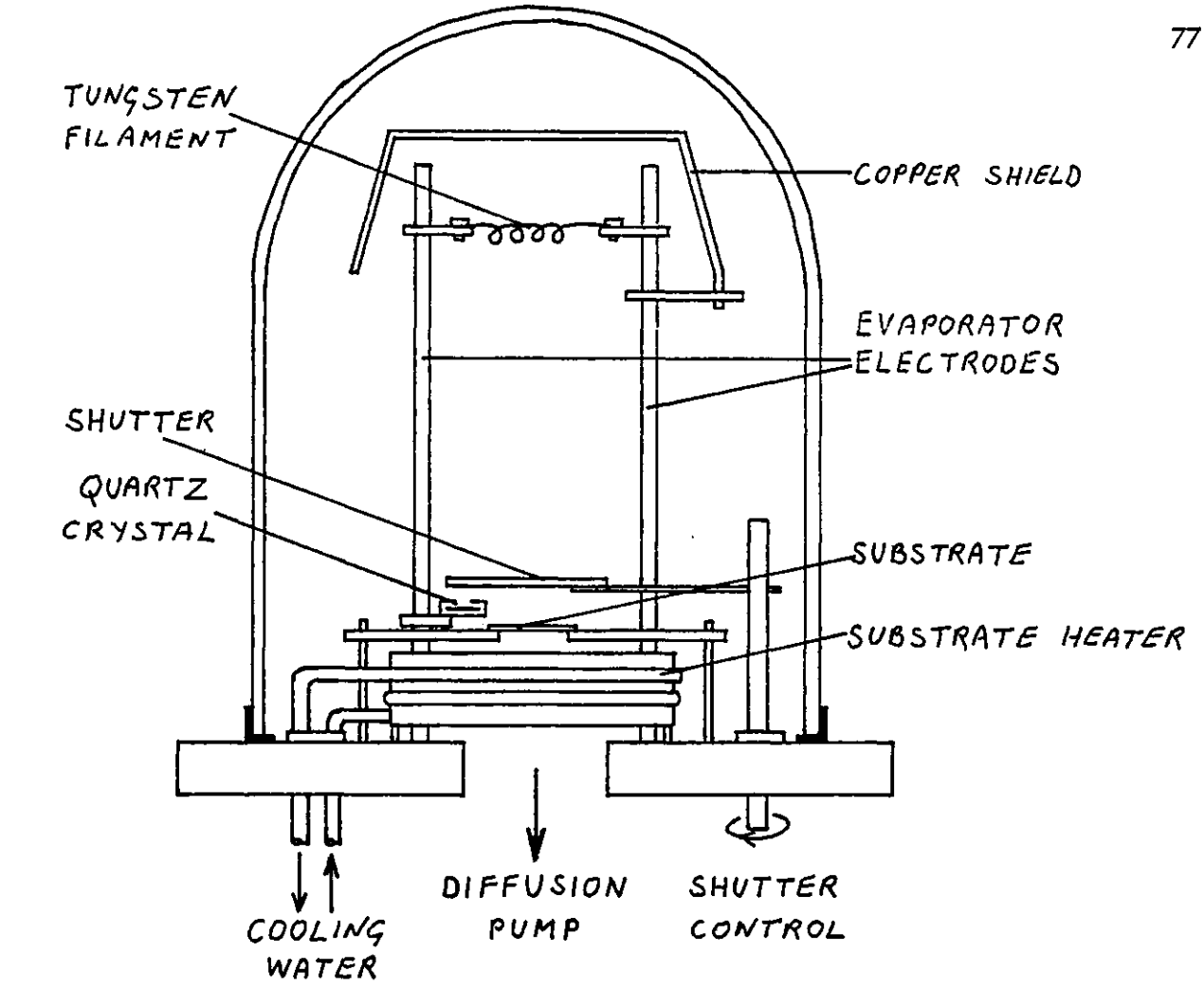

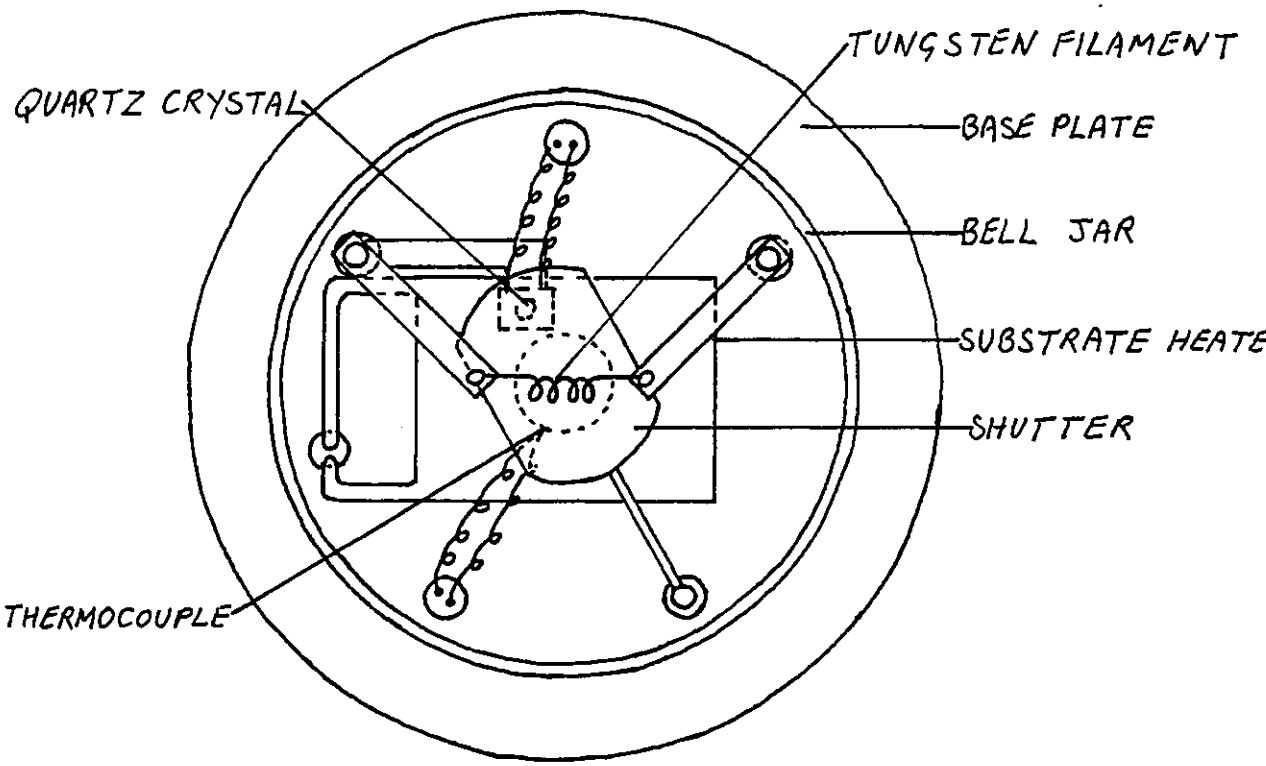

The aluminium evaporation system

FIGURE 4.2

to 400 nm thickness to be deposited. (When thicker films were required, as in Chapter 7, three helical coil evaporators were connected in parallel). The evaporator was heated by alternating current supplied by a Variac via a low voltage transformer. A copper shield was positioned above the evaporator coil to reduce heating of the bell-jar and confine the stream of evaporant to the vicinity of the substrate.

The substrate heater was based on a design of Unvala and Censlive (1973). It consisted of 8 electrically heated strips of tungsten foil (80 mm long, 9 mm wide and 0.1 mm thick) connected in series inside a water-cooled copper box. (See figure 4.3). This type of heater was adopted since it is capable of uniformly heating a 2-inch silicon wafer to 1000 K without undue heating of the bell-jar and its contents. Outgassing is thus reduced. The substrate was located over an aperture in a stainless steel plate 5 mm above the tungsten heaters. Substrates of various sizes were accommodated by plates with different aperture sizes. As the radiating area of the heater (80 mm by 80 mm) was much larger than the substrate area, temperature gradients across the substrate surface were minimized.

Substrate temperature was measured by a chromel-alumel thermocouple positioned at the edge of the substrate and in contact with the stainless steel plate. This thermocouple was calibrated against thermocouples on the substrate surface in a separate calibration experiment. The accuracy of these thermocouples was checked against the melting point of lead. (See Appendix C).

A quartz crystal monitor was used to measure the deposition rate and film thickness. The quartz crystal and substrate were placed close together and equidistant from the vapour source to ensure equal deposition on the substrate and monitor. The 6 MHz crystal controlled the frequency of a simple transistor oscillator (see figure 4.4). The frequency was measured by a digital frequency counter with a precision of 1 Hz.

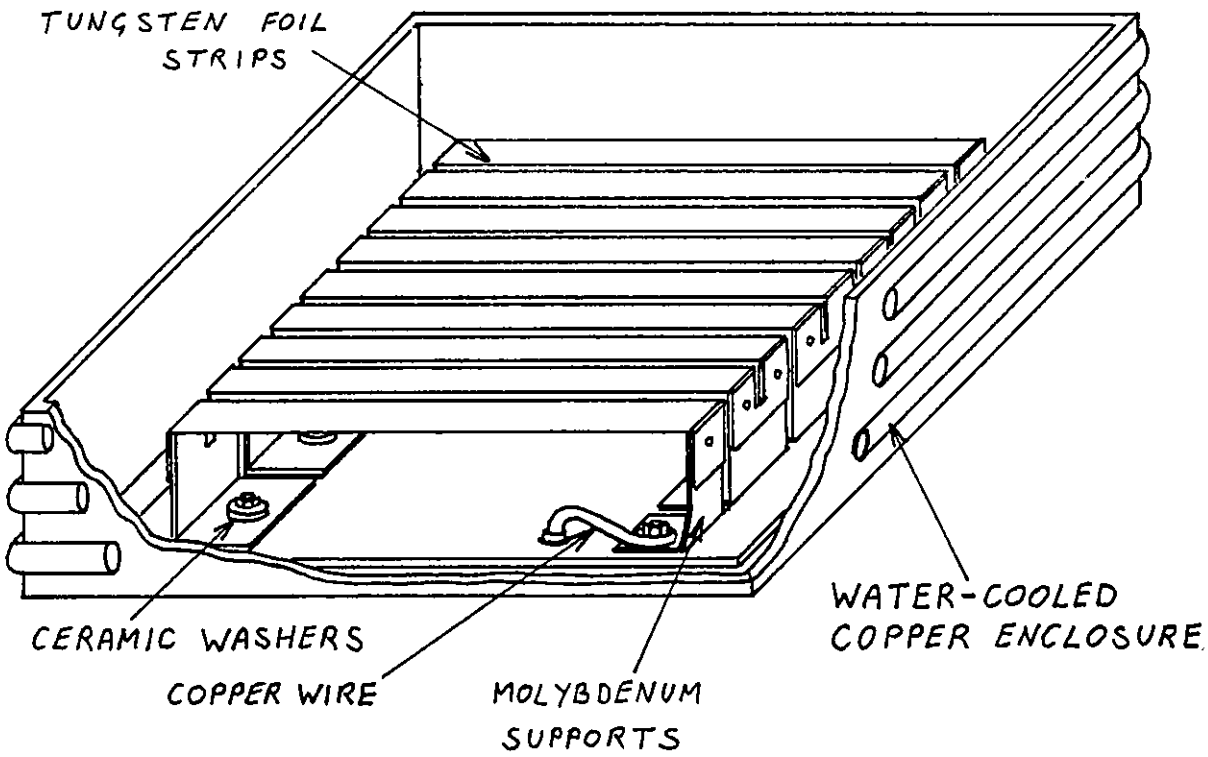

The substrate heater

FIGURE 4.3

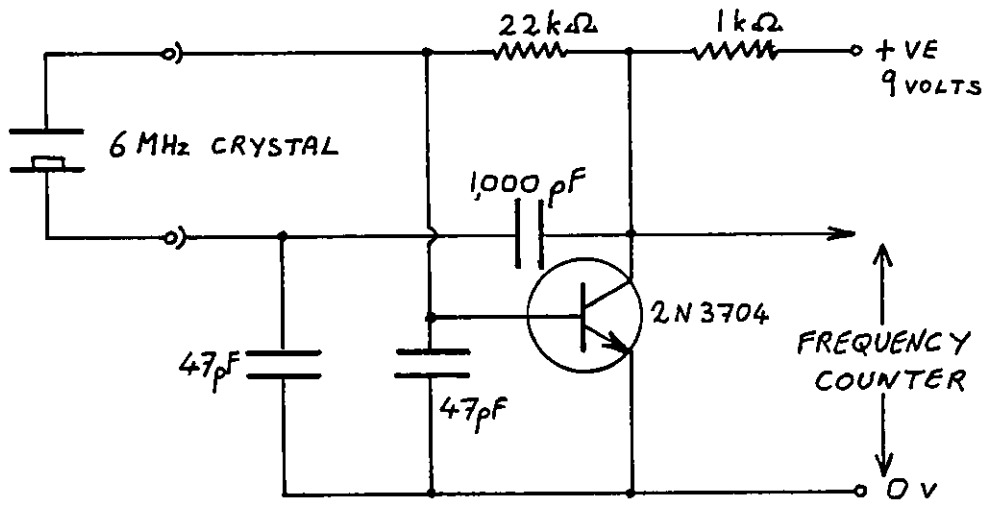

Circuit diagram of the quartz-crystal film thickness monitor

FIGURE 4.4

The counter sampled the frequency once per second, so by noting the frequency change between successive readings, the "instantaneous" deposition rate could be monitored. (The linearity of the response of the monitor and its calibration using multiple beam interferometry are discussed in Appendix B). A stainless steel shutter, operated by a rotary motion feedthrough, was used to control the deposition.

4.2.3 The Jet-Thinning Apparatus

The technique for removing excess silicon from the back of the specimens has been described by Bicknell (1973) and the details of the apparatus (shown in figure 4.5) will not be given here.

The most consistent results were obtained using {100} oriented silicon and an etchant comprising 1 volume of hydrofluoric acid (40%) to 2 volumes of nitric acid (concentrated). This was applied to the specimen (which was rotated at 60 rpm) at a rate of ~200 drops per minute from a 0.5 mm jet positioned 3 mm above the specimen surface. The thinning took approximately 5 minutes and was terminated by the application of deionized water when the specimen was seen to transmit light (in the case of thin aluminium films) or when aluminium could be seen through the Si/SiO_2 layers. The appearance of a thinned specimen is shown schematically in figure 4.6b. Specimens were quite robust and could be handled with tweezers without damage.

4.2.4 The Transmission Electron Microscope

Transmission electron microscopy and diffraction were carried out in a JEM 100 U electron microscope. The column was evacuated by a 4-inch diffusion pump charged with Santovac 5 pumping fluid and backed by a rotary pump. A Centronics AIG 50 mass spectrometer was used to measure total and partial pressures in the specimen chamber. A vacuum of 2×10^{-6} mbar was achieved after 48 hours of pumping. The use of a specimen transfer airlock, rough pumped by an auxiliary rotary pump, enabled the vacuum to be maintained for long periods.

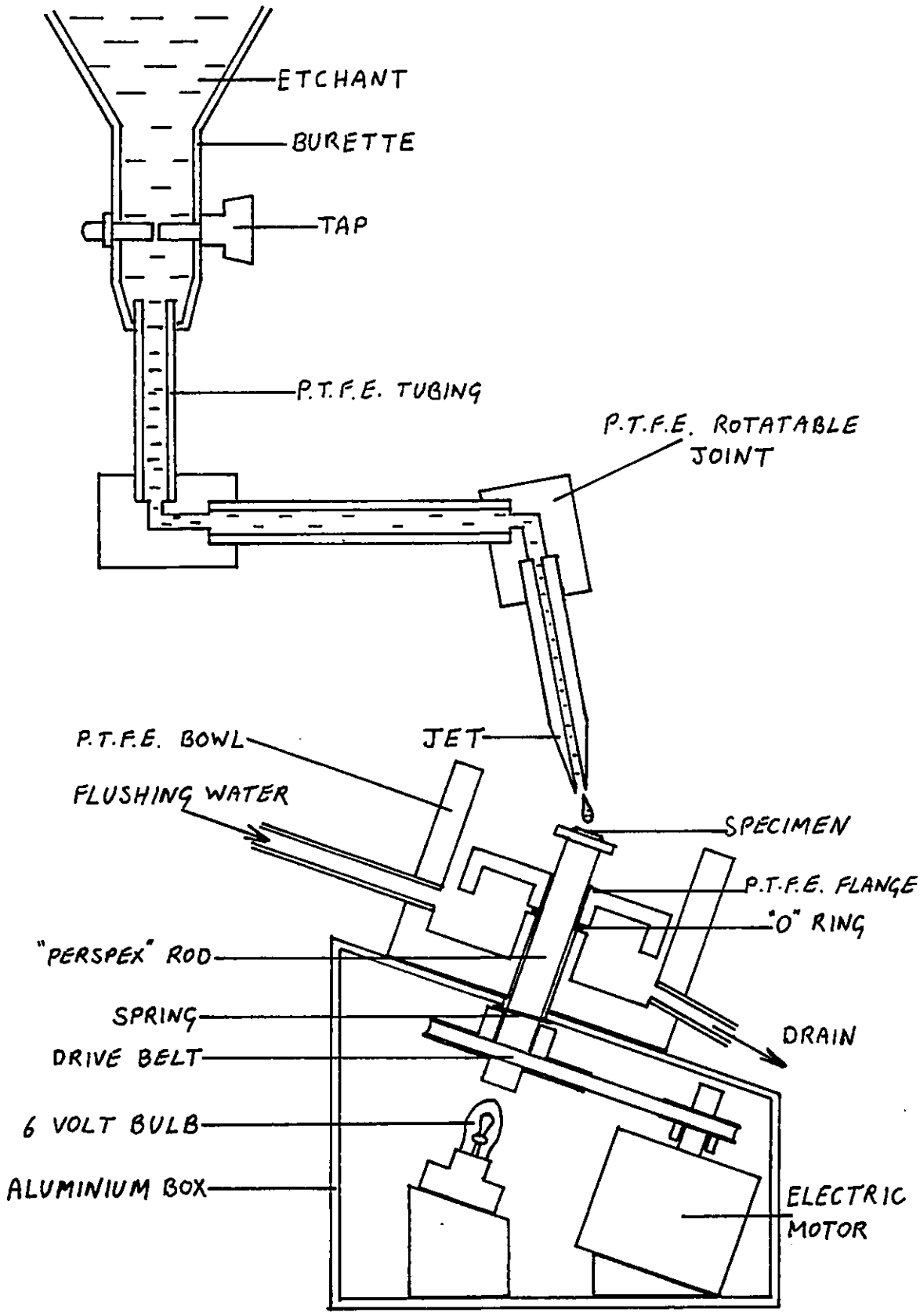

The jet-thinning apparatus

FIGURE 4.5

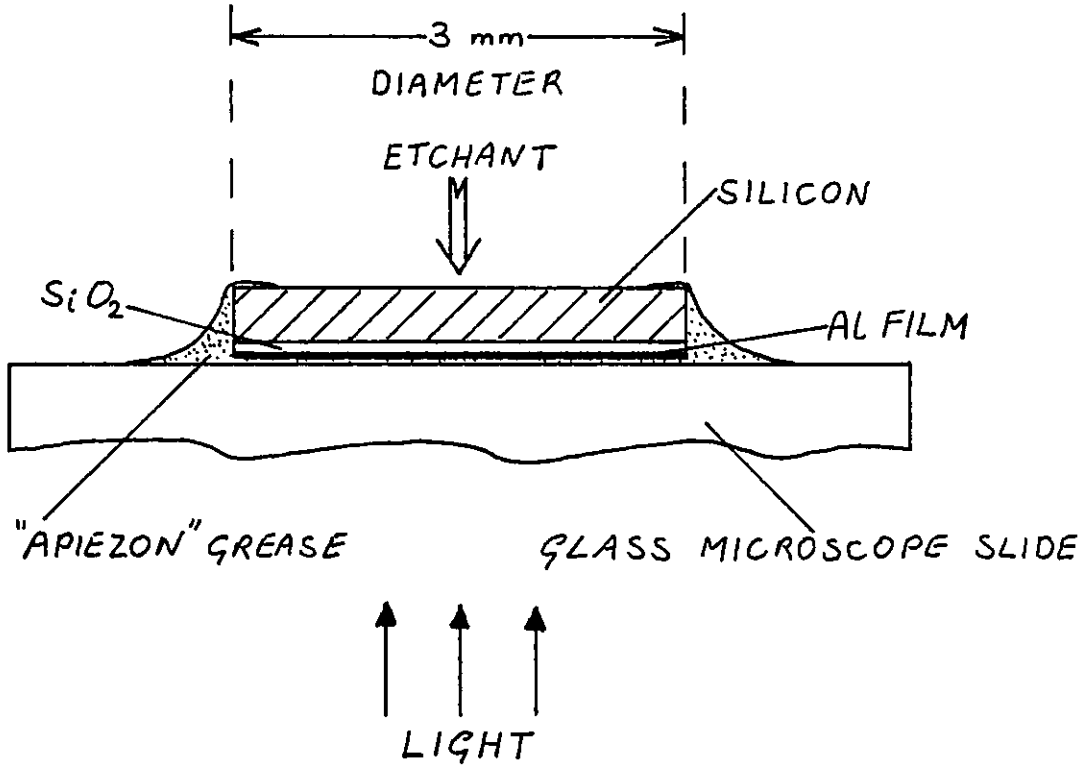

(a)

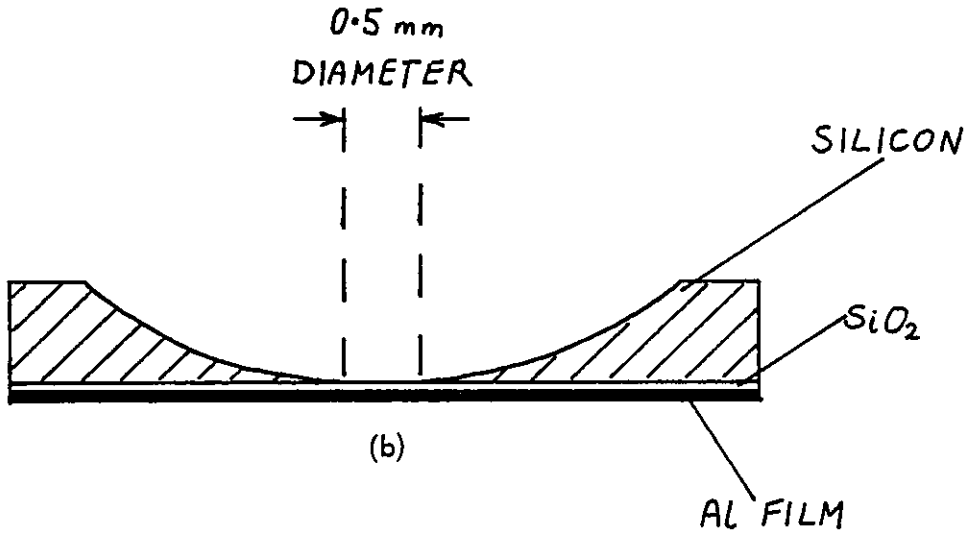

(b)

(a) Method of mounting the specimen during jet-thinning

(b) Cross-section of a thinned specimen

FIGURE 4.6

For aluminium on SiO_2 specimens of total thickness less than 100 nm, an 80 keV electron beam was used. A 100 keV beam was used for thicker specimens. Micrographs and diffraction patterns were recorded on 65 mm by 90 mm "Agfa-Gevaert Scientia" cut film. The camera chamber of the microscope could be isolated from the column and independently evacuated during film replacement. Film was outgassed in a vacuum desiccator for 12 hours prior to loading into the microscope. In this way the time required for film replacement was minimized.

A goniometer specimen stage enabled the specimen to be tilted by 10° and the tilt axis could be rotated through 360°. Tilting of the specimen was used to detect fibre textures which cause arcing of the rings of the diffraction pattern.

4.2.5 Experimental Method

The evaporator coil was outgassed for several minutes at white heat in a vacuum of 1×10^{-5} m bar. The charge of 99.995% purity aluminium wire was loaded into the coil and outgassed to a pressure of 1×10^{-5} m bar by slowly increasing the evaporator current. The substrate (a 1 cm square of oxidized silicon) was placed on the substrate heater, and the chamber was evacuated to 2×10^{-7} m bar.

The water-cooled substrate heater was outgassed until the chamber pressure was less than 5×10^{-7} m bar with the substrate at the required temperature. With the shutter in the closed position, the evaporator was thoroughly outgassed and some aluminium was evaporated. This had the effect of reducing the partial pressures of oxygen and water vapour by gettering.

The shutter was partially opened to expose the quartz crystal to the evaporant and the desired deposition rate (1 nm s^{-1}) was obtained by adjustment of the evaporator current. The shutter was then fully opened for sufficient time for a film of the required thickness (50 nm) to be deposited. Minor corrections to the current were made to maintain a constant deposition rate as the amount of aluminium in the evaporator diminished.

The deposition rate could be controlled to within 20% of the desired value. During the evaporation, the chamber pressure increased to 2×10^{-6} m bar, despite the thorough outgassing procedure. The mass spectrometer showed the major component to be hydrogen.

After turning off the heater, the specimen took approximately one hour to cool to room temperature from 600 K. The specimen was then divided into 5 mm squares by scribing and breaking and these were bonded to a glass slide using wax, the metallized surfaces of the specimens being in contact with the glass. The slide was firmly bonded to the baseplate of an ultrasonic drill, using double-sided adhesive tape, and a 3 mm diameter disc was cut from each specimen. Ultrasonic cutting was performed using grade 400 carborundum paste with a tool consisting of a 3 mm inside diameter brass tube. The specimens were removed by gently warming the wax and cleaned in boiling trichloroethylene. The aluminium film suffered no visible damage due to the cutting procedure.

In order to protect the aluminium during jet-thinning, the specimen discs were mounted on 1 cm glass squares using Apiezon-M grease. The grease was applied to the glass and melted by warming on a laboratory hot-plate. The specimen was placed, aluminium surface downwards, on the glass slide, and on cooling the Apiezon grease formed a seal which was impervious to attack by the etchant (see figure 4.6a).

After thinning, the specimen was removed from the glass by warming in trichloroethylene, washed in 2 baths of acetone and finally rinsed in deionized water before examination in the electron microscope.

Diffraction patterns were measured using a travelling microscope. The effective camera length of the electron microscope, L, multiplied by the electron wavelength, λ, was determined by measurement of the diffraction pattern of aluminium (see section 7.2.2),

the lattice parameter of which is known to a high degree of accuracy (Wyckoff 1963). The value of λL (approximately $3.5 \times 10^6 nm^2$) was found to vary considerably between independent measurements using the same aluminium specimen but taken on different occasions. (This effect may have been a result of hysteresis in the magnetic lenses or fluctuations in the accelerating voltage or lens currents). Therefore, λL was determined individually for each diffraction pattern analysed, by measurement of the aluminium diffraction rings in that pattern. Additional diffraction features (e.g. due to silicon or Al_2O_3) were then interpreted using this value of λL. Interplanar spacings were thus determined to an accuracy of 0.005 nm.

4.2.6 Results

4.2.6.1 The Substrates

The electron diffraction patterns from a thinned specimen of 50 nm of SiO_2 on {100} silicon are shown in figure 4.7. The amorphous nature of the SiO_2 is revealed by the diffuse haloes of the diffraction pattern (figure 4.7a) which was taken from the centre of the thinned area. The diffraction pattern from the edge of the thinned region (figure 4.7b) shows the presence of single crystal {100} oriented silicon. Low-angle shadowed replicas revealed the SiO_2 surface to be smooth down to the resolution of the replication technique ($\sim$5 nm).

4.2.6.2 Aluminium Deposited onto SiO_2 at Room Temperature

50 nm thick aluminium films deposited at a rate of 1 nm s^{-1} onto amorphous SiO_2 at room temperature were seen to be continuous and polycrystalline with a mean grain size of around 50 nm (see figure 4.8a). On tilting the specimen away from normal incidence of the electron beam, the rings of the diffraction pattern broke up into extended arcs (see figure 4.8b). The aluminium film thus had a weak $\langle 11\bar{1} \rangle$ fibre texture, with the fibre axis normal to the film plane (see section 7.2.2). Apart from the

(a)

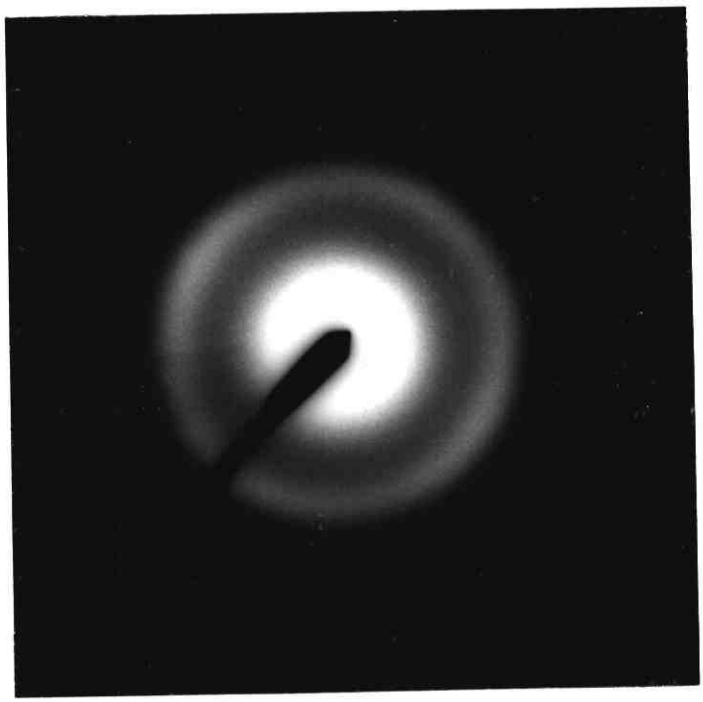

(b)

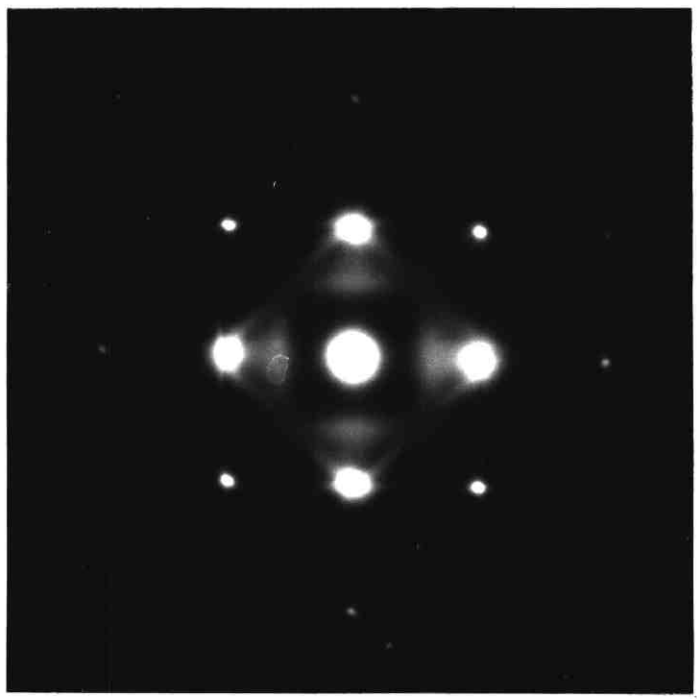

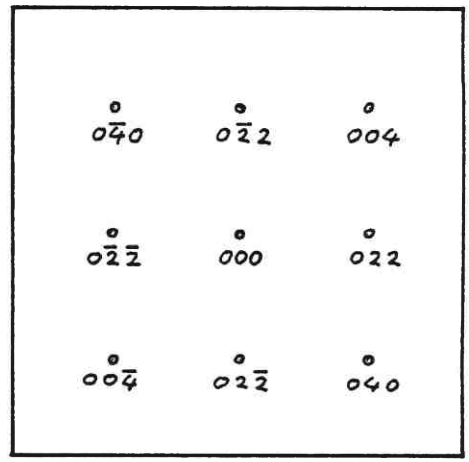

Transmission electron diffraction patterns from the substrate material

(a) Amorphous SiO_2 at the centre of the thinned region

(b) {100}-oriented silicon at the edge of the thinned region

FIGURE 4.7

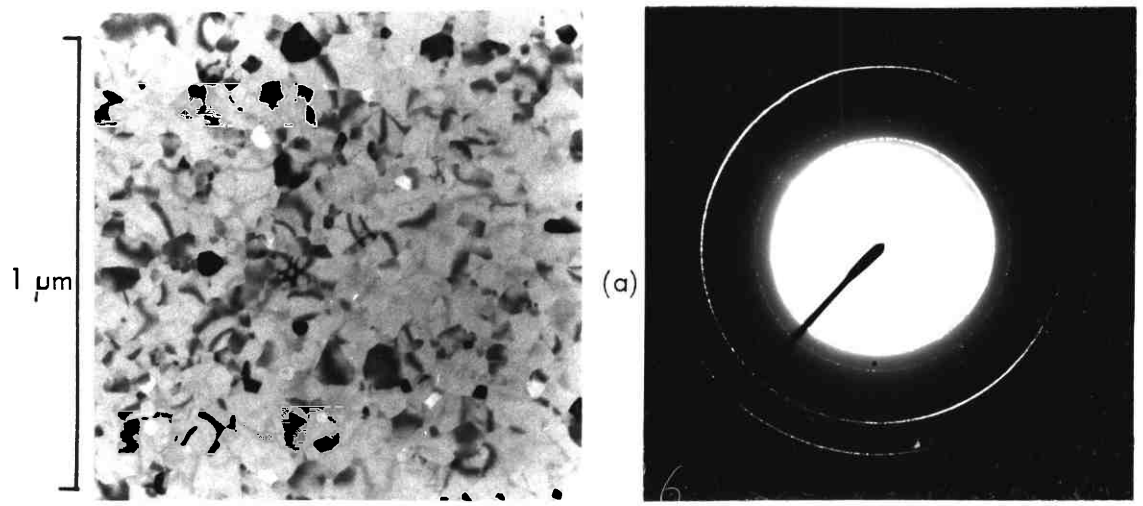

(a) Transmission electron micrograph and (b) diffraction pattern of a 50 nm Al film deposited onto SiO_2 at room temperature.

FIGURE 4.8

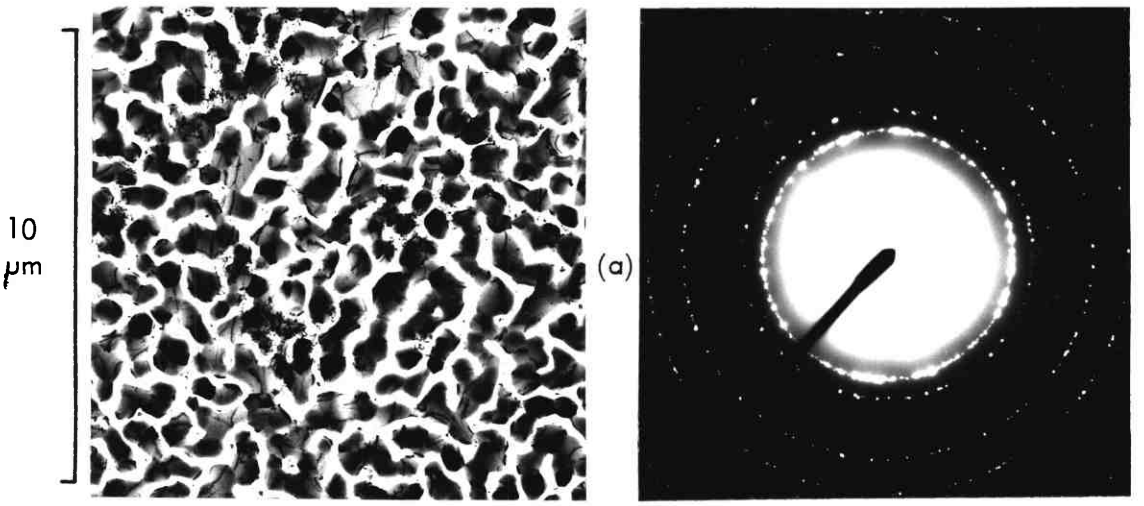

(a) transmission electron micrograph and (b) diffraction pattern of a 50 nm Al film deposited onto SiO_2 at 575 K.

FIGURE 4.9

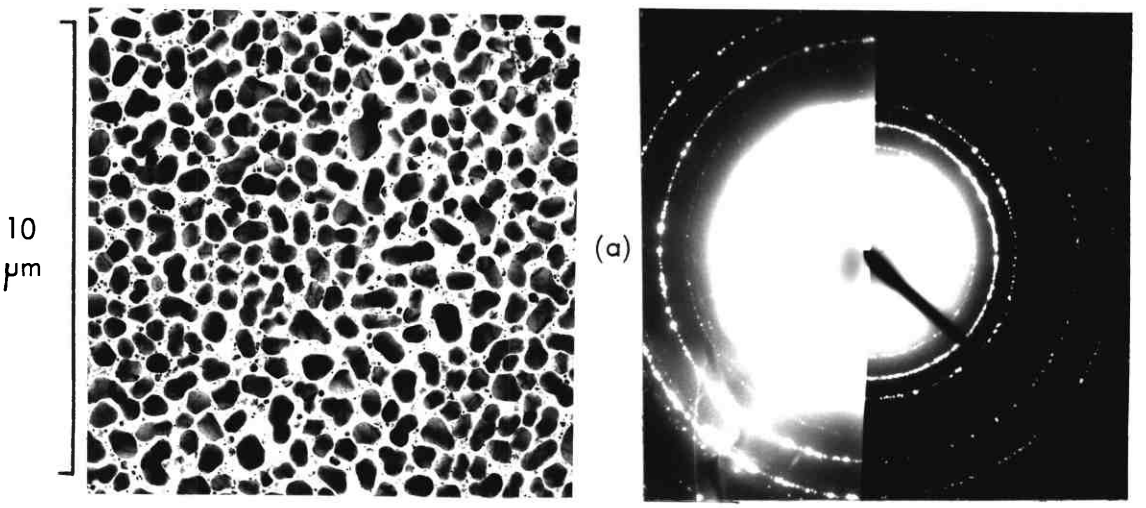

(a) Transmission electron micrograph and (b) diffraction pattern of a 50 nm Al film deposited onto SiO_2 at 650 K.

FIGURE 4.10

diffuse haloes from the underlying SiO_2, no other diffraction features were visible.

4.2.6.3 Aluminium Deposited onto SiO_2 at Elevated Temperatures

Films deposited onto substrates at 575 K consisted of a connected network of aluminium, as shown by the transmission electron micrograph (figure 4.9a). The diffraction pattern (figure 4.9b) shows the film to be polycrystalline with no preferred orientation. The diffraction patterns from some specimens prepared under these conditions contained faint rings corresponding to interplanar spacings of 0.32 nm and 0.19 nm. These were interpreted as the {111} and {220} reflections from polycrystalline silicon, which have interplanar spacings of 0.314 nm and 0.192 nm respectively, as calculated from the lattice parameter given by Wyckoff (1963). These are two of the strongest reflections from polycrystalline silicon and all others were too weak to be observed. The failure to detect even the {111} and {220} rings in some of the specimens was attributed to small differences in the amount of SiO_2 removed during thinning. A more intense diffuse background from a slightly thicker SiO_2 film rendered these faint diffraction features invisible.

Aluminium deposited onto SiO_2 at 650 K consisted of islands of ~500 nm extent and 100 nm height, with smaller islands of ~50 nm extent interspersed between them (figure 4.10a). The diffraction pattern (figure 4.10b) contained, in addition to the polycrystalline aluminium features, a series of rings which were found to correspond to the interplanar spacings of polycrystalline silicon and either η- or γ-alumina. (See table 4.1). Because only the most intense reflections from the alumina were observed, it was not possible to determine whether the phase present was η or γ, as the structures and diffraction patterns of these two phases are very similar. (The structures of the aluminas are discussed in Appendix D).

No evidence of silicon or Al_2O_3 was found in aluminium films deposited onto SiO_2 at temperatures below 575 K.

E.D. Data from Al on SiO_2 d (nm)	Calculated Values				X-Ray Diffraction (Wefers & Bell 1972)	
	Aluminium		Silicon		γ-Al_2O_3	η-Al_2O_3
	h k l	d (nm)	h k l	d (nm)	d (nm)	d (nm)
						0.46
0.33			1 1 1	0.314		
0.285					0.27	0.28
					0.241	0.240
0.233	1 1 1	0.233				
					0.228	0.227
					0.218	
					0.209	
0.202	2 0 0	0.202				
					0.198	0.197
					0.195	
			2 2 0	0.192		
0.164			3 1 1	0.164		
			2 2 2	0.157		
					0.154	0.152
0.143	2 2 0	0.143				
					0.139	0.140
			4 0 0	0.136		
0.126			3 3 1	0.125		
0.122	3 1 1	0.122				
						0.121
0.117	2 2 2	0.117				
					0.114	0.114
0.112			4 2 2	0.111		
					0.104	0.103
0.101	4 0 0	0.101				

Transmission Electron Diffraction Data from Al Deposited onto Amorphous SiO_2 at 650 K.

TABLE 4.1

4.2.6.4 The Effects of Annealing Films Deposited at Room Temperature

Aluminium films deposited onto SiO_2 at room temperature, then immediately annealed at 675 K for 1 hour in vacuo were found to contain silicon and η - or γ-alumina. The annealed films differed from the films deposited at 650 K, however, in that the former were continuous and had a $\langle 111 \rangle$ fibre texture.

No silicon or Al_2O_3 was detected in specimens annealed at temperatures below 650 K.

4.2.6.5 The Effect of Heating the SiO_2 Prior to Aluminium Deposition

SiO_2 substrates were heated at 650 K in a vacuum of 5×10^{-7} mbar for 1 hour and allowed to cool to room temperature. Aluminium was then deposited in the usual way, without the vacuum being broken.

The specimens prepared in this way were undistinguishable from those made by depositing aluminium onto SiO_2 which had not been heated.

4.2.6.6 Aluminium Films on Amorphous Carbon

Amorphous carbon films of approximately 50 nm thickness were deposited onto freshly cleaved rocksalt by evaporation from a carbon arc in vacuo (Holland 1956). The carbon films were floated off in deionized water, washed and collected on molybdenum TEM grids. 50 nm aluminium films were deposited onto the amorphous carbon at 650 K, under conditions identical to those used for the deposition of aluminium onto SiO_2.

The aluminium deposit was found to consist of islands and had no detectable fibre texture. There was no evidence of aluminium oxide in the diffraction pattern.

4.2.7 Discussion

Aluminium films deposited onto amorphous, steam-grown SiO_2 at temperatures of 575 K and above were found to contain polycrystalline silicon and γ- or η-Al_2O_3. These materials were also present in aluminium films deposited onto SiO_2 at room

temperature, then annealed at 650 K in vacuo. Polycrystalline silicon was not seen when the substrate was heated to 650 K and allowed to cool to 300 K before aluminium was deposited. Therefore, the polycrystalline silicon cannot have been formed by recrystallisation of the residual single crystal silicon on the back of the substrate, as a result of heating.

Polycrystalline alumina was not detected in aluminium films deposited onto amorphous carbon substrates at 650 K. It is therefore concluded that oxygen or water vapour, either in the evaporation plant or in the laboratory atmosphere, were not responsible for the formation of the polycrystalline alumina detected in the aluminium on SiO_2 specimens. The presence of both silicon and alumina in these specimens is therefore attributed to chemical reaction at the Al-SiO_2 interface.

As mentioned previously, the diffraction patterns contained insufficient information to enable the alumina to be positively identified as the γ- or η-phase. However, the diffraction evidence cannot be interpreted in terms of any other phase of alumina. The observations of θ- and α-alumina by Prabriputaloong and Piggott (1974) are apparently contradictory to the present findings. It is possible, however, that the different substrate material and deposition conditions used by these workers resulted in the formation of the different alumina phases. Nevertheless, they deposited aluminium onto both vitreous silica and quartz single crystals over a wide range of temperatures, and did not report any variations in the reaction products. The present results are in agreement with those of Chou and Eldridge (1970), which showed the presence of γ-Al_2O_3 in pits formed by the reaction between aluminium and SiO_2 in MOS structures. Clearly, further experiments are necessary to investigate the role of the substrate and deposition conditions in controlling the crystalline nature of the reaction products. Some further results are presented in section 4.3.4.

The first appearance of reaction products at annealing temperatures of 650 K,

in the present experiments, is in good agreement with the XPS results from "as prepared" SiO_2. (See section 3.6.2). The discrepancy between the threshold deposition temperature (575 K) and the threshold annealing temperature (650 K) for the detection of reaction products is thought to be due to radiative heating of the substrate by the evaporator during aluminium deposition. The temperature on the substrate surface has been observed to rise by more than 50 K during deposition.

It must be emphasized that the transmission electron diffraction technique could not reveal amorphous reaction products or crystalline products forming layers less than approximately 2 nm thick. (This is because of the presence of the strong aluminium diffraction pattern and the diffuse background from the amorphous SiO_2, which would effectively mask any faint diffraction features from very thin layers of material). It is therefore possible that some interfacial reaction occurred at temperatures slightly below those stated. Judging by the relative intensities of the diffraction patterns, it is estimated that for aluminium films deposited at 650 K, the interfacial reaction zone was between 5 nm and 10 nm thick.

4.3 The in-situ TEM Experiments

4.3.1 Modifications to the Electron Microscope

The basic JEM 100 U transmission electron microscope is described in section 4.2.4. In order to perform in-situ aluminium evaporation and specimen heating, certain modifications were made to the specimen chamber as described below. The modified specimen chamber is shown in figure 4.11.

Firstly, the specimen goniometer was replaced by a heater stage. This accepted the JEOL specimen furnaces which could attain a temperature of approximately 1300 K for a dissipation of 10 w. Accurate temperature control was provided by a Solartron constant voltage power supply. The rapid specimen exchange facility was retained.

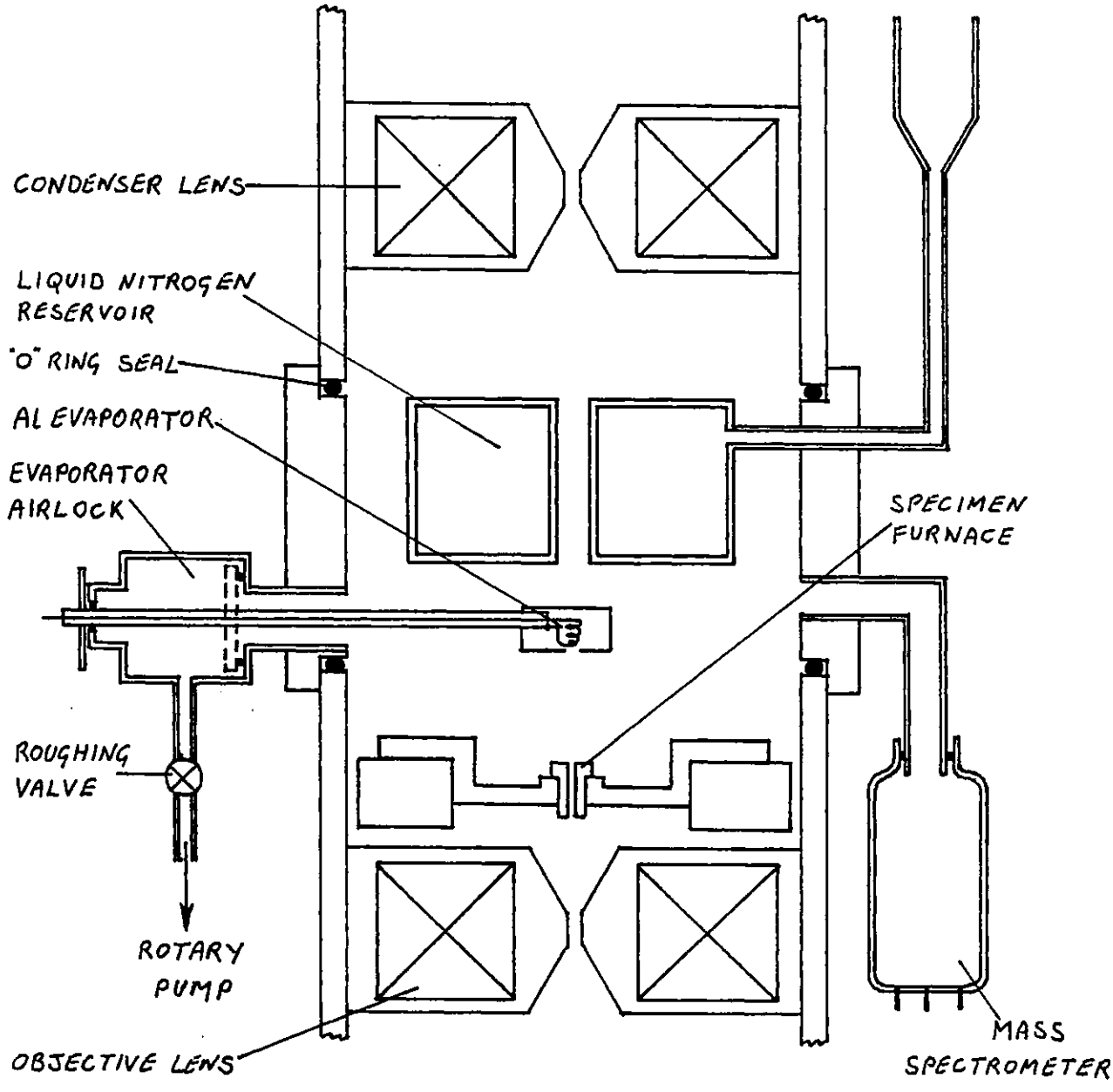

The electron microscope specimen chamber, fitted with liquid nitrogen cryo-pump, aluminium evaporator and specimen furnace.

FIGURE 4.11

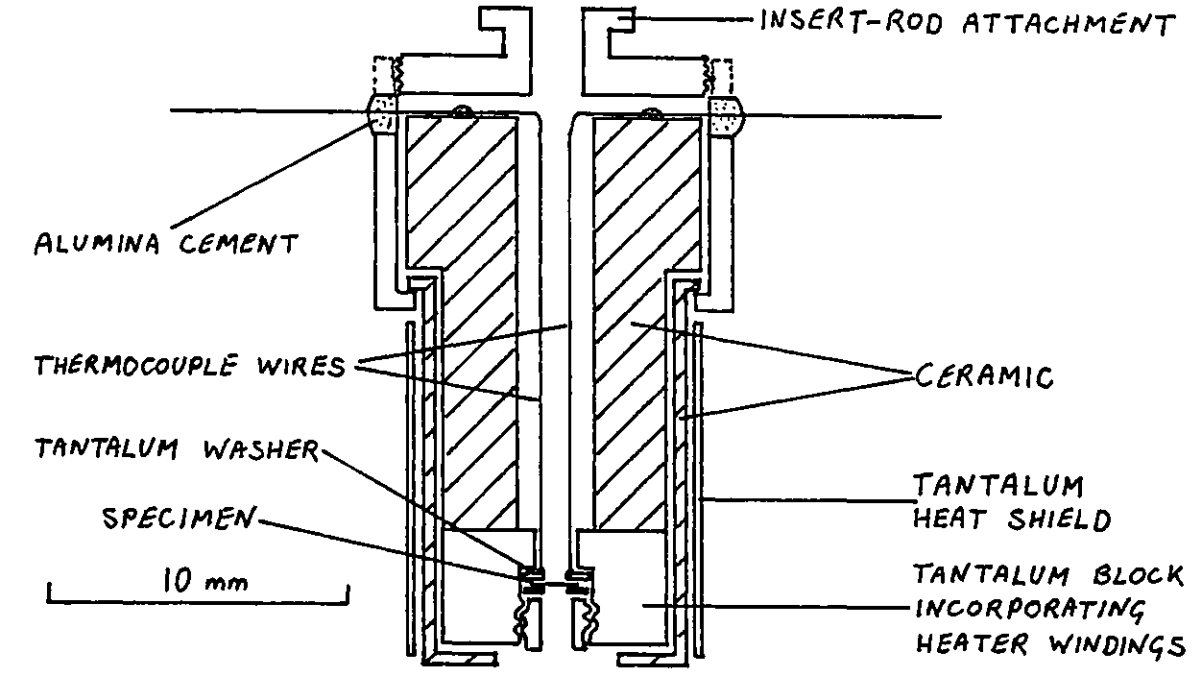

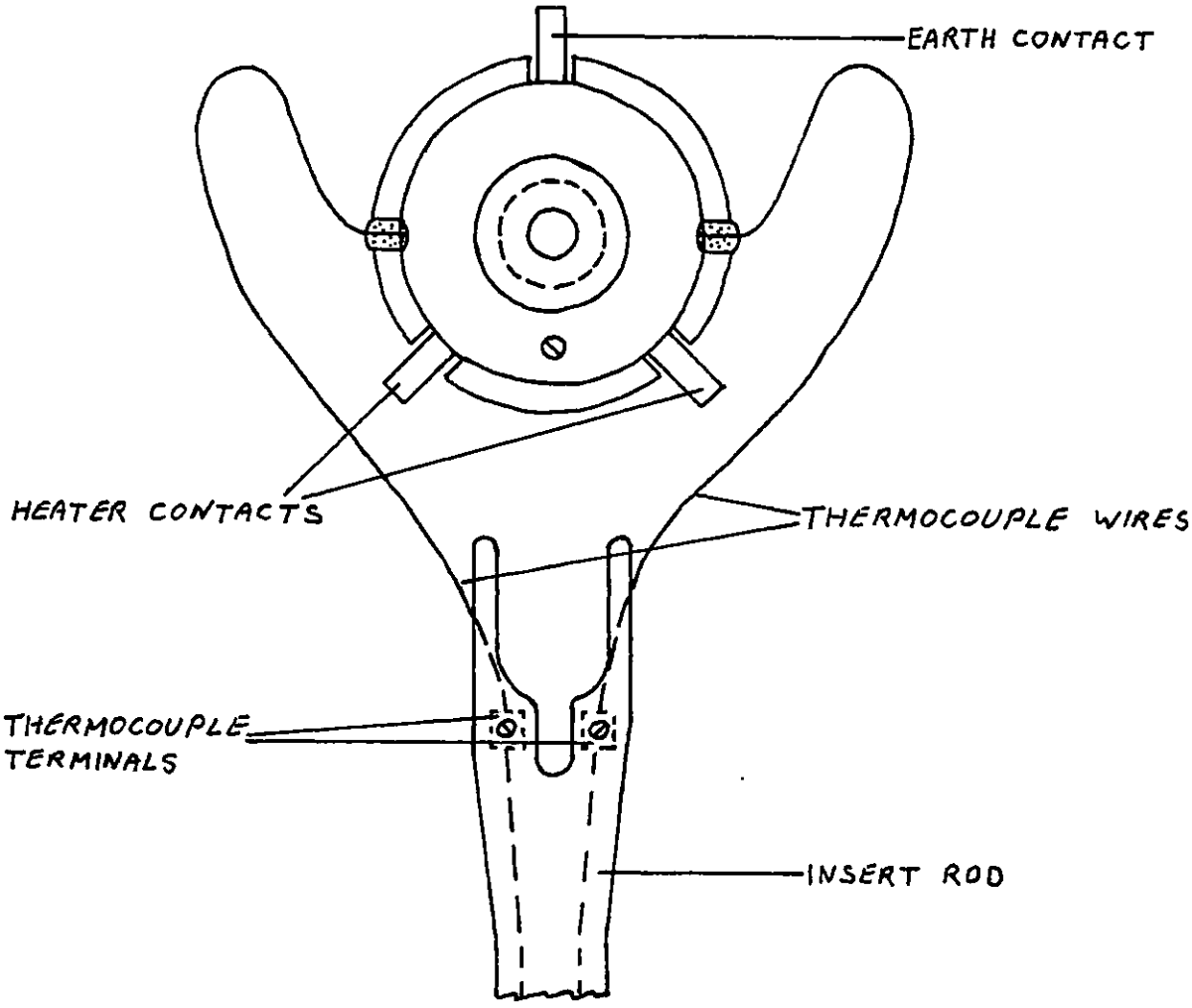

Attachment of chromel-alumel thermocouple to the JEOL specimen furnace.

FIGURE 4.12

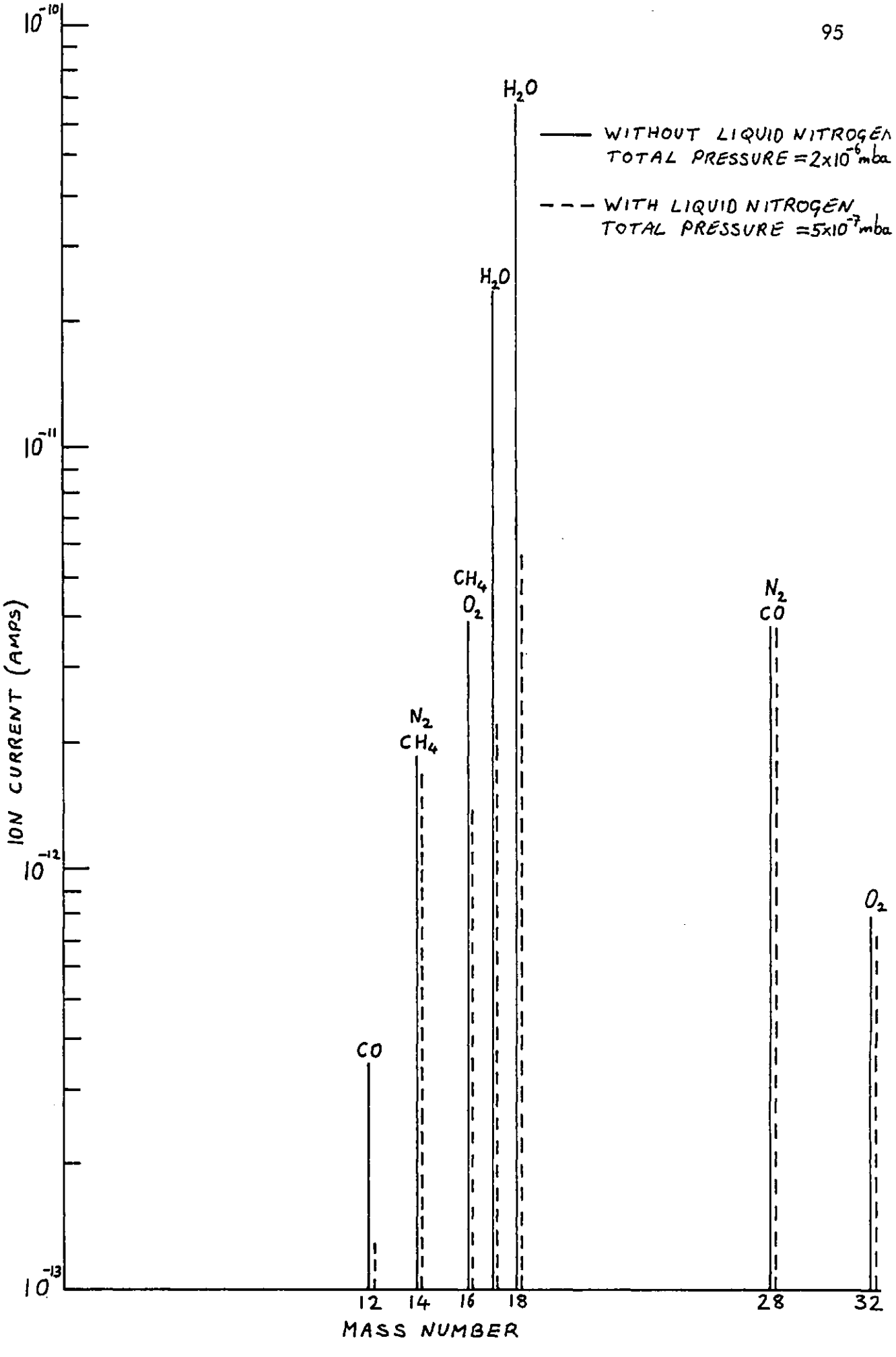

Residual gas spectra from the JEM-100U specimen chamber.

FIGURE 4.13

Specimen temperature was measured by a chromel-alumel thermocouple incorporated in the furnace (see figure 4.12). The external thermocouple circuit comprised an ice junction in series with an EXEL 200 DVM, enabling the temperature to be measured with a precision of 0.2 K. The absolute accuracy, however, was $\sim$1 K. The calibration procedure is described in Appendix C. The construction of the thermocouple system is described fully by Spiller (1979) and further details will not be given here.

Secondly, the specimen chamber was fitted with a liquid nitrogen cryopump, which reduced the pressure to 5×10^{-7} m bar by the condensation of water vapour (see figure 4.13).

Thirdly, a tungsten filament evaporator was added to the specimen chamber. The filament, in the form of a vertical helical coil, was enclosed inside a tantalum foil shield with a 5 mm aperture directly beneath the coil. The evaporant was thus confined to a narrow beam in the vicinity of the specimen. The evaporator could be withdrawn from the microscope into an airlock isolated by a gate valve. This enabled the evaporator to be replaced without significantly disturbing the vacuum in the microscope column. (The tungsten coil was renewed after each evaporation because of alloying with the molten aluminium charge).

Because the substrate was located at the bottom of the narrow base of the specimen furnace, correct positioning of the evaporator was essential to ensure that the substrate was exposed to the evaporant. This was accomplished by removing the tantalum shield and adjusting the position of the evaporator coil until a purple fluorescence indicated that it was in the path of the electron beam and therefore directly above the specimen. The position of the evaporator was noted so that it could be located in the same place after removal for loading with aluminium and replacing the tantalum shield.

The evaporator power supply consisted of a low voltage transformer connected to

a Variac. A current of 13 amps was found to give a deposition rate of approximately 1 nm s^{-1}.

4.3.2 Substrate Preparation

Two types of substrate were used. These were steam-grown SiO_2 on {100} silicon and evaporated SiO. The material for the SiO_2 substrates was similar to that used for the evaporator experiments (see section 4.2.1). In the present case, however, it was cut into 3 mm discs and jet thinned before the aluminium was deposited. A 100 nm thick SiO_2 layer was found to be more robust than a 50 nm layer, which often fragmented after thinning, without the presence of an aluminium film to strengthen it.

Particular care was taken in cleaning the SiO_2 surface after thinning. The substrates were washed in warm trichloroethylene and 2 baths of warm acetone before being vapour-cleaned in isopropyl alcohol and finally rinsed in deionized water. Transmission electron microscopy was used to check the effectiveness of the cleaning procedure, and no residual contamination was detected. Individual substrates, however, were not examined prior to aluminium deposition because of the risk of carbon contamination from oil vapour cracked by the electron beam.

SiO substrates were prepared by evaporation onto freshly cleaved rocksalt or mica in the vacuum evaporation plant shown in figure 4.14. The chamber was evacuated by a 2-inch oil diffusion pump fitted with a liquid nitrogen cold trap and a vacuum of 5×10^{-6} m bar was attained. 50 nm films of SiO were deposited at a rate of 1 nm s^{-1}, as measured by a quartz crystal monitor. The SiO film was scribed into 2 mm squares, floated off the rocksalt or mica in deionized water, and collected on molybdenum TEM grids. Each specimen was washed by agitating in deionized water for several minutes.

The chemical composition of vapour-deposited "silicon monoxide" films is known to vary with deposition rate and residual gas pressure (Holland 1956). The conditions used in the present study were chosen to give SiO with a density roughly equal to that

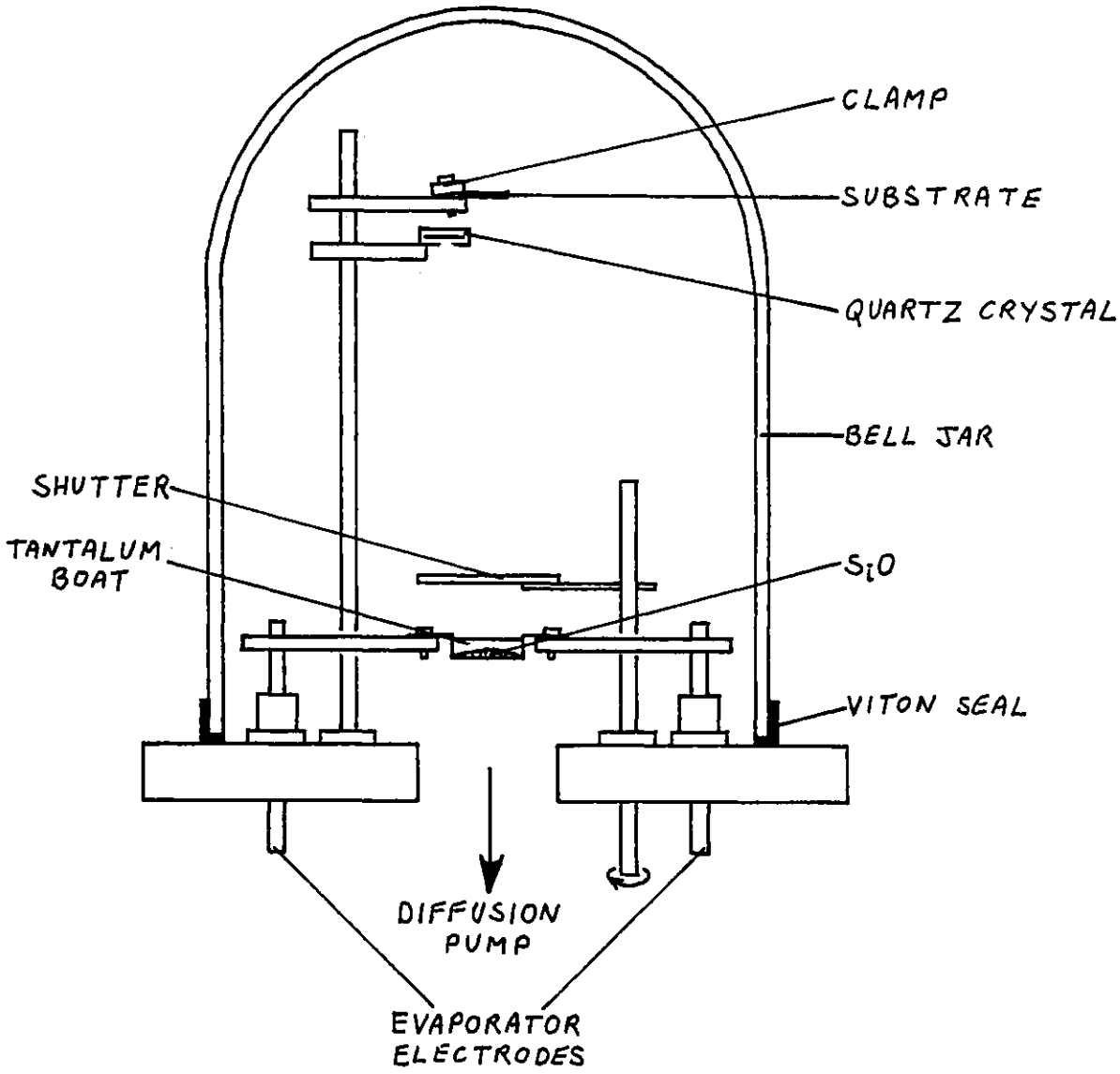

(a)

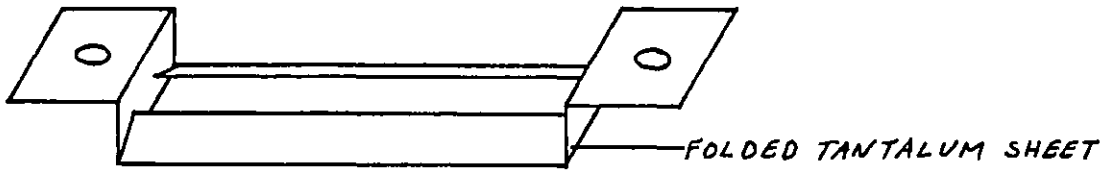

(b)

(a) The SiO evaporation system.

(b) The tantalum boat.

FIGURE 4.14

of the compact bulk substance. A fall in pressure in the vacuum chamber was noted during the evaporation of Si O as a result of its gettering action for oxygen and water vapour. Therefore, a considerable amount of Si O was evaporated before the shutter was opened, so that the material deposited onto the substrate contained a minimum of these impurities from the ambient. Electron diffraction showed the Si O to be amorphous.

4.3.3 Experimental Method

After preliminary outgassing of the evaporator coil and positioning in the electron beam (see section 4.3.1), the aluminium charge was loaded and the tantalum shield fitted. The evaporator was thoroughly outgassed in-situ, then the substrate was inserted into the specimen stage and heated to the desired temperature. Aluminium was deposited, the thickness and deposition rate being estimated from the evaporator current and deposition time. The thickness of a film could be judged from its appearance (grain size or island size), the deposition temperature being known. Standardisation of the evaporation conditions allowed films of consistent appearance to be produced. A deposition rate of 1 nm s^{-1} and a mean film thickness of 50 nm were aimed for. The chamber pressure rose to 2×10^{-5} m bar during deposition, despite the thorough outgassing procedures employed. The main component was found to be hydrogen.

80 keV electrons were used to examine the specimens. Areas of the specimen near the edges of the thinned region were used, to minimize heating of the specimen by the electron beam. (Single crystal silicon is a good conductor of heat, but amorphous SiO_2 is a good thermal insulator). In the case of Si O substrates, areas near to grid bars were used.

In some experiments, specimens were annealed at various temperatures after aluminium had been deposited. Otherwise, specimens were allowed to cool to room temperature after aluminium deposition.

4.3.4 Results

4.3.4.1 Aluminium on Steam-Grown SiO_2

Aluminium deposited onto thinned SiO_2 at 675 K showed no evidence of chemical reaction. The film consisted of islands of similar appearance to those formed when aluminium was deposited onto "as prepared" SiO_2 at 650 K (see section 4.2.6.3). The diffraction pattern revealed that the aluminium was polycrystalline with no preferred orientation. (See figure 4.15a and b).

Annealing the specimens at temperatures up to 900 K for 30 minutes in a vacuum of 5×10^{-7} m bar had little effect on the film morphology or the diffraction pattern, the only effect being a slight increase in the diffuse background intensity. On heating to the melting point of aluminium, however, rapid changes occurred over a period of several minutes. When the aluminium melted, its diffraction pattern disappeared. The diffraction patterns of the reaction products then began to appear and after several minutes were clearly visible (figure 4.15c). The micrograph (figure 4.15d) shows that aluminium was still present in the form of liquid droplets. Analysis of the diffraction pattern showed the reaction products to be polycrystalline silicon and η-alumina (see table 4.2). The observed inter-planar spacings and relative intensities are in good agreement with those determined by x-ray diffraction (Wefers and Bell 1972).

Substrates which were heated at 1075 K for 1 hour in a vacuum of 5×10^{-7} m bar before aluminium was deposited were found to be much more reactive. (This treatment produced no visible changes in the appearance of the SiO_2 or its diffraction pattern). Aluminium films deposited onto these substrates at temperatures in excess of 725 K contained traces of silicon and η - or γ-alumina.

For deposition temperatures below 725 K, there was no evidence of crystalline reaction products in the diffraction pattern. The electron micrograph and transmission electron diffraction pattern of a film deposited onto SiO_2 at 700 K are shown in figure

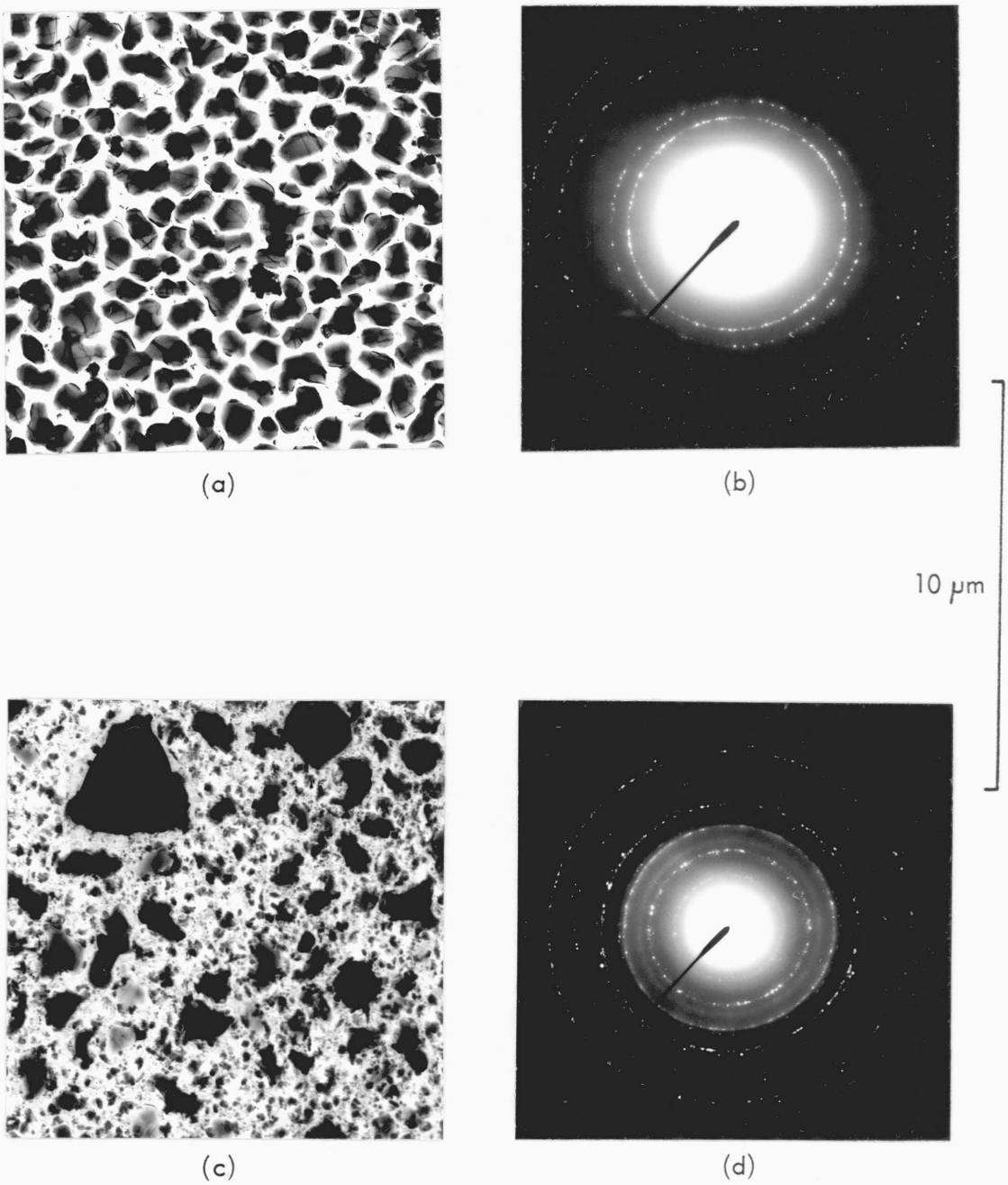

Transmission electron diffraction patterns and micrographs of Al deposited in-situ onto SiO_2 at 675 K: (a) and (b) as deposited;
(c) and (d) after heating to the melting point of aluminium.

FIGURE 4.15

E.D. Data from Al on SiO_2	Calculated Values Silicon		X-Ray Diff.^{n} (Wefers & Bell 1972) η-Al_2O_3
d(nm)	h k l	d (nm)	d (nm)
0·464			0·46
0·313	1 1 1	0·314	
0·280			0·28
0·238			0·240
0·227			0·227
0·196			0·197
0·192	2 2 0	0·192	
0·163	3 1 1	0·164	
0·155	2 2 2	0·157	
			0·152
0·140			0·140
0·136	4 0 0	0·136	
0·125	3 3 1	0·125	
0·121			0·121
			0·114
0·111	4 2 2	0·111	

Electron Diffraction Data from Fully-Reacted Al on SiO_2.

TABLE 4.2

4.16a and b. After heating at 800 K for 15 minutes in vacuo, changes in the film morphology and the diffraction pattern were observed. The electron micrograph (figure 4.16c) shows changes in contrast of the smaller (~100 nm) aluminium islands and the diffraction pattern (figure 4.16d) contains rings due to polycrystalline silicon. Continued annealing for 90 minutes at this temperature resulted in strong silicon and η-alumina diffraction patterns and pronounced changes in the appearance of the specimen (figure 4.16e and f, table 4.3). After annealing for 180 minutes no further changes occurred. The aluminium diffraction pattern at this stage was very weak, showing that almost all of the aluminium had been oxidized. Dark field electron microscopy revealed the presence of many particles of silicon and η-alumina (figure 4.16g).

4.3.4.2 Aluminium on Evaporated Si O

The results for aluminium deposited onto evaporated Si O were similar to those for aluminium on SiO_2 described above. Deposition at 675 K did not lead to reaction but polycrystalline silicon and alumina were produced by annealing at the melting point of aluminium. In this case, however, γ-alumina was found (see table 4.4).

Si O substrates heated at 1075 K for 1 hour in vacuo were more reactive. Polycrystalline silicon and γ-alumina were detected in aluminium films deposited onto these substrates at temperatures of 725 K and above.

4.3.5 Discussion

SiO_2 substrates which had been chemically thinned were less reactive than similar substrates in the "as prepared" condition. The difference is thought to be due to contamination of the surface during thinning. The threshold temperature for the detection of reaction products on thinned substrates was reduced from 933 K to 725 K by heating at 1075 K in vacuo before aluminium deposition. As no changes in the structure of the SiO_2 (e.g. crystallization) were detected, the effect is attributed to

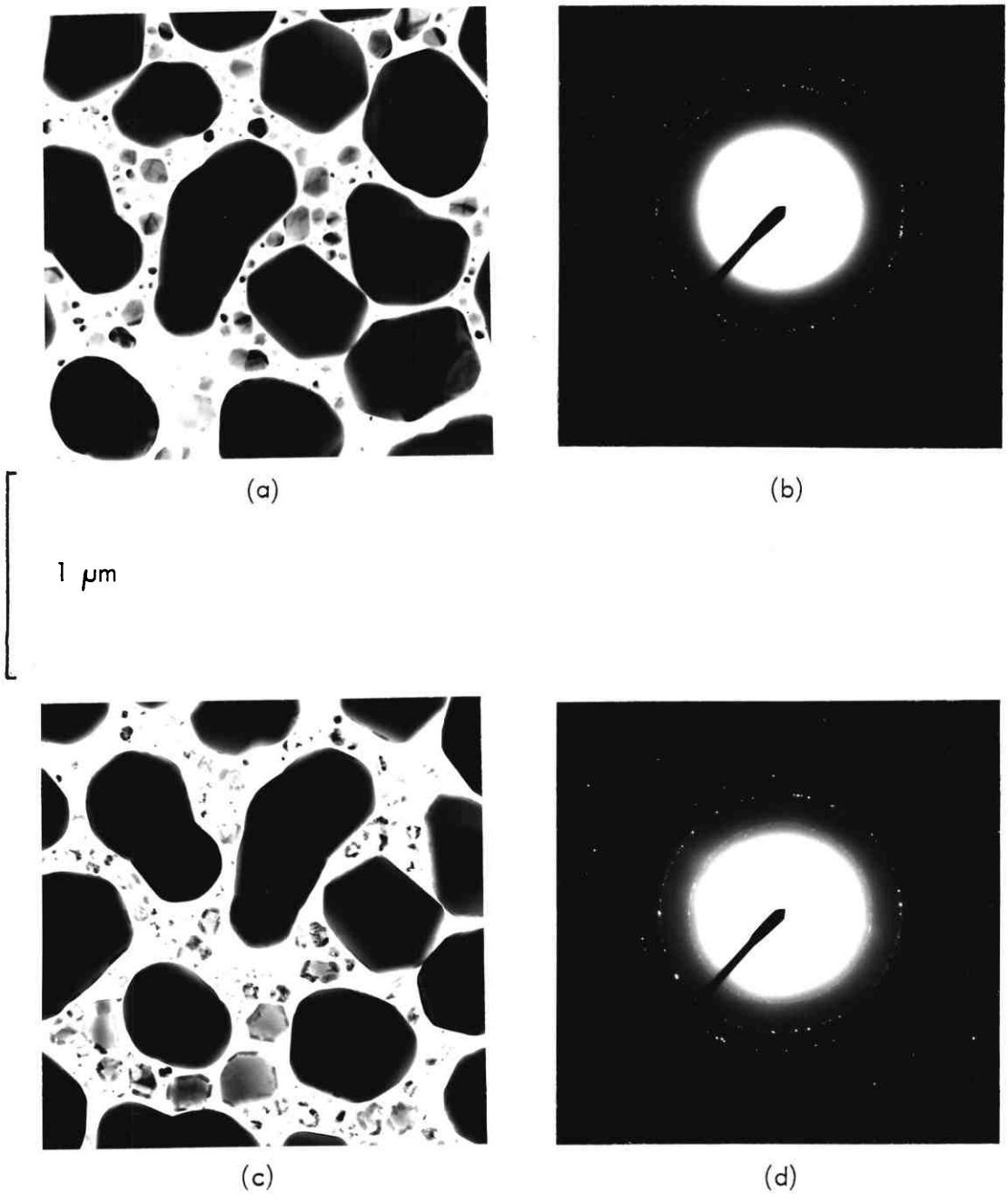

FIGURE 4.16

(continued on next page)

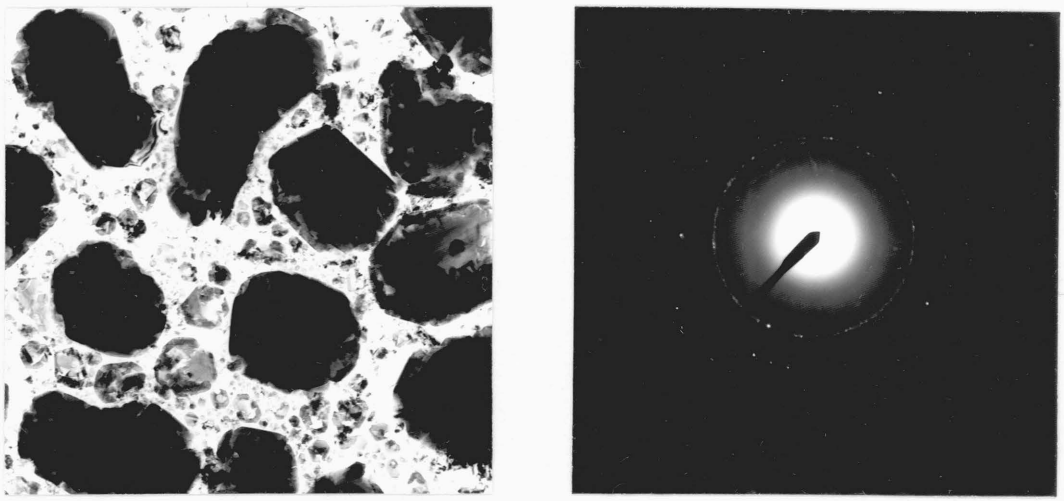

(e) (f)

1 μm

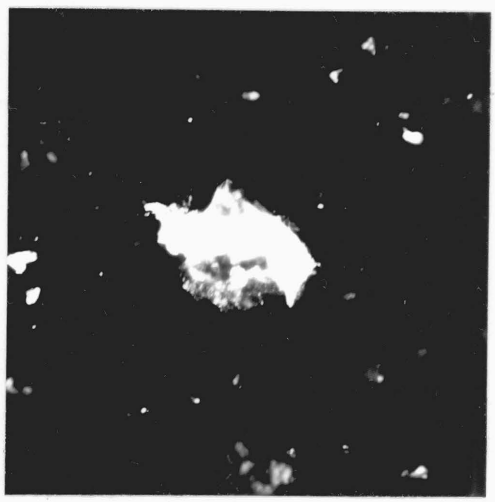

(g)

Reaction sequence of Al deposited in-situ at 700 K onto SiO_2 which had been pre-heated in vacuo at 1075 K: (a) and (b) as deposited;
(c) and (d) after heating at 800 K for 15 minutes;
(e) and (f) after heating at 800 K for 90 minutes;
(g) dark field (220) image of a silicon particle.

FIGURE 4.16

E.D. Data from Al on SiO_2	Calculated Values				X-Ray Diff^n.
	Aluminium		Silicon		η-Al_2O_3
d (nm)	h k l	d (nm)	h k l	d (nm)	d (nm)
0·454					0·46
0·314			1 1 1	0·314	
0·278					0·28
0·238					0·240
	1 1 1	0·233			
0·228					0·227
0·204	2 0 0	0·202			
0·197					0·197
0·191			2 2 0	0·192	
0·164			3 1 1	0·164	
0·157			2 2 2	0·157	
0·152					0·152
0·145	2 2 0	0·143			
0·140					0·140

Electron Diffraction Data from Al Deposited onto SiO_2 at 700K in the T.E.M. and Annealed in-situ for 90 minutes at 800K.

TABLE 4.3

E.D. Data from Al on SiO d (nm)	Calculated Values Silicon				X-Ray Diff^{n}. γ-Al_2O_3 d (nm)
	h	k	l	d (nm)	
0·314	1	1	1	0·314	
					0·27
0·239					0·241
0·230					0·228
					0·218
					0·209
0·199					0·198
					0·195
0·192	2	2	0	0·192	
0·164	3	1	1	0·164	
0·157	2	2	2	0·157	
					0·154
0·140					0·139
0·136	4	0	0	0·136	
0·125	3	3	1	0·125	

Electron Diffraction Data from fully reacted Al on SiO

TABLE 4.4

the desorption of surface contaminants. The most probable contaminants resulting from the thinning process are carbon-based materials (from the Apiezon grease used to mount the specimen) and water (from the washing procedure). It is unlikely that heating at 1075 K in vacuo would remove carbon contamination, but it would be effective in desorbing water.

The Si O substrates were relatively clean, having been prepared by vacuum evaporation. However, these too became more reactive after heating in vacuo. Si O films deposited onto mica and rocksalt gave identical results, indicating that contamination from the substrate was negligible. The most probable source of contamination was the deionized water used to separate the Si O films from their substrates. Hence, the enhanced reactivity of both SiO_2 and Si O substrates heated in vacuo is thought to be due to the desorption of water from their surfaces.

Bateson (1952), using contact angle measurements, showed that freshly prepared glass surfaces became covered with a layer of adsorbed water on exposure to the atmosphere. This layer could not be removed by chemical cleaning, but was removed by heating in vacuo. Recent electron loss studies by Underhill and Gallon (1981) revealed peaks in the bulk band gap of SiO_2, which were thought to be associated with dangling silicon and oxygen bonds on, or just below, the surface. The structure of these peaks was found to be sensitive to hydrogen and water vapour exposure and to heating in vacuo. Hydrogen, in some form, is believed to saturate the dangling bonds but is removed by vacuum baking. The authors suggest further experiments to compare the electron loss spectra from wet and dry silicas in order to elucidate the exact role of hydrogen, but their recent results lend strong support to the hypothesis that adsorbed water greatly reduces the reactivity of the SiO_2 surface.

CHAPTER 5

THE Al - SiO_2 INTERFACE IN SILICON DEVICES

5.1 The Al - SiO_2 Interface - Summary of Results

When approximately one monolayer of aluminium was deposited onto ion bombarded SiO_2 in uhv conditions, reaction occurred at room temperature over a period of several hours, resulting in the formation of silicon and Al_2O_3. After heating to 575 K, almost complete oxidation of the aluminium took place within several minutes. When aluminium was deposited onto "as prepared" SiO_2 under identical conditions, reaction proceeded more slowly. Al_2O_3 was detected, but very little elemental silicon was apparent. The aluminium is believed to have reacted with adsorbed water on the SiO_2 surface.

When aluminium was deposited onto "as prepared" SiO_2 in a conventional evaporation plant, polycrystalline silicon and η - Al_2O_3 were detected by transmission electron diffraction, for deposition temperatures above 575 K. When the substrate temperature was 650 K, the interfacial reaction zone was estimated to be 10 nm thick. Annealing at temperatures of 650 K and above brought about interfacial reaction in specimens prepared by aluminium deposition at lower temperatures.

In-situ TEM experiments indicated that water contamination was effective in preventing Al - SiO_2 reaction, except at temperatures near the melting point of aluminium.

5.2 The Al - SiO_2 Interface in Devices

Some of the ways in which the properties of the Al - SiO_2 interface can affect the performance and reliability of silicon devices were discussed briefly in section 2.1. The effects of Al - SiO_2 interfacial reaction in devices will now be considered in the

light of the present results.

Simplified diagrams of a silicon planar bipolar transistor and a MOSFET, showing the arrangement of the metallization and insulator layers, are given in figure 5.1.

5.2.1 The "Sintering" Process

For proper device operation, good ohmic contact between the metallization and the silicon at the contact windows is essential. When aluminium metallization is used, ohmic contact is established by a "sintering" or "alloying" process, in which the wafer is heated to around 750 K for several minutes after metallization. It is generally believed (e.g. Learn 1976) that the effect of "sintering" is to bring about reaction between the aluminium and the native oxide on the silicon surface, hence promoting electrical contact between the metal and the semiconductor.

The thickness of native SiO_2 at room temperature is approximately 2 nm (Azzam and Bashara 1977). On the basis of the present results from annealing studies of aluminium on "as prepared" SiO_2, heating for several minutes at 750 K should be more than adequate for complete reduction of the native SiO_2. Furthermore, for aluminium metallizations deposited onto wafers at temperatures of approximately 600 K (which is the normal deposition temperature in many metallization processes) reduction of the native SiO_2 would be expected to occur during deposition. If, however, the interface so formed consists of an almost continuous layer of alumina, electrical contact between the aluminium and silicon would still be poor. The sintering process may therefore be necessary to bring about diffusion of aluminium or silicon (or both) across the interfacial alumina layer. Grain boundaries in the silicon and alumina may provide fast diffusion paths, and the small grain size ($\sim$ 50 nm) of the alumina means that the density of such defects is high.

The present results also indicate that contamination of the surface of the wafer

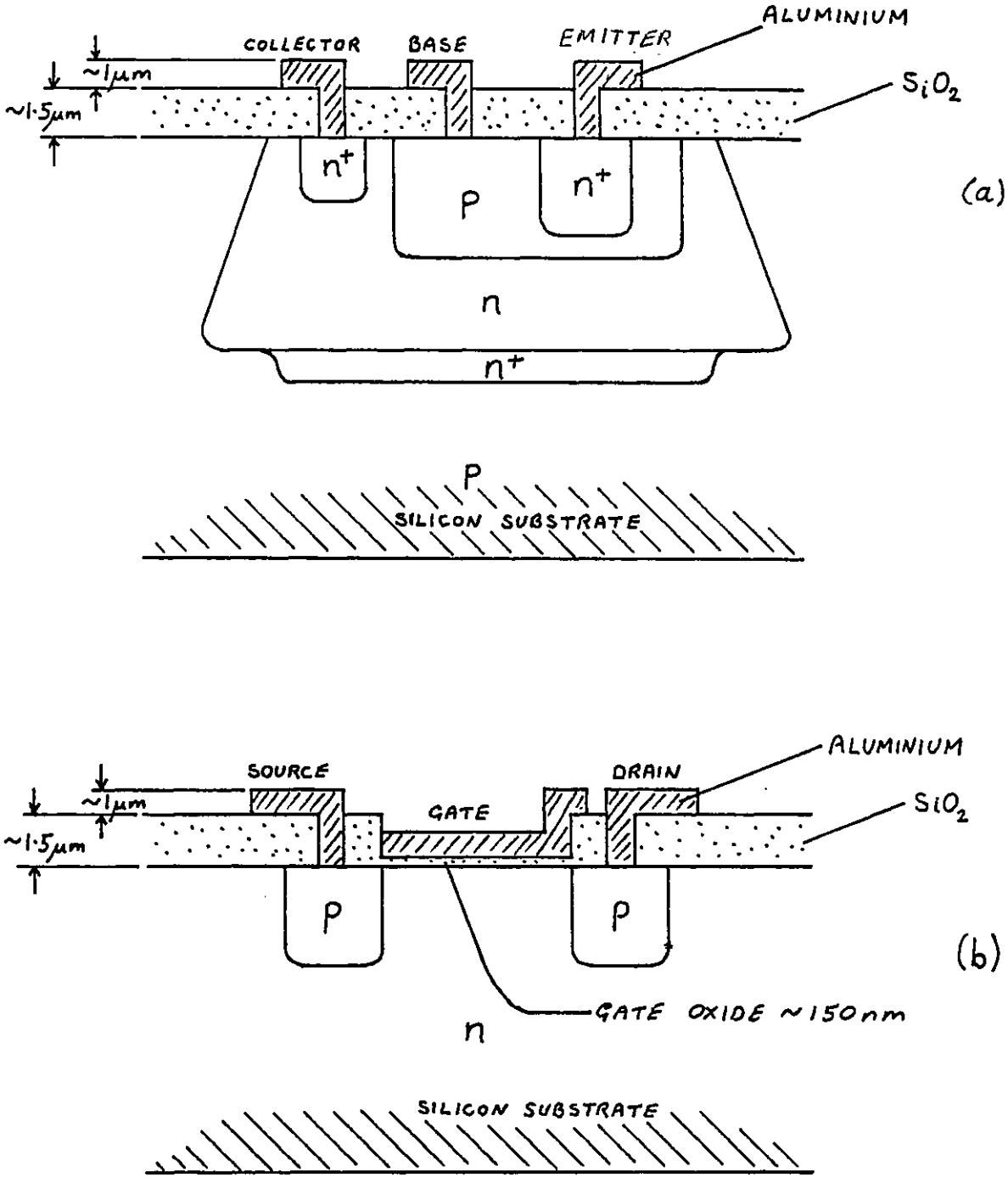

Simplified sections through (a) a bipolar transistor and (b) a MOSFET, showing the arrangement of the metallization and SiO_2 layers.

FIGURE 5.1

by water may prevent Al - SiO_2 reaction at the temperatures normally employed in metallization and "sintering" processes. Such contamination could result from etching or photoresist-stripping procedures, for example. Thorough cleaning of the wafer surface before metallization is therefore expected to improve Al - Si ohmic contact. Extensive heating treatments of wafers in the final stages of processing are not possible, but other cleaning procedures may prove useful. For example, sputter etching of the wafer surface prior to deposition of the aluminium should be effective in removing adsorbed water and other contaminants and could be used to remove the native SiO_2 from the contact windows. Chemical etching using HF is also used for this purpose.

5.2.2 Aluminium - Silicon Dioxide Adhesion

Adhesion between a thin film and a substrate may occur at various types of interface (Chapman 1974). Firstly, the adhesion may be "interfacial", with the film and substrate meeting at a well defined boundary. Secondly, interdiffusion of the materials may provide adhesion by the formation of an interfacial layer of varying composition. Thirdly, reaction between the film and substrate may occur, resulting in a layer of reaction products at the interface. Fourthly, if the substrate surface is rough, mechanical interlocking of the film and substrate may occur.

Adhesion between aluminium and SiO_2 is believed to arise from the reduction of the SiO_2 by the aluminium. It is generally observed that aluminium metallizations deposited by vacuum evaporation onto wafers at low temperatures suffer from poor adhesion. D'Heurle et al (1968) found that deposition temperatures of approximately 450 K and above were required to produce aluminium films which adhered well to SiO_2. These authors also stated that adhesion was particularly poor when boron or phosphorus contamination was present on the surface of the wafer. Lowry and Hogrefe (1980), using AES, detected carbon and sulphur on the back of aluminium films which had peeled from the SiO_2 at the bond pads. The contaminants were thought to be residues from a photo-

resist stripper containing sulphonated hydrocarbons. The above examples demonstrate the importance of wafer processing techniques in obtaining adhesion of aluminium metallizations. Some further results, which show non-adhesion of aluminium deposited onto SiO_2 at room temperature, are presented in section 9.2.3. In these specimens "blistering" of the metallization was seen at the bond pads and at various points along the track. Aluminium deposited onto SiO_2 at 475 K and above was found to adhere well.

It is evident that satisfactory Al - SiO_2 adhesion can be obtained at deposition temperatures below those needed for the formation of detectable amounts of crystalline reaction products in aluminium films on "as prepared" SiO_2 substrates. Nevertheless, the dependence upon substrate surface preparation and temperature suggest that some form of interfacial reaction is involved in the adhesion process. If silicon and alumina were produced in very small quantities at temperatures below 575 K, or if the crystallite size was sufficiently small, their presence would not be established by transmission electron diffraction. It is also possible that reaction between the aluminium and adsorbed OH groups on the SiO_2 surface may provide adhesion, as proposed by Bateson (1952). The use of a highly surface-sensitive technique such as secondary ion mass spectroscopy (SIMS) may enable small amounts of interfacial silicon and alumina to be detected (although interpretation of the SIMS cracking pattern could create difficulties) and would also make possible the detection of hydrogen.

It has been stated (Mattox 1973) that sputter-deposited aluminium films adhere more strongly to SiO_2 than do evaporated films. This effect has been attributed to the higher energy of the sputter-deposited atoms, which tend to clean the substrate surface and create defects, thus promoting film-substrate reaction. When deposition temperatures of around 600 K are used (for example, to produce a large-grained metallization which is resistant to electromigration damage) adhesion of evaporated aluminium is generally satisfactory. However, if a small grain size is required (to give greater

uniformity of etching, for example) a low deposition temperature must be used, and sputter-deposition may produce metallizations with better adhesion.

5.2.3 Mechanical Stress in Aluminium Films on SiO_2 Substrates

The difference between the thermal expansion coefficients of aluminium ($\sim 25 \times 10^{-6} K^{-1}$) and amorphous SiO_2 ($\sim 0.5 \times 10^{-6} K^{-1}$) leads to the generation of thermally induced stress in aluminium films on SiO_2 substrates. The effects of annealing on the stress levels has been investigated by Sinha and Sheng (1978), who reported a small compressive stress in the aluminium on heating and a large tensile stress on cooling to room temperature. Stress relief mechanisms must therefore be operative at high temperatures ($\sim$450 K and above). The "annealing hillocks" observed by d'Heurle et al (1968) and others are believed to result from the relief of compressive stress in the metallization. Work on hillock growth in lead and tin films on glass substrates (Chaudhari 1974) suggests that diffusion of metal atoms along the film-substrate interface is an essential part of the stress relief process. (See section 6.3.4) The structure of the interface may therefore be important in controlling stress relief by hillock growth. An interfacial layer consisting of small-grained polycrystalline silicon and aluminium, as observed at temperatures above 575 K, is expected to provide a fast diffusion path for aluminium atoms and hence enhance hillock formation. Changes in the form of the interface during annealing could lead to changes in the observed stress levels after several annealing cycles, as reported by Sinha and Sheng. (These authors noted signs of Al - SiO_2 reaction in specimens which had been annealed at 750 K several times). However, other factors, such as grain growth, may also be of importance in this respect.

Migration of silicon into the aluminium film, following Al - SiO_2 reaction, could affect the mechanical properties of the metallization and cause changes in the stress levels, as suggested by d'Heurle et al (1968). No experimental evidence for such a process has

been reported in the literature, but it might be expected to occur as a result of the high solubility of silicon in aluminium. (The use of carefully controlled sputter profiling in conjunction with a highly surface sensitive technique such as SIMS could possibly be used to detect silicon in the aluminium film).

The existence of an interfacial reaction zone of finite thickness may provide some degree of matching between the widely different thermal expansion properties of aluminium and SiO_2. The expansivity of silicon ($3 \times 10^{-6} K^{-1}$) is intermediate between the values for silicon dioxide and aluminium. Thermal expansion data for η-alumina is not available, but if this phase behaves in a similar manner to the α-phase (corundum), the expansivity will be around $7 \times 10^{-6} K^{-1}$. The interfacial silicon-alumina layer is therefore expected to take some of the stress resulting from annealing. Thicker interfacial layers would provide a greater degree of matching.

The generation of stress and the growth of hillocks are extremely undesirable in contact metallizations, as cracking of the glass passivation layer may result. The effects are even more serious in multilevel device structures, where hillock growth on the first layer metallization can cause shorting through the insulator film (Vossen et al 1973). Hillock formation may occur during contact "sintering" or during device operation at high temperatures. The incorporation of small amounts of copper, tin or manganese in the aluminium has been found to suppress hillock growth (Herman et al 1972 and Sato et al 1971). The effect may be due to the segregation of the impurity atoms at grain boundaries preventing grain boundary sliding, or segregation at the film-substrate interface inhibiting interfacial diffusion of aluminium atoms.

5.2.4 Surface and Interface Electromigration

In metallization tracks having widths of several microns, electromigration failure is associated primarily with grain boundaries in the metal, which act as fast diffusion paths. (See Section 7.2). The "free" aluminium surface and the metal - SiO_2 interface

might also be expected to provide fast diffusion paths or to act as sources or sinks for vacancies. However, the role of these interfaces in electromigration damage mechanisms has been a matter of much controversy.

In the grain boundary grooving model for electromigration failure (Rosenberg and Ohring 1971), surface diffusion plays an essential part in the damage mechanism. Electromigration in silver films, tested under vacuum, was found to cause roughening of the metal surface (Berenbaum and Rosenberg 1969), and this phenomenon was attributed to surface diffusion. The same workers failed to detect a similar effect in aluminium and concluded that the native oxide of aluminium inhibited surface diffusion or reduced the efficiency of the metal surface as a vacancy source or sink.

Conflicting reports exist as to the effectiveness of SiO_2 passivation layers in suppressing electromigration damage. For example, Black (1969) observed higher activation energies and longer failure times in glass-passivated aluminium metallizations while Attardo and Rosenberg (1970) failed to detect any improvement. As passivation layers are applied on top of the existing native aluminium oxide, which is stable against chemical reaction with SiO_2, a direct effect on diffusion at the aluminium surface would not be expected. The effects of passivation are more likely to be due to the suppression of hillock growth (by the presence of a mechanical constraint) or to grain growth during the passivation process. The role of the Al - SiO_2 interface in electromigration failure is even less well understood and is usually neglected in failure models.

However, surface and interface effects may be dominant in metallizations having track widths of the order of 1 μm. There is evidence that the grain structure in these narrow tracks takes on a "bamboo" appearance, with a tendency for the grain boundaries to lie perpendicular to the length of the track. The electromigration failure mechanisms associated with grain boundary diffusion are therefore greatly impaired, and exceptionally long failure times have been recorded (Kinsbron 1980 and Vaidya et al 1980). If the

"free" aluminium surface is indeed inoperative as a fast diffusion path due to the presence of the native oxide, the Al - SiO_2 interface may prove to be the preferred channel for migrating aluminium atoms.

The presence of aluminium oxide at this interface may tend to inhibit interfacial electromigration, but whereas the native oxide on the "free" surface is amorphous and fairly homogeneous, the interfacial alumina is polycrystalline (with a small grain size), and the η-phase detected in the present experiments has a defective crystal structure. It is therefore postulated that the Al - SiO_2 interface may provide a fast diffusion path for migrating aluminium atoms, and also act as a source of vacancies. Inhomogeneities in the structure or chemical composition of the interface may then give rise to the accumulation or depletion of aluminium and hence act as damage sites. Parameters such as deposition temperature, annealing (e.g. "sintering") treatment and device operating temperature, which affect the structure of the interface, would also influence the electromigration behaviour. Experiments to determine the effects of electromigration in narrow metallizations having a "bamboo" grain configuration should be performed. By varying the deposition temperature, deposition rate, substrate surface preparation (e.g. ion bombardment) and annealing treatment, it should be possible to change the interface structure in a controlled manner, while keeping a constant grain configuration. The influence of the interface on electromigration damage could hence be monitored.

5.2.5 Penetration of Thin SiO_2 Insulators by Aluminium

The experiments of Chou and Eldridge (1970), described in section 2.2, demonstrated that Al - Si O_2 reaction led to penetration of a 100 nm SiO_2 layer after annealing at 773 K for 1 hour. This process can cause failure either by shorting through the SiO_2 insulator or by thinning of the aluminium metallization. The problem is most serious in MOS devices having thin gate oxides and in multilevel structures. Penetration usually occurs as a result of excessive "sintering". Silicon gates form a sufficient barrier

to Al - SiO_2 reaction but cannot always be used. The present results indicate that penetration of the SiO_2 by aluminium is unlikely to occur during device operation under normal conditions.

5.2.6 The Electronic Properties of the Al - SiO_2 Interface

The effects of annealing on the electronic properties of MOS structures were discussed in section 2.2. The present results suggest that the deposition conditions and substrate surface treatment may also be important in controlling the electronic properties. C-V and TSIC measurements of MOS structures with metallizations deposited under various conditions should help to further the understanding of the role of the Al - SiO_2 interface in MOS devices.

CHAPTER 6

A REVIEW OF THE STRUCTURE AND PROPERTIES OF ALUMINIUM THIN FILMS

6.1 Introduction

The suitability of aluminium as a contact metallization is largely dependent upon the microstructure of aluminium thin films, which in turn depends upon the deposition conditions. The various deposition processes commonly used include magnetron sputtering and evaporation from a variety of sources (e.g. electron-beam, tungsten filament, inductively heated). In each of these processes, the important parameters are substrate type, deposition temperature, deposition rate, film thickness, residual gas pressure and purity of the source material. Post-deposition heat treatment may also affect the film properties.

Aluminium thin films on amorphous SiO_2 have been studied extensively, but because of the large number of variables in the deposition process, a thorough characterization of film properties in terms of deposition conditions has not been achieved. Some general trends, however, have been observed.

In this chapter the principles of thin film nucleation and growth are briefly discussed and previous experimental work on the structure and properties of aluminium thin films is reviewed. The effects of film properties on the performance of aluminium contact metallizations are also discussed.

6.2 The Mechanism of Film Formation

In this section, an outline of the general characteristics of film growth from the vapour phase is presented. The various theoretical models for nucleation and growth are not discussed in any detail, however, and the reader is referred to the original papers and the review by Venables and Price (1975).

Three different growth modes have been identified, depending on the condensate-substrate combination. In cases where the adsorbed atoms (adatoms) are much more strongly bound to each other than to the substrate, the film tends to form islands. This growth mode, called the Volmer-Weber mode, is typical of metals deposited on insulators. In the opposite case, when the deposit is strongly bound to the substrate, the film grows in a layer by layer manner known as the Frank - van der Merwe mode. In the intermediate case, called the Stranski-Krastanov mode, island growth follows layer growth.

The process of film formation by the Volmer-Weber growth mode may be divided into certain stages as follows :

1) Condensation and nucleation, during which small clusters (nuclei) of adatoms form on the substrate surface.

2) Growth of the nuclei to form larger islands.

3) Coalescence of the islands to produce a connected network of deposit, and finally a continuous film.

4) Annealing effects (e.g. grain growth) after deposition has ceased.

These stages are briefly discussed in the following.

6.2.1 Condensation and Nucleation

When an atom from the vapour becomes adsorbed on the substrate surface, it remains there for a finite stay time before it is desorbed. During the stay time the adatom may diffuse over the surface and chemical bonding with the substrate may occur. Such chemisorbed atoms have a higher activation energy for desorption and rarely re-evaporate. Alternatively, two or more adatoms may collide on the surface to form a cluster or nucleus. The desorption energy is thus increased above that of a single adatom by an amount equal to the dissociation energy of the cluster. The probability of desorption of a cluster is therefore less than that of a single adatom.

A cluster grows by capturing adatoms diffusing over the surface and by direct impingement from the vapour. Clusters may also participate in surface diffusion.

Various theoretical models of nucleation have been developed. The capillarity model (Hirth et al 1964) treats the nuclei as droplets and applies macroscopic thermodynamic principles to describe their growth. The atomistic theory (Rhodin and Walton 1963) takes into account the bonding between individual adatoms and the substrate and is applicable when a nucleus contains a small number ($\lesssim 10$) atoms. Both theories predict the existence of an activation barrier to the formation of a stable nucleus.

As a nucleus grows, it reaches a size where its total free energy (consisting of bulk and surface contributions) is a maximum. Such a nucleus is termed a critical nucleus. Any larger nucleus is stable and can undergo unlimited growth, whereas any smaller (sub-critical) nucleus has a high probability of disintegration.

The ratio of the number of atoms remaining on a surface to the number of atoms incident is called the sticking or condensation coefficient. The sticking coefficient for any vapour-substrate system tends to diminish as the substrate temperature is increased, due to the greater desorption probability at higher temperature. The presence of adsorbed foreign atoms may affect condensation, either increasing or reducing the sticking coefficient, depending upon the particular vapour-substrate combination. In many cases the sticking coefficient varies as the substrate becomes covered by the deposit. It may either increase or decrease with coverage, depending on whether the bonds between individual atoms are stronger or weaker than the bonds between adatoms and the substrate.

The ratio of the fluxes of impinging and desorbing atoms is called the supersaturation. It increases as the deposition rate is increased and decreases as the substrate temperature is raised. The supersaturation has a strong influence on the rate of formation of critical nuclei. Below some critical value of supersaturation, the

nucleation rate is virtually zero since isolated adatoms desorb before critical nuclei have time to form.

At high values of supersaturation the atomistic theory predicts that a very small cluster of adatoms (maybe even one atom) will constitute a critical nucleus. The tendency to form islands is thus reduced and a continuous film forms at a relatively small mean thickness of deposit. At lower values of supersaturation, the critical nucleus is larger and the film retains its island character until a greater thickness has been attained.

Because of the role of surface diffusion in the process of cluster growth, the nucleation rate is strongly dependent upon the activation energy for surface diffusion. For very high activation energies, nucleation may occur solely by direct impingement of vapour atoms and the nucleation rate will be much reduced.

The activation energy for desorption of adatoms also controls the rate of formation and the size of critical nuclei. The higher the activation energy for desorption, the smaller is the critical nucleus and the higher the nucleation rate. Chemical reaction between the deposit and the substrate therefore has a pronounced effect on nucleation.

6.2.2 Island Growth

Island growth occurs mainly by surface diffusion of individual adatoms and sub-critical nuclei and their subsequent capture by the growing islands. The rate of growth of an island is limited by the slower of the two processes involved: i.e. surface diffusion or interface transfer.

In general, islands have different crystallographic orientations and different conditions for growth. Three-dimensional islands often have well developed crystallographic shapes. These are not necessarily equilibrium forms, however, since the supply of atoms to the growing crystallite is not isotropic. Large islands, with a favourable orientation, grow faster than small ones and this process may be responsible for the

development of fibre textures in films on amorphous substrates (see section 6.2.5).

6.2.3 Coalescence

As the size of the islands increases, some come into mutual contact and coalescence occurs. The large interfacial energy of a system composed of isolated islands is thus reduced. Islands are sometimes seen to behave like liquid droplets during coalescence, though they have well defined crystallographic shapes before and after. It is thought that the energy released during coalescence may be sufficient to cause melting of the deposit and that the resulting larger islands recrystallize from the liquid state. When two islands of different size and orientation coalesce, the resulting island tends to assume the orientation of the larger of the two. The preferred orientation of the film may be modified by this process.

When the island density reaches a certain critical stage, coalescence of the large islands occurs, resulting in a connected network of deposit. This process is initially very rapid but becomes progressively slower as the network is formed. The network initially contains a large number of empty channels in which secondary nucleation occurs. Adatoms in these channels either contribute to the growth of new islands or become incorporated in the existing network structure. The filling of channels is often a slow process, requiring a relatively large amount of deposit.

The coalescence of large islands is thought to be responsible for the presence of dislocations in thin films. When small islands coalesce they can move or rotate to eliminate any difference in orientation. This is no longer possible in the case of large islands and dislocations will arise in the region of contact. Individual nuclei are believed to be relatively defect free.

6.2.4 Final Film Structure and Annealing Effects

In general, vapour deposited thin films have a polycrystalline structure, the grain boundaries arising at the regions of contact between islands of different orientation.

A distribution of grain sizes will be present in any one film, but the mean grain size is expected to increase with increasing substrate temperature, deposition rate and inertness and smoothness of the substrate. Contamination by residual gases during deposition may also affect the grain size. The general trends in grain size for pure metal films are shown in figure 6.1 (Chopra 1969). Note that the effective substrate temperature is a relative value with respect to the melting point of the deposit. The reduction in grain size at very high deposition rates is due to the strong mutual interaction among the condensing vapour atoms, which become adsorbed with little surface diffusion.

The crystallite size may be increased by annealing at temperatures above the deposition temperature. However, the grain size after annealing at a given temperature is different from that obtained by deposition at that temperature. This is because the grain growth due to annealing occurs by a relatively high activation energy process of thermal diffusion, whereas island growth during deposition occurs by the condensation of mobile adatoms. The driving force for grain growth by annealing is the minimization of interfacial (grain boundary) energy.

Annealing also leads to the development of thermally-induced stress in the film. Yielding of the film to relieve the stress may give rise to gross reconstruction of the film. This phenomenon is discussed in detail in section 6.3.4.

6.2.5 Preferred Orientations in Films on Amorphous Substrates

The crystallites or grains of a thin film may have randomly distributed crystallographic orientations (figure 6.2a) or some preferred orientation. Figure 6.2b shows the orientation of grains in a film possessing a fibre texture or one-degree orientation. In this type of orientation only one crystallographic axis of the crystallites points preferentially in a given direction (called the fibre axis). If two axes point in preferred directions, the film is said to have a two-degree orientation, as shown in

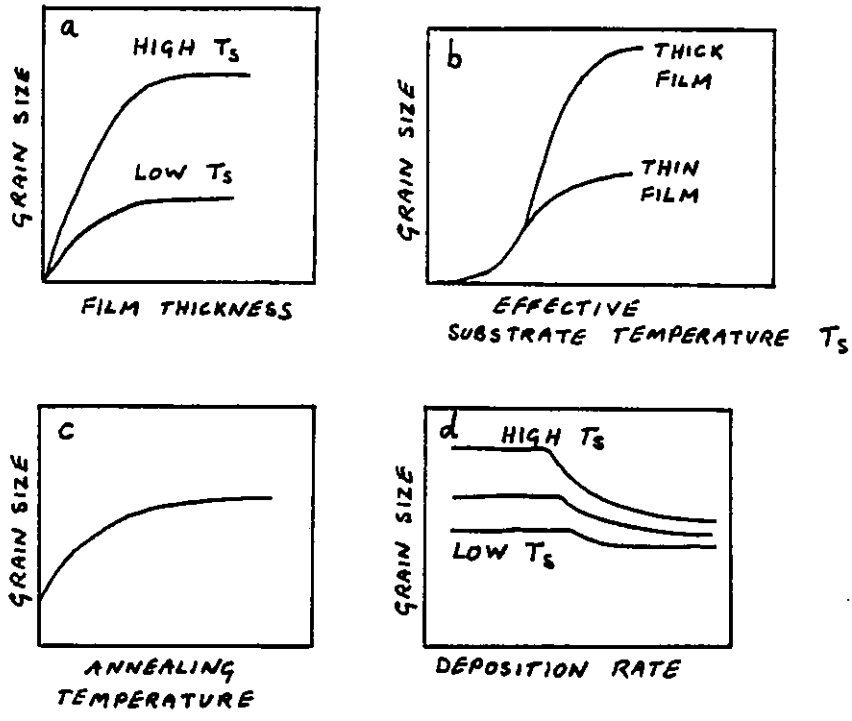

Dependence of grain size on (a) film thickness; (b) substrate temperature; (c) annealing temperature and (d) deposition rate (from Chopra 1969)

FIGURE 6.1

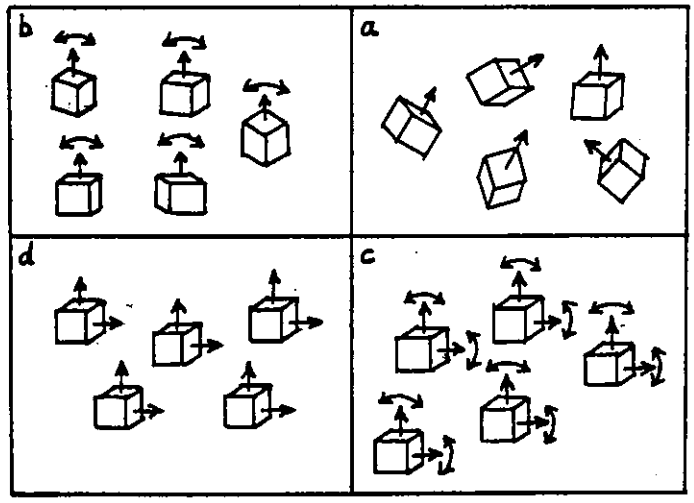

Preferred orientations: (a) random; (b) one-degree orientation (fibre texture); (c) two-degree orientation; (d) single-crystal orientation.

FIGURE 6.2

figure 6.2c. The limiting case of the two-degree orientation for small deviations is the single crystal orientation (figure 6.2d).

Preferred orientations can occur in the initial or final stages of film deposition and may originate from nucleation or growth processes. The equilibrium form of a crystal is given by Wulff's law :

$$\frac{\gamma_1}{h_1} = \frac{\gamma_2}{h_2} = \ldots \frac{\gamma_i}{h_i} \qquad (6.1)$$

where γ_i is the specific free surface energy of the crystal plane denoted by i, and h_i is the distance of this plane from the centre of the crystal (see figure 6.3). Wulff's law may not be strictly valid under the conditions prevalent during vacuum evaporation, as mentioned in section 6.2.2. Nevertheless, this does not usually lead to the appearance of new planes on the surface of small crystallites. The planes predicted by Walff's law still tend to occur on the surface, but with different areas to those of the equilibrium form. For most face centred cubic (f.c.c.) metals, such as aluminium, the equilibrium form varies from the truncated octahedron to the tetradecahedron (see figure 6.4).

Initial orientations of deposits on amorphous substrates may be due to the preferred formation of nuclei with certain orientations (nucleation orientations) or the preferred growth of some crystallites (growth orientations). For the occurrence of nucleation orientations, the following conditions must apply :

1) The interaction between the substrate and the adatoms must be weak compared to the interaction between the adatoms in a nucleus.

2) The supersaturation must be low enough to prevent any small cluster from becoming a critical nucleus, but not so low that nucleation occurs only at imperfections in the substrate surface.

3) The partial pressures of reactive gases must be low enough so that the formation

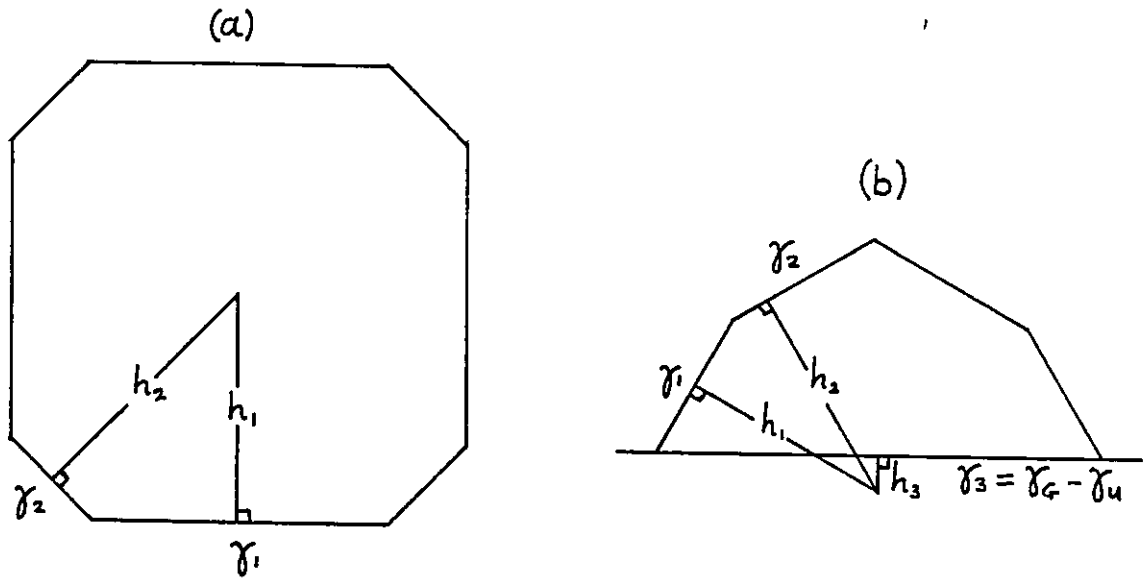

Wulff's law for the equilibrium form of crystals: (a) all surfaces are free; (b) crystal with interface (free energy γ_s) on a surface (free energy γ_u).

FIGURE 6.3

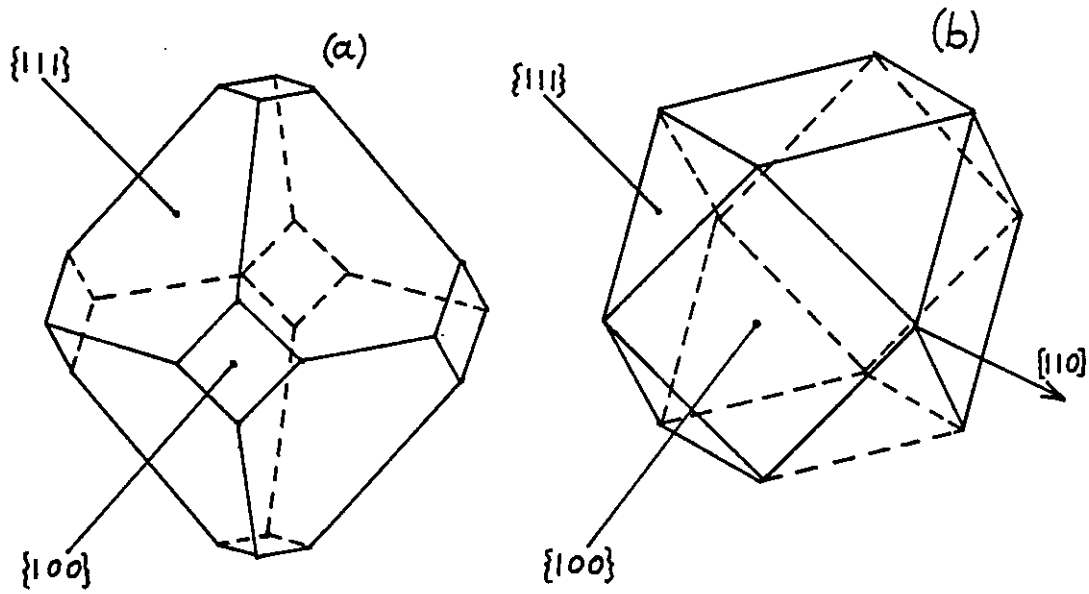

The equilibrium forms of f.c.c. metals: (a) the truncated octahedron; (b) the tetradecahedron.

FIGURE 6.4

of reaction products does not affect the form of the nucleus.

4) The nuclei must be sufficiently large for their surfaces to be described in terms of crystallographic planes. The ⟨111⟩ fibre textures of some f.c.c. metals (e.g. gold and silver on glass substrates, Dobson 1968) may be nucleation orientations.

Final growth orientations in relatively thick films are the result of growth competition between crystallites of different orientations. The number of atoms condensing on any crystallite per unit time is determined by the habit of the crystallite and its orientation with respect to the incident vapour beam. The angular dependence of the condensation coefficient and the self-shadowing effect of three-dimensional crystallites are thought to be important in the development of final growth orientations. For oblique vapour incidence, a two-degree final orientation is often observed (Bauer 1963). For normal vapour incidence Bauer states that most f.c.c. metals have a ⟨110⟩ final orientation.

6.3 The Properties of Aluminium Thin Films

6.3.1 The General Growth Characteristics of Aluminium on Amorphous SiO_2

One of the first detailed investigations of the growth of aluminium thin films on SiO_2 was conducted by d'Heurle et al (1968). The substrates were p-type silicon wafers oxidized to a thickness of 600 nm by heating in wet oxygen. The evaporation system consisted of a glass chamber evacuated by a liquid nitrogen-trapped oil diffusion pump and titanium getters to a base pressure of around 10^{-7} mbar. 99.999% purity aluminium was evaporated by r.f. heating from crucibles of boron nitride or a $BN-TiB_2$ composite, or by electron beam heating from a water-cooled copper hearth. The deposition rate was 1 nm s^{-1} in most cases. Films were examined by the transmission electron microscope replica technique and by x-ray diffraction.

Films of mean thickness in the range 5 nm to 10 nm deposited from $BN-TiB_2$

crucibles onto substrates at 473 K consisted of individual islands. As the thickness of the deposit increased, the structure changed to an irregular network and finally to a continuous film at a thickness of 40 nm. These films had a smooth surface and shadowed replicas showed the surface grain size to be approximately 200 nm. Films of 160 nm thickness and above had rougher surfaces. The grain size was approximately equal to the thickness for 500 nm films and continued to increase with thickness, but with a tendency to remain less than the film thickness. For films between 500 nm and 1.5 μm thick, the grain size was not significantly affected by substrate temperature in the range 473 K to 673 K or by residual gas pressure in the range 10^{-7} mbar to 7×10^{-6} mbar. These films had a "milky" appearance resulting from their rough surfaces. Lowering the substrate temperature to 373 K caused a 3-fold reduction in grain size and an increase in reflectivity of the film surface. All films were found to have a random grain orientation when examined by x-ray diffraction.

The above observations are in qualitative agreement with the expected growth behaviour discussed in section 6.2. The formation of a continuous film at a relatively low value of mean thickness (40 nm) is probably a consequence of the Al - SiO_2 interfacial reaction which increases the binding energy of aluminium atoms and lowers the nucleation barrier. The tendency to form large islands is thus decreased. The Al - SiO_2 reaction may also be responsible for the absence of any nucleation orientation. The lack of any preferred orientation in aluminium films of thickness between 5 nm and 1.5 μm, however, is in conflict with other published results discussed later. Also the independence of grain size on temperature between 473 K and 673 K is not expected on theoretical grounds, nor is it supported by other experimental observations.

Replicas of thick films deposited at 473 K revealed the presence of "steps" or "wrinkles" on the surface of the aluminium. These features were parallel within the

confines of a single grain and were thought by the authors to be low index growth planes. "Growth hillocks", in the form of mounds ~50% higher than the mean film thickness and of the same diameter as the grains, were also observed. Some hillocks appeared to be 4-fold or 6-fold truncated pyraminds, indicating ⟨100⟩ and ⟨111⟩ orientations, respectively. Hillocks were more pronounced in thicker films, but their appearance was independent of deposition rate (in the range 0.2 nm s^{-1} to 10 nm s^{-1}), temperature (from 373 K to 623 K) and residual gas pressure (from 4×10^{-7} mbar to 4×10^{-5} mbar). Films deposited from BN crucibles or from the e-beam source were more reflective and did not possess surface steps or hillocks. In addition, these films had a weak ⟨111⟩ fibre texture, with the fibre axis normal to the film plane. The subject of surface topography is discussed in detail in section 6.3.4.

The aluminium in the BN-TiB_2 crucible was found to contain 300 ppm boron after 10 evaporation cycles, but no titanium contamination was detected. The level of boron contamination in the films was also around 300 ppm and the titanium content was estimated at less than 100 ppm. It is possible that such contaminants affect the structure of the films, although their concentration is quite small.

The grain size of aluminium films as a function of deposition temperature was determined by Saito and Hirota (1974). Aluminium was deposited at a rate of 3 nm s^{-1} from a tungsten filament source onto thermally oxidized silicon, under a vacuum of 2×10^{-5} mbar. The mean grain size of 1 μm thick films ranged from less than 1 μm at 373 K to 6 μm at 773 K (see figure 6.5). Films of 0.8 μ grain size, deposited at 353 K, were found to have a random grain orientation. Films deposited at 573 K and above, however, had a ⟨111⟩ fibre texture.

Dobson (1968) using grazing incidence x-ray diffraction, detected a ⟨111⟩ fibre texture in 200 nm aluminium films deposited on pyrex glass at 300 K. A ⟨100⟩ fibre orientation in 1 μm thick aluminium films deposited onto borosilicate glass at

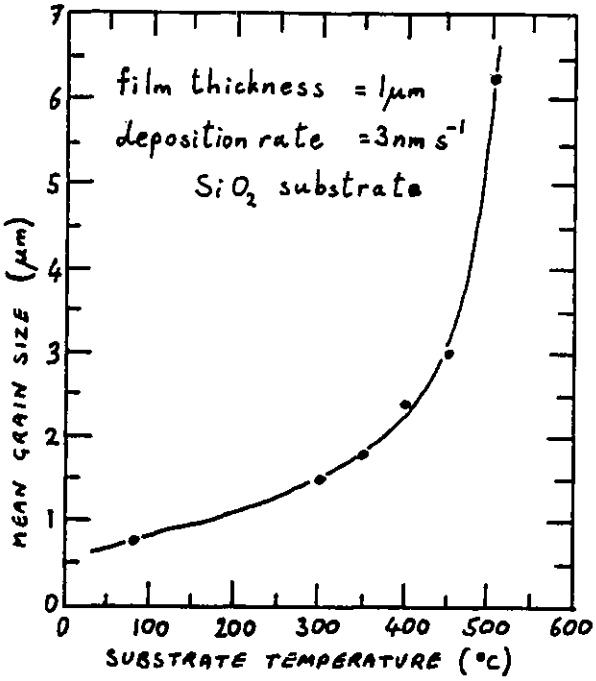

Grain size versus deposition temperature (from Saito and Hirota 1974).

FIGURE 6.5

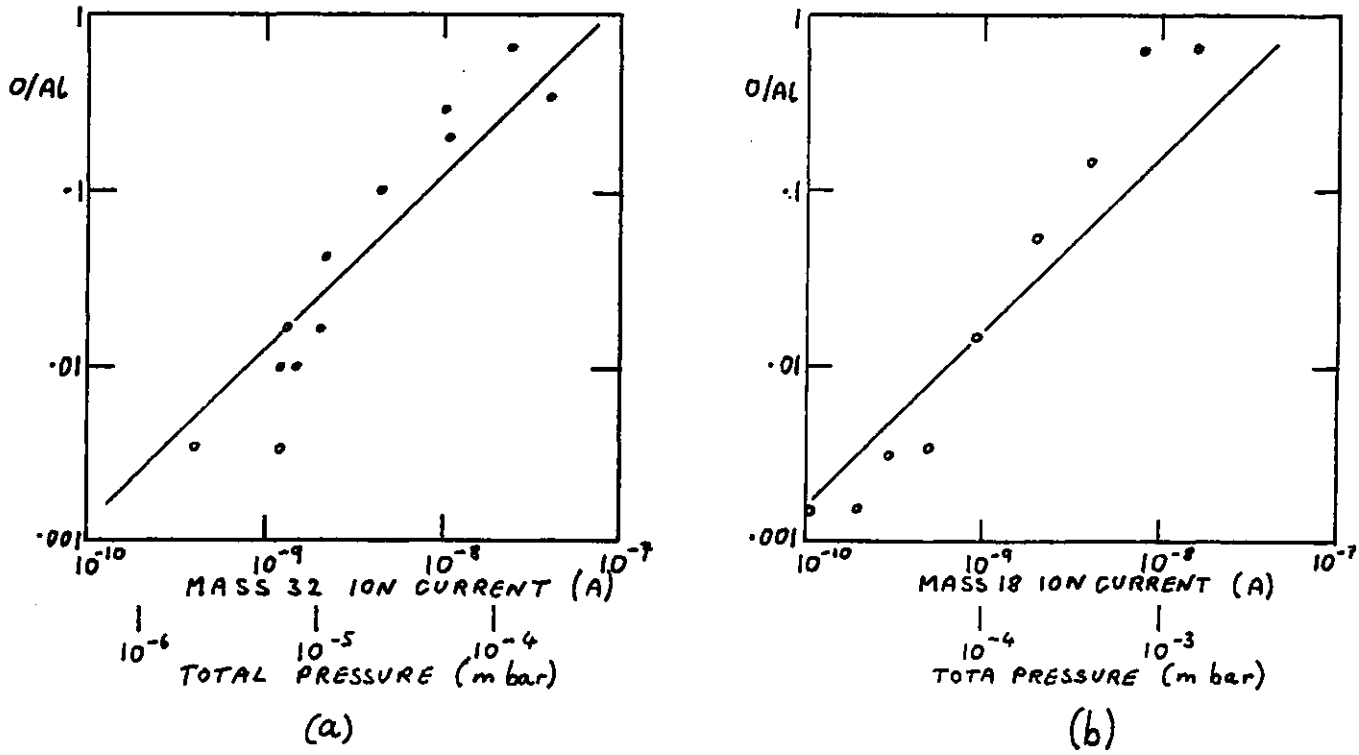

Oxygen to aluminium ratio versus: (a) oxygen pressure; (b) water-vapour pressure during film deposition (from Springer and Catlett 1978).

FIGURE 6.6

423 K was observed by Dhere et al (1975). This result, however, is not supported by other experiments.

6.3.2 The Effects of Residual Gases on the Properties of Aluminium Films on Amorphous SiO_2

A comprehensive study of the effects of the evaporation ambient on the contamination levels in aluminium thin films was carried out by Springer and Catlett (1978). 1 μm aluminium films were electron-beam evaporated onto glass slides at room temperature in a stainless steel chamber evacuated by a turbomolecular pump and liquid nitrogen trap. The base pressure was 3×10^{-8} mbar, but the pressure during deposition was purposely increased by admitting controlled amounts of various pure gases or by throttling the high vacuum valve. The residual gas partial pressures were measured by a quadrupole mass spectrometer and the total pressure by an ion gauge. The chemical composition of the films was determined by a scanning Auger microprobe and depth profiling was performed using a beam of 5 keV argon ions. Carbon contamination from the analysis chamber meant that the limit for carbon detection was 500 to 1000 ppm. The minimum detectable concentrations of oxygen and nitrogen were 100 ppm.

When the pressure in the evaporation plant was controlled by throttling the high vacuum valve, the partial pressures of H_2, N_2 (or CO), CO_2 and water vapour were seen to track the total pressure. Many smaller mass peaks between 50 and 100 amu (thought to be due to heavy hydrocarbons) showed a reduced variation, however. The level of carbon contamination in the films was found to follow these peaks more closely than it followed the total pressure. It was therefore concluded that carbon contamination was due mainly to the heavier hydrocarbons. Supporting evidence came from the negligible difference between the carbon contamination levels in aluminium films deposited in the presence of 10^{-4} mbar of methane, carbon monoxide and carbon dioxide.

The sticking coefficient of these gases was estimated to be less than 5×10^{-5}.

The oxygen content of aluminium films, however, was found to be strongly dependent on the oxygen partial pressure, as shown in figure 6.6a. The visual appearance of the films was found to vary with oxygen content, changing from "milky" for low levels of oxygen to "dark and shiny" for high oxygen content. The sticking coefficient of oxygen on aluminium was measured by Kreuger and Pollock (1972a) and found to be approximately 1 up to a coverage of 100%, at which point it falls rapidly to around 0.03. This value is in agreement with the results of Springer and Catlett.

Oxygen content was also found to be strongly dependent upon the water vapour partial pressure (see figure 6.6b) and the films suffered similar changes in appearance when water vapour was present during deposition. The mass spectrometer showed the ambient to be mainly hydrogen during aluminium evaporation when water vapour was admitted, indicating that dissociation of the water molecules occurred, probably at the surface of the growing film. The sticking coefficient of water vapour on aluminium at room temperature was found by Kreuger and Pollock (1972b) to be 0.05.

Variation of the nitrogen partial pressure in the range 4×10^{-5} mbar to 6×10^{-4} mbar had little effect on the appearance of the films or their nitrogen content, which was approximately 5×10^{-4} in all cases. This finding is consistent with the low value of the sticking coefficient of nitrogen on aluminium (10^{-3} falling to 5×10^{-5} with increasing coverage) measured by Mayer and Fromm (1977).

D'Heurle et al (1968) reported similar changes in appearance of aluminium films deposited in the presence of high oxygen partial pressures. Darkening first occurred at 1×10^{-6} mbar of oxygen for a substrate temperature of 473 K. The effect was attributed to enhanced grain boundary grooving which resulted in light trapping in the film surface. At oxygen pressures of 4×10^{-5} mbar and above, the grain size

of the aluminium was reduced by a factor of three compared to films deposited under conditions of high vacuum. X-ray diffraction did not reveal the presence of any crystalline alumina. It was therefore concluded that the oxide formed was either amorphous or in the form of highly dispersed crystalline particles. Contrary to the observations of Springer and Catlett, d'Heurle et al found that water vapour present during deposition had little effect on the film properties.

6.3.3 The Resistivity of Aluminium Thin Films

The electrical resistivity of a bulk material is due to scattering of the conduction electrons by phonons and by geometrical (structural) defects and impurities in the crystal lattice. According to the Matthiesen rule, the total resistivity ρ_B is given by :

$$\rho_B = \rho_{ph} + \rho_g \qquad (6.2)$$

where ρ_{ph} and ρ_g are the phonon and geometrical contributions respectively. ("Geometrical" defects include vacancies, interstitials, dislocations and grain boundaries, as well as impurity atoms).

In the case of a thin film of thickness comparable to the electron mean free path due to electron-phonon interactions, scattering of the conduction electrons by both surfaces of the film may also make a significant contribution to the resistivity. The total resistivity is therefore given by :

$$\rho = \rho_{ph} + \rho_g + \rho_s \qquad (6.3)$$

where ρ_s is the component corresponding to surface scattering.

The theory of surface scattering was developed by Fuchs (1938) and extended by Sondheimer (1950 and 1952). The mean free path of conduction electrons in aluminium was determined by Grigorovici et al (1962) to be 16.9 nm at 273 K. These workers evaporated aluminium in a vacuum of 1×10^{-6} mbar and annealed the resulting

films to bring about recrystallization and minimize their resistivity. From their results, shown in figure 6.7, it is apparent that surface scattering makes a negligible contribution to the resistivity of aluminium films of thickness greater than 400 nm.

D'Heurle et al (1968) used a four-point probe technique to measure the resistivity of 500nm thick aluminium films on SiO_2 as a function of oxygen partial pressure during deposition. Their results (see figure 6.8) show an increase in resistivity with oxygen pressure, corresponding to a decrease in the purity of the aluminium film. The value of $3 \times 10^{-8} \Omega$ m obtained for films deposited at 1×10^{-7} mbar oxygen partial pressure is approximately 13% higher than the resistivity of pure bulk aluminium ($2.65 \times 10^{-8} \Omega$ m). This is probably due to contamination from the evaporation source.

An indication of the purity of the films was gained by measurement of the resistivity ratio (ρ_{300K}/ρ_{77K}). At liquid nitrogen temperature the phonon scattering contribution ρ_{ph} is negligible, so the magnitude of the geometrical (and surface) contributions to the resistivity can be evaluated. The resistivity ratio is given by :

$$\frac{\rho_{300K}}{\rho_{77K}} \simeq \frac{\rho_{ph} + \rho_g + \rho_s}{\rho_g + \rho_s} \qquad (6.4)$$

The resistivity ratio of the aluminium source material was 12. Films deposited from a $BN-TiB_2$ crucible at a residual gas pressure of 3×10^{-7} mbar had a resistivity ratio of 5.1 for a substrate temperature of 373 K, rising to 7.9 for deposition at 573 K. This dependence on deposition temperature is thought to reflect the decrease in sticking coefficient of residual gases as the temperature is increased. Films deposited from BN crucibles onto substrates at 473 K had resistivity ratios of around 9. This was indicative of their lower level of boron contamination (30 ppm, compared to 300 ppm for films deposited from a $BN-TiB_2$ source). Electron-beam deposited films had low resistivity ratios because of copper contamination from the hearth.

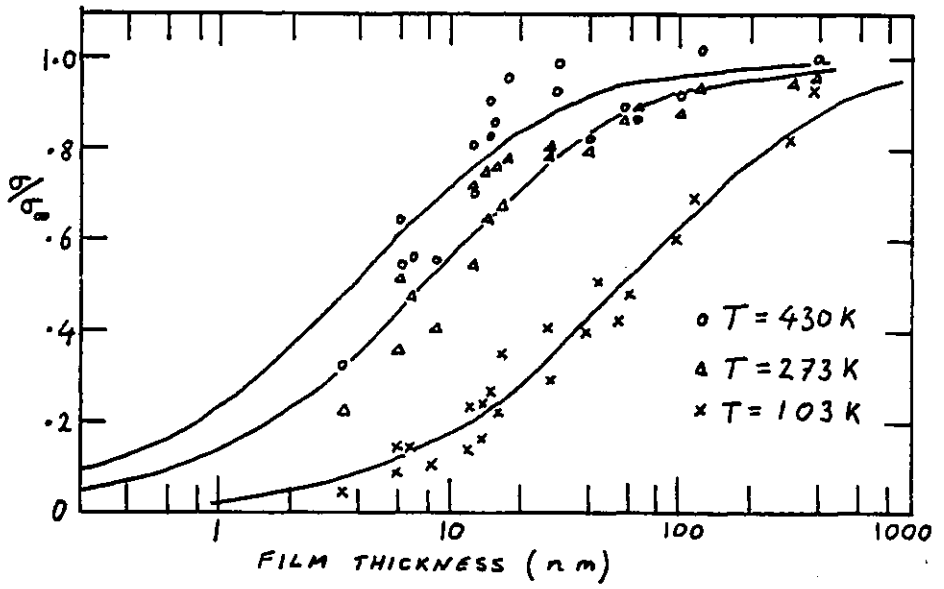

The ratio between the conductivity σ of a thin Al film and the conductivity σ_∞ of bulk aluminium (from Grigorovici et al 1962).

FIGURE 6.7

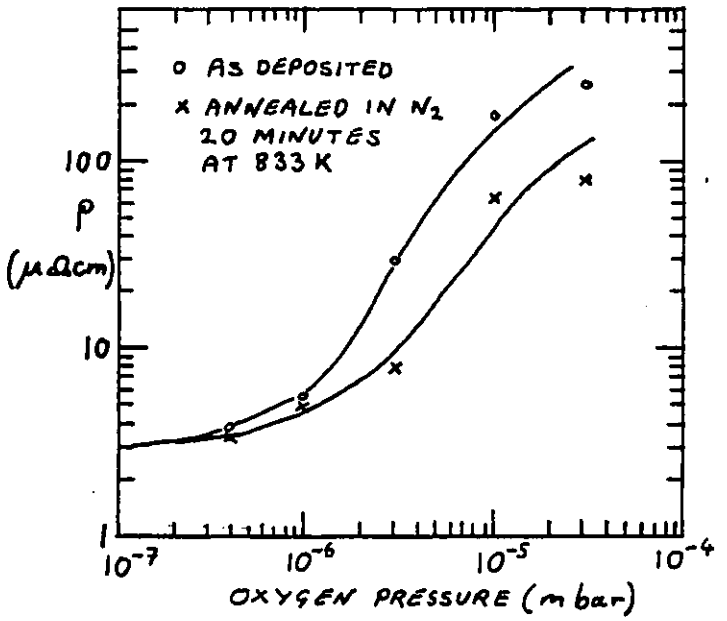

Room-temperature resistivity ρ versus oxygen pressure during evaporation of a 500 nm thick Al film deposited at 2 nm s^{-1} onto a substrate at 473 K (from d'Heurle et al 1968).

FIGURE 6.8

6.3.4 The Surface Topography of Aluminium Thin Films

The growth hillocks and wrinkles seen on the surface of some aluminium films by d'Heurle et al (1968) were described in section 6.3.1. These workers also reported the development of "annealing hillocks" during high temperature treatment of the films, regardless of the deposition conditions. Annealing hillocks tended to be rounded in shape and often extended beyond the confines of a single grain. They were sometimes surrounded by a moat-like depression, suggesting that the hillock grew by the migration of material from the immediate vicinity. A 30 minute anneal at 723 K in nitrogen was sufficient to produce many hillocks in a 1.1 μm thick aluminium film.

The authors suggested that annealing hillocks formed as a result of the relief of thermally induced stress in the film. The stress was determined from the curvature of the wafer measured by interferometry. The room temperature stress in films deposited at 473 K from BN - TiB_2 crucibles was tensile and had a value of 1.3×10^8 N m^{-2}. The lattice parameter, determined by x-ray diffraction, was found to be 0.40454 nm. After correction for stress this gave a value of 0.40506 nm for the relaxed material, in good agreement with the value of 0.404958 nm for pure bulk aluminium (Wyckoff, 1963). Films deposited under similar conditions from a BN crucible were under a tensile stress of 2.0×10^8 N m^{-2}. The lattice parameter was 0.40434 nm, giving a value of 0.40511 nm for the relaxed film.

Annealing at 833 K in nitrogen resulted in an increase in the room temperature stress. For example, a film having an initial stress of 1.3×10^8 N m^{-2} had a stress of 1.8×10^8 N m^{-2} after annealing, and had a reduced lattice parameter. These levels of stress can be accounted for by the difference between the thermal contractions of aluminium and silicon over a temperature range of only 60 K, indicating that considerable relaxation took place during cooling from the deposition temperature of 473 K to room temperature.

Thermally induced stress in aluminium films on oxidized silicon was studied in greater detail by Sinha and Sheng (1978). Their results are in qualitative agreement with those of d'Heurle et al. Aluminium was deposited at 6 nm s^{-1} onto steam-oxidized {100} silicon wafers by electron-beam evaporation from a BN crucible. The background pressure was approximately 10^{-6} mbar and most films were deposited at room temperature. 0.2 μm films were found to be under a tensile stress of 2×10^{7} N m^{-2} in the as-deposited condition. On annealing the stress became compressive, reaching a maximum of $\sim 10^{8}$ N m^{-2} at 373 K, then falling to around zero at 473 K. On cooling from 723 K, the stress again became tensile, attaining a value of 8×10^{8} N m^{-2} at room temperature (see figure 6.9a). Further temperature cycling did not significantly affect the final room temperature stress. Thicker (0.45 μm and 0.89 μm) films behaved in a similar manner but the final room temperature stress became progressively smaller as the thickness increased. However, it was still greater than the as-deposited stress (see figures 6.9b and 6.9c). For 1.56 μm films, the final tensile stress was less than the as-deposited stress (figure 6.9d). 1.62 μm films deposited at 603 K showed similar behaviour. After the first thermal cycle these films could not sustain any significant compressive stress and could only support a tensile stress of 5×10^{7} N m^{-2} at room temperature (figure 6.9e). TEM examination revealed that grain growth (by a factor of $\sim$ 10) had occurred as a result of annealing. Dislocation networks within each grain were also observed and were attributed to deformation during the cooling cycle.

The total biaxial stress σ at the film-substrate interface is the resultant of two components; the intrinsic stress σ_i and the thermal stress σ_{th} :

$$\sigma = \sigma_i + \sigma_{th} \qquad (6.5)$$

The intrinsic component may be due to differences between the film temperature and the substrate temperature during film growth and/or differences between the surface

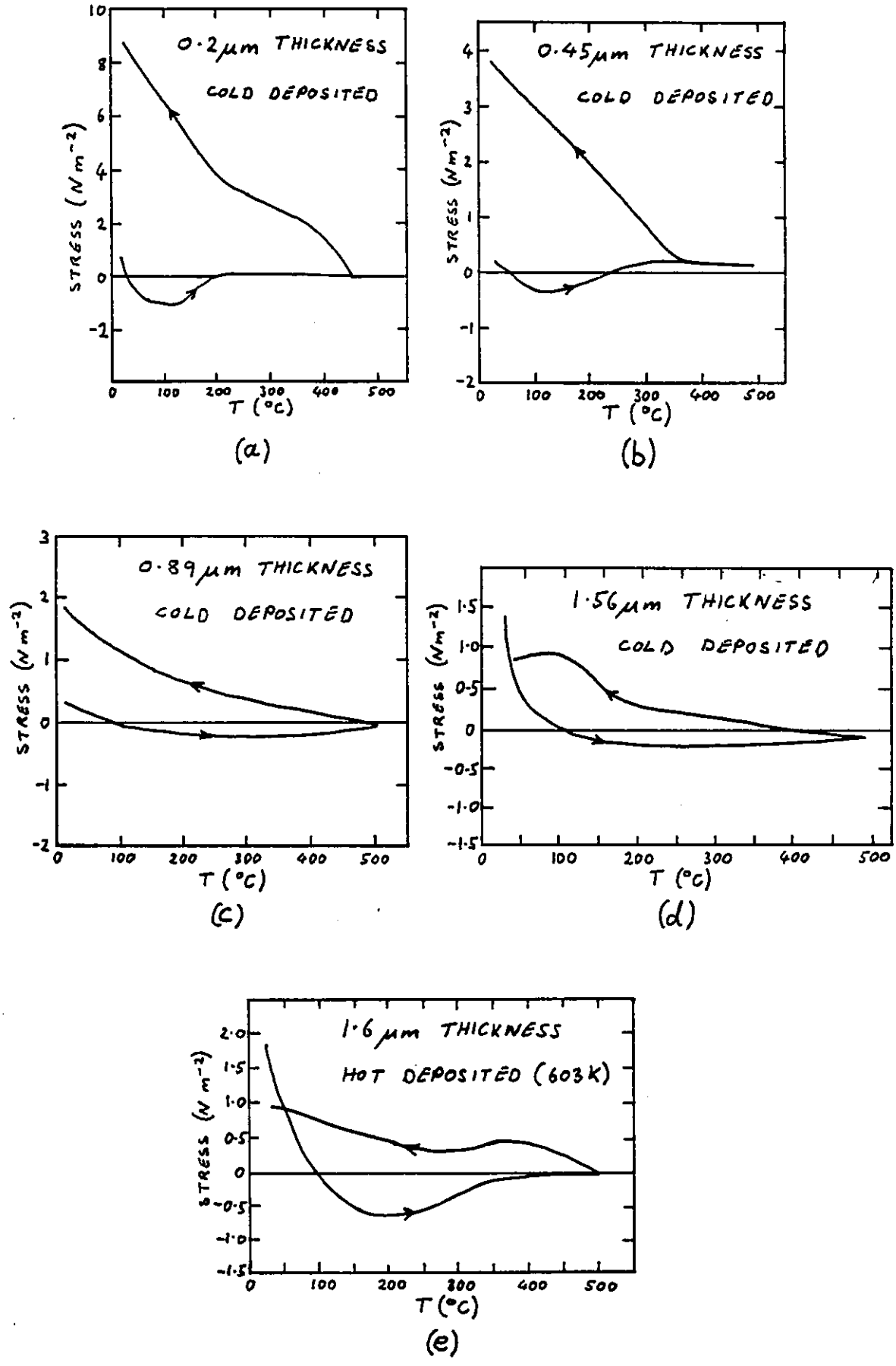

Stress versus temperature for Al films on oxidized silicon (from Sinha and Sheng 1978)

FIGURE 6.9

tensions of the film-substrate and film-air (or vacuum) interfaces. The thermal stress component is a result of thermal expansion mismatch at the film-substrate interface :

$$\sigma_{th} = \frac{E_f}{1-\nu_f} \int_{T_1}^{T_2} (\alpha_s - \alpha_f)\, dT \qquad (6.6)$$

where E_f and ν_f are the Young's modulus and the Poisson's ratio for the film, T_1 and T_2 are the initial and final temperatures and α_s and α_f are the thermal expansion coefficients of the substrate and film. From equations 6.5 and 6.6 :

$$\frac{d\sigma}{dT} = \frac{E_f}{1-\nu_f} (\alpha_s - \alpha_f) \qquad (6.7)$$

Taking values of $E_f = 7.06 \times 10^{10}$ N m^{-2}, $\nu_f = 0.345$, $\alpha_f = 23.5 \times 10^{-6}$K^{-1} and $\alpha_s = 2.5 \times 10^{-6}$K^{-1} gives a result of -2×10^6 N m^{-2} K^{-1} for $d\sigma/dT$. (The negative sign indicates that the stress is compressive). σ_{th} is thought to be much greater than σ_i in aluminium films on oxidized silicon.

After thermal cycling, nearly all of the resultant stress was developed during cooling, since at 750 K the stress was virtually zero. This led Sinha and Sheng to the conclusion that the compressive stress developed during heating was relieved by hillock formation at high temperatures. If no yielding of the aluminium occurred on cooling, the final room temperature tensile stress should be of the order of 10^9 N m^{-2}, irrespective of film thickness. However, the actual room temperature stress was smaller than this and was strongly thickness dependent. Tensile stress must therefore be relieved by plastic flow on cooling. The mechanism may involve dislocation slip, which would account for the thickness dependence of the stress relief. (The critical stress for the generation of dislocation loops is an inverse function of film thickness and/or grain size).

Santoro (1969) investigated the effect of thermal cycling (as opposed to

continuous annealing) on the formation of hillocks. 700 nm aluminium films were deposited onto oxidized silicon substrates at temperatures of 300 K, 473 K and 673 K and had average grain sizes of $<1\ \mu m$, $1\ \mu m$ and $5\ \mu m$ respectively. Thermal cycling, using a 15 minute cycle time, was performed in a nitrogen atmosphere. In addition, control samples were tested continuously for an equivalent time at temperature. Surface reconstruction was observed using optical microscopy, SEM and the TEM-replication technique. The results showing the cycled and uncycled hillock densities are listed in table 6.1 and the dependence of hillock density on deposition temperature is shown in figure 6.10. The data includes hillocks of base diameter greater than $1\ \mu m$ and height of around $1.5\ \mu m$.

It is apparent that thermal cycling promotes a higher hillock density than continuous annealing and that hillocks are more numerous in small-grained films. The grain structure was also found to affect the shape of the hillocks and three classes of hillocks, originating from different grain boundary configurations, were identified (see figure 6.11). The author proposed that grain boundary diffusion was responsible for the mass flow during hillock growth, and also suggested the following explanation for the greater hillock densities produced by thermal cycling.

When a film is annealed continuously, compressive stress is relieved by progressive hillock growth until equilibrium at the annealing temperature is attained. When a film is cycled, however, stress reversal occurs during cooling and some relief of this tensile stress may take place by gross thinning of the film or by separation at the grain boundaries, rather than by shrinkage of the hillocks. On the next heating cycle, new hillocks are formed as the compressive stress is renewed, and growth of the existing hillocks also takes place. The density and average size of hillocks is thus increased.

Santoro's results were confirmed by Herman et al (1972), who also noted the

Deposition Temp. (°C)	Anneal Temp. (°C)	Cycled Hillock Density (m^{-2})	Uncycled Hillock Density (m^{-2})	Cycled / Uncycled Density
R.T.	430	8.7×10^{11}	4.0×10^{11}	2.2
200	430	1.5×10^{10}	5.0×10^{9}	3.0
400	430	3.4×10^{8}	6.0×10^{7}	5.7
R.T.	223	6.2×10^{10}	3.2×10^{10}	1.9
200	179	5.2×10^{9}	2.8×10^{9}	1.8
400	237	0	0	—

Hillock Densities for Aluminium Films Deposited at Various Temperatures (from Santoro 1969).

TABLE 6.1

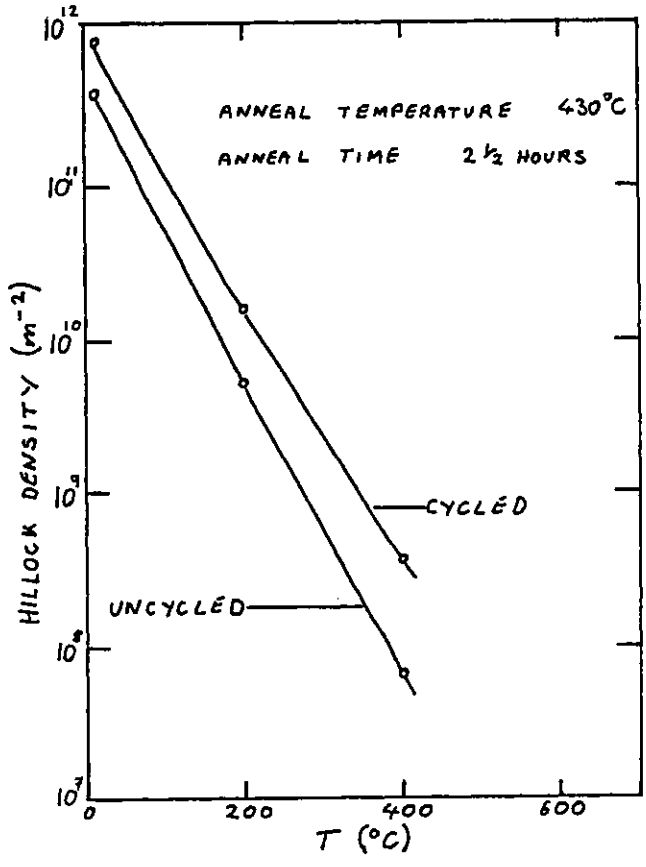

Dependence of hillock density on deposition temperature for films annealed at 430° C (from Santoro 1969).

FIGURE 6.10

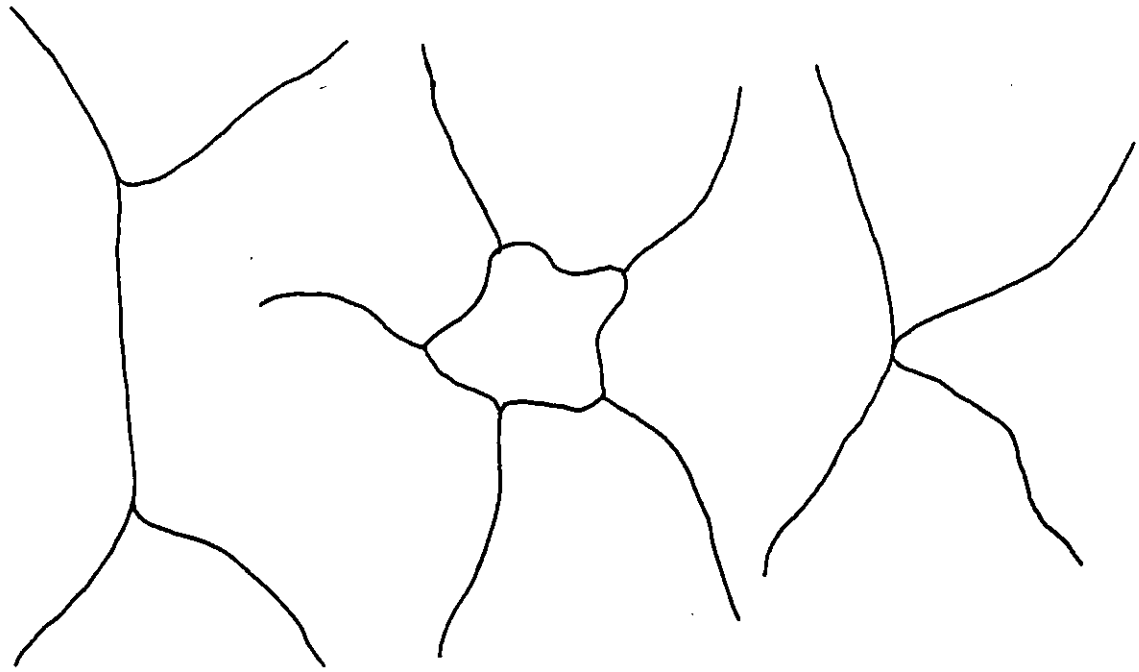

Three grain boundary configurations giving rise to hillock growth (from Santoro 1969).

FIGURE 6.11

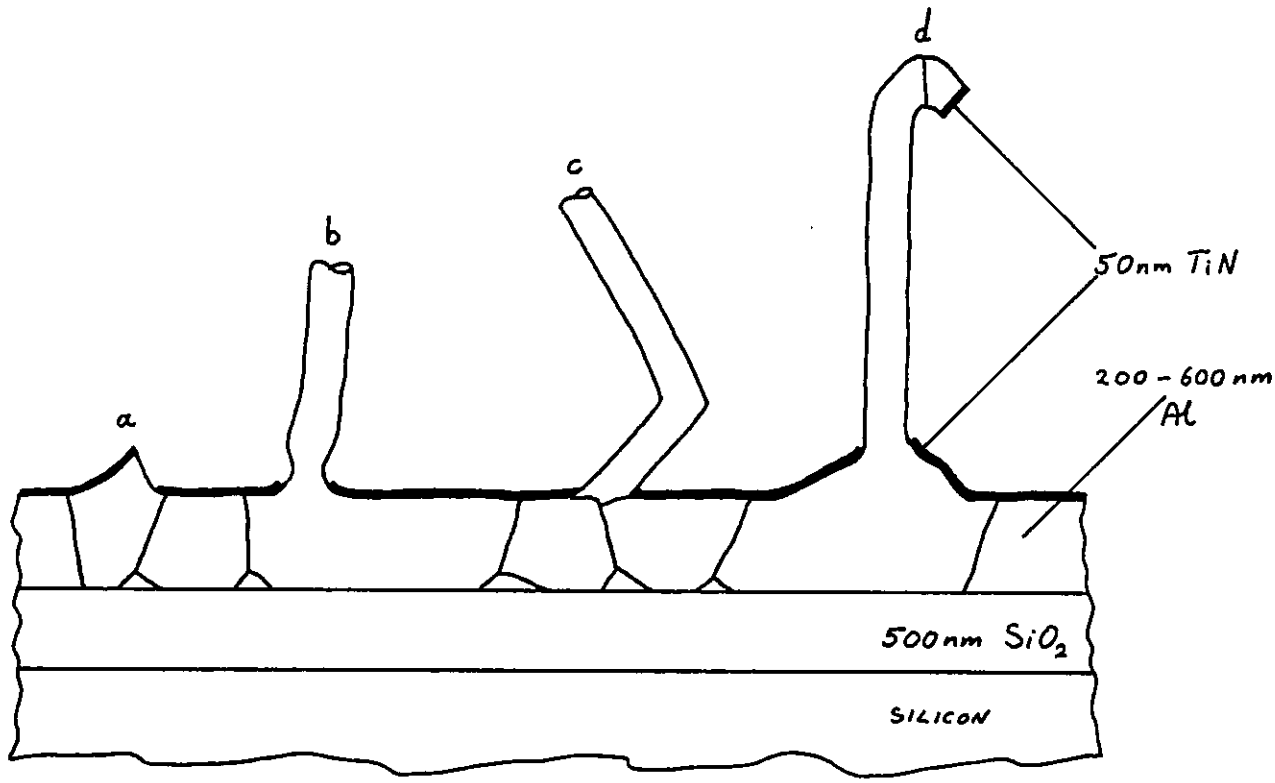

(a) Nucleating whisker emerging through fractured TiN; (b) whisker emerging from single grain; (c) kinked whisker emerging from grain boundary; (d) whisker emerging from a hillock (from Blech et al 1975).

FIGURE 6.12

presence of annealing depressions. In some films the density of depressions was greater than that of hillocks.

Philofsky et al (1971) investigated the effects of thermal cycling in 1 μm aluminium films having various mean grain sizes in the range 0.5 μm to 8 μm. Again, the surface reconstruction was more severe in cycled films than in those continuously annealed. Films of grain size less than 1 μm developed many large hillocks which appeared to emanate from grain boundary triple points or extend over complete grains. Other grains were seen to be sunken with respect to their neighbours and grain boundary voids were also apparent. In larger grained films the size and density of hillocks and voids was reduced and in films of 8 μm grain size the predominant mode of surface reconstruction was wrinkling within individual grains, as reported by d'Heurle et al (1968).

Philofsky et al suggested that diffusional creep was responsible for stress relaxation and hillock growth at high temperatures, with grain boundary triple points acting as preferential nucleation sites for hillock growth. In large grained films, however, where the density of grain boundaries is low, hillock growth is no longer an efficient means of stress relaxation and wrinkling becomes important. The wrinkles are similar in appearance to the ductile striations seen on the surface of fatigued metals (Forsyth 1963). These features are due to the build-up of microscopic slip steps during plastic deformation. Wrinkling is thought to occur in those grains containing shear planes which experience a maximum resolved shear stress greater than the critical resolved shear stress for plastic flow on those planes.

Following careful observations of hillock growth in lead and tin films on glass substrates, Chaudhari (1974) proposed a detailed model for surface reconstruction which may also be applicable in the case of aluminium films on SiO_2. The model is based on the assumption that a thin film on a substrate, when subjected to a compressive biaxial

stress, contains some areas where dislocation slip or twinning leads to localized stress relaxation. A potential gradient therefore exists between the relaxed areas and the surrounding film. Mass then flows towards the relaxed region, which grows out of the film to form a hillock. If the hillock extrudes out of the film by sliding along the grain boundaries, then any grain boundary ledges or jogs initially present will have to be removed before hillock growth can occur. The "incubation period" before hillock growth reported by some experimenters (Presland et al 1972 and Lahiri 1970) is thus explained. Nabarro-Herring (diffusional) creep leads to a simultaneous overall relaxation of the film. The different film thickness dependences of these two competing relaxation processes account for the observed increase in hillock density with film thickness.

The diffusion of atoms towards the growing hillocks may be expected to occur via the grain boundaries, the free surface or the film-substrate interface. Chaudhari performed an experiment in which a 2 μm tin film was evaporated onto a quartz substrate, half of which had previously been coated with 30 nm of nickel. After thermal cycling between liquid nitrogen temperature and room temperature, the hillock density on the tin film was much lower in the area where the nickel layer was present. The effect was attributed to a reduction in the interfacial diffusion of tin atoms. If this is the case, then interfacial diffusion must be the dominant mode of mass flow in hillock growth. It is possible, however, that the nickel precipitated at grain boundaries in the tin film and hence reduced grain boundary diffusion.

Alloying as a means of suppressing hillock formation was investigated by Sato et al (1971). 5 μm thick films of pure aluminium, Al-Sn alloy and Al-Mn alloy were evaporated onto alumina substrates at 623 K. Thermal cycling between room temperature and 473 K was found to produce hillocks in the pure aluminium film but not in either of the alloy films. The grain size of the Al-Sn films was 20 μm, compared to 8 μm for

the pure aluminium films. This was explained on the basis of the large atomic diameter of tin relative to aluminium and the high binding energy of tin atoms with lattice vacancies in aluminium. Tin therefore segregates to the grain boundaries, increasing the grain boundary energy and promoting grain growth and grain boundary grooving. The authors claimed that the low hillock density in these films was due to a reduction in grain boundary diffusion because of the large size of the grains and the presence of tin at the grain boundaries. Al-Mn films had a mean grain size comparable to that of pure aluminium, but TEM examination revealed fine particles on the grain boundaries. These were thought to be due to the precipitation of manganese. These results indicate that grain boundary diffusion plays an active role in the formation of annealing hillocks.

"Passivation" of the surface of aluminium films by layers of SiO_2 ranging from 100 nm to 1 μm in thickness was found to be effective in suppressing hillock growth (Santoro 1969). This may be due to a reduction in the surface diffusion of aluminium atoms or, more likely, to the presence of a mechanical constraint.

Associated with the phenomenon of annealing hillocks is the growth of whiskers. These have been studied in some detail by Blech et al (1975) who used the TEM to examine 200 nm to 600 nm aluminium films on oxidized silicon, after chemical thinning of the substrate. Annealing for 20 hours at 623 K did not cause whisker growth on *bare* aluminium films, but films coated with 50 nm to 100 nm of Ti N suffered rapid whisker growth at this temperature.

Whiskers were seen to nucleate at various types of site, including grain boundary junctions, single grains and hillocks (see figure 6.12). Whiskers were typically 0.5 μm in diameter and up to 0.5 mm long. After an initial nucleation period of several minutes, growth rates were usually of the order of 5 nm s^{-1}, but rates as high as 50 nm s^{-1} were occasionally observed. The density of whiskers on the surface was typically 10^8 m^{-2} after a 2 hour anneal at 623 K.

Whiskers were often seen to grow initially in a curved manner, followed by uniform straight growth. The orientation of several whiskers was investigated by electron diffraction and they were all found to have axes parallel to the ⟨110⟩ direction. The nucleation and growth of whiskers is thought to be related to flaws in the Ti N passivation film and the growth mechanism may be dependent upon grain boundary, surface or interface diffusion. For whiskers growing from within large grains the latter two processes are thought to be necessary.

In contrast to the large volume of published work on annealing phenomena, very little work appears to have been done on growth hillocks on aluminium films. These features have been studied, however, by Reicha and Barna (1980) using high voltage TEM and replica techniques. The occurrence of growth hillocks was monitored as a function of the oxygen partial pressure during aluminium deposition. The relevant parameter was taken to be K_0, the ratio of rate of impingement of oxygen molecules to that of aluminium atoms. (An oxygen partial pressure of 10^{-6} mbar corresponds to an impingement rate of approximately 1 monolayer per second).

1 μm films deposited onto amorphous substrates at room temperature and with K_0 between 10^{-2} and 10^{-3} had a ⟨111⟩ fibre texture and a grain size of 1 μm to 10 μm. The surfaces of these films were relatively flat. Apart from the grain boundary grooves, the only surface features were shallow flat-topped protrusions and depressions within the confines of large single grains. These are thought to be related to growth steps.

Films deposited at higher oxygen partial pressures ($K_0 \sim 10^{-1}$ to 10^{-2}), however, had a random orientation and a grain size of around 1 μm. Some grains exhibited abnormal growth above the surface of the film and appeared identical to the growth hillocks observed by d'Heurle et al (1968). These hillocks were often in the form of truncated octahedra with very smooth surfaces. At even higher oxygen pressures ($K_0 \sim 1$) the average grain size was even further reduced but occasional larger crystallites of well

developed shapes protruded above the surface.

The authors tentatively explained the importance of oxygen in the formation of growth hillocks in terms of the different ways in which oxygen binds to the {100} and {111} faces of aluminium. Oxide growth is thought to start at the corners and edges between {111} faces. This destroys these corners and edges and tends to promote the growth of truncated octahedra which are bounded by {100} and {111} faces and by edges between these faces.

6.4 Aluminium as a Contact Metallization

The ideal contact metallization should have the following properties :

1) Ease of deposition
2) Low electrical resistivity
3) Uniform coverage of surface topography of the device
4) Uniformity and selectivity of etching
5) Resistance to oxidation and corrosion
6) Bond reliability
7) Stability of metal-silicon contacts
8) Resistance to electromigration failure
9) Compatibility with processes for multilevel device structures
10) Good adhesion to SiO_2
11) Low contact resistance to silicon.

Aluminium satisfies many of the above requirements and has the additional virtue of low cost. Aluminium (or an aluminium-based alloy) is therefore the standard metallization system for most silicon devices, other metals (e.g. gold) only being used when high reliability under extreme conditions is called for.

Each of the above requirements is reviewed briefly in the following. The reader is referred to the papers by Philofsky and Hall (1975) and Learn (1976) for a

more detailed discussion.

6.4.1 Deposition Methods

The simplest deposition technique is evaporation from a tungsten or tantalum filament or boat. However, aluminium alloys readily with these refractory metals at high temperatures and restricts the life of the evaporator. Aluminium films deposited by this method also tend to contain substantial amounts of alkali metal contamination and are therefore unsuitable for use in MOS devices. Flash evaporation, performed by continuously feeding an aluminium wire onto a heated bar of a refractory material (e.g. BN - TiB_2) allows relatively thick films to be deposited and high deposition rates to be attained (Learn 1974). The technique can also be used to deposit alloy films by replacing the pure aluminium wire by one of the appropriate alloy.

Electron-beam or r.f. inductive heating are commonly used to evaporate aluminium from refractory crucibles and can give high deposition rates, thereby reducing contamination of the film by residual gases and minimizing process time. Films of high purity can be prepared by electron beam evaporation as it is possible to melt only the central region of the aluminium charge so that molten aluminium never comes into contact with the crucible. These techniques cannot easily be used to deposit alloy films from a single source, because of the different vapour pressures of the constituents. Alloys are most conveniently deposited by magnetron sputtering from an alloy cathode. Sputtering, however, has the disadvantage of low deposition rate.

6.4.2 Electrical Resistivity

As discussed in section 6.3.3, size effects (surface scattering) do not contribute significantly to the resistivity of aluminium film of thickness around 1 μm. The resistivity of the film can therefore approach that of the bulk material and is quite tolerant to deposition conditions unless exceptionally poor vacuum or low deposition rates are employed. Satisfactory resistivity may be attained using a total residual gas

pressure of 10^{-5} mbar and a deposition rate of 10 nm s^{-1}. The addition of alloying elements may increase the resistivity by up to 15%, but even this is tolerable in most instances.

6.4.3 Step Coverage

The coverage of oxide steps and other surface irregularities is of great importance in obtaining reliable contact metallizations. The presence of microcracks in the metallization in the vicinity of a step can result in the trapping of etchants and subsequent corrosion problems. Thin regions of metallization, caused by the shadowing effect of a step, are potential areas for rapid electromigration damage due to the higher local temperature and current density.

The shadowing effect may be overcome to some extent by the use of extended or multiple evaporation sources (Blech 1970) or more commonly by planetary motion of the substrates during deposition. Heating of the substrate to around 600 K, in order to increase the mobility of aluminium atoms during deposition, may also yield better step coverage.

Sputter deposition might be expected to give improved coverage because of the large area of the source and because of the scattering of the impinging aluminium species by the relatively high pressure of sputtering gas in the chamber (e.g. 10^{-3} mbar of argon). It has been demonstrated, however, that sputter deposited films also tend to develop cracks at severe steps and planetary motion of the substrates is still advantageous (Fuller and Ghate 1979).

6.4.4 Etching

In order to produce metallization patterns by photolithography, it must be possible to etch the metal without damaging the SiO_2 or silicon. Aluminium is usually etched using a phosphoric acid-based solution which does not etch silicon or SiO_2. Aluminium can also be plasma etched using CCl_4. Etching tends to take place preferentially at the

grain boundaries, but the uniformity of etching is generally satisfactory, especially in small-grained films.

6.4.5 Oxidation and Corrosion

The oxidation of aluminium in air is a self-limiting process and leads to several nanometres of native oxide at room temperature. In hermetically sealed packages, where there is negligible water vapour present, oxidation and corrosion are virtually non-existent. Plastic packages, however, are permeable to water vapour and corrosion can be a serious problem. Phosphorus (from the passivation layer or the phosphorus diffusion, for example) dissolves in any water which is present to form an electrolyte. A potential difference between two adjacent aluminium conductors can then give rise to rapid electrochemical corrosion (Nagasima et al 1974). Aluminium metallizations are therefore not reliable when used in conjunction with plastic encapsulations in hot and humid conditions.

6.4.6 Bonding

Some problems associated with bonding were described in section 2.1. When Al - SiO_2 adhesion is good, however, ultrasonic wedge bonding using aluminium or aluminium-silicon wire gives excellent results.

6.4.7 Aluminium-Silicon Contact Stability

Silicon is fairly soluble in aluminium at the temperatures experienced during device manufacture (e.g. the solid solubility of Si in Al is 0.8% at 773 K) and degradation of the junctions may result (Totta and Sopher 1969). The mechanism is believed to be dissolution of silicon in the metallization followed by diffusion of the dissolved silicon away from the contact region. This allows more silicon to dissolve and aluminium also enters the silicon in the form of spikes. The result is excessive leakage and ultimately, shorting of the underlying junction. The problem is particularly serious in the case of shallow junctions.

Aluminium-silicon interdiffusion may be prevented by the use of a suitable thin film diffusion barrier, such as titanium (Bower 1973). However, chemical reaction beteeen the barrier material and the aluminium or silicon can be problematic. Alternatively, a "sacrificial" film of silicon may be deposited prior to the aluminium to satisfy the solubility limit of silicon in aluminium. Both of these techniques, however, involve an extra processing step. The most widely used method of preventing Al-Si interdiffusion is the use of an alloy metallization containing 1 to 2% silicon. Such an alloy can be deposited by evaporation from individual aluminium and silicon sources, or more conveniently by sputtering from an alloy target.

6.4.8 Electromigration Failure

Electromigration failure is the subject of chapters 8 and 9 and will not be discussed in detail here. Suffice it to say that electromigration is a serious problem in aluminium metallizations operating at high current densities and temperatures. Reliability is generally improved by the use of large-grained films and certain alloy additions.

6.4.9 Multilevel Metallization

Many complex large scale integrated circuits require more than one level of metallization and aluminium is commonly used for all levels. The intermediate insulator layers may be SiO_2 or phosphosilicate glass (deposited by chemical vapour deposition), polyimide or anodic aluminium oxide.

Extra demands are placed upon the lower levels of metallization as they form the "substrate" for subsequent layers of the device. In particular, the metallization should have a smooth surface (i.e. be free from growth hillocks) to ensure uniform coverage by the adjacent insulator layer. The development of annealing hillocks during device processing or operation should also be suppressed, as cracking of the insulation, leading to inter-level shorting, may result. Hillock formation may be

reduced by using films of large grain size (high deposition temperature) and by the addition of suitable alloying elements (e.g. tin). It is also advantageous to keep the metallization as thin as possible.

6.4.10 Al - SiO_2 Reaction

Al - SiO_2 reaction provides good adhesion between the metallization and the oxide layer and also allows Al - Si electrical contacts to be established by "alloying" or "sintering". The subject is discussed fully in chapter 5.

CHAPTER 7

THE MICROSTRUCTURE OF ALUMINIUM THIN FILMS ON AMORPHOUS SiO_2

7.1 Introduction

The experiments described in this chapter form part of an investigation into the effects of the microstructure of aluminium thin films on their electromigration performance (see Chapter 9). Owing to the strong dependence of microstructural properties on deposition conditions (Chapter 6), it was necessary to individually characterize the films used in the electromigration experiments.

The film properties thought to be of greatest importance in controlling electromigration failure are the grain size distribution, degree of preferred orientation and surface topography. These properties were studied as functions of film deposition rate, substrate temperature and annealing treatment, using a variety of techniques. Most films were deposited by evaporation from tungsten filaments. Some electron-beam and sputter-deposited films were also examined.

Apart from characterization of the relatively thick (1 μm) films used for electromigration assessment, the present study includes an investigation of the earlier stages of growth of aluminium films on amorphous SiO_2.

7.2 Structural Analysis Techniques

The grain structure of the films was examined mainly by transmission electron microscopy and transmission high energy electron diffraction, in conjunction with chemical jet-thinning. For thicker films, grazing incidence x-ray diffraction was used to detect preferred orientations. Surface topography was studied by the transmission electron microscope/shadowed replica technique, and in some cases by scanning electron microscopy and optical microscopy.

7.2.1 Transmission Electron Microscopy

The principles of operation of the electron microscope are beyond the scope of this thesis, and the reader is referred to Hirsch et al (1965) for a comprehensive treatment of the subject.

The instrument used in the present work was a JEM 100U fitted with a goniometer stage (see section 4.2.4). An 80 keV electron beam was used to examine replicas and aluminium films less than $\sim$ 25 nm thick and a 100 keV beam was used for thicker specimens. Individual grains in aluminium films up to 1 μm thick were visible by diffraction contrast in bright-field imaging mode, though the quality of the image from the thicker specimens was relatively poor. Dark-field imaging was also employed on some of the thinner specimens. Magnifications of up to 10^5 were used, and were calibrated by use of standard specimens obtained from Polaron Ltd.

7.2.2 Transmission High Energy Electron Diffraction

This is a well established technique for analysis of the crystalline structure of thin films. Most features of the diffraction patterns can be interpreted on the basis of the kinematical theory of electron diffraction, by application of the Ewald sphere construction (Vainshtein 1964).

For a randomly oriented polycrystalline aggregate, reciprocal space consists of a series of concentric spheres traced out by the reciprocal lattice points when the lattice

is rotated through all angles. The intersection of these spheres with the Ewald sphere gives a diffraction pattern composed of concentric Debye rings (see figure 7.1). Because of the short wavelength of high energy electrons (λ = 0.0037 nm at 100 keV), the radius of the Ewald sphere is very large compared to the reciprocal lattice dimensions, and the surface of the Ewald sphere approximates to a plane.

The radii R_{hkl} of the Debye rings are given by the approximation:

$$R_{hkl}\, d_{hkl} \simeq \lambda L \qquad (7.1)$$

which is valid for small angles of diffraction. λ is the electron wavelength, L the "camera length" (i.e. the distance from the specimen to the photographic plate), and d_{hkl} the spacing of planes giving rise to the diffracted beam.

The sequence of allowed rings is given by the structure factor appropriate to the crystal symmetry. Measurement of ring radii thus enables the crystal type and lattice parameter to be determined.

If the film has a fibre texture, reciprocal space consists of parallel sets of concentric circles, lying in planes normal to the fibre axis (see figure 7.2). If the incident electron beam is parallel to the fibre axis, the diffraction pattern again consists of Debye rings, but not all those allowed by the structure factor are now present. The type of fibre orientation can be deduced from the observed sequence of rings (Pinsker 1953). If the crystal is tilted from normal incidence, the Ewald sphere cuts the reciprocal lattice rings to give a series of arcs. The orientation of the fibre axis can hence be determined.

In the present study transmission electron diffraction was performed in the JEM 100U. The effective camera length in the microscope is not merely the specimen-photographic plate distance, as the magnetic lenses are used to form the image of the diffraction pattern (Hirsch 1965). The camera length was found to vary slightly

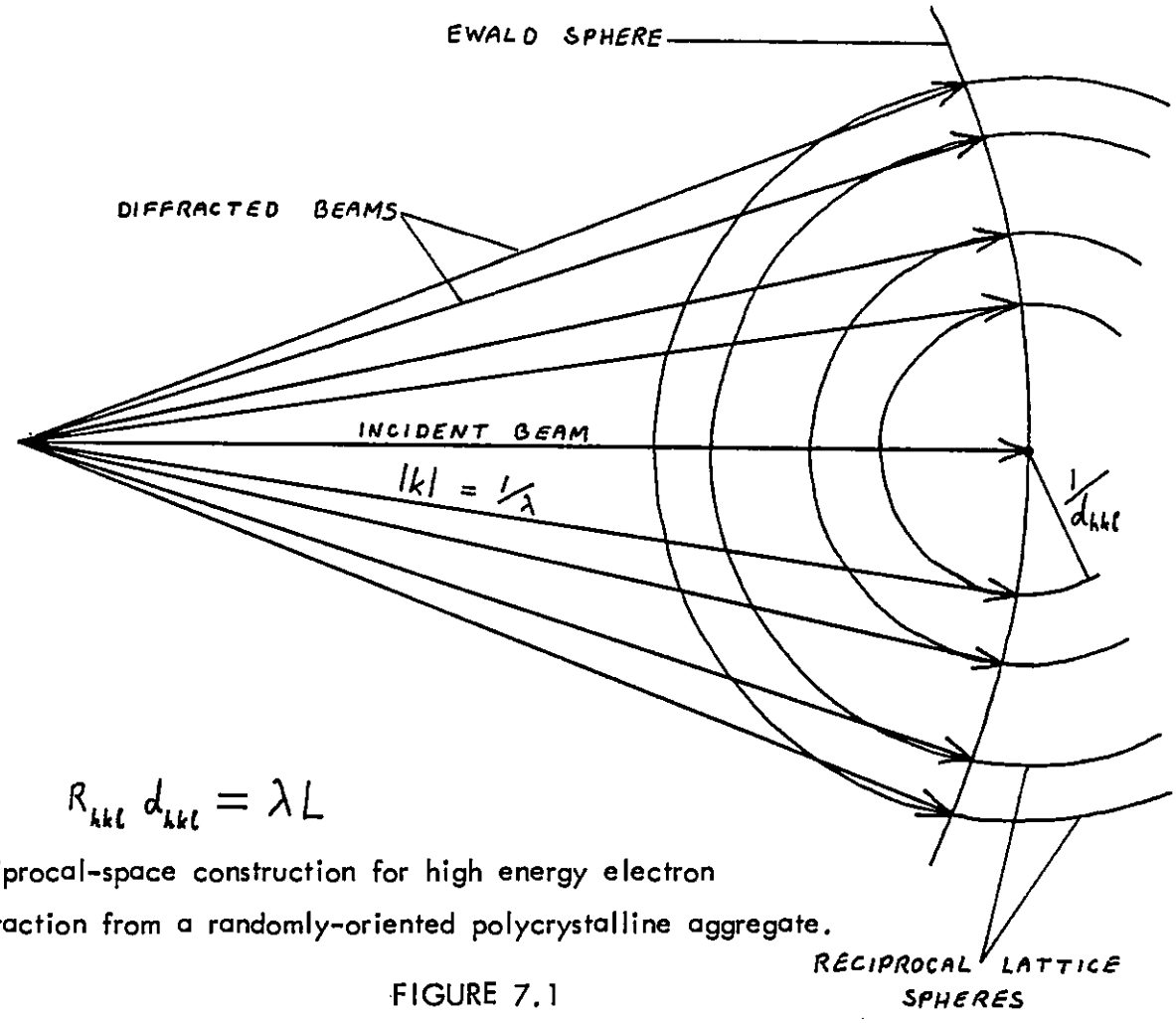

Reciprocal-space construction for high energy electron diffraction from a randomly-oriented polycrystalline aggregate.

FIGURE 7.1

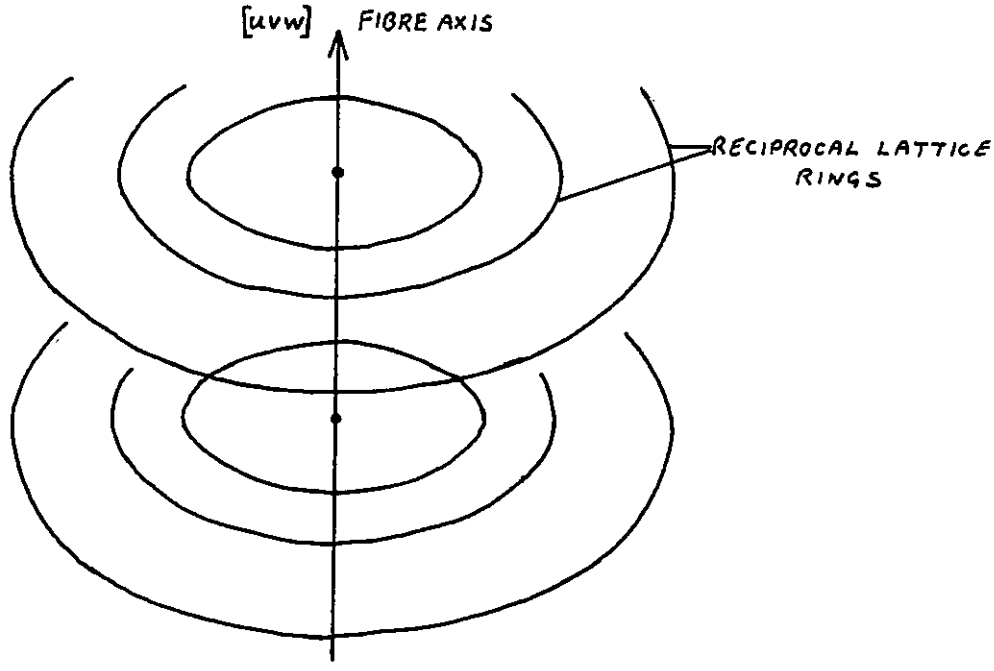

The reciprocal lattice rings due to a textured polycrystalline aggregate.

FIGURE 7.2

between successive operations of the microscope owing to fluctuations in the lens excitations and hysteresis effects. This was not a serious problem in the present work, however, as the accurate measurement of lattice parameters was not necessary, and the aluminium film itself could be used as a "standard".

7.2.3 Grazing Incidence X-Ray Diffraction

This technique, apparently first used by Dobson (1968), enables examination of fibre textures in films too thick for analysis by transmission electron diffraction. A filtered quasi-monochromatic beam of x-rays is directed at grazing incidence onto the surface of the specimen. The path length of the x-rays through the film is thus increased and the sampled depth is reduced.

The diffraction pattern can be interpreted using the Ewald sphere construction, as for electron diffraction. The wavelength of x-rays is much greater than that of high energy electrons, however ($\lambda = 0.154$ nm for Cu Kα radiation) and the radius of the Ewald sphere is comparable with the reciprocal lattice dimensions. If the film has a random grain orientation, the diffraction pattern consists of Debye rings. If there is a fibre texture present, with the fibre axis normal to the film plane, then the rings are broken into arcs (and finally spots for perfect alignment of the crystallites along the fibre axis). Because of the low angle of incidence, the incident wave-vector is almost normal to the fibre axis, and the Ewald sphere cuts the sets of reciprocal lattice circles to form a pattern of spots lying on "layer lines" (see figure 7.3).

Grazing incidence x-ray diffraction patterns can be interpreted by comparison with reflection high energy electron diffraction (RHEED) patterns. The main difference is the smaller radius of the Ewald sphere for x-rays, which means that only the first one or two layer lines appear. Calculated RHEED patterns (Dobson 1968) from one-degree oriented f.c.c. structures are shown in figure 7.4. Because of the finite sizes

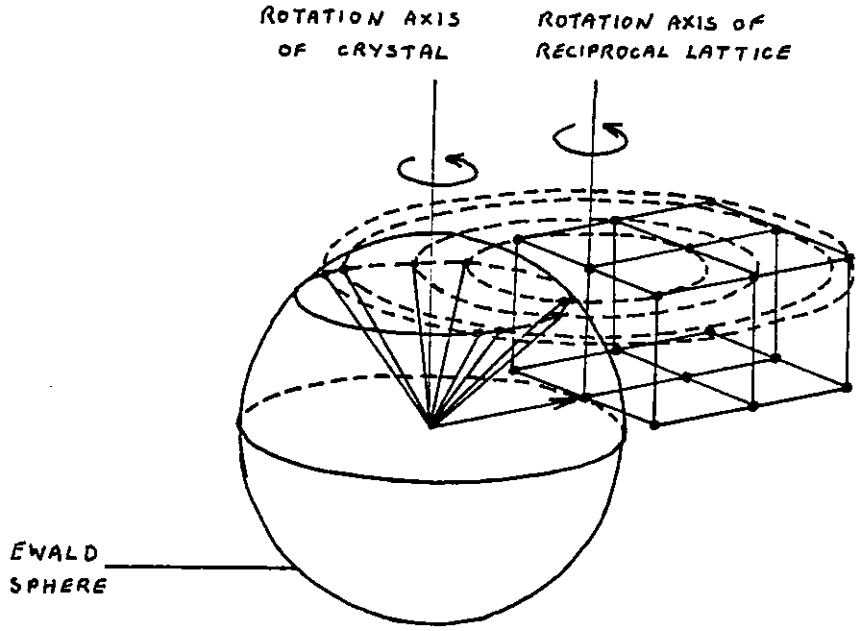

Reciprocal-space construction for grazing incidence x-ray diffraction.

FIGURE 7.3

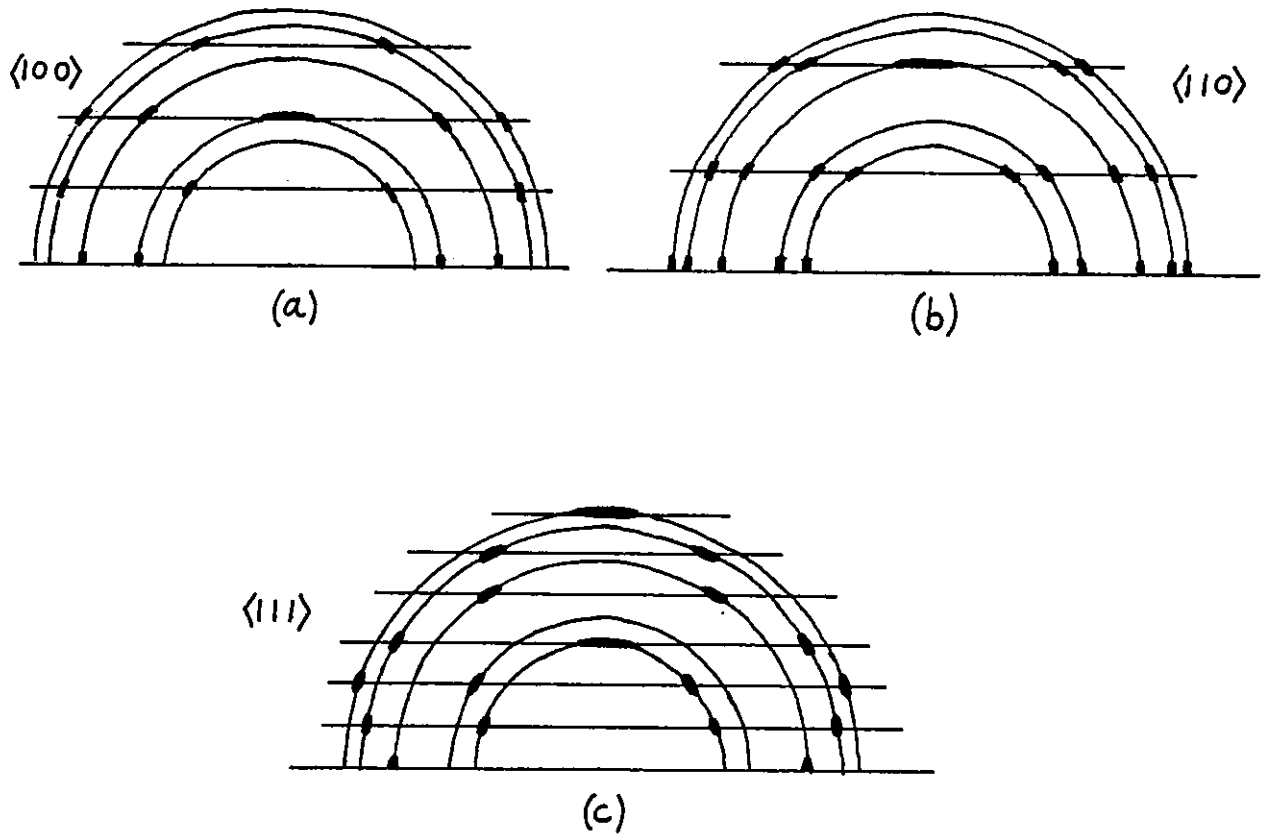

Calculated RHEED patterns from one-degree-oriented f.c.c. structures (from Dobson 1968).

FIGURE 7.4

of the x-ray beam and the specimen, some geometrical broadening of the diffraction pattern is inevitable. This may be minimized by keeping the specimen and collimator as small as possible.

Diffraction patterns were obtained using a Philips PW 1008 x-ray generator with a micro focus copper anode, a nickel filter (to reduce the $K\beta$ radiation intensity) and a 1 mm aperture collimator (see figure 7.5). The specimen, consisting of a section of metallized wafer, was mounted on a 3-circle goniometer with the aluminium surface uppermost. The tilt was set to zero, and the height of the specimen adjusted until its surface bisected the circular aperture of the collimator. The specimen was then tilted through the required angle (3°), as shown in figure 7.6.

The diffraction pattern was recorded on Kodak NS - 59T x-ray film, held 3 cm from the specimen centre. The diffraction pattern from a 1 μm thick aluminium film required an exposure of 2 to 4 hours when the x-ray tube was operated at 33 kV and 20 mA.

7.2.4 Replica Technique

Single-stage carbon/platinum shadowed replicas were used to reveal the specimen topography. Carbon and platinum were evaporated simultaneously from an arc struck between two carbon rods, one of which contained a length of 1 mm diameter "Specpure" platinum wire. The evaporation was carried out in a bell-jar system evacuated to 1×10^{-5} mbar by a rotary pump and diffusion pump. The rotary pump was turned off during evaporation to minimize vibration and hence achieve optimum definition in the replica.

The ultimate resolution of the replica depends upon background structure in the shadowing material. Evaporated carbon/platinum films are amorphous and have a background structure of 2 to 3 nm. The resolution is thus limited to a similar value (Bradley 1961).

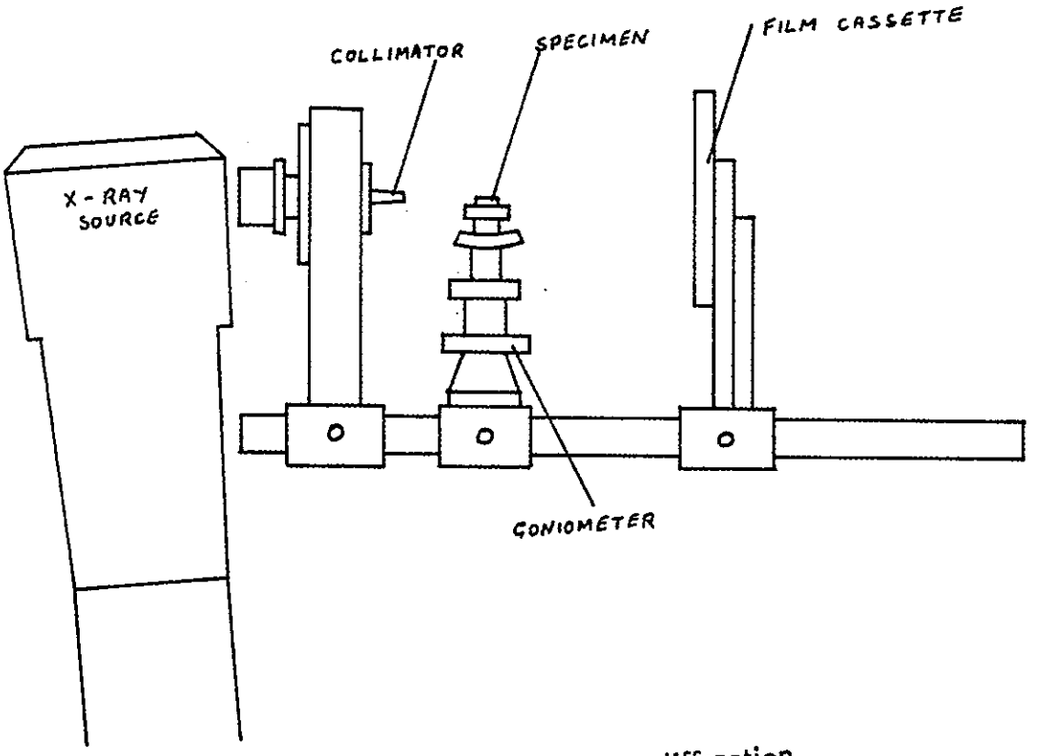

Experimental arrangement for grazing incidence x-ray diffraction.

FIGURE 7.5

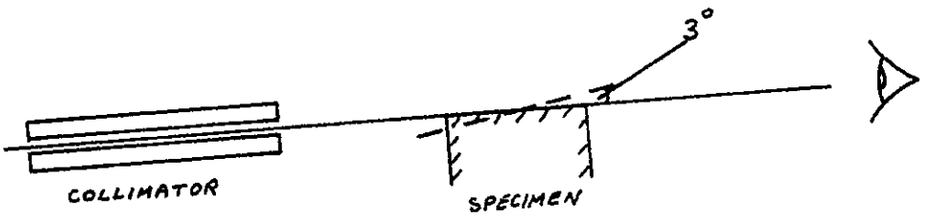

Alignment procedure.

FIGURE 7.6

Replicas were removed from the specimens by lightly scoring into 3 mm squares and floating off in deionized water, the pieces being collected on copper TEM grids. However, with some specimens (particularly those with a rough surface), difficulty was experienced in separation of the replica from the specimen. Dissolving the aluminium film in 50% hydrochloric acid released the replica film, but the bubbles of hydrogen produced by the reaction tended to disrupt the replica. A more successful technique was to immerse the specimen in a dilute ($\sim$ 5%) solution of "Teepol" and allow to drain before deposition of the replica film. In this way the carbon/platinum film was separated from the specimen surface by a thin layer of water-soluble compound and was therefore easily stripped by immersion in water. Replicas made using each of the above techniques gave identical results.

Micrographs of the replicas were obtained in the JEM 100U using an 80 keV electron beam. Interpretation of the micrographs is straightforward if the shadowing angle and direction are known (for example, see Hall 1966) and the height and lateral dimensions of surface features are readily obtained. A shadowing angle of 15^{o} was found to give optimum results for the majority of specimens.

7.2.5 Scanning Electron Microscopy

Some specimens were examined by scanning electron microscopy in order to check for artefacts in the replication process. A JEOL TEMSCAN operating in secondary electron mode was used.

7.2.6 Optical Microscopy

Optical microscopy was used to examine the surfaces of 1 μm thick aluminium films which had grain sizes of the order of several microns. The microscope used was a Nikon "Labophot". Micrographs were obtained under normal incidence reflected illumination and recorded using a 35 mm camera. The maximum magnification employed was 450, without the need for oil immersion.

7.3 Experimental Method

7.3.1 Film Deposition

The substrates consisted of sections of 2-inch {100} -oriented silicon wafers, with 50 nm of steam-grown oxide (see Appendix A). Tungsten-filament evaporation of aluminium (99.995% purity) was carried out in the bell-jar vacuum system described in sections 4.2.2 and 4.2.5. The pressure was less than 2×10^{-6} mbar during evaporation. In order to deposit 1 μm films, three tungsten-filament evaporators were connected in parallel. The thickness of films was monitored during deposition using a quartz crystal monitor and some thicknesses were checked on a "Talystep" stylus profilometer.

In experiments in which the effects of residual gases present during deposition were investigated, the chamber was evacuated to its base pressure before the required gas was admitted and the chamber was continuously pumped to maintain cleanliness of the ambient gases. High purity (BOC "Research Grade") gases were used.

Electron-beam evaporation was performed in a glass chamber evacuated by a liquid nitrogen-trapped oil diffusion pump and rotary pump. The base pressure was approximately 1×10^{-6} mbar, rising to 1×10^{-5} mbar during evaporation. The substrate wafers were held in a planetary motion device and heated by radiation from tungsten filaments. The evaporation source was a magnetically focussed Airco Temscal unit with a water-cooled copper hearth. The deposition rate was kept constant at 10 nm s^{-1} by a control loop incorporating a water-cooled quartz crystal monitor. 99.999% purity aluminium was used for all e-beam evaporations.

Sputter-deposited films of pure aluminium and Al - 1.5% Si were produced in a CVC AST601 magnetron sputtering plant operating at 5 kw with an argon pressure of 2×10^{-3} mbar.

7.3.2 Examination of the Films

After removal from the evaporation system the metallized wafers were scribed

and broken into specimens for examination by the various techniques. Specimens for TEM analysis were prepared by ultrasonic cutting and chemical jet thinning, as described in section 4.2.5. For examination by the other techniques, no preparation was required.

Grain size distributions were determined from the transmission electron micrographs. A grid was overlaid on the micrograph and the areas of individual grains were determined by counting squares. Grain "diameters" were calculated assuming the grains to be square and the size distribution was plotted on log-normal graph paper, in order to obtain the mean, median and standard deviation. (See Appendix E).

In many cases, only the mean grain diameter was needed. This was determined by counting the number of grains per unit area and hence obtaining the mean area and diameter of the grains.

The surface roughness, as determined from electron micrographs of the shadowed replicas, is characterized by two parameters; the peak height of the asperities and the distance between them in the film plane. These quantities roughly correspond to the r.m.s. roughness and correlation length which can be determined by light scattering experiments. For surfaces covered by well-defined hillocks, the term "hillock density" (i.e. number of hillocks per unit area of the surface) is used.

7.4 Results

7.4.1 The Growth of Evaporated Aluminium Films on SiO_2 at Room Temperature

Aluminium films of various thicknesses were deposited at 1 nm s^{-1} by tungsten filament evaporation onto amorphous SiO_2 substrates at 295 K. Figures 7.7 to 7.11 show transmission electron micrographs and diffraction patterns representative of the successive stages of film growth.

Aluminium films of 2 nm mean thickness were found to consist of individual

islands of ~10 nm diameter (figure 7.7a). Shadowed replicas showed the height of the islands to be around 2.5 nm. The corresponding diffraction pattern (figure 7.7b), obtained at an angle of incidence of 10° showed the aluminium to have a randomly oriented polycrystalline structure. The diffuse nature of the diffraction pattern is due to the small crystallite size (~10 nm) which gives rise to broadening of the Debye rings (Hirsch et al 1965).

Films of 5 nm thickness were at the connected network stage, as shown in figure 7.8a, with a coverage of approximately 80%. The "empty" channels contained many secondary nuclei of ~2 nm diameter. The diffraction pattern again indicated a randomly oriented deposit, but the Debye rings were sharper because of the relatively large (~30 nm) crystallite size.

As the mean thickness of films was increased, the coverage increased, becoming 100% at a mean thickness of approximately 15 nm. The 19 nm film shown in figure 7.9a was continuous and had a mean grain size of 50 nm. In the transmission electron diffraction pattern obtained at normal incidence (figure 7.9b) the {111}, {200}, {311}, {222} and {420} rings were of low intensity compared to the {200} and {422} rings, indicating a weak ⟨111⟩ fibre texture (see section 7.2.2). Tilting the specimen 10° from normal incidence caused slight arcing of the rings, thus confirming the existence of a fibre texture with the fibre axis normal to the film plane (figure 7.9c). 15° carbon/platinum replicas (figure 7.9d) revealed surface roughness on a scale of approximately 50 nm (i.e. equal to the grain size). The roughness was in the form of small hillocks, approximately 5 nm high, which corresponded to grains of varying heights. The film appeared highly reflective to the naked eye.

The grain size, surface roughness and strength of the ⟨111⟩ fibre texture were found to increase monotonically with film thickness. 200 nm films had a grain size roughly equal to their mean thickness (figure 7.10a). The ⟨111⟩ fibre texture was well developed, as indicated by the almost total absence of the {111}, {200} etc.

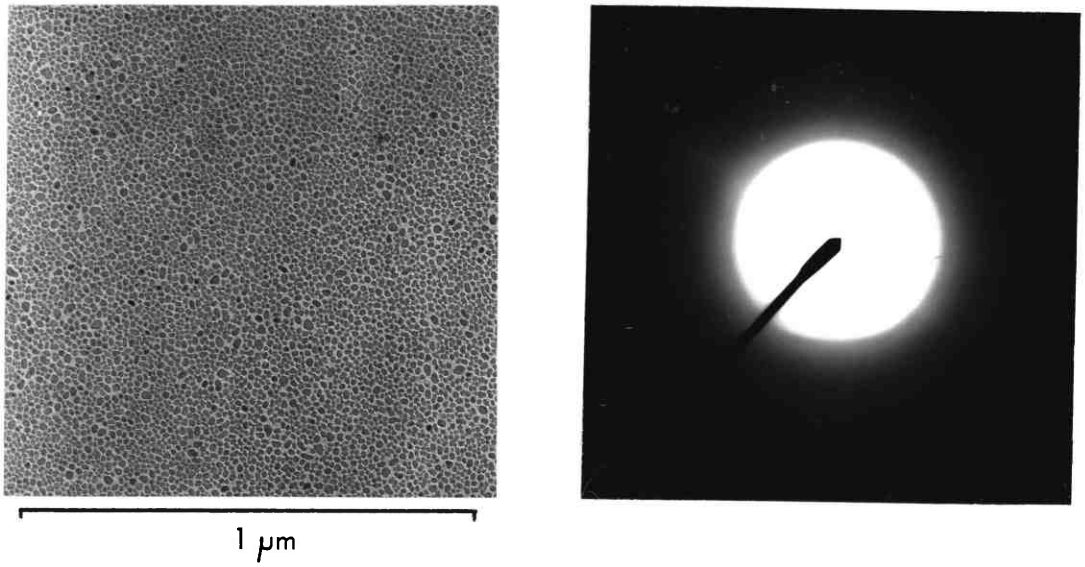

(a) (b)

2 nm mean thickness of aluminium deposited onto amorphous SiO_2 at room temperature.

FIGURE 7.7

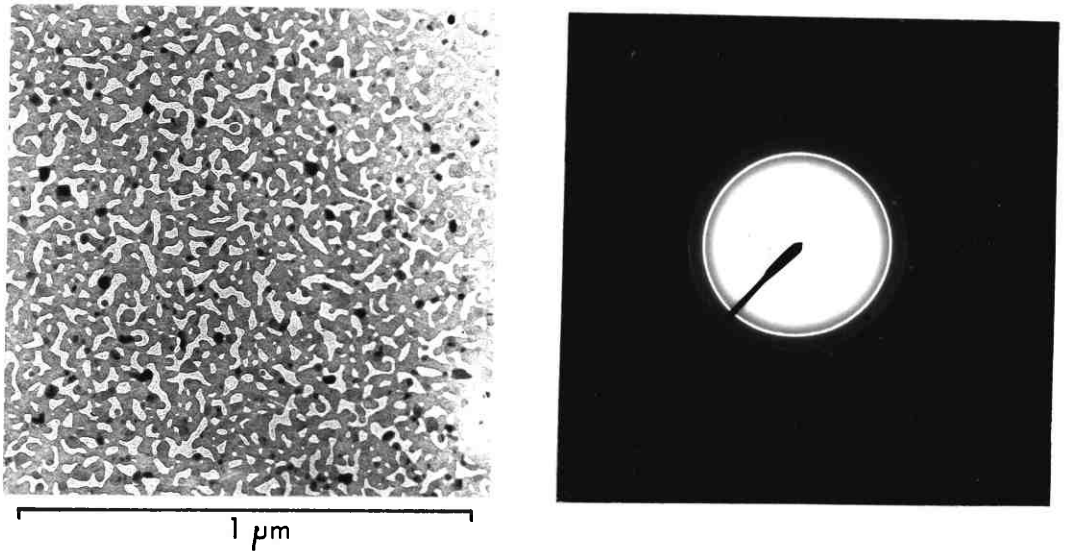

(a) (b)

5 nm mean thickness of aluminium deposited onto amorphous SiO_2 at room temperature.

FIGURE 7.8

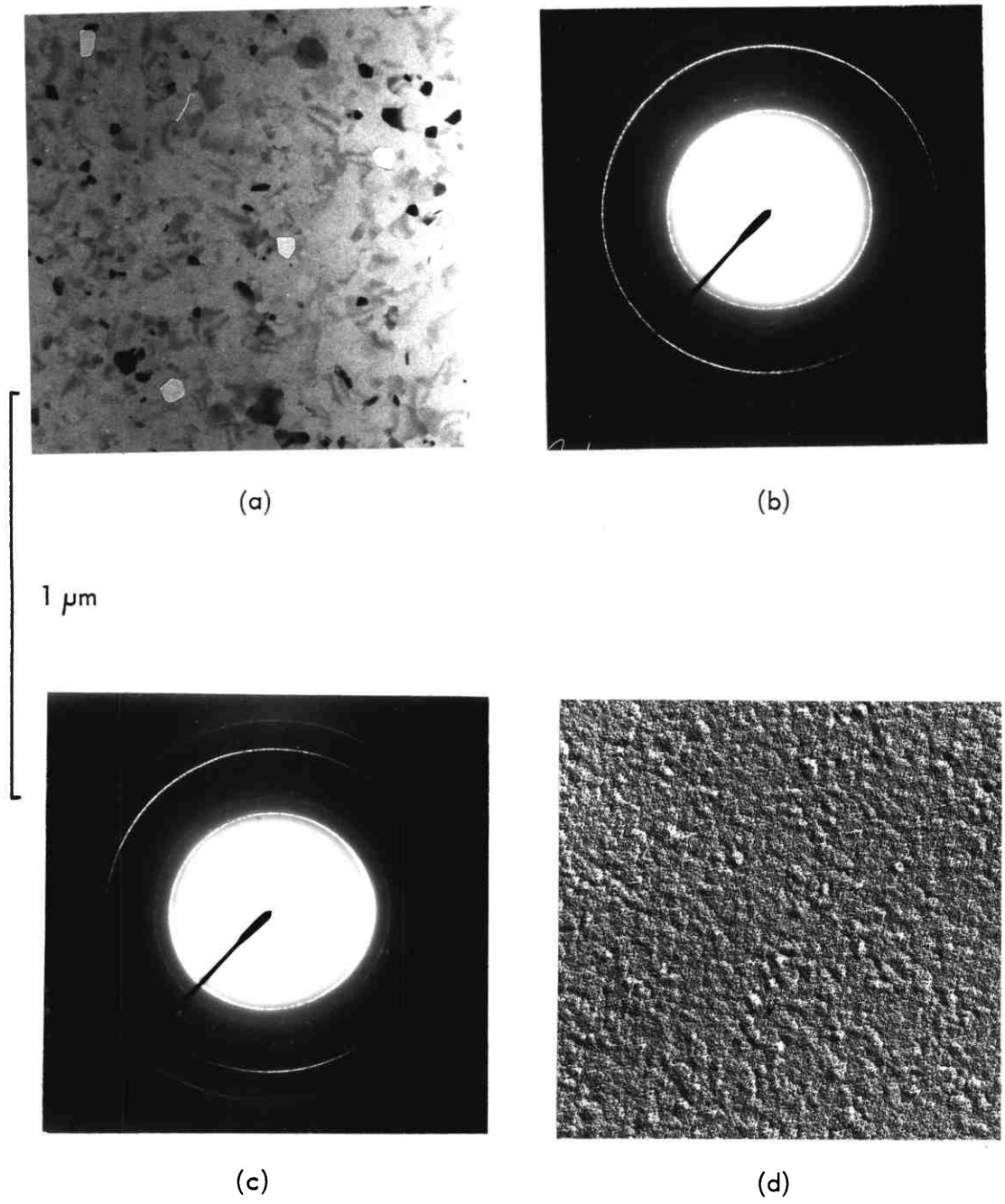

19 nm mean thickness of aluminium deposited onto amorphous SiO_2 at room temperature:
(a) transmission electron micrograph;
(b) transmission electron diffraction pattern at normal incidence;
(c) transmission electron diffraction pattern at 10° from normal incidence;
(d) 15° carbon/platinum replica.

FIGURE 7.9

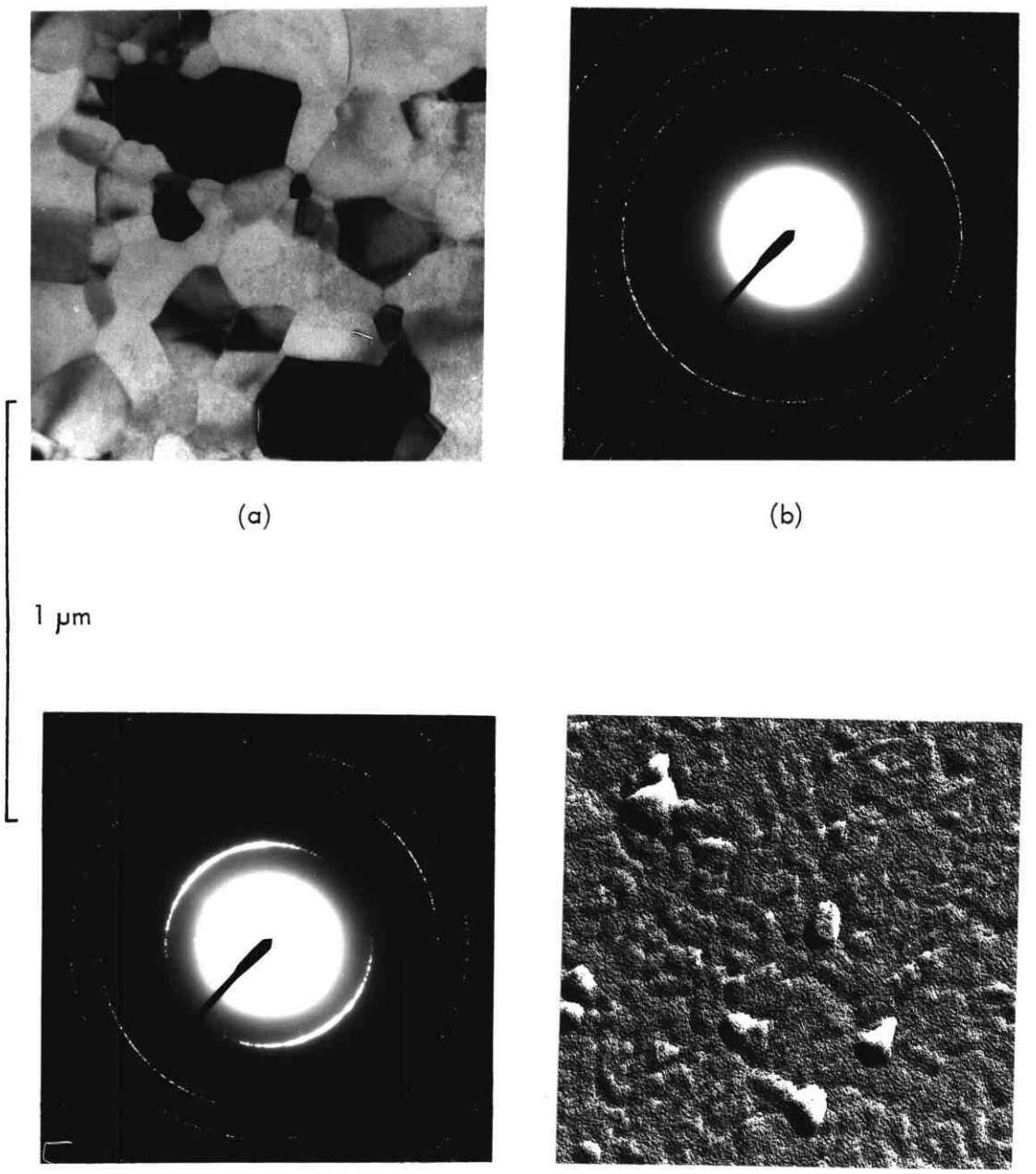

200 nm mean thickness of Al deposited onto amorphous SiO_2 at room temperature:
(a) transmission electron micrograph;
(b) transmission electron diffraction pattern at normal incidence;
(c) transmission electron diffraction pattern at 10° from normal incidence;
(d) 15° carbon/platinum replica.

FIGURE 7.10

(a)

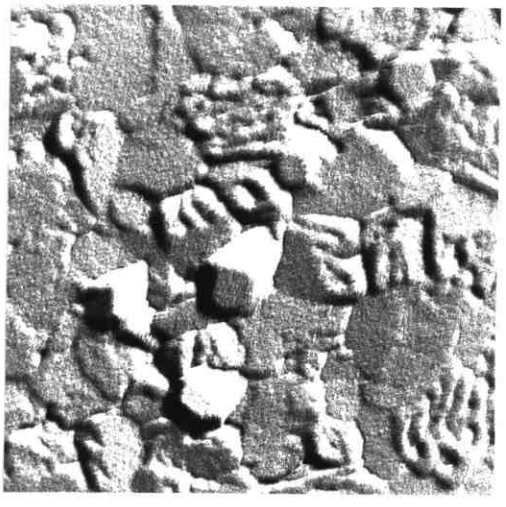

1 μm

(b)

450 nm mean thickness of Al deposited onto amorphous SiO_2 at room temperature:
(a) transmission electron micrograph;
(b) 15° carbon/platinum replica.

FIGURE 7.11

rings in the normal incidence diffraction pattern (figure 7.10b) and the pronounced arcing of the Debye rings in the diffraction pattern from the tilted specimen (figure 7.10c). The "spotty" nature of the diffraction pattern is due to the large crystallite size. The 200 nm films had a slightly milky appearance to the naked eye. Shadowed replicas revealed growth hillocks of base diameter ~ 50 nm and height ~ 10 nm, with a density of 3×10^{12} m^{-2} (figure 7.10d).

450 nm films had a mean grain size of 250 nm (figure 7.11a). These films had a very milky appearance and replicas revealed growth hillocks of approximately 100 nm diameter and 50 nm height, with a density of 2×10^{12} m^{-2}. Parallel steps or wrinkles within individual grains were also observed (figure 7.11b). These films had a strong ⟨111⟩ fibre texture.

7.4.2 The Growth of Evaporated Aluminium Films on SiO_2 at Elevated Temperatures

The growth sequence of aluminium on SiO_2 at 625 K is shown in figures 7.12 to 7.14. Films of 12.5 nm mean thickness consisted mainly of islands of approximately 100 nm diameter and 20 nm height, with smaller islands (less than 10 nm diameter) in the spaces between them (figures 7.12a and b). The coverage was approximately 50%. Many of the larger islands were of elongated shape and contained grain boundaries, suggesting that they were formed by the coalescence of 2 or more smaller islands of roughly circular shape. The orientation was again random.

A connected network existed at a mean thickness of 50 nm, and complete coverage was attained at approximately 100 nm. The 125 nm film shown in figure 7.14 had a mean grain size of 300 nm. Replicas revealed deep grain boundary grooves but no growth hillocks or wrinkles. The diffraction pattern was indicative of large, randomly oriented crystallites.

The growth characteristics of aluminium deposited at 475 K were intermediate

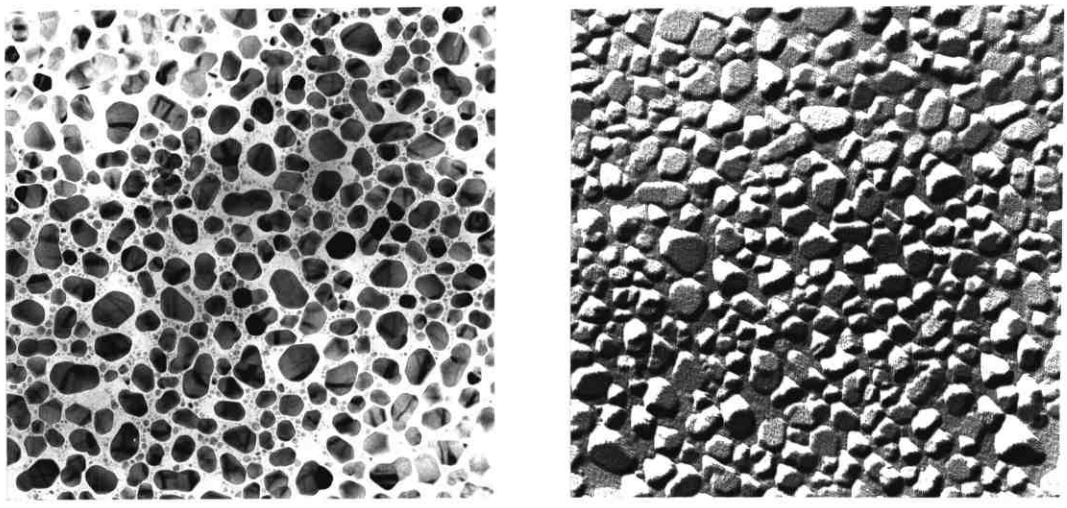

(a) (b)

1 μm

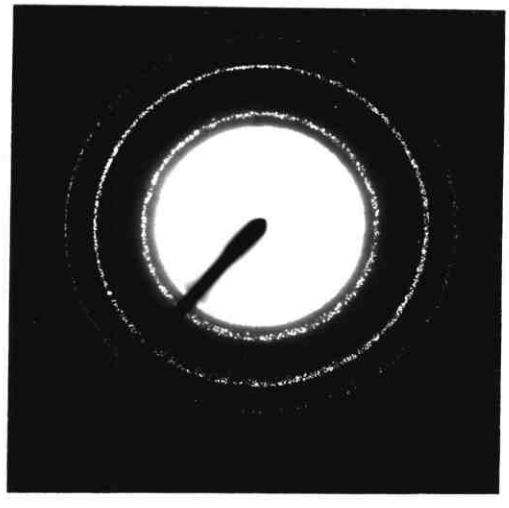

(c)

12.5 nm mean thickness of Al deposited onto amorphous SiO_2 at 625 K:
(a) transmission electron micrograph;
(b) 15° carbon/platinum replica;
(c) transmission electron diffraction pattern at 10° from normal incidence.

FIGURE 7.12

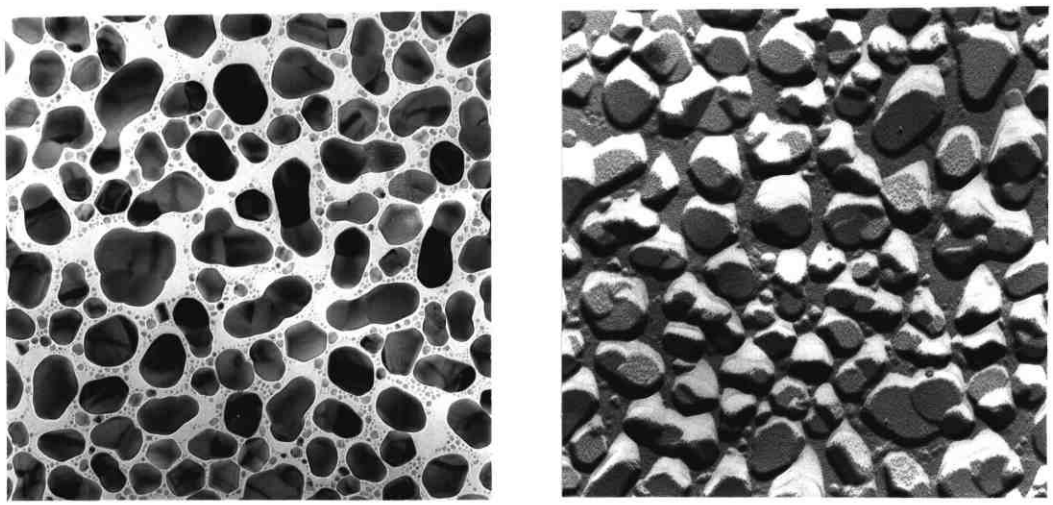

(a) (b)

1 μm

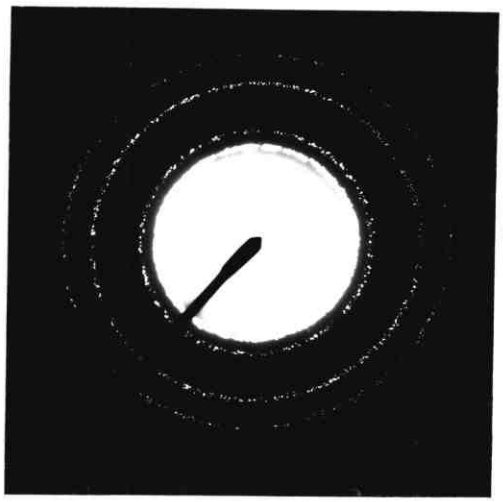

(c)

25 nm mean thickness of Al deposited onto amorphous SiO_2 at 625 K:
(a) transmission electron micrograph;
(b) 15° carbon/platinum replica;
(c) transmission electron diffraction pattern at 10° from normal incidence.

FIGURE 7.13

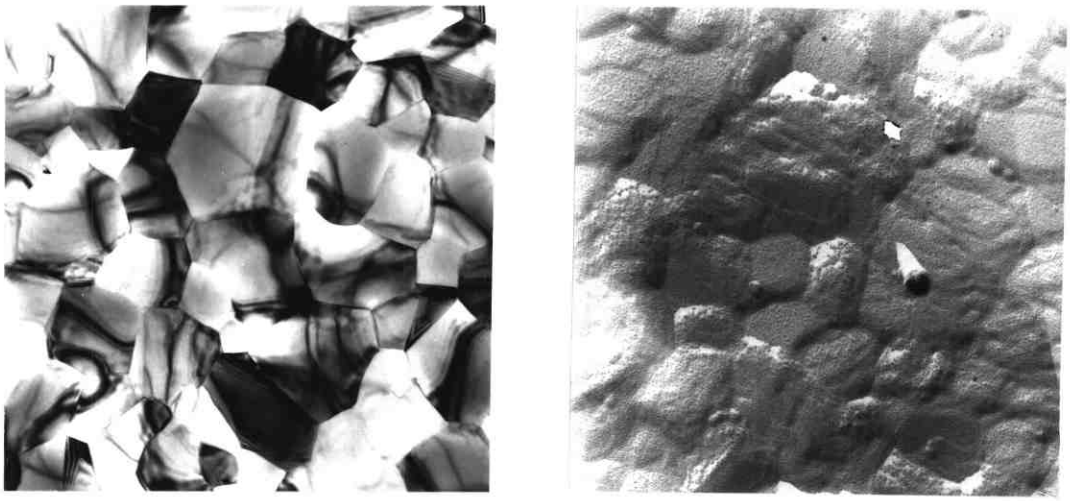

(a) (b)

1 μm

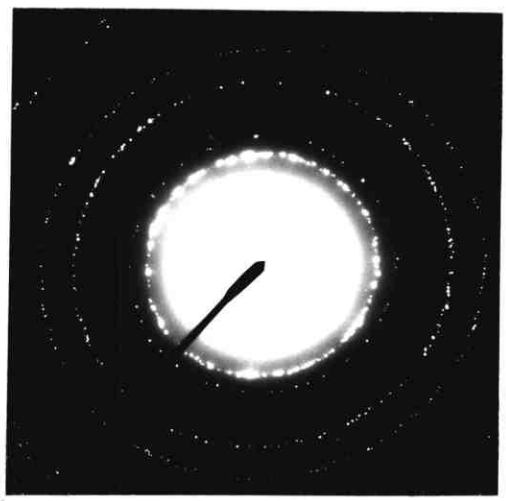

(c)

125 nm mean thickness of Al deposited onto amorphous SiO_2 at 625 K:
(a) transmission electron micrograph;
(b) 15° carbon/platinum replica;
(c) transmission electron diffraction pattern at 10° from normal incidence.

FIGURE 7.14

between those of films deposited at room temperature and 625 K. A connected network was formed at a mean thickness of 25 nm, the coverage being 70% (figure 7.15). The mean diameter of grains in the network was 100 nm, and small ($\sim$ 20 nm) islands were visible in the channels. The orientation was random.

100% coverage was attained at a thickness of approximately 50 nm. The 110 nm film shown in figure 7.16 was continuous and had a mean grain size of 200 nm. The surface exhibited grain boundary grooves and small hillocks of approximately 100 nm diameter and 10 nm height. The film had a $\langle 111 \rangle$ fibre texture.

The increase in grain size with film thickness for substrate temperatures of 295 K, 475 K and 625 K is plotted in figure 7.17.

7.4.3 The Effect of Annealing

Annealing effects were studied in 100 nm films deposited at room temperature. Annealing was carried out in the evaporation chamber immediately after deposition, without breaking the vacuum. A 6 hour anneal at 625 K caused the mean grain size to increase from 110 nm to 150 nm, but no other structural changes were detected. Both the annealed and as-deposited films had a pronounced $\langle 111 \rangle$ fibre texture and relatively smooth, hillock-free surfaces.

7.4.4 The Effect of Residual Gases Present During Deposition

450 nm films were deposited in the presence of 7×10^{-5} mbar of oxygen and nitrogen, the conditions being otherwise identical to those described in section 7.4.1. Films deposited in a nitrogen ambient had a mean grain size of 150 nm (figure 7.18a) compared to 250 nm for films of equal thickness deposited in a vacuum of 2×10^{-6} mbar (figure 7.11). Both films possessed growth hillocks of a similar size and density, but the film deposited in nitrogen did not exhibit surface wrinkling (figure 7.18b). Both films had a $\langle 111 \rangle$ fibre texture.

Films deposited in the presence of oxygen had a mean grain diameter of

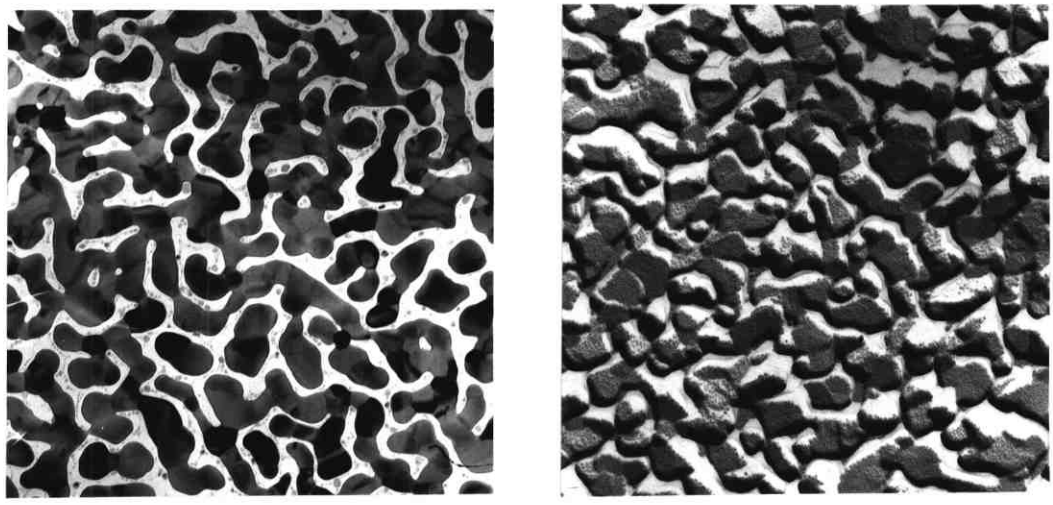

(a) (b)

1 μm

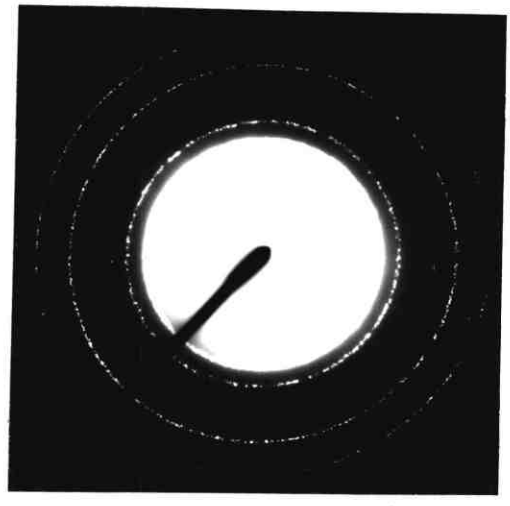

(c)

25 nm mean thickness of Al deposited onto amorphous SiO_2 at 475 K:

(a) transmission electron micrograph;

(b) 15° carbon/platinum replica;

(c) transmission electron diffraction pattern at 10° from normal incidence.

FIGURE 7.15

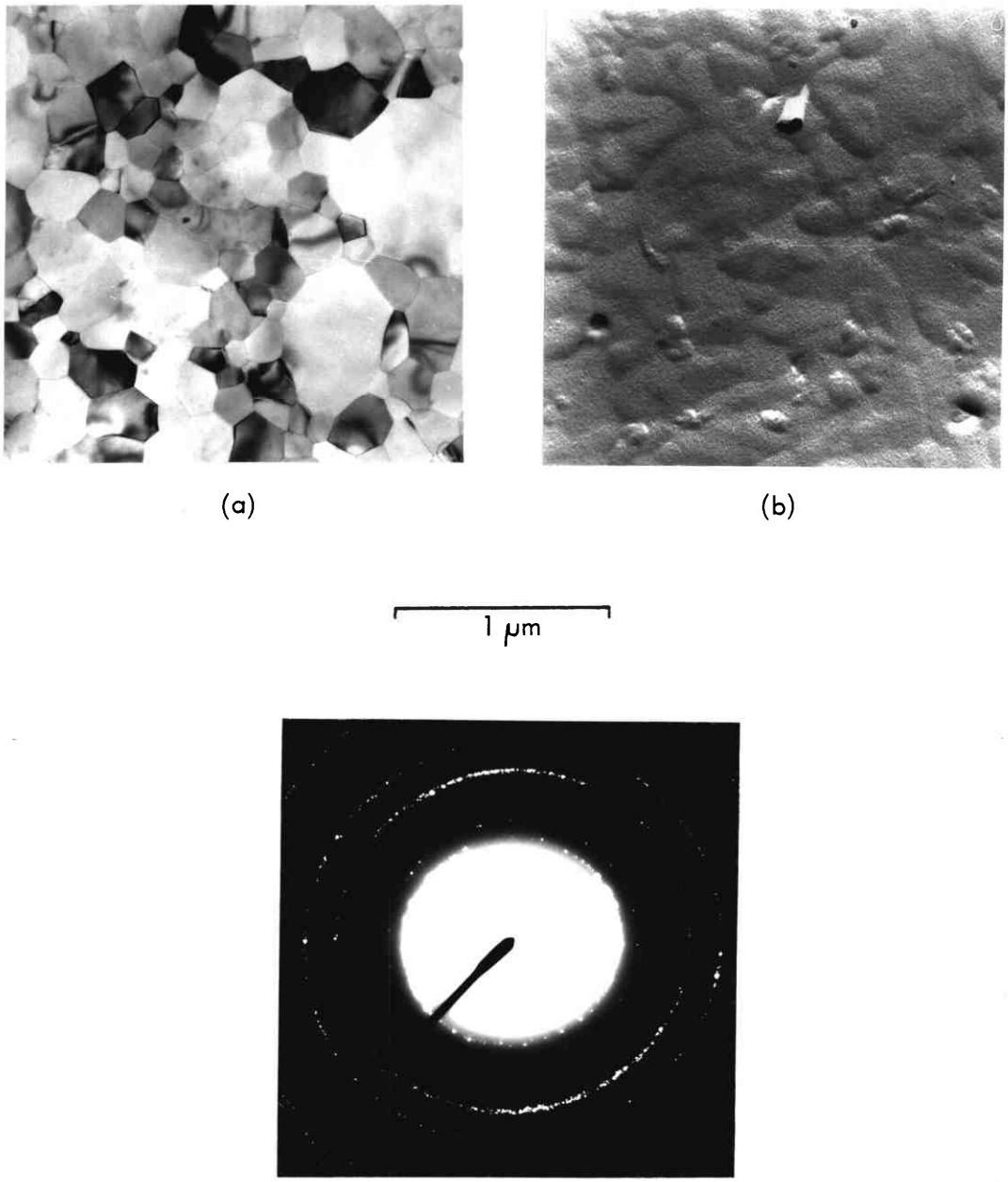

110 nm mean thickness of Al deposited onto amorphous SiO_2 at 475 K:
(a) transmission electron micrograph;
(b) 15^{o} carbon/platinum replica;
(c) transmission electron diffraction pattern at 10^{o} from normal incidence.

FIGURE 7.16

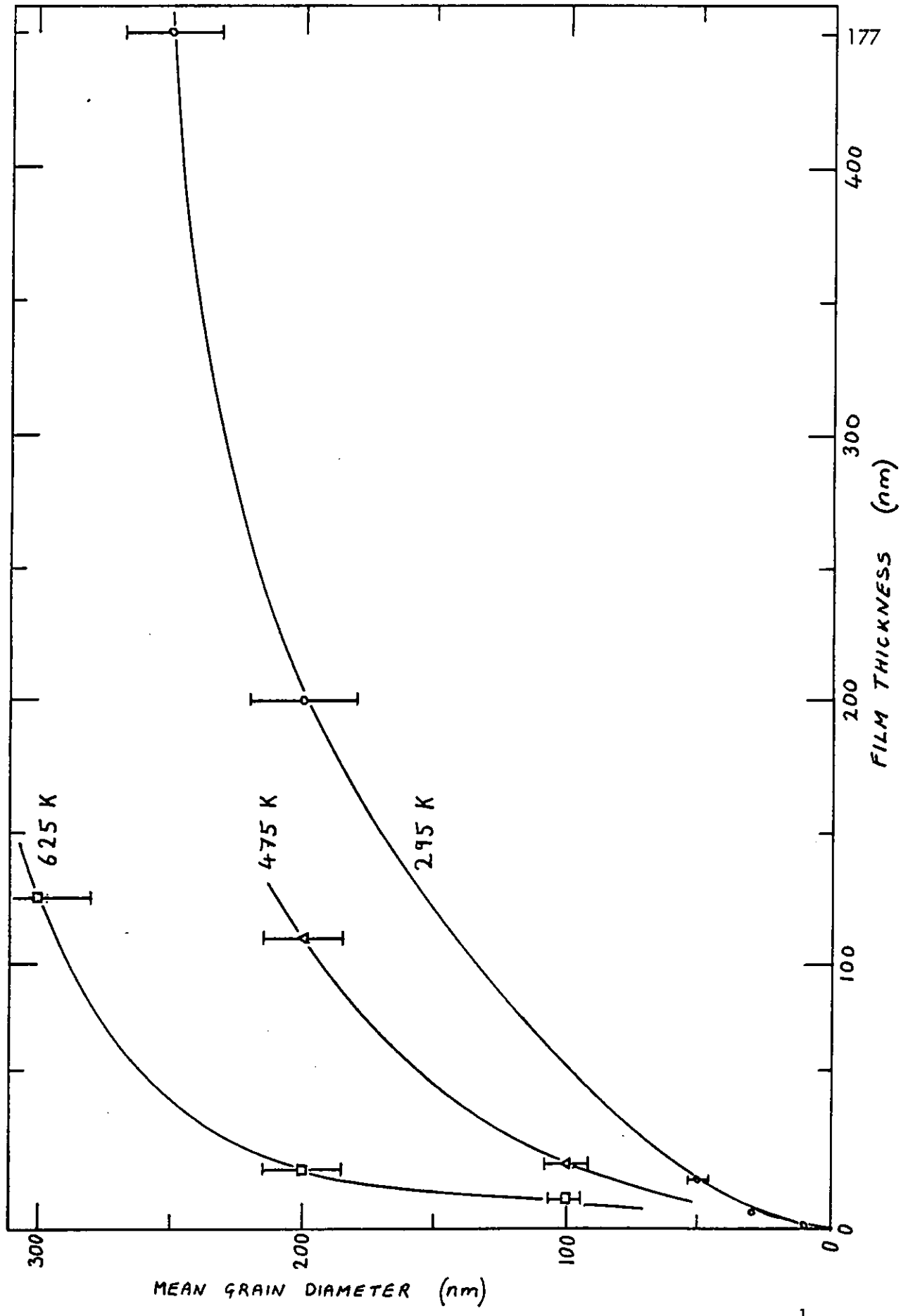

Mean grain size versus film thickness, for aluminium films deposited at 1 nm s^{-1} onto SiO_2 substrates at temperatures of 295 K, 475 K, and 625 K.

FIGURE 7.17

100 nm (figure 7.18c) and a high density (5×10^{12} m^{-2}) of growth hillocks of 100 nm base diameter and 75 nm height (figure 7.18d). No fibre texture was apparent in these films.

7.4.5 The Microstructure of 1 μm-Thick Tungsten-Filament Evaporated Aluminium Films

Films were deposited at temperatures ranging from 295 K to 675K. (The deposition temperature quoted is the temperature at the beginning of the deposition process. Radiative heating by the evaporator caused the substrate temperature to rise by as much as 50 K during deposition). Most films were deposited at 10 nm s^{-1} as this is typical of the deposition rates used in industrial metallization processes. Some films were deposited at 1 nm s^{-1} to determine the effects of deposition rate on the microstructure. Annealing effects were also investigated.

The transmission electron micrographs in figure 7.19 show the grain structure of 1 μm films deposited at 10 nm s^{-1} onto substrates at 295 K, 475 K and 575 K, and of a film deposited at 475 K, then annealed for 2 hours at 700 K. The grains tended to be equiaxed and had varying numbers of sides. The distribution shown in figure 7.20 is typical of all the films examined and shows that hexagonal grains were more common than grains of any other shape. The smaller grains had straight or convex sides, but some of the larger grains were concave. The grains appeared to be columnar (i.e. extend throughout the thickness of the film).

The grain size distributions of films deposited at 475 K, 575 K and 675 K were determined and plotted on log-normal graph paper (figure 7.21). It is evident that the data are well represented by log-normal distributions. The median grain size and logarithmic standard deviation were determined for each film from the best straight line fit to the data, as indicated in the figure. The results are shown in histogram form in figure 7.22 The log-normal curves shown for comparison were obtained using the

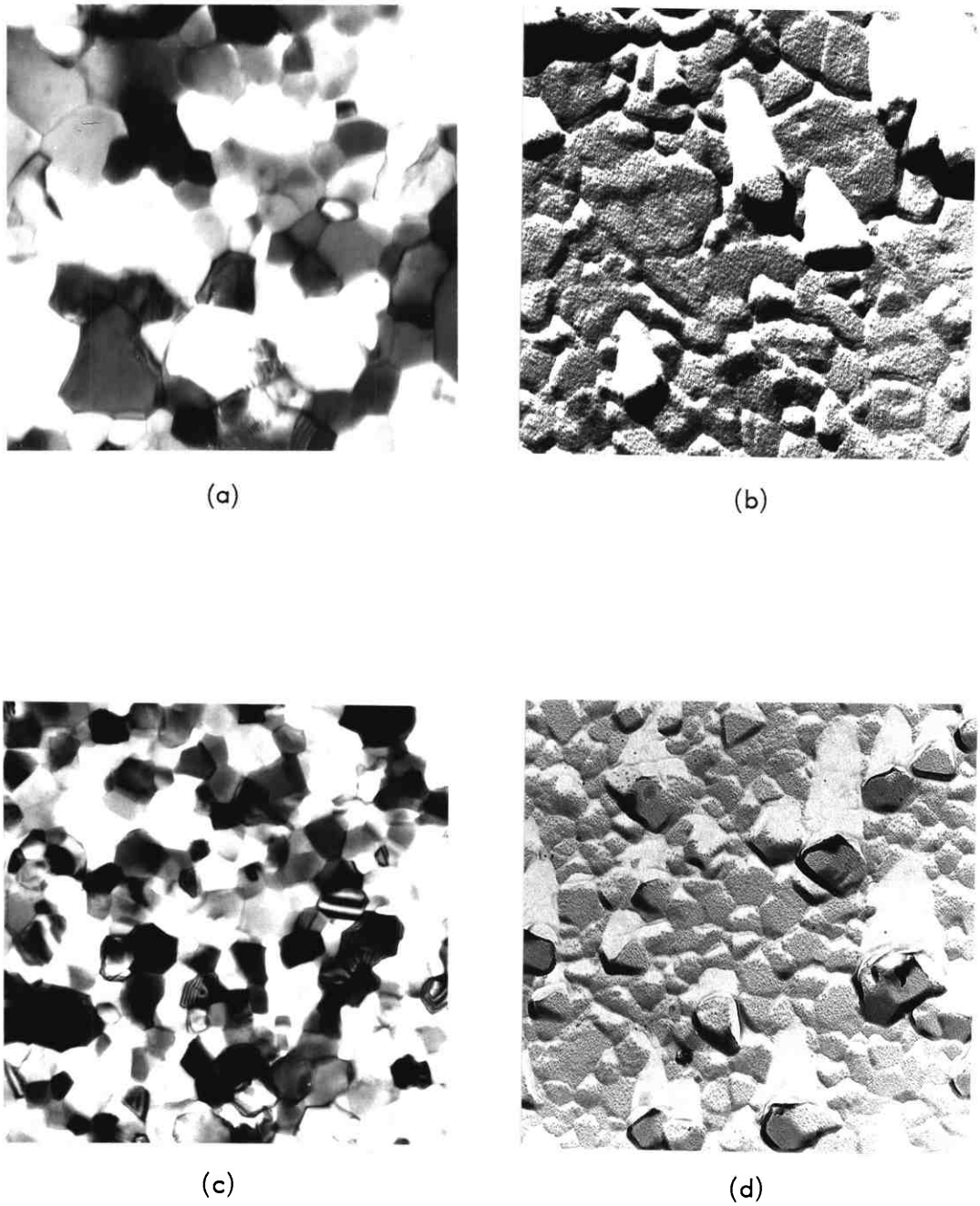

450 nm of Al deposited onto amorphous SiO_2 at room temperature in the presence of 7×10^{-5} m bar of nitrogen (a and b) and oxygen (c and d).

FIGURE 7.18

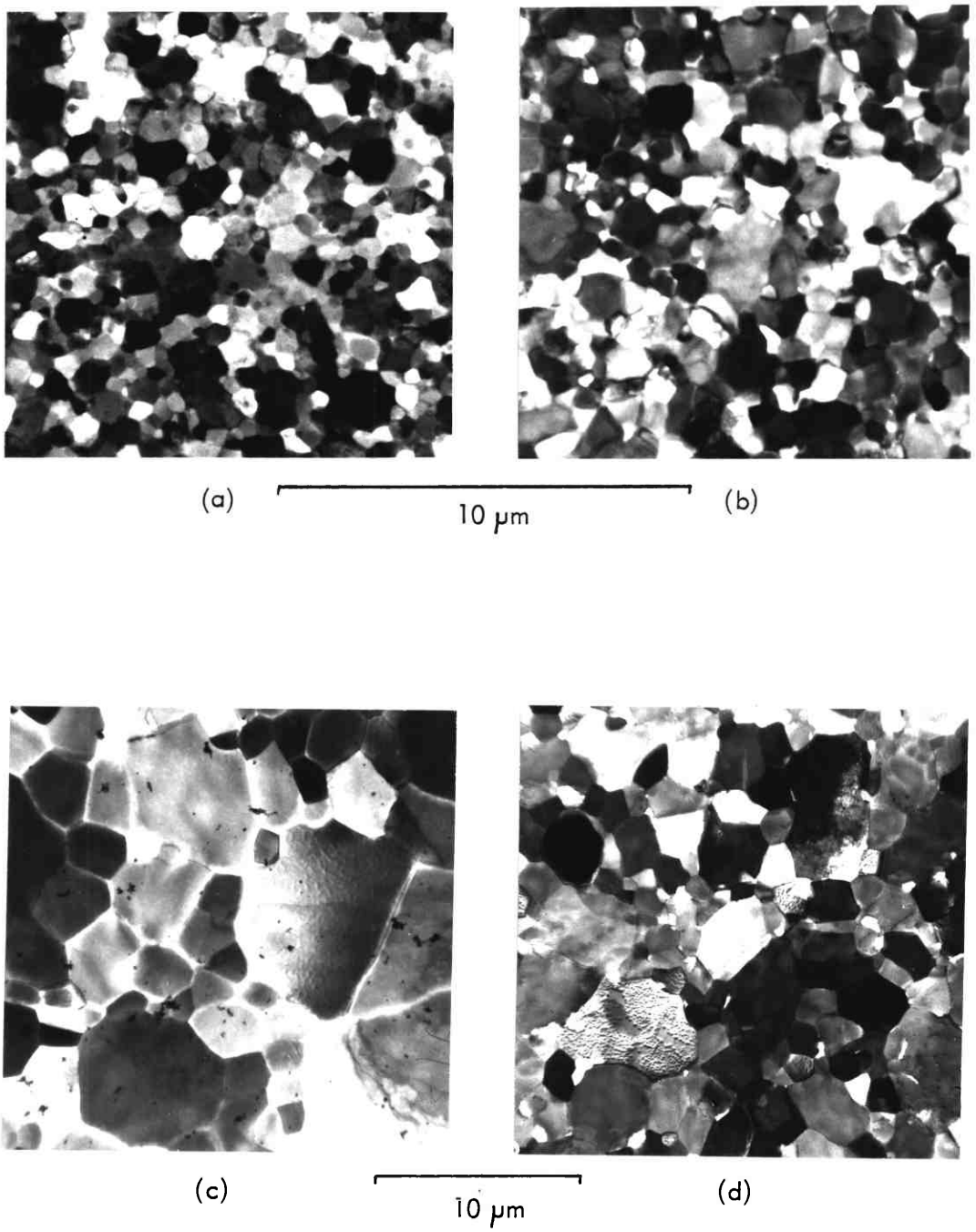

Transmission electron micrographs showing the grain structure of 1 μm thick Al films deposited at 10 nm s^{-1} onto amorphous SiO_2 at temperatures of:

(a) 295 K;

(b) 475 K;

(c) 575 K;

(d) 475 K, then annealed in vacuo at 700 K for 2 hours.

FIGURE 7.19

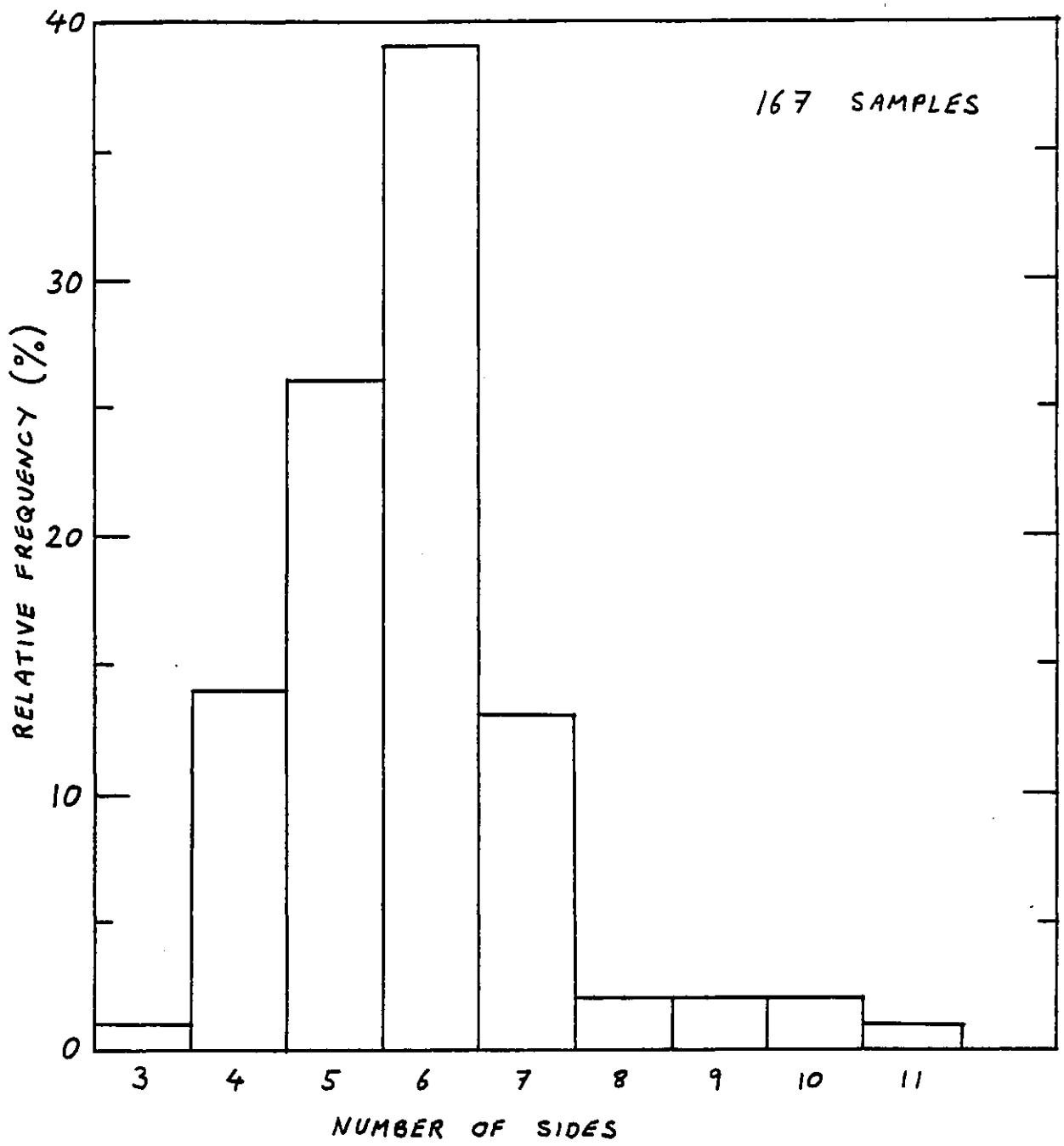

Distribution of the number of sides of individual grains in a 1 μm Al film.

FIGURE 7.20

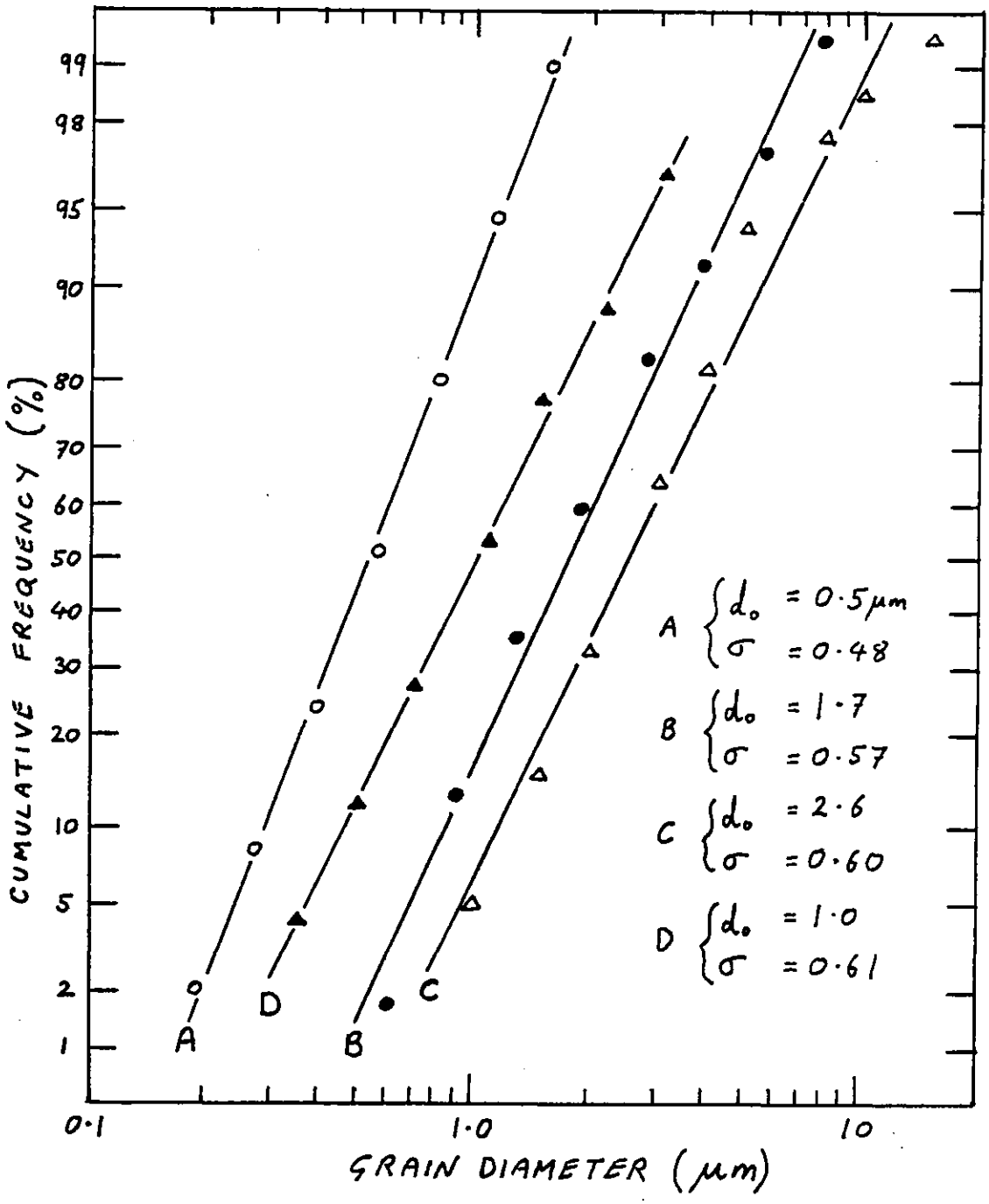

Log-normal plot of the grain size distributions of 1 μm aluminium films deposited at 10 nm s^{-1}.

Film A: deposited at 475 K.

Film B: deposited at 575 K.

Film C: deposited at 675 K.

Film D: deposited at 475 K, followed by a 2 hour anneal at 700 K.

FIGURE 7.21

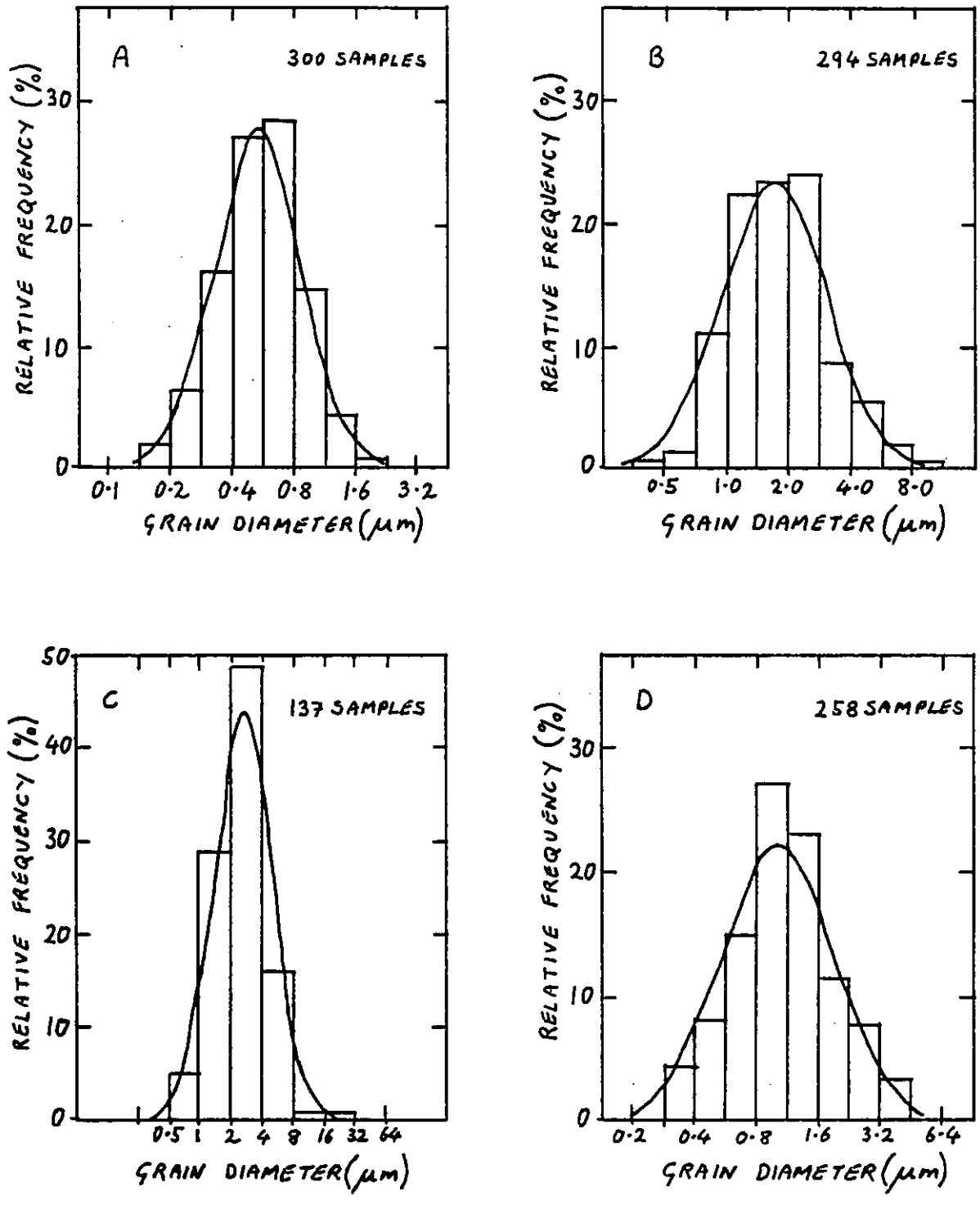

Grain size distributions of the 1 um aluminium films in histogram form, with calculated log-normal distributions for comparison.

FIGURE 7.22

median and standard deviation of the experimental data. The median grain size was found to increase monotonically with deposition temperature, from 520 nm at 475 K to 2.6 μm at 675 K. The standard deviation of the grain size distribution also increased with temperature, ranging from 0.47 at 475 K to 0.61 at 675 K. The mean grain size ranged from 450 nm at 295 K to 4.1 μm at 675 K, as shown in figure 7.23. (The mean is always greater than the median since the distribution of the logarithms of the grain sizes is normal).

The reflectivity of the films decreased with increasing deposition temperature. Films deposited at 295 K were highly reflective. Shadowed replicas and scanning electron microscopy showed the surface to be covered by hillocks of 400 nm base diameter and 150 nm height with a density of $5 \times 10^{11} m^{-2}$ (figures 7.24a and b). Many of the hillocks had well developed crystallographic shapes, the truncated hexagonal pyramid being particularly common (figure 7.24c). Parallel steps or wrinkles were also visible.

Films deposited at 475 K had a slightly milky appearance to the naked eye. Their surfaces were relatively free of growth hillocks, but grain boundary grooves and wrinkles were observed (figure 7.25a).

For deposition temperatures between 575 K and 675 K the films had a milky appearance. Their surfaces were almost completely free from hillocks, but contained deep grain boundary grooves and steps within some large grains. Shadowed replicas are shown in figures 7.25b and c, and an optical micrograph in figure 7.25d.

Films deposited at room temperature at 1 nm s^{-1} had a smaller mean grain size (350 nm) than films deposited at 10 nm s^{-1}. Their surfaces were covered by relatively large growth hillocks, however, and the aluminium had a milky appearance. The hillocks were typically of 1 μm base diameter and 400 nm height, with a density of $2.5 \times 10^{11} m^{-2}$. Many had distinct crystallographic shapes (figure 7.26). Changing

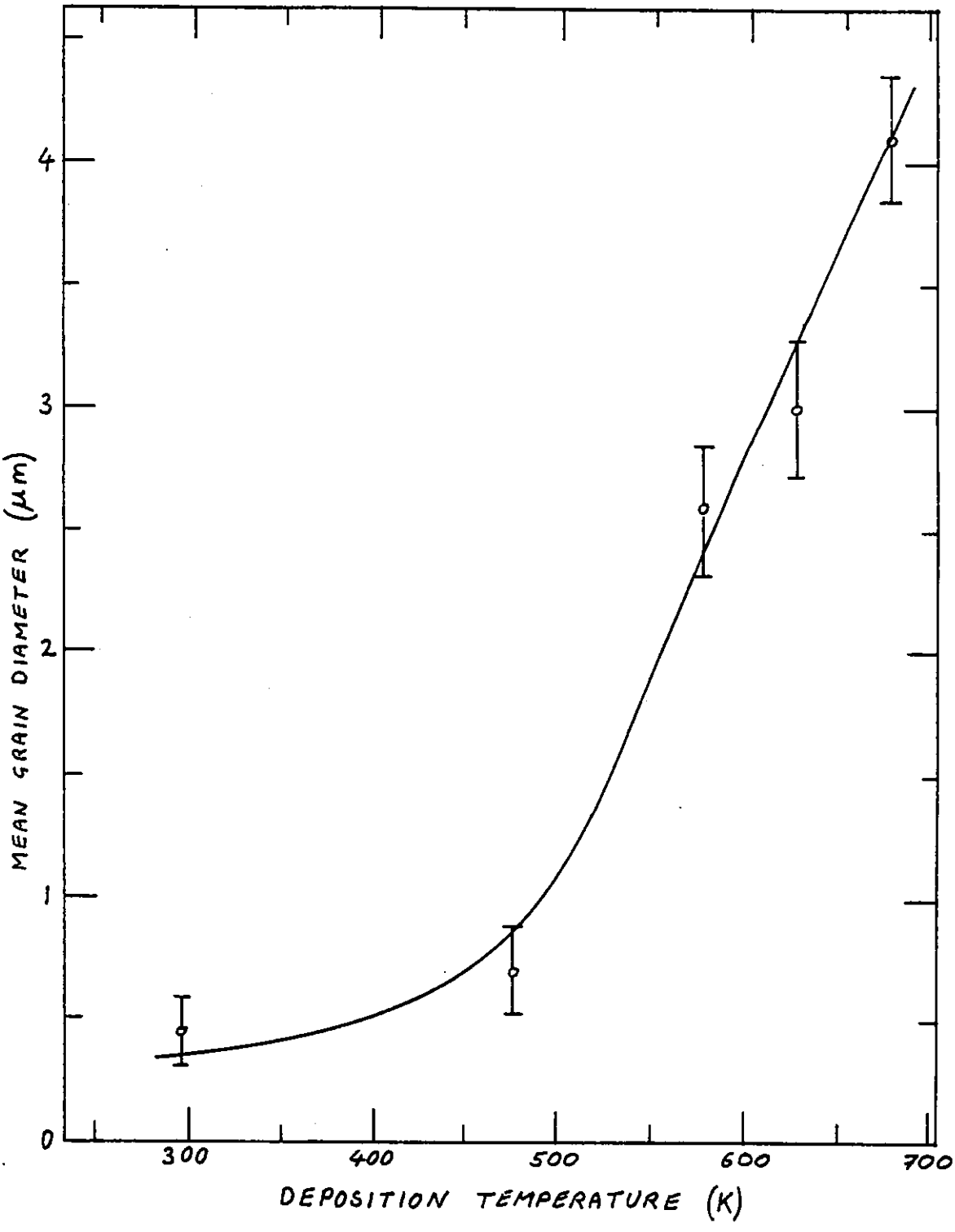

Mean grain size versus deposition temperature for 1 μm Al films deposited onto oxidized silicon at 10 nm s^{-1}.

FIGURE 7.23

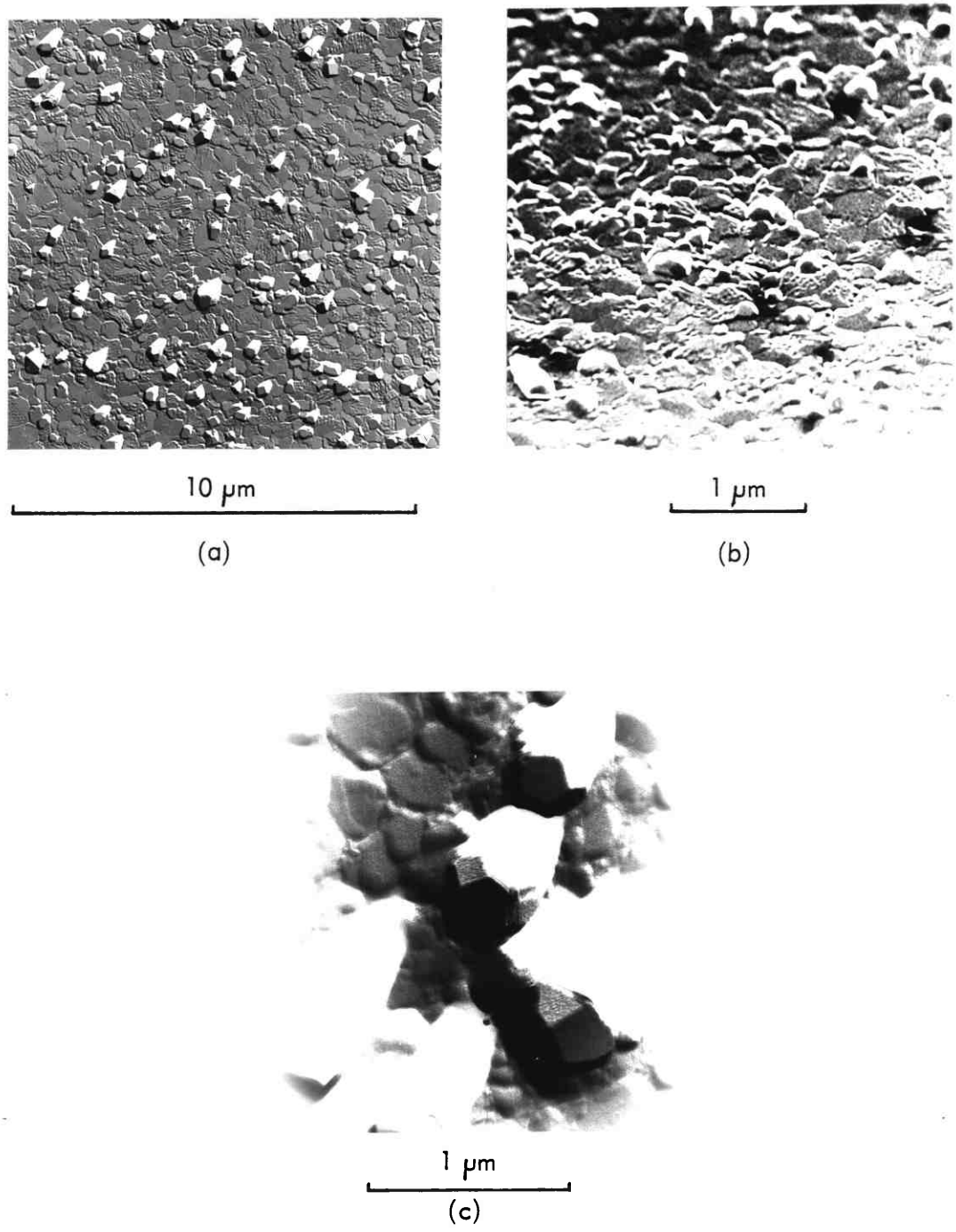

1 um thick Al film deposited at 10 nm s^{-1} onto amorphous SiO_2 at 295 K:
(a) and (c) 15° carbon/platinum replicas;
(b) scanning electron micrograph.

FIGURE 7.24

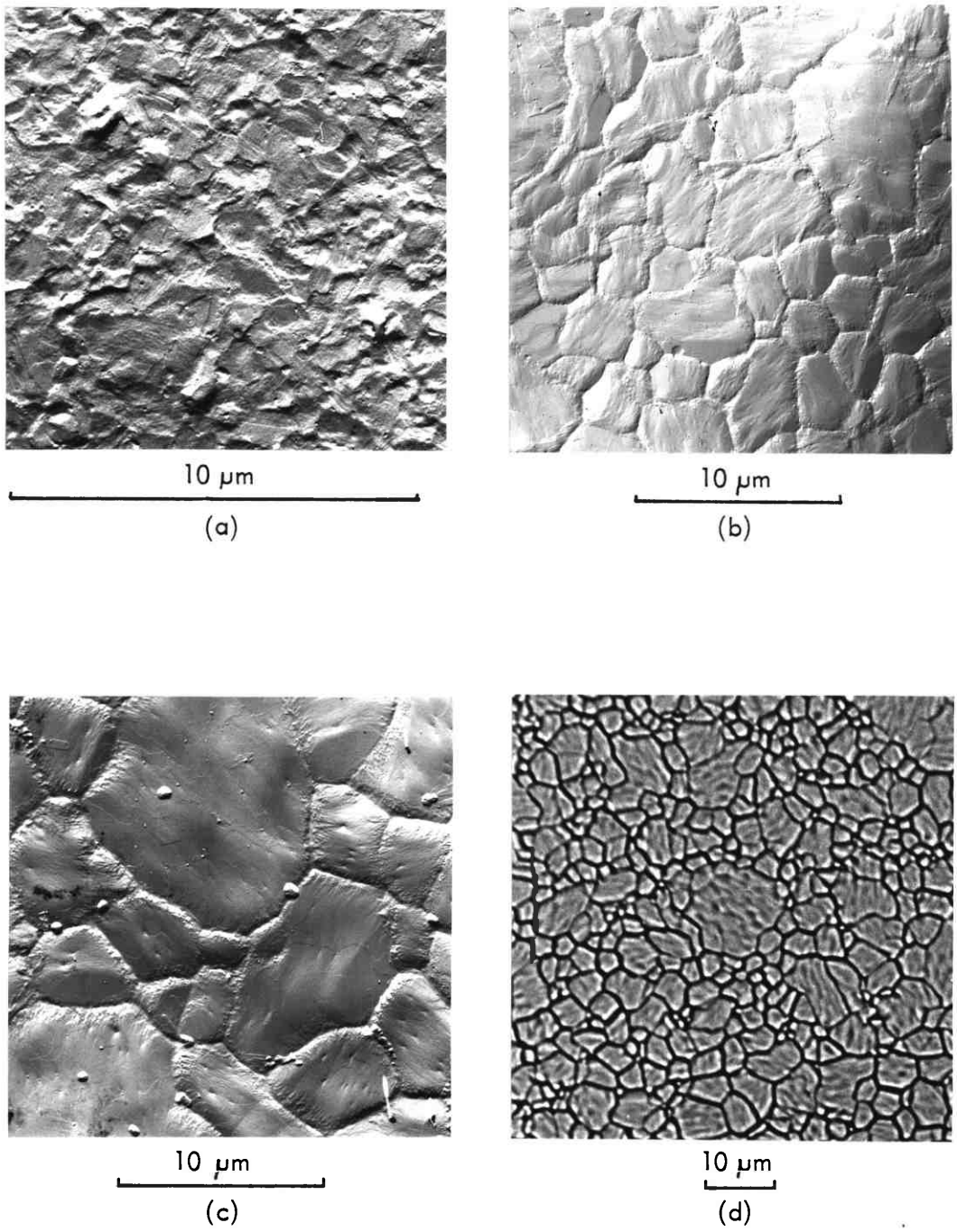

The surface roughness of 1 um thick Al films deposited onto amorphous SiO_2 at 10 nm s^{-1}

(a) 15° carbon/platinum replica of a film deposited at 475 K;

(b) 15° carbon/platinum replica of a film deposited at 575 K;

(c) 15° carbon/platinum replica of a film deposited at 675 K;

(d) optical micrograph of a film deposited at 675 K.

FIGURE 7.25

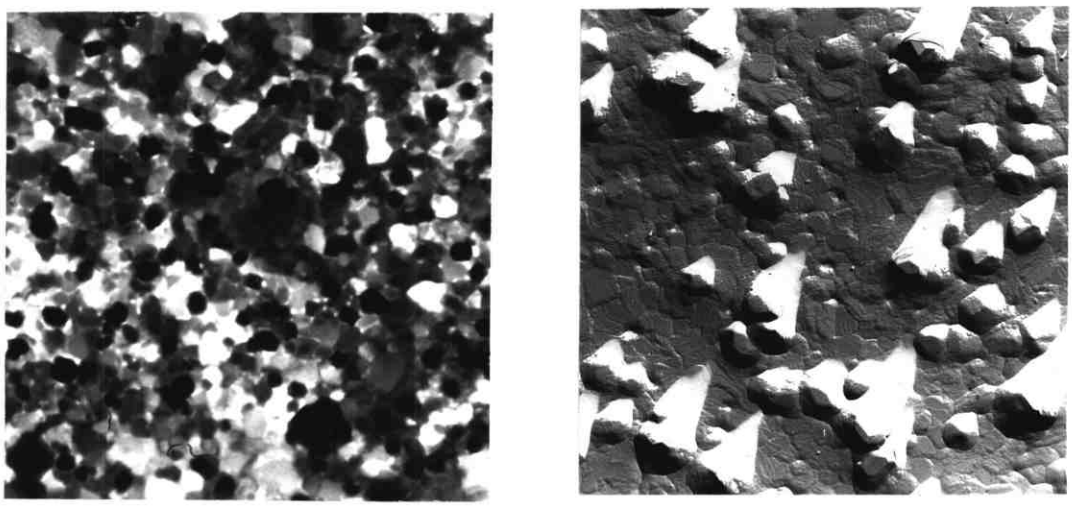

1 um thick Al film deposited at 1 nm s^{-1} onto SiO_2 at 295 K:
(a) transmission electron micrograph;
(b) 15° carbon/platinum replica.

FIGURE 7.26

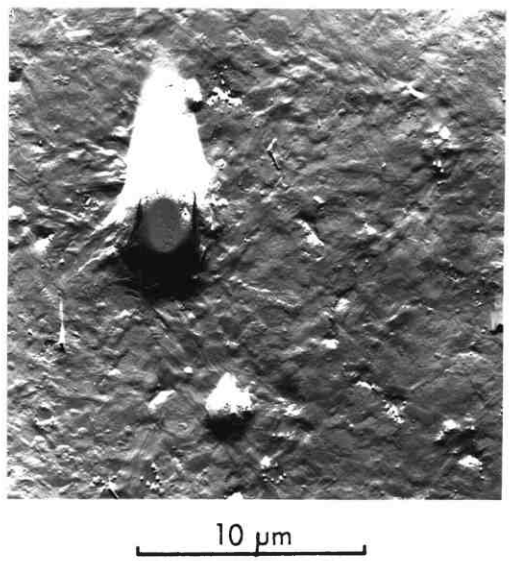

15° carbon/platinum replica showing annealing hillocks in a 1 um thick Al film deposited at 10 nm s^{-1} onto SiO_2 at 475 K, then heated in-vacuo for 2 hours at 700K.

FIGURE 7.27

the deposition rate had negligible effect on the grain size or topography of films deposited at 625 K.

A 2 hour anneal at 700 K produced considerable reconstruction in films deposited at 475 K (figure 7.19d). The mean grain size increased from 0.7 μm to 1.6 μm and the standard deviation of the lognormal distribution increased from 0.47 to 0.61 (figures 7.21 and 7.22d). The initially smooth, fairly reflective surface of the film developed hillocks of up to 2 μm base diameter and 1 μm height and became milky in appearance. Unlike the growth hillocks described above, these annealing hillocks tended to be of rounded shape (figure 7.27).

All of the 1 μm films gave grazing incidence x-ray diffraction patterns consisting of short arcs, indicative of a strongly preferred orientation (figures 7.28). Comparison with figure 7.4 shows the orientation to be a ⟨111⟩ fibre texture normal to the substrate plane. The diffraction patterns from the films deposited at 675 K were spotty because of the large crystallite size, whereas the small-grained films deposited at 475 K gave diffraction patterns consisting of "continuous" arcs. The pattern of well defined spots superposed on the aluminium diffraction pattern is due to diffraction by the underlying layer of single crystal silicon.

7.4.6 The Microstructure of 1 μm-Thick Electron-Beam Deposited Films

Films deposited at 10 nm s^{-1} onto SiO_2 substrates at 625 K had a mean grain size of 1.5 μm (compared to 3.0 μm for films deposited under similar conditions by tungsten-filament evaporation). The films had a milky appearance and shadowed-replicas revealed deep grain boundary grooves and growth hillocks of 500 nm diameter and 25 nm height with a density of $1 \times 10^{10} m^{-2}$. A strong ⟨111⟩ fibre texture was identified by grazing incidence x-ray diffraction.

7.4.7 The Microstructure of Sputter-Deposited Aluminium and Al-Si Films

A 0.5 μm film of pure aluminium sputter-deposited onto SiO_2 at 295 K had

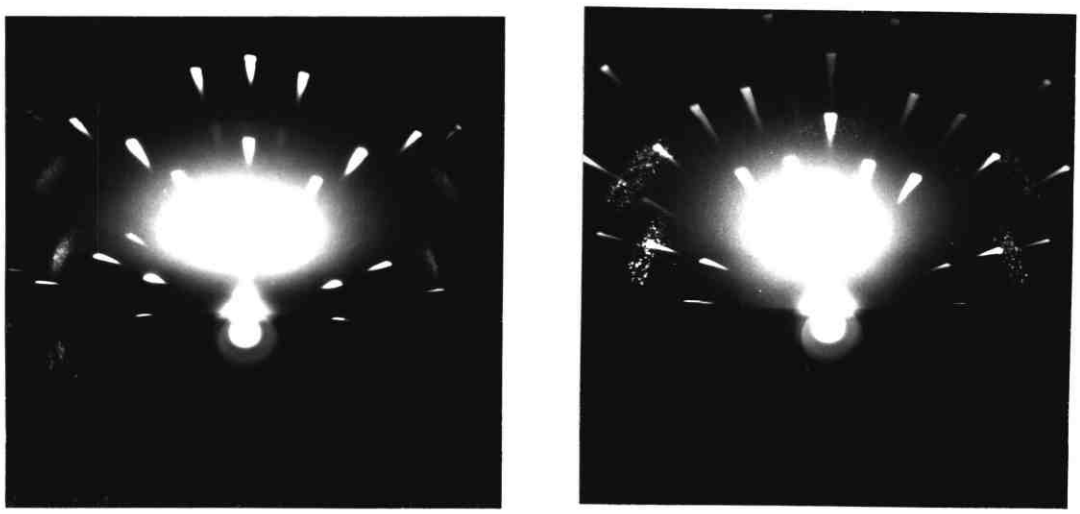

(a) (b)

(c)

Grazing incidence x-ray diffraction patterns from 1 um thick Al films deposited at 10 nm s^{-1} onto amorphous SiO_2 at temperatures of:

(a) 475 K;

(b) 675 K;

(c) 475 K, then annealed in vacuo for 2 hours at 700 K.

FIGURE 7.28

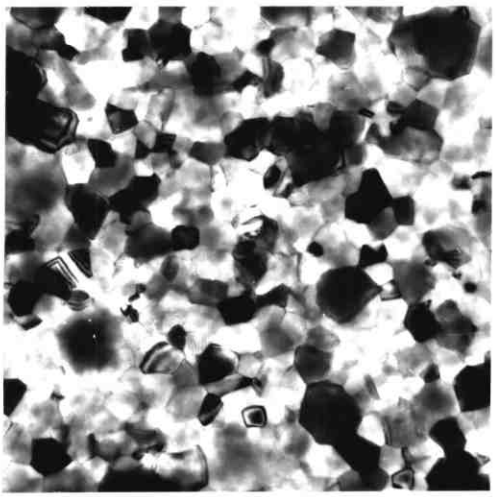

(a)

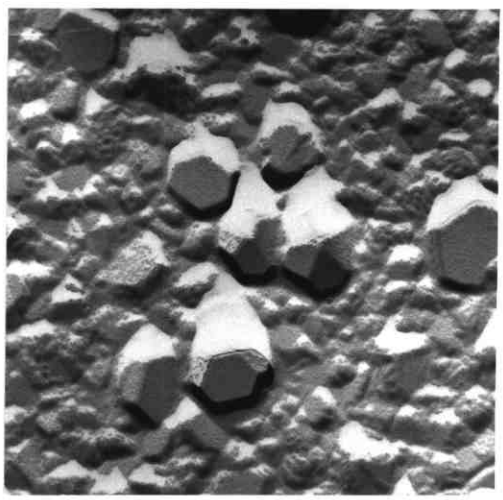

(b)

1 μm

500 nm thick pure Al film sputter-deposited onto amorphous SiO_2 at 295 K:
(a) transmission electron micrograph;
(b) 15° carbon/platinum replica.

FIGURE 7.29

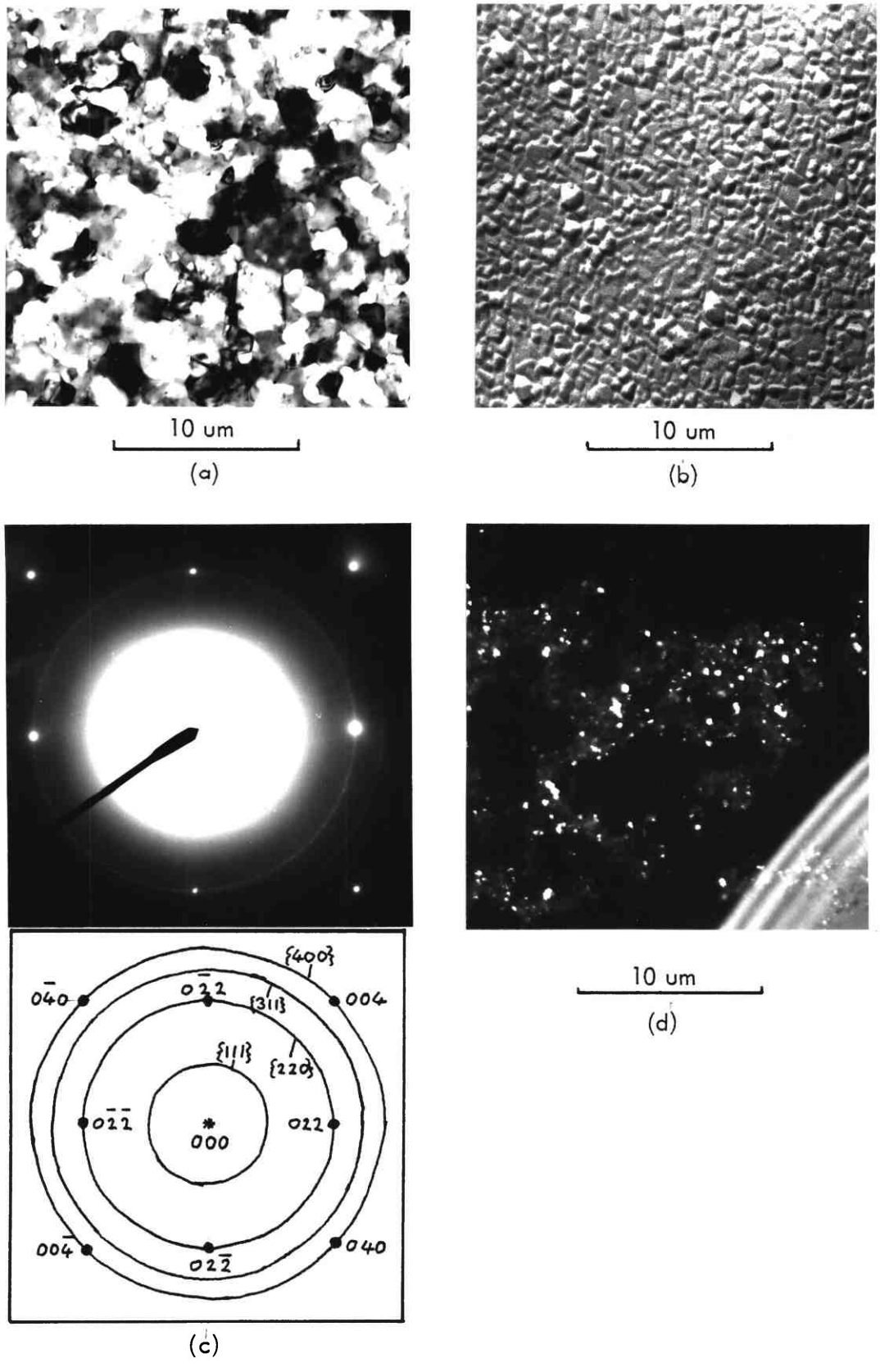

500 nm thick Al-1.5% Si film, sputter-deposited onto amorphous SiO_2 at 295 K:
(a) and (b) transmission electron micrograph and 15° carbon/platinum replica of the as-prepared film;
(c) and (d) transmission electron diffraction pattern and micrograph of the residual silicon, after chemical removal of the aluminium.

FIGURE 7.30

a mean grain size of 150 nm. The transmission electron micrograph showed evidence of "overlapping" of the grains, suggesting that the film consisted of more than one layer of crystallites (figure 7.29a). The surface had a high density ($\sim 1 \times 10^{12} m^{-2}$) of growth hillocks, as shown in figure 7.29 b. These hillocks were largely hexagonal in form and had diameters of around 250 nm and heights of 50 nm. No preferred orientation was detected by transmission electron diffraction.

A 0.5 μm film of Al - 1.5% Si deposited under identical conditions consisted of a disordered aggregate of overlapping small grains of mean diameter around 100 nm, as shown in figure 7.30 a. The surface was rough on a scale of 50 nm, but no large hillocks of crystallographic form were observed (figure 7.30 b). The electron diffraction pattern indicated a weak ⟨111⟩ fibre texture in the aluminium, but no diffraction pattern from the silicon was visible. However, when the aluminium film was dissolved in 50% HCl, the specimen gave a diffraction pattern consisting of Debye rings from polycrystalline silicon, as shown in figure 7.30 c. (The spots are due to the underlying single crystal silicon at the edges of the thinned region of the specimen). Dark field imaging using the {220} ring revealed particles of silicon of ~15 nm diameter (figure 7.30 d).

7.5 Summary and Discussion

Aluminium deposited by tungsten-filament evaporation onto amorphous SiO_2 at temperatures between 295 K and 625 K was seen to follow the Volmer-Weber growth mode (see section 6.2) as reported by d'Heurle et al (1968). In the initial stages of film formation, the deposit consisted of randomly distributed single crystal islands. With continued deposition, growth of the islands occurred, followed by coalescence to form a polycrystalline network. Nucleation on the clear areas of the substrate continued, and these secondary islands became incorporated in the growing network

until a continuous film was produced.

The thickness at which complete coverage was attained was found to increase with increasing substrate temperature (i.e. decreasing supersaturation). Al - SiO_2 reaction is thought to be responsible for the relatively small film thickness required for continuity. For deposition at 475 K, films were found to attain continuity at a thickness of 500 nm, in good agreement with the value of 400 nm reported by d'Heurle et al (1968).

7.5.1 Grain Growth

Continuous films were composed of columnar grains which tended to be equi-axed in the film plane (thus minimizing the grain boundary area and grain boundary energy) and were predominantly six sided. The distribution of grain sizes was log-normal, as reported by Attardo et al (1971). The grain size was found to increase with film thickness and deposition temperature. Grain growth was rapid in the initial stages of film formation, becoming slower as the thickness increased. Changes in deposition temperature between 295 K and 475 K had only a small effect on the grain size. However, grain size was very temperature sensitive in the range 475 K - 675 K. This observation contradicts d'Heurle's result (grain size is temperature independent in this range), but is consistent with the exponential temperature dependence predicted by theory.

At the onset of coalescence, the grain size is determined by the size of the islands (which increases with temperature). When crystallites come into contact, however, grain boundary movement can occur, resulting in grain growth. The driving force for this process is the minimization of grain boundary energy. Atoms arriving at the surface of the film from the vapour phase are highly mobile and thus easily incorporated into the growing grains, giving the observed rapid grain growth. During post-deposition annealing, however, the energy available is due solely to the specimen

temperature and grain growth proceeds more slowly, as observed.

Grain growth in a 2-dimensional film may be analyzed using the model of Pearmain and Dorey (1967). Consider a film of uniform thickness composed of columnar hexagonal grains of side r_o (figure 7.31). The area of the hexagonal face of each grain is given by :

$$A_o = 3\sqrt{3}\ \frac{r_o^2}{2} \tag{7.2}$$

and the perimeter of the grain by :

$$L_o = 6 r_o \tag{7.3}$$

The grain boundary length per unit area of the film is therefore :

$$\lambda = \frac{L_o}{2 A_o} = \frac{2}{r_o \sqrt{3}} \tag{7.4}$$

Now consider a hexagonal grain of side r growing into the film. Let its area increase from A to $A + \delta A$ as r increases to $r + \delta r$.

From (7.2) : $$\delta A = 3\sqrt{3}\ r\, \delta r \tag{7.5}$$

and from (7.4) the decrease in the grain boundary length of the surrounding film is :

$$\lambda \delta A = 6 r \frac{\delta r}{r_o} \tag{7.6}$$

The increase in grain boundary length of the expanding grain is :

$$\delta L = 6\, \delta r \tag{7.7}$$

From equations (7.6) and (7.7) the net increase in grain boundary length is

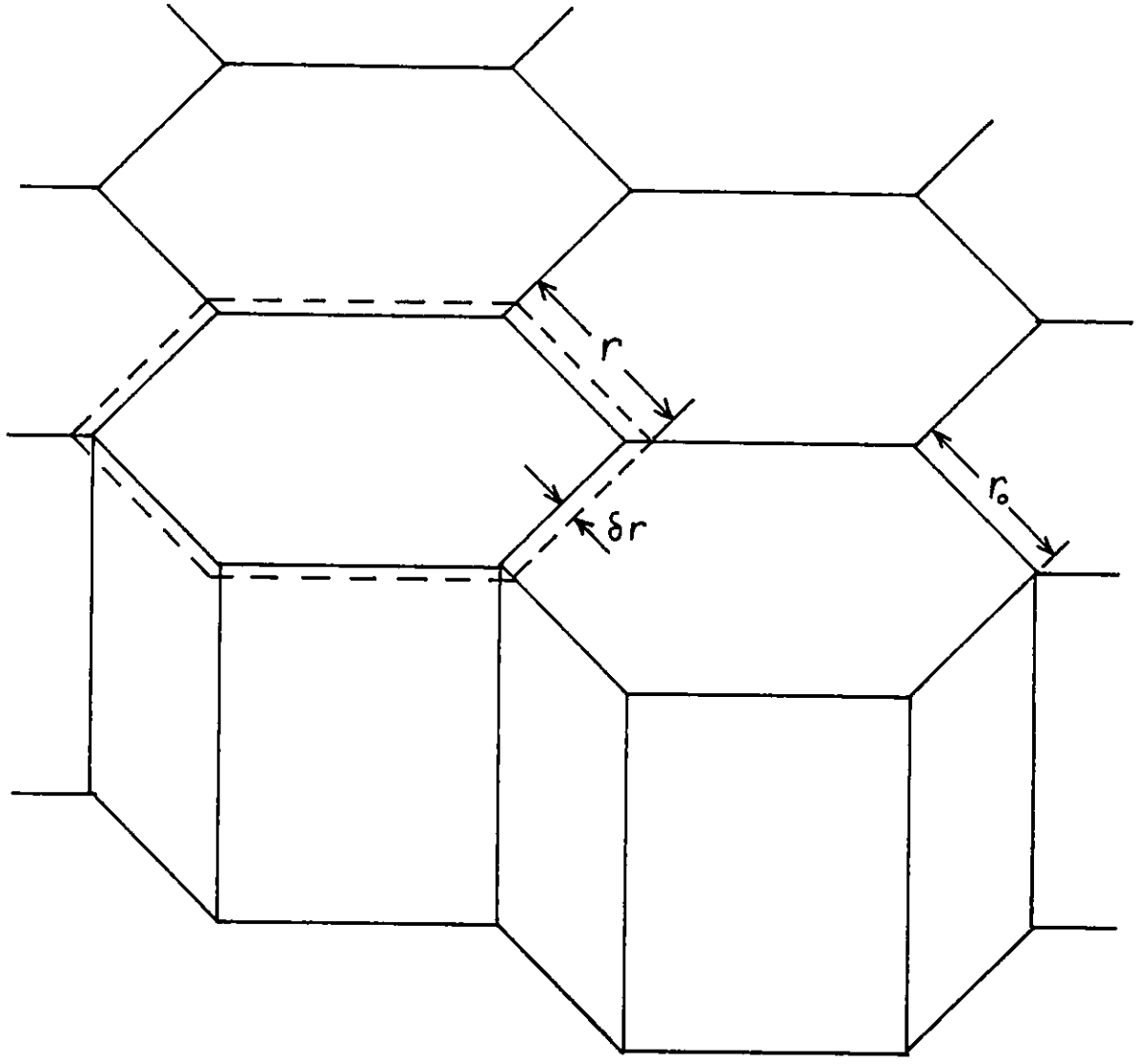

Grain growth in a thin film composed of hexagonal columnar grains.

FIGURE 7.31

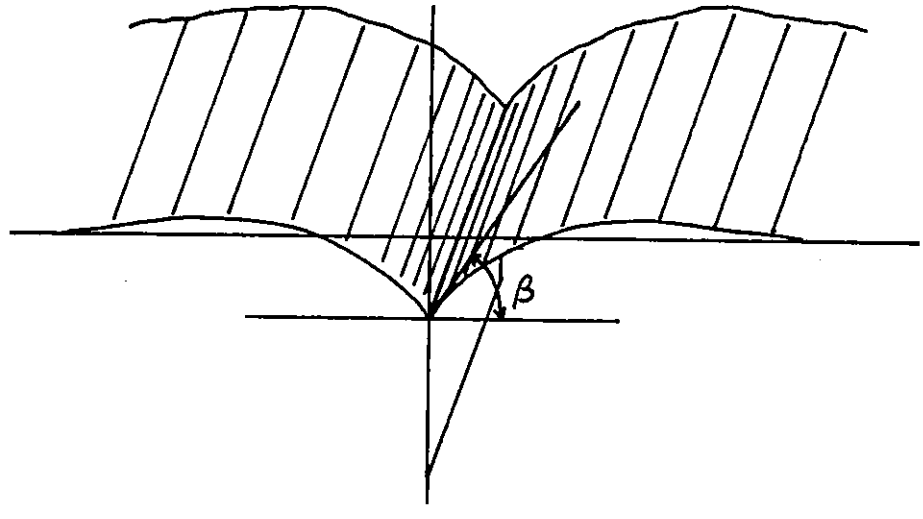

Section showing profile of an ideal thermal groove (vertical exaggeration ~ 5x).

FIGURE 7.32

$$\delta L - \lambda \delta A = 6\delta r\left(1 - r/r_o\right) \qquad (7.8)$$

If the grain boundary energy per unit area is γ_b and there are N atoms per unit area, then the net increase in energy is :

$$\delta E = \frac{\gamma_b}{N}\left(\frac{1}{r} - \frac{1}{r_o}\right)\delta r \text{ per atom} \qquad (7.9)$$

If $r > r_o$, then δE is negative and the grain will grow. Large grains therefore grow at the expense of small ones.

The force on each grain boundary atom is given by :

$$F = -\frac{dE}{dr}$$

$$= \frac{\gamma_b}{N}\left(\frac{1}{r_o} - \frac{1}{r}\right) \qquad (7.10)$$

Now the mobility of a boundary atom is :

$$M = \frac{D_m}{kT} \qquad (7.11)$$

and the diffusion coefficient is given by :

$$D_m = D_o \exp\left(-\frac{Q_m}{kT}\right) \qquad (7.12)$$

where Q_m is the activation energy for grain boundary migration, T is the temperature and k is Boltzmann's constant.

The velocity of the boundary atom is given by the product of the force and the mobility :

$$\text{i.e. } \frac{dr}{dt} = \frac{D_m}{kT}\,\frac{\gamma_b}{N}\left(\frac{1}{r_o} - \frac{1}{r}\right) \qquad (7.13)$$

If the surrounding grains expand at the same rate as the grain being considered, then

$$r_o = C r \tag{7.14}$$

Hence,

$$\frac{dr}{dt} = \frac{D_m \gamma_b}{kTN} \left(\frac{1-C}{C}\right) \frac{1}{r} \tag{7.15}$$

The observation that in a growing film the rate of grain growth falls off with increasing grain size is in qualitative agreement with equation (7.15).

Integrating equation (7.15) we obtain :

$$r_f^2 - r_i^2 = \frac{D_m \gamma_b}{kTN} \left(\frac{1-C}{C}\right) (t_f - t_i) \tag{7.16}$$

where i and f denote initial and final values respectively.

1 μm films subjected to a post-deposition anneal at 700 K for 2 hours suffered an increase in grain size from 700 nm to 1.6 μm. Therefore, high temperature processes in device production such as "sintering" may substantially affect the grain size of aluminium metallizations.

Taking the value of Q_m as 1.2 eV (Nowak 1976), application of equations 7.12 and 7.16 shows that at a temperature of 450 K, for example, the increase in grain size over a period of 10,000 hours would be approximately 100 nm. Therefore, during accelerated electromigration life testing or normal device operation (in which the temperature is usually much less than 450 K) grain growth should be negligible.

7.5.2 Surface Topography

The surface roughness of evaporated aluminium films was found to be dependent upon thickness, substrate temperature, deposition rate and vacuum. Films deposited at 10 nm s^{-1} under high vacuum conditions onto substrates at room temperature began to develop growth hillocks at a mean thickness of ~20 nm. The average size of the

hillocks increased with film thickness. Many hillocks had flat hexagonal tops which are thought to be the $\{111\}$ faces of truncated octahedra (the equilibrium form of most f.c.c. metals). This indicates that a large proportion of the hillocks had a $\langle 111 \rangle$ axis normal to the film plane. The growth hillocks appeared to correspond to single grains of above average height.

The temperature of the films during "room temperature" deposition never rose above 350 K. It therefore seems unlikely that the growth hillocks were caused by thermal stress in the film. They were more probably due to the preferential condensation of vapour atoms on certain crystallographic planes (e.g. $\{111\}$ planes) as discussed by Bauer (1964). The steps or wrinkles seen within some grains are thought to be of the same origin. The absence of growth hillocks in films deposited at 475 K and above supports this conclusion, since thermal stresses are much higher in these films. The absence of hillocks at high temperatures may be a result of the higher mobility of the adatoms which enables them to migrate so as to form a flatter surface, thus minimizing the surface free energy.

Films deposited at higher temperatures exhibited deep grain boundary grooves. These grooves develop in order that the surface and grain boundary tensions balance along the line of intersection of the boundary with the surface (figure 7.32). The equilibrium angle is given by :

$$2\gamma_s \sin\beta = \gamma_b \qquad (7.17)$$

where γ_s and γ_b are respectively the surface and grain boundary free energies per unit area. The rapid establishment of the equilibrium angle by atomic diffusion in the localized region of intersection produces sharp ridges on each side of the boundary. These ridges then flatten by preferential evaporation or surface diffusion, thus upsetting the equilibrium angle and causing the groove to deepen (Mullins 1957).

Annealing at 700 K produced hillocks in 1 μm films deposited at 475 K. These annealing hillocks were of different form to the growth hillocks, having a rounded shape with no obviously crystallographic features. They are believed to be the result of thermally induced stress, as discussed in section 6.3.4.

The use of low deposition rates or poor vacuum conditions was found to enhance hillock growth in films deposited at room temperature. This effect may be due to interaction between the ambient gases (particularly water vapour and oxygen) and the growing film, as suggested by Reicha and Barna (1980). At higher substrate temperatures the deposition rate or residual gas pressure had negligible effect on the topography, maybe as a result of the reduced sticking coefficient for water vapour and oxygen.

A definite correlation was observed between the surface topography of films and their appearance to the naked eye. Films appeared highly reflective if the scale of the surface roughness was less than the wavelength of visible light ($\sim$400 nm). Therefore, films with a high density of small hillocks were reflective, whereas hillock-free films having a large grain size and pronounced grain boundary grooves had a milky appearance.

7.5.3 Preferred Orientations

In the early stages of film formation, no preferred orientation was detected in any of the films examined. Therefore, the $\langle 111 \rangle$ nucleation orientation reported for some f.c.c. metals on amorphous substrates (section 6.2.5) is not present in aluminium on SiO_2. This may be due to the $Al - SiO_2$ reaction decreasing the mobility of aluminium atoms on the surface and increasing the nucleation density for islands of all orientations.

With continued deposition, a $\langle 111 \rangle$ fibre orientation appeared. The thickness at which this orientation became apparent was found to increase with deposition temperature, and no fibre texture was observed in any film before 100% coverage had

been attained. The strength of the fibre texture increased initially with film thickness and became constant at thicknesses of several hundred nanometres. Post-deposition annealing did not affect the orientation.. It is suggested that the ⟨111⟩ fibre texture is an initial growth orientation resulting from the lower interfacial free energy of crystallites which have ⟨111⟩ planes parallel to the substrate. Similar orientations have been reported for other systems, for example Cd Te on Pyrex (Goldstein and Pensak 1959). It is unlikely that the ⟨111⟩ fibre texture is a final growth orientation (due to preferential condensation) as there seems to be no correlation between the occurrence of the fibre texture and the presence of surface roughness (e.g. growth hillocks). An investigation into the effects of oblique vapour incidence would help to resolve this uncertainty.

7.5.4 Electron-Beam and Sputter-Deposited Films

Electron-beam deposited films had a similar microstructure to tungsten-filament evaporated films prepared under the same nominal conditions. Variations between the precise values of substrate temperature, deposition rate and residual gas pressure for the two processes may account for the smaller grain size and higher hillock density of the e-beam deposited films. Further experiments are required to evaluate the importance of these parameters in the case of e-beam deposition and to investigate the effects of planetary motion of the substrate during deposition.

Sputter deposited films of pure aluminium had a much smaller grain size than evaporated films and had no fibre texture. The addition of 1.5% silicon suppressed hillock growth in these films and promoted a ⟨111⟩ fibre texture. Particles of silicon were observed after chemical removal of the aluminium, but silicon could not be detected in the Al - Si film by electron microscopy and diffraction.

A detailed investigation of the early growth stages of sputter-deposited aluminium and Al - Si films may further the understanding of the differences between these and

evaporated films.

7.6 Conclusions

i) Evaporated aluminium films on amorphous SiO_2 follow the Volmer-Weber (island) growth mode.

ii) Continuous films have a log-normal grain size distribution.

iii) The mean grain size increases with deposition temperature slowly in the range 295 K to 475 K and rapidly in the range 475 K to 675 K.

iv) Post-deposition annealing causes grain growth but the process is slow at temperatures of 450 K or less.

v) Growth hillocks are suppressed by the use of high deposition temperature ($\gtrsim$ 475 K), high deposition rate and good vacuum conditions.

vi) All evaporated 1 μm thick aluminium films have a strong $\langle 111 \rangle$ fibre texture.

vii) Electron-beam deposited films are very similar in structure to filament-deposited films.

viii) Sputter-deposited films are characterized by a small grain size and a random orientation.

CHAPTER 8

A REVIEW OF ELECTROMIGRATION

8.1 Introduction

Electromigration (or electrotransport) is the name given to the motion of atoms which results from the passage of a direct electric current through a conducting material. Electromigration in liquid alloys was first reported by Gerardin in 1861. After electrolysis in the molten state, lead-tin alloys were found to become brittle near one electrode and soft near the other, and sodium-mercury alloys were found to decompose water at one end only. These effects were attributed to motion of the metal ions in the applied electric field, as in the electrolysis of molten salts.

Electromigration takes place much more slowly in solid metals than in liquid metals and for a number of years it was thought that the phenomenon did not occur at all in solids. However, in the early 1930's, several experimentalists demonstrated electromigration in solid metals by using sufficiently high current densities and temperatures.

Later experiments (e.g. those of Seith and Wever 1953 and Wever and Seith 1955) showed that the direction of mass transport in certain binary alloys was dependent upon the composition. The effect was thought to be associated with a modification of the band structure involving a change from electron to hole conduction. Seith suggested that momentum transfer between the conduction electrons and the ions might provide the major part of the driving force for electromigration. (The idea was originally proposed by Skaupy in 1914). Wever extended the study to self-electromigration in pure copper in 1956. He observed the motion of scratches on the surface of specimens carrying a current density of 2×10^8 A m^{-2} over a period of one or two days. At temperatures below 1,225 K the scratches moved towards the cathode, corresponding to

mass transport towards the anode. It was concluded that at these temperatures momentum transfer from the conduction electrons was responsible for electromigration. At higher temperatures the direction of mass flow was reversed.

Early studies of electromigration were mainly of purely academic interest, such as the study of the interaction between point defects and charge carriers, though electromigration has been put to practical use as a method of purification and isotope separation in molten metals. The most important practical implications of electromigration, however, have been in the field of reliability. Johnson (1938) found that tungsten lamp filaments powered by direct current developed stepped surfaces while a.c.-powered filaments retained smooth surfaces. The steps, which could lead to thinning and failure of the filament, were attributed to electromigration along the surface of the filament.

In 1966 Blech and Sello identified many of the open-circuit failures of aluminium contact metallizations as being due to electromigration damage. The efficient heat sinking of these thin film metallizations permits operation at current densities much greater than those encountered in "bulk" conductors, and electromigration is consequently relatively rapid. Most of the recent interest in electromigration has been stimulated by the need for more reliable thin film metallizations and though much progress has been made, electromigration continues to be a problem as the scale of device geometries is reduced.

In this chapter the various theories of electromigration in solid metals are outlined, and the experimental approaches to bulk and thin film electromigration studies are briefly described. The nature of electromigration damage in thin film metallizations is then discussed, with consideration of both the microscopic damage mechanisms and the statistical aspects of failure. The scope of this chapter is necessarily limited, and emphasis is placed on electromigration failure in pure aluminium metallizations. The excellent review papers by d'Heurle and Rosenberg (1973) and d'Heurle and Ho (1978)

cover some other aspects of electromigration damage, including alloying effects and electromigration in other pure metals, while Verhoeven (1963) reviews the early theoretical developments.

8.2 Theory

A metal can be considered as an array of positive ions in a "fluid" of conduction electrons. The charge on each ion is equal to Ze where Z is the valence and -e is the charge on the electron. If screening by the conduction electrons can be neglected, in an electric field E the ions experience an electrostatic force of magnitude

$$F_E = Z e E \qquad (8.1)$$

directed towards the cathode. Huntington (1975) claims that screening by the conduction electrons does not affect the electrostatic force experienced by the ion, since the ion's motion does not cause any net displacement of the electronic fluid. Early theories, such as those due to Wagner (1933) considered electromigration as a result of the electrostatic interaction only, and hence gave poor agreement with experiment.

In 1959 Fiks constructed a theory of electromigration which took into account both the electrostatic and "frictional" or "electron wind" forces. The latter force is calculated by considering the collisions between the conduction electrons and a moving ion. The conduction electrons are treated as being free, and in each collision the electron is assumed to lose all the additional momentum which it gained during acceleration in the electric field since the previous collision. This momentum is equal to $e E \tau$ where τ is the mean time between collisions and is equal to the mean free path l, divided by the mean drift velocity v. The number of collisions per unit time is equal to $n v \Sigma$ where n is the number density of conduction electrons, and Σ is the scattering cross section of ions for electrons. The frictional force on an ion is hence

given by :-

$$F_f = -eE\ell n\Sigma \qquad (8.2)$$

The minus sign indicates that the frictional force is opposed to the electrostatic force. The resultant force F on an ion is therefore given by :-

$$F = eE(1 - n\ell\Sigma) \qquad (8.3)$$

The frictional force experienced by an ion varies over the diffusion jump, being a maximum at the saddle point and a minimum at each lattice site. The potential barrier for an ion making a diffusion jump is reduced in the direction of the resultant force and increased in the opposite direction, thus causing a net flow of ions. The direction of the mass flow depends on the relative magnitudes of the electrostatic and frictional components of the driving force. Experiment shows that for simple electron conductors, such as sodium, electromigration proceeds towards the anode, indicating that the frictional force is dominant.

A similar theoretical model was put forward by Huntington and Grone in 1961. Electrons are again assumed to be scattered only by defects in the crystal lattice, which can be vacancies or interstitials. (Self electromigration in a pure metal is thought to occur by a vacancy mechanism). These defects are assumed to be decoupled from the lattice, resulting in scattering without the creation or annihilation of phonons. The rate of momentum transfer from the conduction electrons to the ions is calculated using a quantum mechanical argument in which the electron momentum is expressed as the electron rest mass m_o multiplied by the group velocity of the Bloch wave v_g. The frictional force on each defect is thus found to be :-

$$F_f = -\frac{m_o j}{N_d e \tau} \qquad (8.4)$$

where j is the electric current density. Equation (8.4) is equivalent to equation (8.2) derived by Fiks. The collision time τ can be expressed in terms of the defect contribution to the electrical resistivity ρ_d, using the equation :-

$$\rho_d = \frac{|m^*|}{n e^2 \tau} \qquad (8.5)$$

where n is the number density of electrons and m* is the effective mass of the conduction electrons. Equation (8.4) may thus be rewritten :-

$$F_f = -\frac{n e j \rho_d m_o}{N_d |m^*|} \qquad (8.4a)$$

Replacing j by the electric field E divided by the total resistivity ρ and n by the number density of ions N times the valency Z, Huntington obtains :-

$$F_f = -eEZ \frac{N \rho_d}{\rho N_d} \frac{m_o}{|m^*|} \qquad (8.6)$$

Since this equation contains only the <u>modulus</u> of the effective mass, the direction of electromigration is independent of the band structure, contrary to experimental evidence. A modified version of the theory (Huntington and Ho 1963) uses the pseudo-momentum (i.e. the momentum of the electron plus lattice) $\hbar k$ instead of $m_o v_g$, with the result that the direction of the frictional force depends on the sign of the effective electron mass :-

$$F_f = -eEZ \frac{N \rho_d}{\rho N_d} \frac{m^*}{|m^*|} \qquad (8.7)$$

The density of conduction electrons is of the order of 10^{29} m^{-3} and their average velocity is around 10^6 m s^{-1}. Hence, for a defect with a collision cross section of 10^{-19} m^2 the rate of collisions is approximately 10^{16} s^{-1}. Because the exclusion

principle limits scattering to those electrons near the Fermi surface, only a fraction ($\sim 1\%$) of collision gives rise to scattering. Since the time required for an ion moving at thermal velocity to travel one lattice distance is around 10^{-13}s, it appears that an ion experiences approximately 10 scattering events during a lattice diffusion jump. The effect of electron-ion collisions may therefore be approximated by a continuous force on the ion.

The variation of the frictional force along a jump of length a in direction y is assumed to be :-

$$F_f(y) = F_o \sin^2(\pi y/a) \qquad (8.8)$$

The potential barrier for the lattice jump is thus increased in one direction and reduced in the other direction by an amount

$$\Delta Q_j = \int_o^{\frac{1}{2}a_j} F_f(y)\, dy$$

$$= \frac{1}{4} a_j F_o \cos\theta_j \qquad (8.9)$$

where θ_j is the angle between the jump and the direction of the frictional force. The net flow of ions caused by electron collisions is thus given by :-

$$J_f = \sum_j c\nu_o \exp\left(\frac{-Q}{kT}\right) a_j \cos\theta_j \sinh\left(\frac{\Delta Q_j}{kT}\right) \qquad (8.10)$$

where ν_o is the frequency of atomic vibrations, c is the concentration of ions in the metal, Q is the activation energy for vacancy diffusion and $\sum_j$ represents the summation over all possible jumps.

J_f can be expressed in terms of an uncorrelated diffusion coefficient :-

$$J_f = c\, D_o \exp\left(-\frac{Q}{kT}\right) \frac{F_o}{2kT} \tag{8.11}$$

where $$D_o = \frac{1}{2} \nu_o \sum_j a_j^2 \cos\theta_j \tag{8.12}$$

Equation (8.11) differs from the Nernst-Einstein relation only in the factor of 2 in the denominator, which results from the averaging of the frictional force over the jump length.

Huntington expressed the total force on the moving ion, resulting from both the electrostatic and frictional contributions, as Z*eE. eZ* is the "effective charge" given by :-

$$eZ^* = eZ \left\{ 1 - \frac{1}{2} \frac{\rho_d N}{N_d \rho} \frac{m^*}{|m^*|} \right\} \tag{8.13}$$

Although this terminology is commonly used in the literature, it is felt by the author to be misleading as the terms "effective charge" or "effective valency" when used in this context have no bearing on the actual charge associated with the moving ion. The terms merely indicate the magnitude and direction of the resultant force on a moving metal ion in an applied electric field. The resultant flux of ions due to the electrostatic and "frictional" forces is given by :-

$$J_t = c \frac{D_o}{kT} \exp\left(-\frac{Q}{kT}\right) Z^* e E \tag{8.14}$$

The velocity v of a marker in a metal specimen is related to the net ion flow by :-

$$v = \alpha \frac{J_t}{c} \tag{8.15}$$

where $\alpha \leq 1$ takes into account changes in the dimensions of the sample due to the creation or annihilation of vacancies.

One serious limitation of the Fiks and Huntington approaches is the difficulty

in determining how the momentum of the scattered charge carriers is distributed between the "activated complex" (e.g. moving ion-vacancy) and the surrounding lattice. This problem is avoided in the theory of Bosvieux and Friedel (1962), in which the net force on a moving ion or defect resulting from polarization of the electron charge distribution is considered. The detailed quantum mechanical calculations will not be reproduced here, but qualitatively the argument is as follows. A positively charged defect perturbs the trajectories of the conduction electrons so as to increase their velocity on the cathode side of the defect and reduce the velocity on the anode side. This results in an increase in the electron charge density "downstream" from the defect and a corresponding increase "upstream". The net result is a localized electric field which tends to draw the defect towards the anode. For hole conduction the resultant force acts in the opposite direction. In the case of interstitial migration, the Bosvieux and Friedel theory gives the same net force as the Huntington theory. However, for the case of vacancies and substitutional impurities, the results are somewhat different.

The theories considered so far have all been based on the free electron model for a metal. Although reasonable results were obtained for pure electron and pure hole conduction, the theories cannot be applied rigorously to metals with complex band structures. The polarization model has been developed further by Sorbello (1973) by using pseudopotential theory to determine the electron charge distribution. Real metal properties can thus be incorporated into the model, and good agreement with experimental data has been obtained.

8.3 Experiments on Single Crystals

Lattice electromigration in single crystal specimens of various pure metals has been investigated by observing the motion of markers on the specimen surface or radioactive tracers within the specimen. The marker or tracer velocities are used to determine

$D_o Z^*$ by application of equation (8.15) for the Huntington theory (or the corresponding equations for the other theories). By making measurements over a range of temperatures the activation energy for electromigration can be obtained. In order to determine Z^*, D_o must be evaluated by a separate diffusion experiment.

Gilder and Lazarus (1966) used a radio-tracer technique to investigate electromigration and self diffusion in gold single crystals. An activation energy for electromigration of 1.9 ± 0.1 eV was obtained, in good agreement with their value of 1.83 ± 0.01 eV for the self diffusion activation energy. D_o was found to be 2×10^{-5} giving a value for Z^* of -9 ± 1 at 1148 K (i.e. electromigration was towards the anode).

Electromigration in aluminium single crystals was studied by Penney (1964), using surface scratches as markers. The value of 1.4 eV obtained for the activation energy is in excellent agreement with the value of 1.4 ± 0.1 eV obtained by Spokas and Slichter (1959) in a self diffusion experiment. Penney found Z^* to be strongly temperature dependent, ranging from -12 at 1173 K to -30 at 1023 K. The above results are consistent with a vacancy model of lattice electromigration, where the activation energy is equal to the sum of the energies for vacancy formation and vacancy motion.

8.4 Experiments on Polycrystalline Thin Films

Electromigration in polycrystalline thin films differs from electromigration in single crystals in that the former is dominated by the presence of grain boundaries which may act as fast diffusion paths and vacancy sources or sinks. It is the effects of grain boundary electromigration which lead to degradation in thin film contact metallizations. There are two basic types of thin film electromigration experiment : (a) direct measurements of some parameter which can be related to the mass transport and used to determine the activation energy, diffusion coefficient, etc.; and (b) reliability studies in which the effects of certain parameters on the damage rate are investigated.

In this section, experiments of type (a) will be considered. Electromigration damage and reliability will be treated in sections 8.5 to 8.7.

8.4.1 Measurement techniques

Measurements are usually carried out at a temperature of less than half the melting point of the metal, where the lattice contribution to the mass flow is negligible. Current densities of the order of $10^{10} A\ m^{-2}$ are commonly used to provide reasonably rapid mass transport. It is imperative that the temperature distribution along the specimen (usually in the form of a narrow stripe with large end pads) is uniform. The sample geometry and film-substrate adhesion must therefore be carefully controlled. The precise dimensions of the stripe must also be known in order to determine the current density, and ideally all specimens should have the same grain structure.

The most direct method of measuring the electromigration parameters of thin films is the radioactive tracer technique employed by Sun and Ohring (1976) and Tai and Ohring (1977). Samples were prepared by first evaporating approximately 400 nm of the metal through a mask to form a stripe on a glass substrate. A narrow band of the tracer isotope was then evaporated across the stripe and annealed for a sufficient time for it to diffuse into the metal film. The specimen was then subjected to the required temperature and current density for a fixed period. Motion of the band of tracer was detected either by use of a specially constructed scanning scintillation counter or by a technique of autoradiography in which the radiotracer formed its own image on a photographic plate. The technique has apparently been applied successfully only to gold and tin films because of the availability of suitable isotopes. The results are relatively easy to interpret as they yield the drift velocity directly. The same specimen geometry can also be used to study self diffusion in thin films.

Another method of measuring the drift velocity makes use of a thin film stripe of

the metal on a substrate of high resistivity (see figure 8.1). When a voltage is applied the current is constrained to flow through the sample stripe because of its low resistivity. Electromigration causes metal to be depleted from one end of the stripe and accumulated at the other. The motion of the end of the stripe is measured by optical microscopy and the drift velocity hence determined. This technique has been used by Blech and Kinsbron (1975) to study electromigration in gold films on molybdenum substrates and by Blech (1976) to study aluminium films on titanium nitride.

Measurement of the amount of mass accumulation or depletion in a conventional conducting stripe has also been used to investigate electromigration in thin films. The passage of a direct current usually results in the formation of hillocks and/or voids in the film due to divergence of the mass flux at certain structural defects (see section 8.5.2). However, in the absence of such effects a more uniform thickness change occurs. The total amount of mass accumulation or depletion is equal to the net mass transport and can be determined by measurement of the total volume of hillocks or voids. Several methods have been adopted. Blech and Meieran (1969) used transmission electron microscopy to record void formation in an in-situ experiment. A 300 nm aluminium film was evaporated onto oxidized silicon and photolithographically processed to form a stripe 25 μm wide and 280 μm long on a 3 mm square die. A hole was etched in the silicon through a mask, to leave the central area of the test stripe suspended on a 100 nm layer of SiO_2 (see figure 8.2). The sample was held in a specially constructed holder in the electron microscope and direct current was passed along the stripe. Joule heating caused the temperature of the suspended region of the stripe to rise, while the ends remained near ambient temperature. This temperature profile caused void formation near the cathode, and hillock and whisker growth near the anode (see section 8.5.1). The total volume of voids was determined from electron micrographs and the mean drift velocity was taken to be the rate of increase of the void volume divided by the

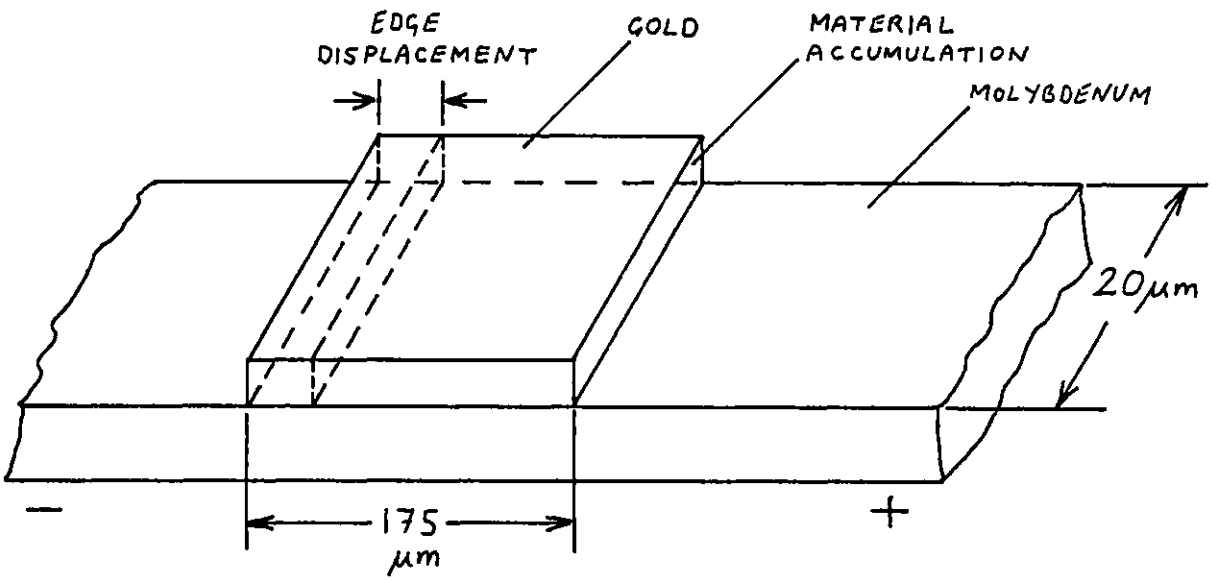

Sample configuration used by Blech and Kinsbron(1975) to measure drift velocity in thin gold films.

FIGURE 8.1

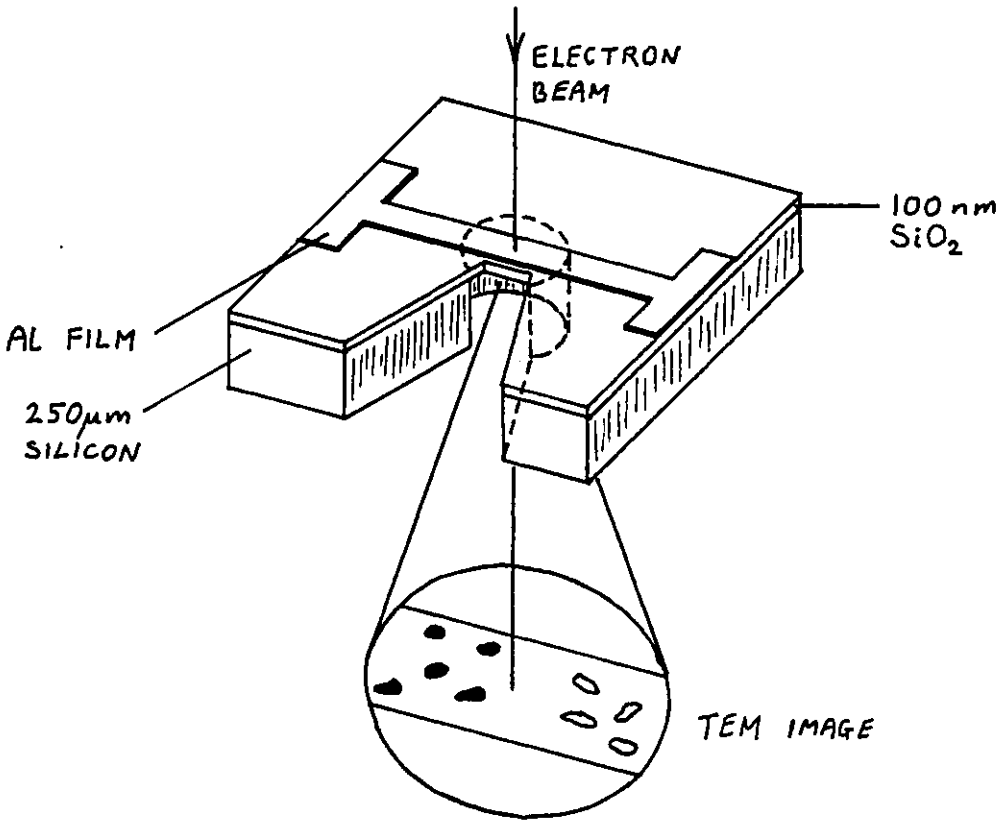

The sample configuration in the in-situ TEM experiment of Blech and Meieran (1969).

FIGURE 8.2

cross sectional area of the stripe.

Rosenberg (1970) used scanning electron micrographs to measure void and hillock growth in aluminium films. This technique does not necessitate thinning of the wafer, and hence gives a more even temperature distribution along the test stripe. Weise (1972) determined the mass distribution along a 1 μm thick aluminium test stripe on a thinned silicon substrate by measurement of the transmitted intensity of a scanning high energy electron beam. He detected local thickness variations (i.e. voids and hillocks) superimposed on an overall redistribution of mass from the cathode to the anode. Mass accumulation or depletion measurements can be used to determine the activation energy for electromigration in thin films and the product $D_o Z^*$. The effective charge and the diffusion coefficient cannot, however, be determined individually.

During the passage of direct current through a test stripe, the electrical resistance is seen to change with time. Such changes can be caused by mass accumulation and depletion or by changes in the film microstructure. Hummel et al (1976) found that in the early stages of electromigration the resistance changes resulted only from small changes in thickness along the stripe due to localized flux divergences. In this regime the mean drift velocity was shown to be given by :-

$$\bar{v} = \frac{\Delta R}{R_o} \frac{L}{t} \qquad (8.16)$$

where $\Delta R/R_o$ is the fractional change in resistance after time t and L is the length of stripe between the points of measurement. Stripes with several measurement electrodes were used so that the variation of ion velocity along the stripe could be determined (figure 8.3). The temperature at the centre of the stripe was measured by a thin film thermocouple. Activation energy can be determined either by testing several stripes at different temperatures and obtaining the drift velocity as a function of temperature, or by suddenly increasing the temperature of one test stripe and measuring the change

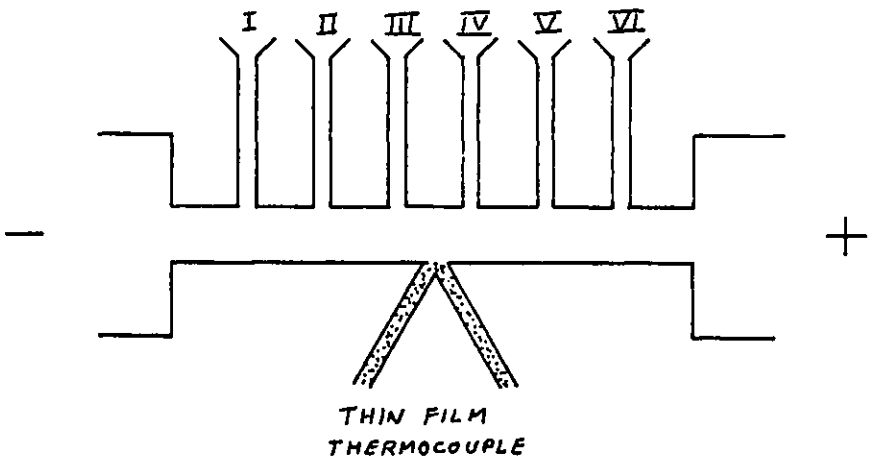

The sample configuration used by Hummel et al (1976) to measure resistance changes along a metallization stripe.

FIGURE 8.3

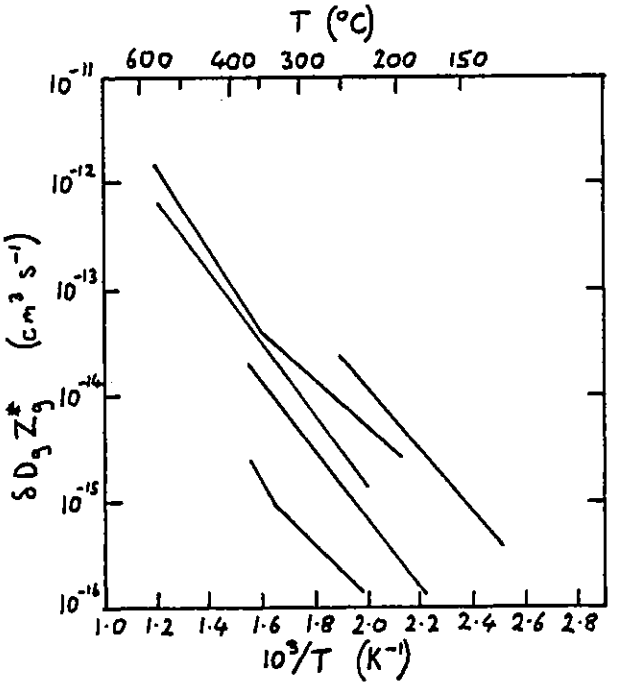

Compilation of results for electromigration in pure aluminium films by several workers (from d'Heurle and Ho 1978).

FIGURE 8.4

in slope of the resistance versus time curve. The latter method was employed by Rosenberg and Berenbaum (1968) to measure the activation energy for electromigration in aluminium films. The resistometric technique is simple to use, but it only allows the activation energy to be measured. Moreover, it is an indirect method, and its validity depends upon the correct relationship between resistance change and rate of electromigration.

Some workers have used lifetest data to obtain an "activation energy" for electromigration in thin films. The results should be treated with caution since the open circuit failure modes due to electromigration damage are complex and effects other than straightforward electromigration may be of importance (see section 8.6).

When measurements of ionic flux are used to determine the electromigration parameters of polycrystalline thin films, account must be taken of the role played by the grain boundaries. If the temperature is low enough so that lattice diffusion may be neglected (i.e. electromigration occurs solely via the grain boundaries), then equation (8.14) may be rewritten as :-

$$J_g = c_g \frac{\delta}{\bar{d}} \frac{D_g}{kT} e^{-Q_g/kT} Z_g^* e E \qquad (8.17)$$

where the subscript g refers to grain boundary parameters (which are in general different from the corresponding bulk parameters), δ is the effective grain boundary width and $\bar{d}$ is the mean grain size.

8.4.2 Results and Discussion

Measurements of electromigration in aluminium thin films have been made using most of the techniques described above. Results from a number of studies have been compiled by d'Heurle and Ho (1978), and are shown graphically in figure 8.4. The large discrepancies (up to 2 orders of magnitude) between the experimental values of $\delta D_g Z_g^*$ are thought to result from errors in temperature measurement and calibration

of the amount of mass transport and from differences between the microstructures of the various films. However, the slopes of the curves (which are proportional to the activation energy) are roughly equal. Two of the curves have an abrupt change in gradient at approximately 625 K. This is thought to indicate the onset of lattice electromigration at this temperature as the slope of the curves above 625 K gives an activation energy of around 1.4 eV. Since an independent measurement of D_g does not appear to have been made, it is not possible to separate the value of Z_g^* from the product $\delta D_g Z_g^*$. Z_g^* is known to be positive, however, as in all cases the net mass flow was towards the anode.

The activation energies for electromigration, measured by various experimentalists, are listed in table 8.1. The results are remarkably consistent, considering the wide range of experimental techniques employed. The activation energies range from 0.5 eV to 0.7 eV and are therefore roughly half of the value for lattice electromigration. These values are consistent with the hypothesis that electromigration in thin films takes place predominantly via the grain boundaries. A model for grain boundary diffusion put forward by Gifkin (1967), in which a high angle grain boundary is considered as an array of vacancy channels, predicts an activation energy between 0.7 eV and 1.1 eV for aluminium. This is in reasonable agreement with the results from electromigration experiments. It is possible that the measured activation energies for grain boundary diffusion and electromigration may differ slightly, because of the (unknown) temperature dependence of Z_g^*. A self-diffusion experiment using polycrystalline aluminium films does not appear to have been carried out.

The possible effects of surface electromigration in these thin film studies cannot be ruled out. However, radiotracer experiments using gold films have shown that the activation energies for electromigration and diffusion in the plane of the film are equal to the activation energy for diffusion normal to the film plane (Gupta et al 1973). In

Measurement Technique	Temperature Range (K)	Grain Size (μm)	Activation Energy Q (eV)	Reference
Void Growth (TEM)	453 – 623	~ 0·5	0·7 ± 0·2	Blech and Meieran (1969)
Void Growth (TEM)	633 ± 40	~ 4	0·7 ± 0·1	Berenbaum (1971)
Void Growth (TEM)	448 – 623	~ 2	0·63	Horowitz and Blech (1972)
Mass Depl-etion (SEM)	513 – 823	1	0·7	Weise (1972)
Drift Vel^{y} " "	523 – 673	1 – 1·5 single Xtal.	0·55 1·3	Blech (1976)
Resistance Change	493 – 633	~0·3 single Xtal.	0·53 1·2	Hummel et al (1976)
Resistance Change	333 – 423	?	0·5 – 0·6	Rosenberg and Berenbaum (1968)

Activation Energies for Electromigration in Aluminium Thin Films.

TABLE 8.1

the latter case the effects of surface diffusion are negligible. Hence it appears that atomic transport is dominated by the grain boundaries.

8.5 Electromigration Failure Modes

Electromigration failure in thin film metallizations rarely results from an overall thinning of the conductor due to the net flow of mass between the electrodes. Failure usually occurs as a result of void formation which increases the resistance of the conductor and eventually causes an open circuit to develop. Other electromigration failure modes include the shorting together of adjacent conductor stripes by hillocks or whiskers and the dissolution of silicon at Al-Si contacts. These failure modes are associated with structural defects or temperature gradients, which give rise to divergence of the electromigration flux. The microstructure and thermal properties of the metallizations therefore determine their susceptibility to electromigration damage. In this section, models for the various failure modes will be discussed and the experimental evidence for their occurrence reviewed.

8.5.1 Temperature Effects

As can be seen from equation (8.17), the electromigration flux depends exponentially on the film temperature. Thus, differences in temperature along a metallization track will result in variations in the rate of mass flow over its length. Such temperature variations may arise from dissipation in active devices on the die or from Joule heating in the metallization itself. A typical temperature profile due to Joule heating is shown in figure 8.5a (d'Heurle and Ho 1978). The resulting atomic flux due to electromigration varies along the length of the conductor, as shown in figure 8.5b. The gradient of this curve gives the divergence of the atomic flux (figure 8.5c). Mass depletion is expected to occur in regions where the flux divergence is positive (i.e. near the cathode) and mass accumulation where the divergence is

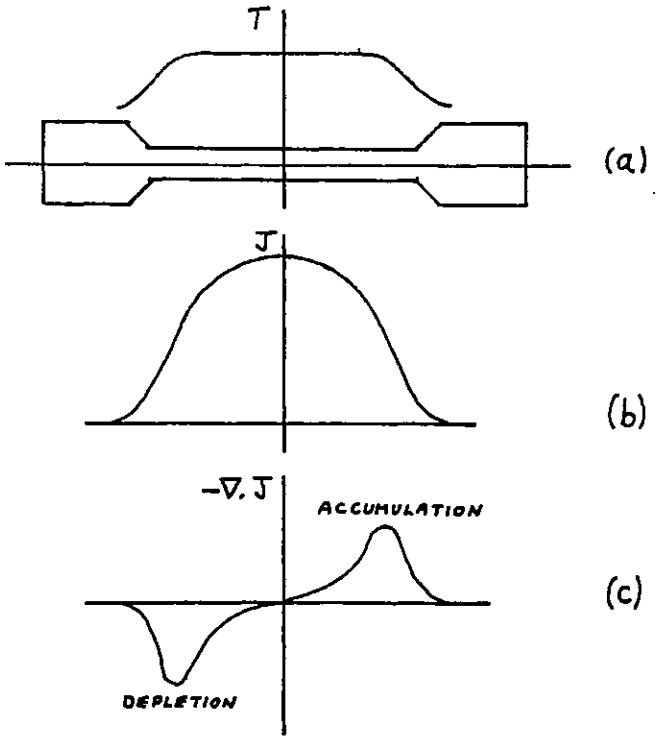

Flux divergence due to Joule heating in a thin film conductor stripe (from d'Heurle and Ho 1978).

FIGURE 8.5

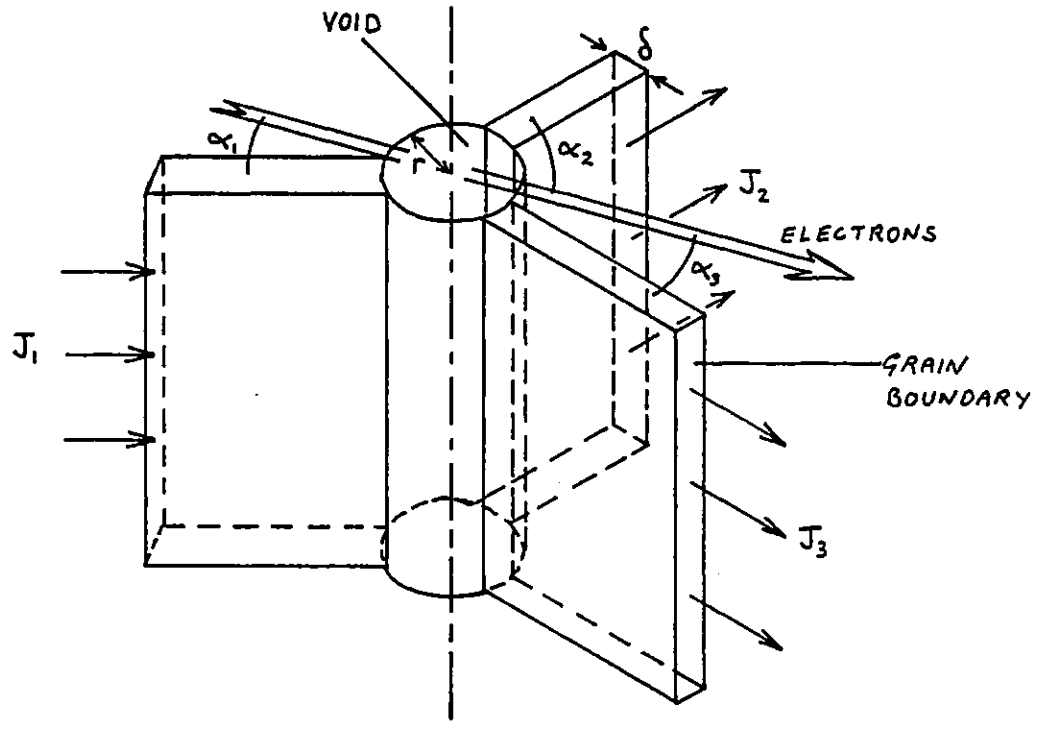

Flux divergence and void growth at a grain boundary triple-point (from Rosenberg and Ohring 1971).

FIGURE 8.6

negative (i.e. near the anode). This effect was observed by Blech and Meieran (1969) in their in-situ TEM experiments, where the relatively large temperature gradient along the suspended section of the track caused the formation of voids near the cathode and hillocks near the anode. These workers also noted that when the direction of the current was reversed, the mass flow reversed, causing the voids to shrink and finally disappear.

Under normal conditions, however, where the metallization is in good thermal contact with the substrate, the temperature rise due to Joule heating is much smaller. Calculations by Chang and Huang (1976) have shown that the steady state temperature at the mid-point of a 120 μm long aluminium track on a silicon substrate is only 4 K above ambient, for a current density of $1 \times 10^{10} A\ m^{-2}$. In practice, temperature rises are certainly no larger than this, as shown by Stephens and Sinnadurai (1974), using liquid crystals to measure the track temperature. Consequently, mass accumulation and depletion due to a temperature gradient are rarely seen under normal device operating conditions. For example, in an experiment by Hersener and Ricker (1973), in which electromigration damage in aluminium metallizations on oxidized silicon was observed in-situ in a scanning electron microscope, void and hillock formation were seen to occur randomly along the conductor. It was therefore concluded that thermal effects were negligible in comparison with the effects of structural irregularities, even for current densities as high as $2 \times 10^{10} A\ m^{-2}$.

At sites of non-adhesion between the metallization and substrate, the local temperature rise has been shown to lead to rapid electromigration failure. Rosenberg and Berenbaum (1968) demonstrated this phenomenon in aluminium films on rocksalt, where the adhesion is poor. However, aluminium generally adheres well to SiO_2 unless there is some deficiency in the metallization process (see Chapter 5) and localized "hot-spots" are not common in practice.

8.5.2 Grain Boundary Effects

Because electromigration in thin films occurs mainly via the grain boundaries, the majority of damage sites are associated with certain irregularities in the grain boundary network. In films consisting of small grains of uniform size, the major potential damage site is thought to be the three-grain-boundary junction (often called a "triple point"). The damage mechanism at such a site has been analyzed by Rosenberg and Ohring (1971). They considered the growth of a cylindrical void of radius r at the intersection of 3 grain boundaries, which are approximated by rectangular slabs of effective width δ and height equal to the film thickness h. (See figure 8.6). The net flow of vacancies into the growing void consists of three possible components.

(1) The *net* flux of vacancies ΔJ_v along the grain boundaries resulting from electromigration :

$$\Delta J_v = \frac{c_v Z^* e E}{kT} \left(D_{g_1} \cos\alpha_1 - D_{g_2} \cos\alpha_2 - D_{g_3} \cos\alpha_3 \right) \tag{8.19}$$

where c_v is the vacancy concentration, D_g is the grain boundary diffusivity, α is the angle between the grain boundary and the direction of current flow and the subscripts 1, 2, 3 refer to the three grain boundaries.

(2) The net vacancy flux from the grain boundaries into the void due to any biaxial stress in the film.

(3) The vacancy flux away from the void to nearby sinks (such as other grain boundaries or the film surfaces).

The latter two contributions are believed to be negligible in comparison with the vacancy flux due to electromigration. The rate of growth of the void is thus given by :

$$\frac{dr}{dt} = \frac{\Omega \delta}{2\pi r} \Delta J_v \qquad (8.20)$$

where Ω is the atomic volume.

For a 500 nm thick aluminium film carrying a current density of $7 \times 10^{10} A m^{-2}$ at 373 K, Rosenberg and Ohring calculated that the time required for a void to grow to a diameter equal to the film thickness is between 10 and 100 hours. This is in order of magnitude agreement with the "incubation time" for the appearance of voids reported by the same workers.

Before a void can grow, nucleation from a supersaturation of vacancies must occur. Rosenberg and Ohring calculated the vacancy supersaturation (equal to $\frac{c_v}{c_o} - 1$ where c_o is the equilibrium vacancy concentration) due to grain boundary electromigration at a triple point in the presence of vacancy sinks at a mean distance of 100 nm. The steady state supersaturation was found to be less than 1. Homogeneous void nucleation is therefore unlikely. The authors suggested the intersections of grain boundaries with the native Al_2O_3 layer as possible sites for preferred nucleation. In view of the Al - SiO_2 interface structure (see Chapter 4) void nucleation at silicon or aluminium oxide particles in the Al - SiO_2 interface also seems plausible. The time taken for the vacancy supersaturation to attain its steady state value is of the order of several minutes. Void formation is thus a growth-controlled process.

A consequence of the finite time required to achieve vacancy supersaturation is the reduced electromigration damage rate under pulsed d.c. loading conditions. This effect has been observed by English et al (1972) in Ti - Au films.

Void formation at grain boundary triple points has been observed by a number of workers (e.g. d'Heurle and Rosenberg 1973). Hillocks and whisker-like growths have also been seen to emanate from grain boundary junctions (e.g. Berenbaum and Rosenberg 1969) as expected on the basis of the Rosenberg and Ohring model if the

triple point is arranged so as to produce a negative divergence of the mass flux.

The effectiveness of the grain boundary triple point as a source of electromigration damage is dependent upon the differences between the rate of mass transport in the three grain boundaries involved. For equal grain boundary diffusivities and equilibrium dihedral angles, no flux divergence results, regardless of the orientation of the triple point with respect to the current flow. The properties of a grain boundary are highly anisotropic and depend on the orientation mismatch between the grains. Therefore, in a textured film, where the mismatch is similar for all grain boundaries, the triple point is expected to be less effective as a damage site. There is some experimental evidence in support of this hypothesis. For example, Attardo and Rosenberg (1970) claimed a longer median lifetime, higher "activation energy" and smaller standard deviation of the failure distribution (see section 8.6.2) for aluminium films with a ⟨111⟩ fibre texture than for randomly oriented films. As the textured film also had the larger grain size, the reduced damage rate may not have been wholly due to the orientation effect. However, the smaller standard deviation is thought to indicate that fewer failure modes were operative in the textured film. The higher "activation energy" is easily understood in terms of the dislocation model of a tilt boundary. In a film with a strong ⟨111⟩ fibre texture, the grain boundaries are formed by a tilt about the ⟨111⟩ axis which is normal to the film plane. The grain boundary dislocations are therefore also normal to the film plane and to the direction of current flow. Atomic transport occurs more readily along the dislocations than in a direction normal to them. The activation energy for electromigration is therefore higher in a textured film than in a randomly oriented film in which some of the grain boundary dislocations are at low angles to the direction of current flow.

In textured films, therefore, electromigration damage is dominated by a different type of structural irregularity. This is the boundary between localized regions of the

metallization which have widely different grain sizes. Such situations arise because of the broad distribution of grain sizes normally present in thin films, and are particularly common where the median grain size is comparable with the track width. The result is an abrupt change in the number of grain boundary electromigration paths, which gives rise to a divergence of the mass flux (see figure 8.7). Where the electron flow is from a region of large grain size to a region of small grain size, void formation occurs. This type of damage mode has been shown to account for approximately 80% of failures in large-grained aluminium. The situation is particularly damaging if a single large grain spans the stripe.

A similar damage mode occurs at the boundary between textured and randomly oriented grains. The textured region has a lower grain boundary diffusivity and tends to block the electromigration flux. This was demonstrated by Howard and Ross (1968) in an aluminium stripe, half of which was deposited onto single crystal silicon (to give a textured region) and half onto amorphous SiO_2 (to give a randomly oriented region). When electrons flowed from the textured to the random region, void formation occurred at the boundary.

8.5.3 Surface Effects

The roles played by the "free" aluminium surface and the Al - SiO_2 interface in electromigration damage mechanisms are poorly understood. The activation energy for diffusion on a clean surface is certainly no larger than that for grain boundary diffusion, so some flow of surface atoms would be expected. This flow may be restricted in real films by the presence of a native oxide. The transport properties of the Al - SiO_2 interface are likely to depend on the chemical and crystalline state of the interfacial reaction zone (see Chapters 3, 4 and 5) and are even less clearly understood. The Al - SiO_2 interface, however, seems a more likely path for electromigration than the "free surface", since the interface has a disordered polycrystalline structure, whereas the

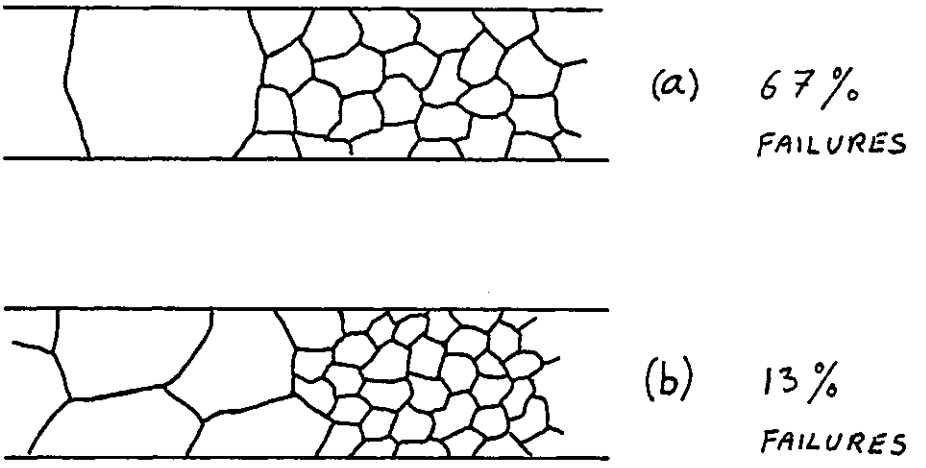

Electromigration failure sites: (a) large grain size divergence; (b) moderate grain size divergence (from Attardo and Rosenberg 1970).

FIGURE 8.7

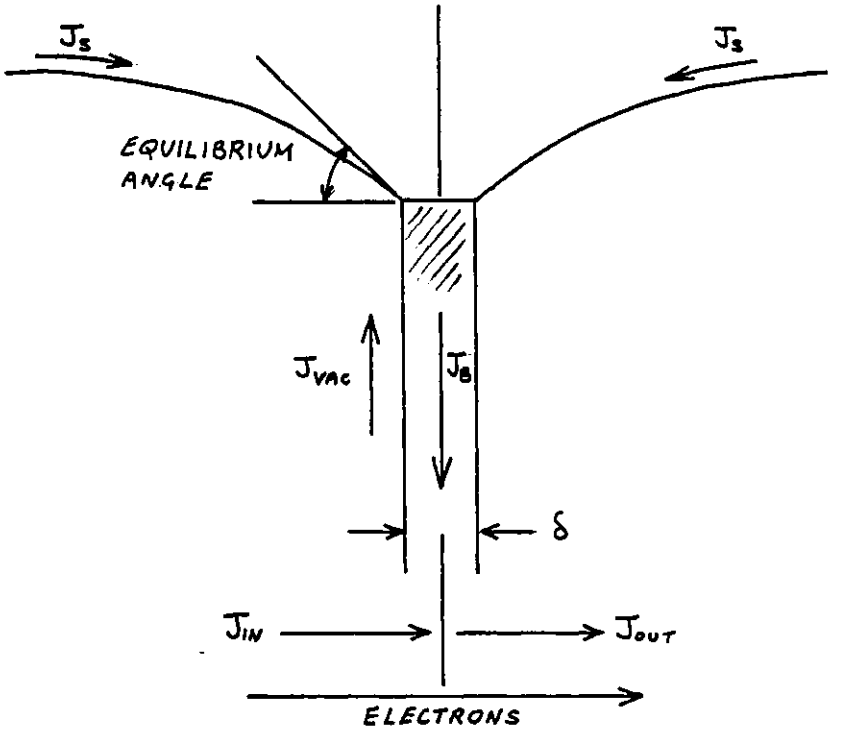

Grain boundary groove model for void growth (from Rosenberg and Ohring 1971).

FIGURE 8.8

surface of aluminium has a uniform covering of amorphous oxide. The effects of surface and interface electromigration, if they do occur, are not known.

The surfaces of a thin film conductor may contribute to electromigration damage by acting as sources or sinks for vacancies. An example of this type of behaviour is the grain boundary grooving model of electromigation damage proposed by Rosenberg and Ohring (1971). If there is a divergence in the grain boundary electromigration flux, excess vacancies will flow into the tip of a grain boundary groove (see figure 8.8). The equilibrium dihedral angle of the groove is thus disturbed and atoms diffuse along the film surface to restore the equilibrium angle. The process continues with progressive deepening of the groove until a hole and eventually an open circuit is formed. The rate of void growth by this mechanism is thought to be similar to that due to flux divergence at a triple point. However, unlike the damage modes described in section 8.5.2, the grain boundary grooving model does not depend upon a nucleation stage and can occur at any level of vacancy supersaturation. Enhanced grain boundary grooving during electromigration has been observed in thin films of silver (Berenbaum and Rosenberg 1969), but similar effects in aluminium films have not been reported. Presumably, the native oxide of aluminium effectively blocks surface diffusion. However, the Al - Al_2O_3 interface structure is not known in detail, and its effect on surface diffusion is not clearly understood.

8.5.4 Contact Effects

At the Al - Si contacts, the aluminium electromigration flux is obviously discontinuous. Where electrons flow from aluminium into silicon, accumulation of aluminium occurs, resulting in the growth of hillocks and whiskers. Where electrons flow from silicon into aluminium, silicon migrates into the metallization and is carried away from the contact by electromigration (Black 1969). This process leads to the formation of etch pits in the silicon, which can become filled with aluminium and hence

cause shorts between adjacent diffusion layers. Excessive Joule heating due to current crowding at the contact is believed to accelerate the degradation process (Prokop et al 1970).

8.6 Accelerated Life Testing and the Assessment of Electromigration Failure

8.6.1 General Observations

Under normal device operating conditions (i.e. current densities below $10^9 A m^{-2}$ and track temperatures less than 375 K) electromigration failure may be expected to occur after, say, 10^5 hours of continuous operation. It is clearly impractical to test metallizations for this length of time in order to assess their electromigration performance. A method of accelerated life testing is therefore employed, in which the samples are subjected to temperatures of around 450 K and current densities of the order of $10^{10} A m^{-2}$. The samples may either be sections of the metallization track on a real device or specially designed test patterns. The latter usually take the form of a "meander" of the required thickness and width on an oxidized silicon die. The track may run over oxide steps or other discontinuities in order to evaluate the importance of these features as preferred sites for electromigration failure, or the oxide may be flat if only the intrinsic properties of the metal are to be investigated. The test dice are mounted on headers and encapsulated in the usual way, and then placed in a constant temperature oven during testing so that all the specimens in the batch are stressed under the same conditions.

The early results (e.g. Black 1969) showed that the failure times of a batch of identical specimens could be represented reasonably well by a log-normal distribution. That is, the probability of failure at time t is given by :-

$$p(t) = \frac{1}{\sqrt{2\pi}\,\sigma_f}\,\frac{1}{t}\exp\left[\frac{-1}{2\sigma_f^2}(\ln t - \mu)^2\right] \qquad (8.21)$$

where μ is a numerical constant and σ_f is the standard deviation (for details see Appendix E). The log-normal distribution has been used universally for the analysis of accelerated life test data, with very little physical justification. If the cumulative number of failures is plotted on a normal probability scale against the logarithm of the time, the data points should lie on a straight line. In practice, the fit is often poor and the values of t_{50} and σ_f cannot be determined with any accuracy, especially when the number of samples is small.

The measurement of t_{50} and σ_f is the aim of accelerated life tests. Both of these parameters are important for reliability considerations. Obviously, t_{50} should be as large as possible, but also σ_f should be low, so that the spread in failure times is small.

In order to predict the failure times of metallizations under normal operating conditions, the accelerated life test data must be extrapolated to lower values of temperature and current density. This is only possible if the failure modes occurring at the test conditions are the same as those occurring at operating conditions. The test conditions, therefore, cannot be made too extreme, or completely new failure mechanisms (e.g. melting) may occur.

Early workers in the field (e.g. Black 1969) found empirically that the median time to failure was related to the test conditions by an equation of the form :-

$$t_{50} = A j^{-n} \exp\left(\frac{\phi}{kT}\right) \qquad (8.22)$$

where ϕ is the effective "activation energy" for electromigration damage, n is a positive number of order unity, and A is a constant which accounts for the film structure, dimensions and thermal properties. ϕ has been experimentally determined by a multitude of workers. It is generally believed to lie in the range 0.5 - 0.7 eV for aluminium

(see table 8.2) and it has been referred to as the activation energy for electromigration by some authors. This is misleading, however, since there is no reason why Q_g and ϕ should be equal. The former is simply the activation energy for grain boundary electromigration, while the latter is the resultant of a number of temperature dependent processes (void growth kinetics, electromigration, "annealing" effects, etc.) involved in electromigration failure. The value of n has been found to vary with experimental conditions. The rate of mass transport has a linear j dependence. Values of n around 1 have been reported for failure at Al - Si contacts (Prokop and Joseph 1972). For other types of failure, however, higher values of n have been found (see table 8.3).

A complete model for electromigration failure should predict the relationship between the median time to failure and such parameters as film grain structure, dimensions, thermal conductivity and current density. Although a completely satisfactory formulation has not been achieved, some insight is given by the various models described below.

8.6.2 Failure Models

The model formulated by Venables and Lye (1972) treats failure as a result of the increasing porosity of the metallization due to void growth at grain boundary triple points (or other damage sites) distributed randomly throughout the film. The porosity reduces the effective cross sectional area of the current-carrying stripe and hence increases the local current density in the vicinity of the voids. The local electromigration flux is thus increased, due to the direct effect of the increased current density and also because of the greater Joule heating. Void growth therefore proceeds at an accelerating rate until catastrophic failure of the stripe occurs. The process responsible for ultimate failure was taken to be melting of the region of highest porosity, although reaction of the metal with the substrate or environment could be more

Temp. Range (K)	Grain Size (μm)	"Activation Energy" ϕ (eV)	Reference
382 – 533	1·2 – 8	0·48 – 0·8	Black (1969)
413 – 573	2 – 8	0·51 – 0·73	Attardo and Rosenberg (1970)
398 – 448	?	0·5 – 0·7	Ames et al (1970)
393 – 453	10	0·55	Sim (1979)
393 – 490	3·5	0·60	" "
393 – 453	2	0·42	" "

Effective Activation Energies from Accelerated Life Tests.

TABLE 8.2

Test Temp. (K)	Current Density Range ($A\,m^{-2}$)	Grain Size (μm)	n	Reference
453	$5 \times 10^{9} - 2 \times 10^{10}$	1·2 – 8	2	Black (1969)
423	$1 \times 10^{10} - 2 \times 10^{10}$	0·35	5	Blair et al (1970)
473	$5 \times 10^{9} - 2 \times 10^{10}$	3	2·5 to 4·5	Saito and Hirota (1974)
500	$5 \times 10^{9} - 2 \times 10^{10}$	?	2·5	Learn (1973)
453	$2 \times 10^{9} - 2 \times 10^{10}$	2 – 10	2	Sim (1979)
?	$3 \times 10^{7} - 1.6 \times 10^{8}$	?	1	Prokop and Joseph (1972)

The Current Density Exponent, n, from Accelerated Life Tests.

TABLE 8.3

appropriate in some cases.

The median time to failure is shown to have a complex dependence on the initial current density and cannot be represented by a simple power law over the whole range of j values encountered in practice. If, however, a j^{-n} dependence is assumed to be valid over a small range of current density, then n is found to increase from 1 for $j \lesssim 10^{9} A m^{-2}$ to 2 or more for $j \sim 10^{10} A m^{-2}$. Moreover, the j dependence is found to vary with the degree of thermal contact between the metallization and the substrate, which determines the temperature rise Δ T due to Joule heating (see figure 8.9). The dependence of the MTF on the ambient temperature is also complex, although Arrhenius plots of MTF against reciprocal temperature yield approximate straight lines. The effective activation energy, however, as given by the slope of the straight line, is found to vary with test conditions. For a current density of $2 \times 10^{10} A\ m^{-2}$, ϕ is 0.05 eV lower than the *true* activation energy for grain boundary electromigration Q_g (see figure 8.10). Even for low current densities, however, ϕ is not equal to Q_g. The variation of ϕ with j is dependent on the thermal contact between the metallization and the substrate. If the contact is poor, the deviation of ϕ from Q_g is even more pronounced.

Sigsbee (1973) developed a model in which failure is assumed to occur by the propagation of a crack-like void across the stripe. The analysis is similar to that used by Venables and Lye and the results are essentially the same. In addition, it is evident from Sigsbee's model that the MTF increases with stripe width, for a constant current density. The effect of increasing the stripe width is threefold. It increases the total crack length necessary for open circuit failure, reduces the initial Joule heating (compared to a narrow, thick stripe of equal cross section) and delays the onset of excessive Joule heating due to current-crowding in the vicinity of the crack tip. The model does not, however, take into account the statistical distribution of potential

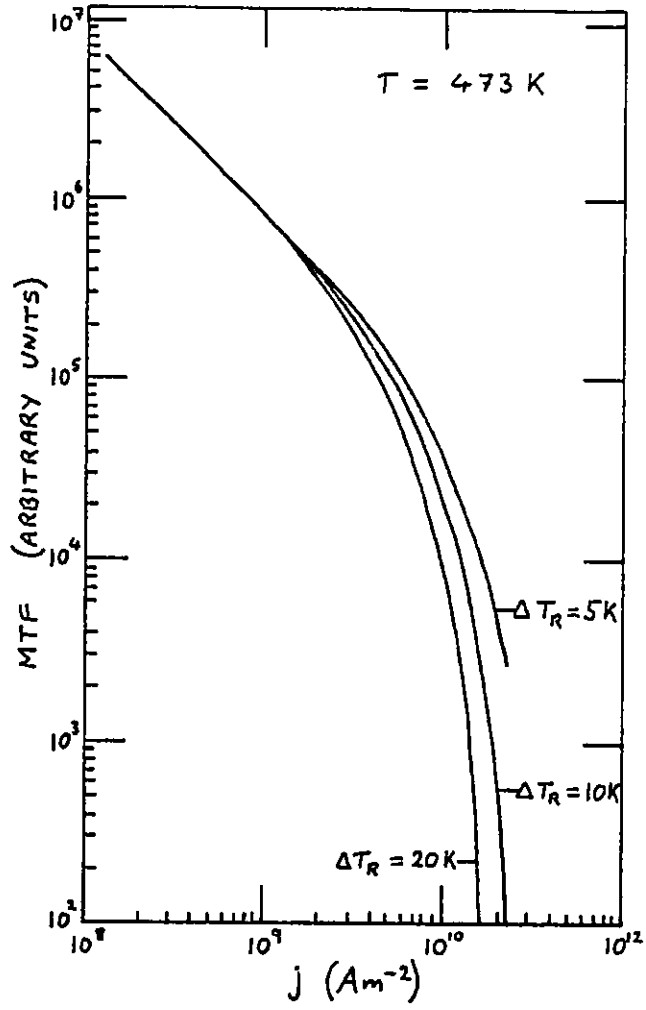

FIGURE 8.9

Median time to failure versus current density, for different values of ΔT_R (the rise in track temperature due to Joule heating (computed by Venables and Lye 1972).

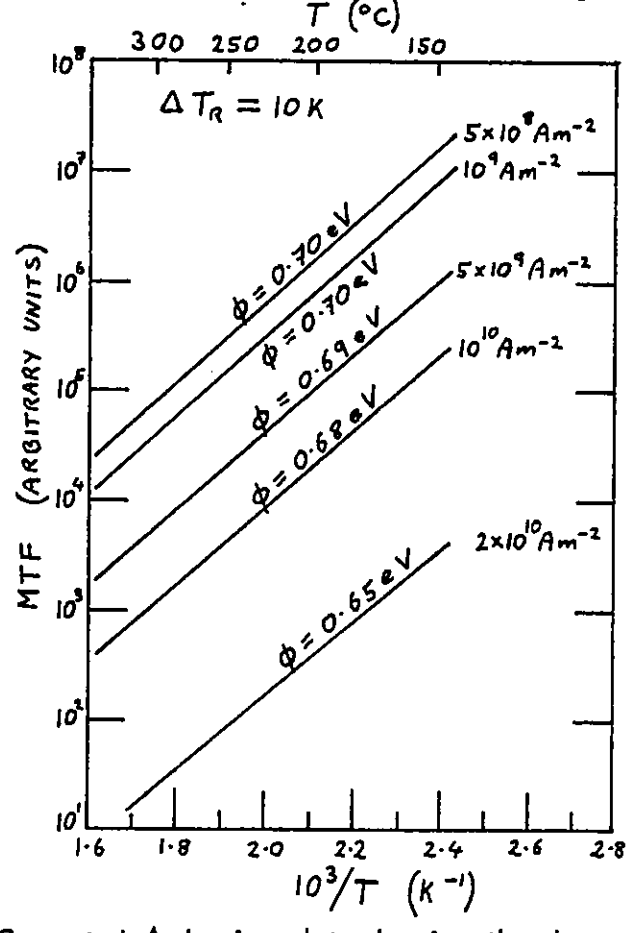

FIGURE 8.10

Computed Arrhenius plots, showing the dependence of ϕ on test conditions (from Venables and Lye 1972).

failure sites in the metallization or the fact that in a real film, a crack tends to propagate along the grain boundaries rather than in a straight line across the stripe.

An experimental study of the effects of track length and width on electromigration life time was made by Agarwala et al (1970) using 2 μm thick aluminium films of 1 - 2 μm grain size prepared by evaporation onto oxidized silicon. Stripes of various lengths and widths were prepared by photolithography and tested at a current density of 7.5×10^{9} A m^{-2} and a temperature of 403 K. Failure was seen to occur by transverse cracks, randomly distributed along the length of the conductor, and the failure-time distribution was roughly log-normal. The MTF was found to fall drastically as the stripe length was increased up to a value of $\sim$ 150 μm, after which it remained fairly constant. The standard deviation of the failure time distribution also exhibited an initially rapid fall with increasing stripe length, then became constant for lengths of 500 μm and more. The MTF increased linearly with stripe width in the range 5 to 15 μm.

These results led the authors to propose a simple statistical model for electromigration failure. This model was later extended by Attardo et al (1971). The conductor is treated as a series of short sections of length equal to one grain diameter randomly chosen according to a log-normal grain size distribution. Across the stripe, each section contains enough grains to make up the width of the stripe. The electromigration flux in each grain boundary is a function of the (randomly chosen) angle between adjoining grains and of the angle between the grain boundary and the direction of current flow. The time to failure is inversely proportional to the maximum flux divergence at the interface between two adjacent sections. The life of the conductor stripe is therefore limited by the life of this "critical interface".

Attardo used a computer to simulate 10^{5} interfaces, and hence obtained the failure time distribution. Let f(t) be the probability that an interface will fail before

time t. If a track has length L and mean grain size $\bar{d}$, the track has $L/\bar{d}$ sections and $L/\bar{d} - 1 \approx L/\bar{d}$ interfaces. The probability that the track will fail before time t is therefore :-

$$F(t) = 1 - \left[1 - f(t)\right]^{L/\bar{d}} \qquad (8.23)$$

The results (see figure 8.11) show that the MTF and the standard deviation of the failure distribution decrease with increasing track length. This is easily understood on the basis that the probability of a track containing the "most critical section" increases with the track length. The MTF was found to increase almost linearly with track width and mean grain size and to decrease with increasing grain size standard deviation. The failure time distribution was approximately log-normal.

A slightly modified computer simulation has recently been carried out by Schoen (1980). The main difference is that in Schoen's model, a number of hypothetical tracks are constructed, each having a realistic number of sections (i.e. $\ll 10^5$). The failure time of each track is computed, using the same techniques as used by Attardo et al. However, the failure time distribution is now determined using a number of different hypothetical tracks, rather than by application of equation 8.23. The failure times are now found to lie on a log-extreme value distribution (see Appendix E). However, except in the case where median grain size exceeds track width, the data can still be well represented by a log-normal distribution. The predictions of Schoen's model concerning the track length and track width dependence of the MTF are very similar to those of Attardo's model. In addition, Schoen calculated the variation of the standard deviation of the failure time distribution with the track width. The form of the dependence is complex, but is in qualitative agreement with the experimental results of Scoggan et al (1975), as shown in figure 8.12. Schoen also calculated the dependence of the standard deviation of the failure distribution on the median grain

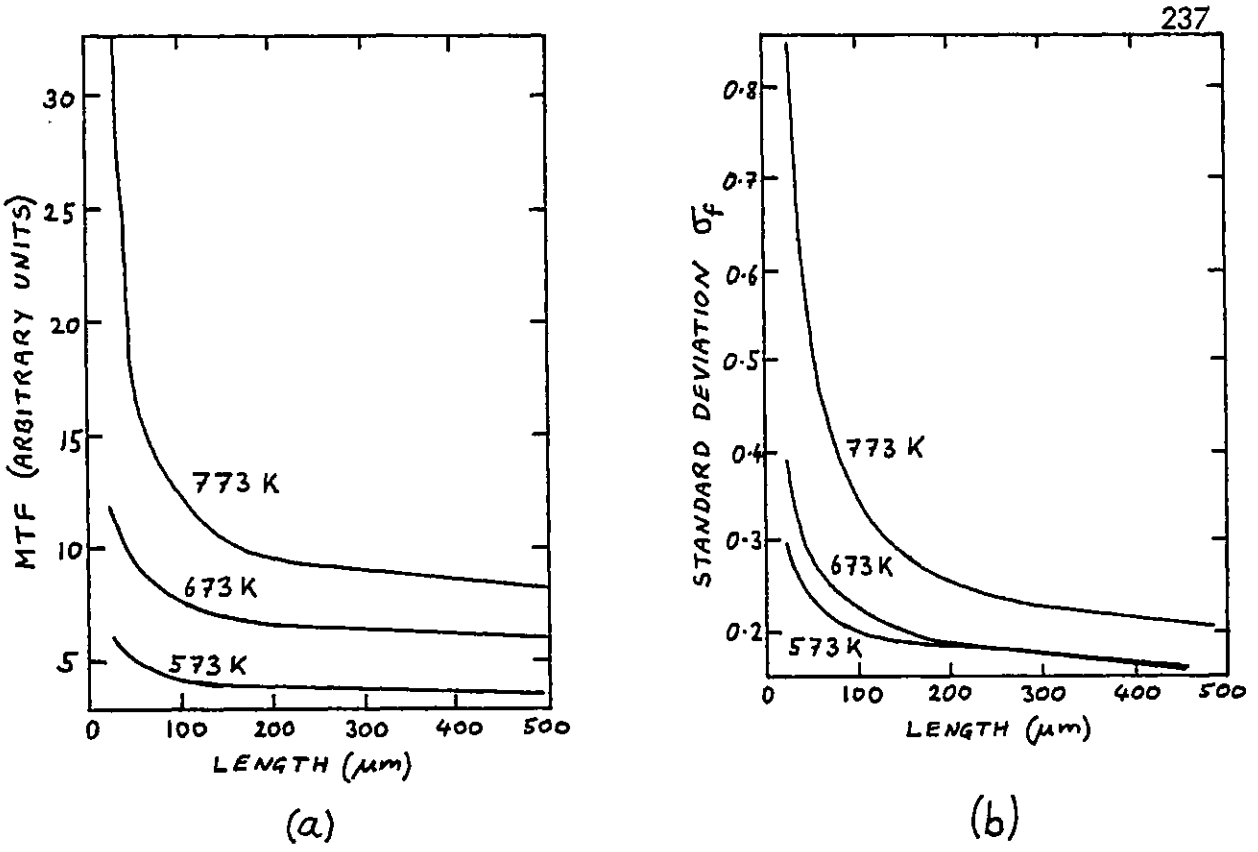

Computer-simulated length dependence of (a) median time to failure and (b) failure-time standard deviation of a 12 μm wide conductor stripe (from Attardo et al 1971).

FIGURE 8.11

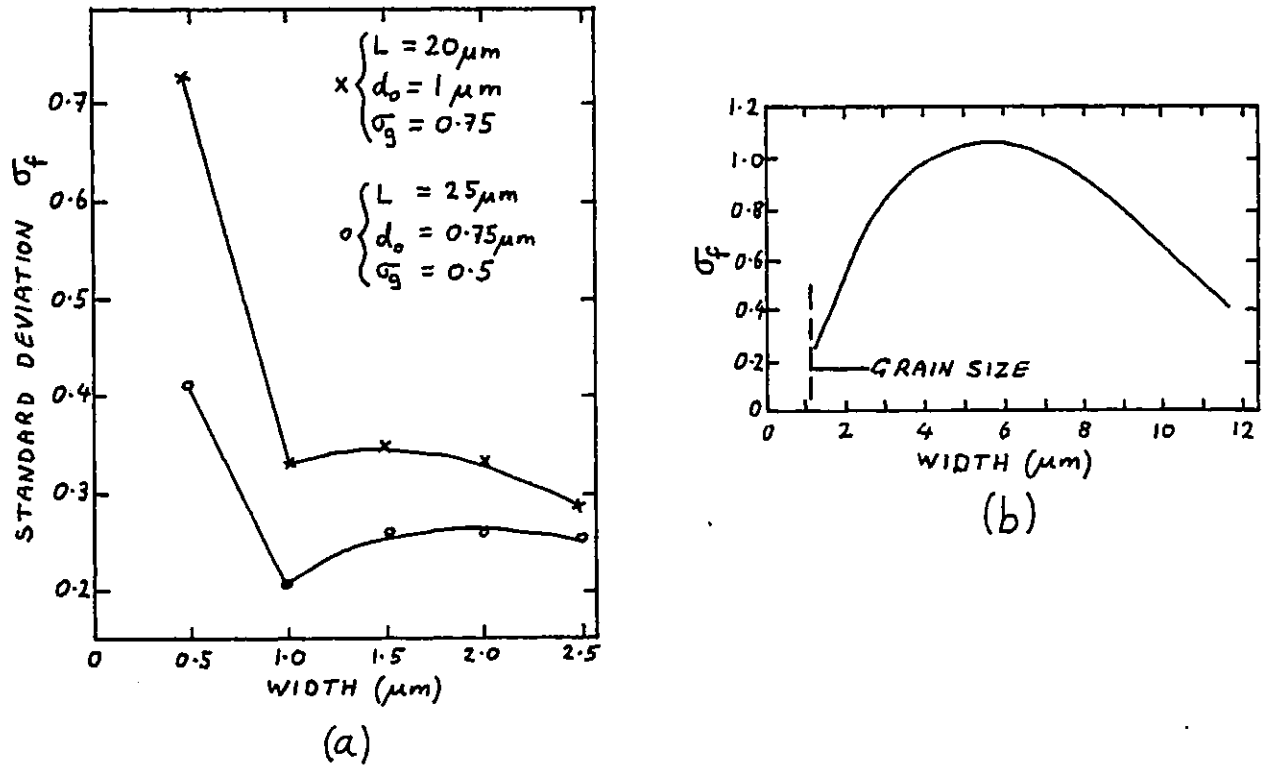

Variation of failure time standard deviation with stripe width: (a) computer--simulation (Schoen 1980) and (b) experimental data (Scoggan et al 1975).

FIGURE 8.12

size (see figure 8.13). The standard deviation is seen to increase with grain size and decrease with track width. This behaviour is expected intuitively since the spread in the failure distribution increases as the number of potential failure sites decreases.

Saito and Hirota (1974) investigated the effects of grain size and track width on the MTF of 1 μm thick, tungsten filament-evaporated aluminium films on oxidized silicon. They found that, when tested at 446 K and 1×10^{10} A m^{-2}, the metallizations failed by the growth of randomly distributed voids and the results are therefore suitable for analysis in terms of the Attardo or Schoen models. The small number of samples tested by Saito and Hirota (~ 5 per batch) did not allow the failure time distribution to be accurately determined, and their results are therefore subject to large errors. However, their data (see figure 8.14) show that the MTF increases linearly with mean grain size (in the range 0.8 to 6.0 μm) and track width (in the range 7 to 20 μm), in agreement with the theoretical models. Unfortunately, no data relating to the grain size standard deviation is given, so further predictions of the Schoen model cannot be tested.

8.6.3 Anomalous Effects in Narrow Tracks

With the advent of VLSI devices there has been much recent interest in electromigration failure in very narrow (~1 μm) metallizations. Vaidya et al (1980a) evaluated 25 mm long e-beam evaporated Al - 0.5% Cu tracks having widths in the range 1 - 4 μm. The results show that the trend of decreasing MTF with decreasing width, observed for wider tracks, breaks down below 2 μm, and narrower tracks have anomalously long lifetimes (see figure 8.15). Similar results were obtained by Kinsbron (1980) using 250 μm long Al - 0.5% Cu tracks (figure 8.16).

The effect was attributed to the geometry of the grain boundary network when the track width is smaller than the median grain size (in this case ~ 4 μm). The

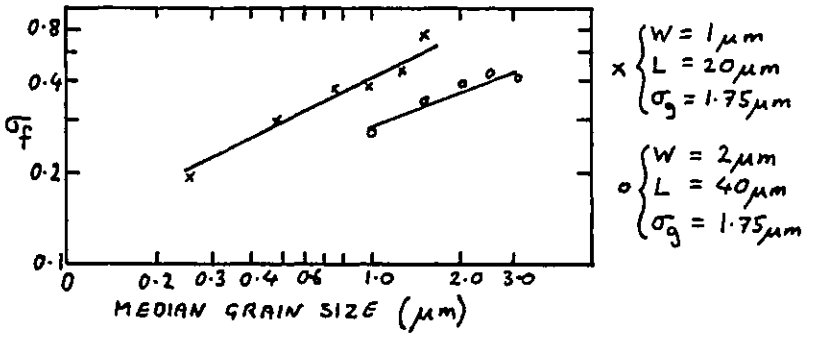

Computer-simulated variation of the failure time standard deviation with the median grain size of the metallization (from Schoen 1980).

FIGURE 8.13

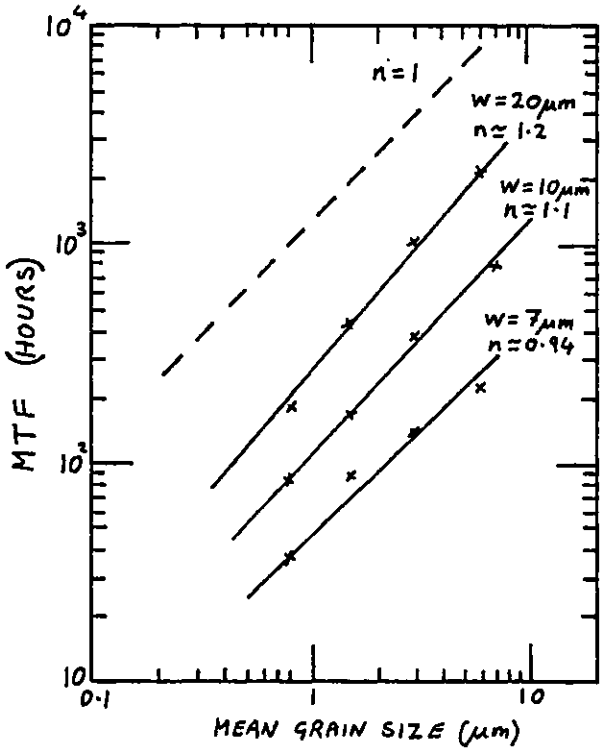

Median time to failure as a function of mean grain size and stripe width (from Saito and Hirota 1974).

FIGURE 8.14

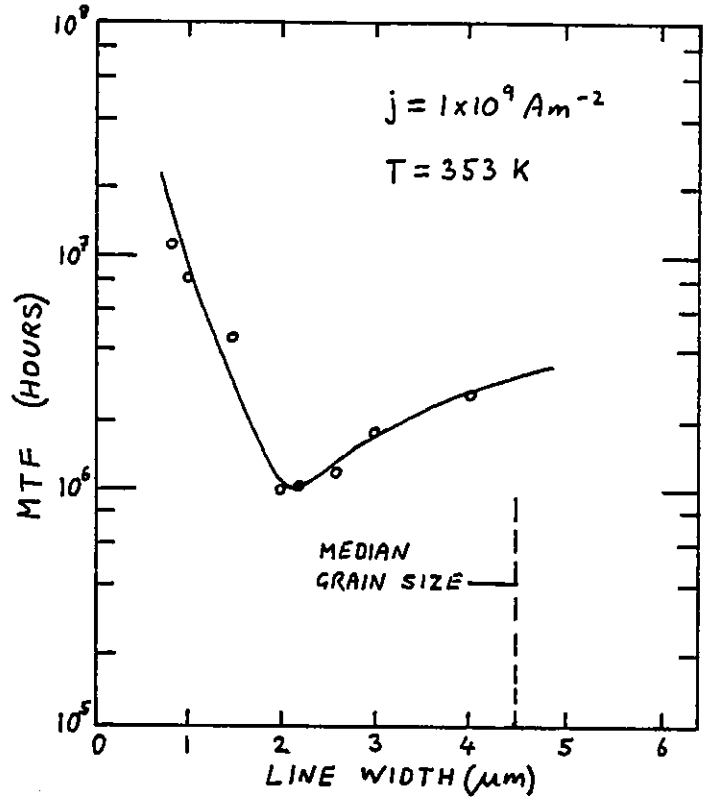

Median time to failure versus stripe width for narrow conductors (from Vaidya et al 1980 a).

FIGURE 8.15

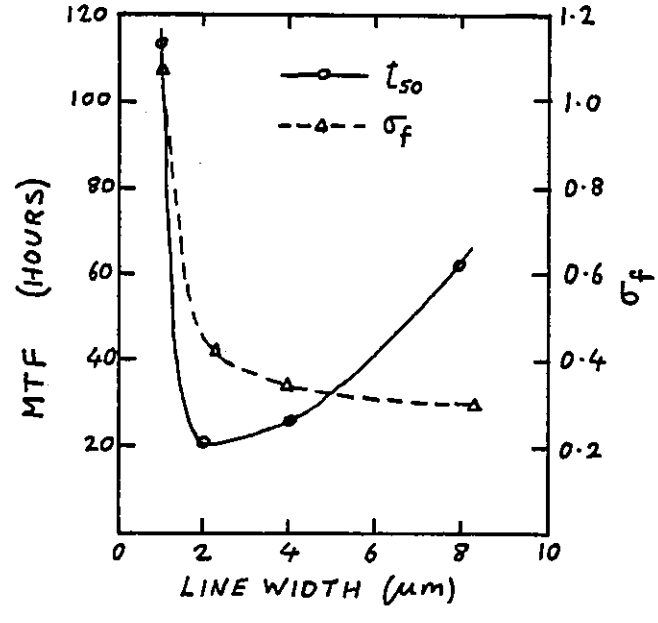

Median time to failure and failure time standard deviation versus stripe width for narrow conductors (from Kinsbron 1980).

FIGURE 8.16

irregular arrangement of grain boundary triple points and abrupt changes in grain size found in wider tracks is replaced by a "bamboo" structure in narrow tracks (figure 8.17). The grain boundaries run perpendicular to the direction of current flow and hence do not contribute to the electromigration flux. The "bamboo" structure is thought to be promoted by the strong ⟨111⟩ fibre texture found in these films (Vaidya et al 1980). Failure may occur at sites where the bamboo structure is not perfect, or surface and interface electromigration may be involved in the dominant failure mode. Clearly, further work is required to identify the potential damage sites and the mechanism responsible for failure.

8.6.4 Annealing Effects during Testing

Sim (1979) carried out accelerated life tests on 1 μm thick by 10 μm wide pure aluminium metallizations on oxidized silicon. Three films were deposited by tungsten-filament or electron-beam evaporation and had mean grain sizes of 2, 3.5 and 10 μm. Two of the films (those of 2 and 10 μm grain size) had an overglaze (see section 8.7.1). The test dice were encapsulated in TO5 packages and mounted in a temperature-controlled heat sink during testing.

When tested at 453 K and current densities in the range 2×10^{9} to 2.5×10^{10} A m^{-2}, the films of 2 and 3.5 μm grain size gave log-normal failure time distributions. However, the film of 10 μm mean grain size gave what appears to be a bi-modal failure distribution for current densities less than 1.5×10^{10} A m^{-2} (see figure 8.18a). Sim suggested that after approximately 500 hours at 453 K, "annealing" of the metallization took place, resulting in a change in the failure distribution. At 518 K, the change in failure distribution occurred after less than 30 hours (see figure 8.18b). Examination of the failed specimens revealed that those which had undergone "annealing" failed by localized void growth, without the random void distribution seen in other specimens. No obvious change (e.g. grain growth) could be detected. It is possible that reaction

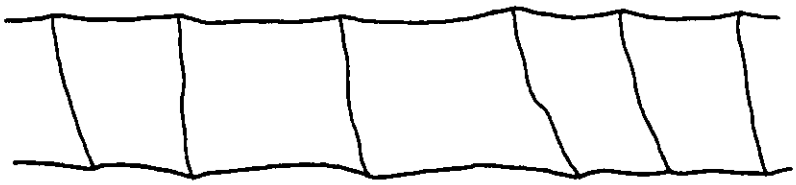

The "bamboo" grain structure in a 1 μm wide Al-0.5% Cu stripe (from Vaidya et al 1980 a).

FIGURE 8.17

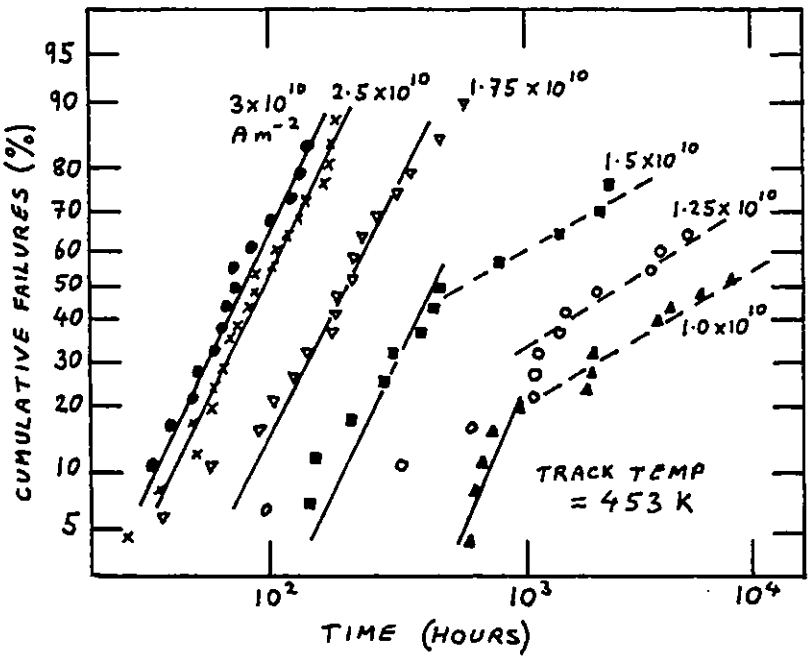

(a)

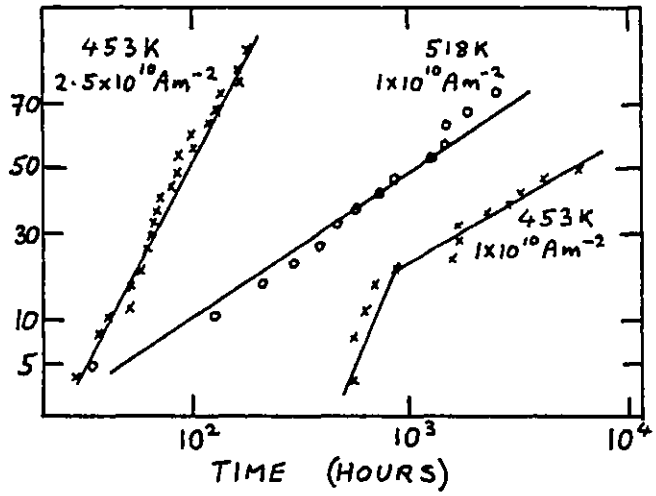

(b)

The effects of (a) current density and (b) excessive temperature/time on the failure distribution of pure Al metallizations of large grain size (from Sim 1979).

FIGURE 8.18

of the aluminium with the substrate (or overglaze) occurred, which may have improved the thermal contact between the metallization and the die. It is also possible that the apparent changes in slope of the failure distributions are due to statistical fluctuations in the data. This is thought to be unlikely, however, as Sim's data from other test batches show very little scatter in a log-normal plot, and the number of samples is reasonably large ($\sim$ 25 per batch). Replotting the data on log-extreme value graph paper did not improve the fit, despite the predictions of Schoen's model (see section 8.6.2).

8.7 Methods of Improving Aluminium Metallizations

In addition to optimizing the microstructure, geometry, etc. of the metallization, the MTF can be improved by several other means. These are described briefly in the following.

8.7.1 Glass Passivation

A passivation layer or overglaze is often employed with aluminium metallizations to protect against corrosion. It has been claimed by some workers (e.g. Black 1969) that a dielectric surface coating greatly extends the electromigration MTF, while others (e.g. Attardo and Rosenberg 1970) have observed negligible effect. Various materials and processes have been used to deposit the passivation layer (see d'Heurle and Rosenberg 1973), common examples being sputtered SiO_2 and anodic Al_2O_3.

The mechanism by which the passivation film reduces the rate of electromigration damage (if, in fact, it does) is not clearly understood. The presence of such a coating might reduce the mobility of surface atoms and hence impede damage modes such as grain boundary grooving, which rely on surface diffusion. However, since aluminium has a native oxide film, the effect of any additional surface layers is expected to be

small. It has also been suggested that the overglaze might provide a mechanical restraint, opposing the morphological changes associated with electromigration damage. However, Ainslie et al (1972) have shown that a typical overglaze could not maintain the stress required to give an appreciable reduction in the damage rate. Another possibility is that the temperature rise associated with some of the glazing processes causes microstructural changes in the aluminium (e.g. grain growth) and hence increases the MTF. Further experimentation is required to resolve these questions.

8.7.2 Alloy Additions

Certain aluminium alloys have been shown to have much greater resistance to electromigration damage than pure aluminium. The most commonly used alloy addition is copper, usually in amounts of 0.5 - 4 wt%. The effect is believed to be due to segregation of the copper atoms to the aluminium grain boundaries, thus blocking the electromigration flux. The copper atoms themselves undergo rapid electromigration, but the grain boundaries remain saturated with copper for a long period due to dissolution of a precipitate phase. Agarwala et al (1976), using scanning electron microscopy and microprobe analysis, showed that failure finally occurred at sites depleted of copper. (These were usually associated with an abrupt change in grain size). Al - Cu metallizations can be readily deposited using e-beam evaporation.

Silicon is also a common additive in aluminium metallizations. Its main purpose is to suppress silicon dissolution at Al-Si contacts, but it can also have the effect of reducing electromigration damage (van Gurp 1971). The addition of copper to Al-Si films gives a further increase in the MTF. However, because of the difficulty in evaporating silicon, Al-Si and Al-Si-Cu metallizations are usually prepared by sputter-deposition. Vaidya et al (1980b) have shown that sputter-deposited Al-Si-Cu films have a shorter MTF than e-beam deposited Al-Cu films. This is attributed to the

small-grained, randomly oriented structure of the sputtered films as opposed to the larger grain size and ⟨111⟩ fibre texture of the evaporated films. It is therefore important to assess the effects of alloy additions on the film microstructure if optimum reliability is to be achieved.

The addition of a third element (e.g. In, Sn or Ag) to Al-Cu films in order to further increase the lifetime has proved unsuccessful (d'Heurle and Gangulee 1973), but further work in this area may yield useful results.

CHAPTER 9

AN EXPERIMENTAL STUDY OF ELECTROMIGRATION IN THIN FILMS OF ALUMINIUM

9.1 Introduction

The experiments described in this chapter constitute an investigation into the effects of microstructure on the electromigration performance of aluminium thin film metallizations. Although similar studies have been carried out by other workers (see Chapter 8), the deposition conditions and the resulting microstructure of the films were not fully characterized. In the present work, pure aluminium films were deposited in the same evaporation plant under identical conditions of deposition rate, residual gas pressure and substrate preparation technique. The deposition temperature and annealing treatment were adjusted in a controlled manner to produce films of different microstructures. These were characterized by a variety of techniques, as described in Chapter 7. The metallizations were subjected to accelerated life testing and the results (from physical examination of the failed specimens as well as statistical failure data) were interpreted in terms of published failure models. Correlations were drawn between deposition parameters, film microstructure and electromigration performance, which go some way towards predicting the electromigration performance from physical examination of the metallization, without the need for accelerated life testing.

9.2 Specimen Preparation

9.2.1 The Substrates

The substrates consisted of polished 2-inch wafers of {100} silicon with 1 μm of steam-grown SiO_2 (see Appendix A). Originally, wafers with 50 nm of SiO_2 were employed so that the metallization could be examined by chemical jet thinning and

transmission electron microscopy when electromigration failure had occurred. However, the thin oxide layer led to additional failure modes not directly related to electromigration and tests on these specimens had to be abandoned (see section 9.6.5). The oxide surface was scored into 1.5 mm squares to facilitate dicing. The SiO_2 surface was not cleaned prior to metallization. Similar surfaces were shown by XPS to be contaminated with less than a quarter of a monolayer of carbon (see section 3.6.2).

9.2.2 Metallization

Aluminium was deposited by tungsten-filament evaporation in the bell-jar system described in section 4.2.2. All films were nominally 1 μm thick and were deposited at a rate of 10 nm s^{-1} in a vacuum of better than 2×10^{-6} m bar. Films were deposited onto substrates at 295 K, 475 K, 575 K and 675 K and given no further treatment prior to pattern definition. One film was also deposited at 475 K and annealed at 700 K for 2 hours in vacuuo to simulate the "sintering" process. The films were examined by optical microscopy and grazing incidence x-ray diffraction, but transmission electron microscopy could not be used owing to the thickness of the SiO_2 layer. Films deposited under identical conditions but onto 50 nm of SiO_2 were also examined by transmission electron microscopy (see section 7.4.5). The grain size distributions for these films were assumed to be the same as for the films deposited onto 1 μm of SiO_2. The microstructural properties are summarized in table 9.1.

9.2.3 Pattern Definition

Standard photolithographic processing was used to define a metallization geometry suitable for electromigration life testing. The aluminium track was 1 μm thick, 10 μm wide, and 3 mm long, and was terminated by 200 μm square bond pads (figure 9.1). The various other structures on the die were not used in the present study. In order to avoid complicating effects and to facilitate post-mortem examination, a passivation film was not used.

	Film Thickness (μm)	Deposition Rate ($nm\ s^{-1}$)	Deposition Temperature (K)	Anneal	Grain Size			Preferred Orientation	Track Resistance (Ω)	Surface Topography	Thermal Resistance ($K\ W^{-1}$)
					Mean (μm)	Median (μm)	Standard Deviation				
Wafer A	1·04	10	475	None	0·7	0·5	0·48	⟨111⟩	4·9	Grain Boundary Grooves	78
Wafer B	1·01	10	575	None	2·6	1·7	0·57	⟨111⟩	5·1	Grain Boundary Grooves	72
Wafer C	1·02	10	675	None	4·1	2·6	0·60	⟨111⟩	5·5	Grain Boundary Grooves	77
Wafer D	1·03	10	475	2 hours at 700K	1·6	1·0	0·61	⟨111⟩	5·5	Annealing Hillocks	64
Wafer E	0·99	10	295	None	0·5	/	/	⟨111⟩	/	Growth Hillocks	/

Properties of the Metallizations

TABLE 9.1

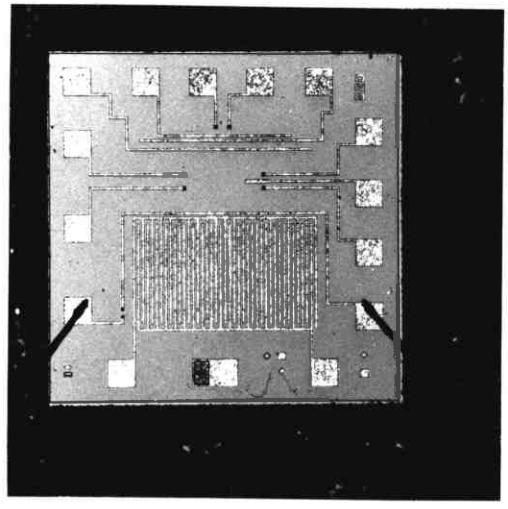

Optical micrograph of a test die.

FIGURE 9.1

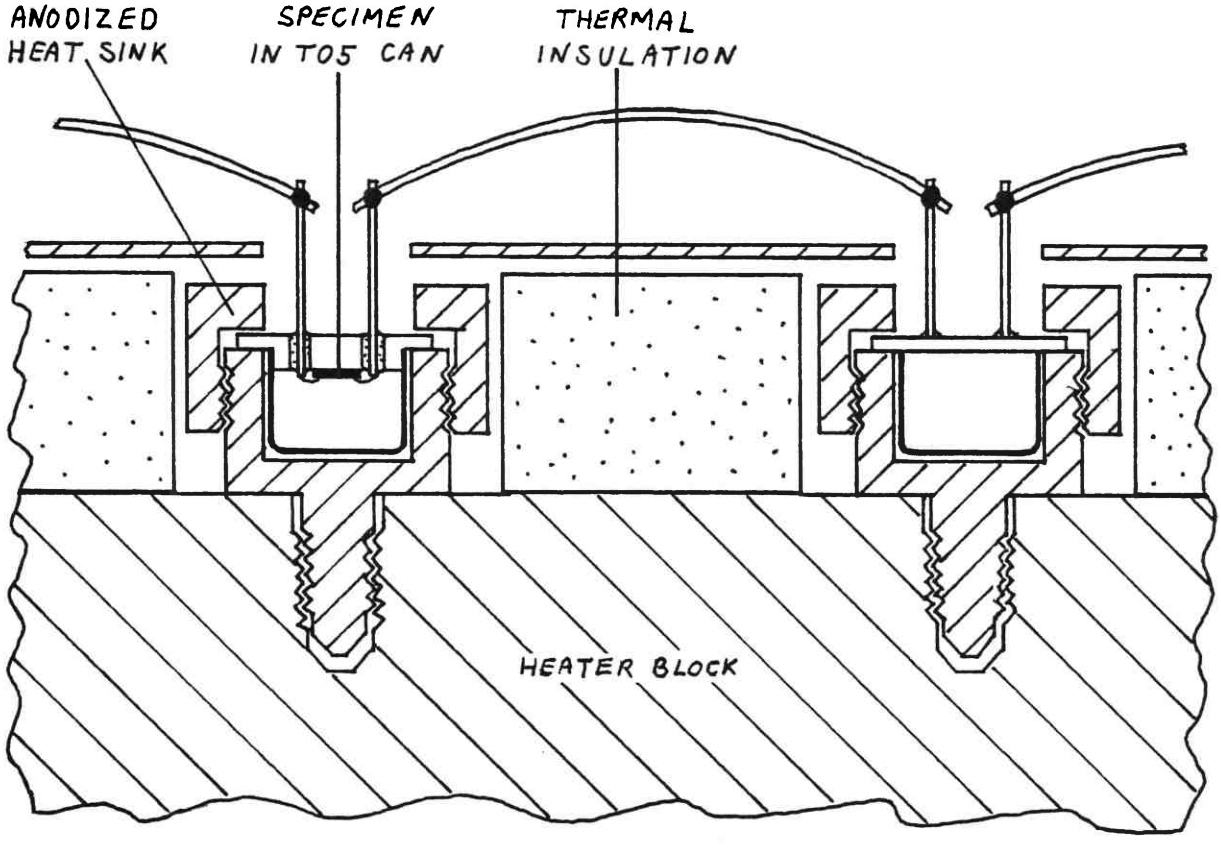

Cross section of the heater block, showing specimen mounting arrangement.

FIGURE 9.2

Films deposited at 295 K were found to peel and blister during processing. This effect was attributed to poor adhesion of the film to the substrate due to lack of Al - SiO_2 interfacial reaction at room temperature (see section 3.6.2). Consequently, these films were not used for life testing.

9.2.4 Bonding and Encapsulation

The patterned wafer was broken into dice which were gold eutectic bonded onto TO5 headers. Connection was made to each end of the track by ultrasonic aluminium wire bonding and the devices were sealed in standard TO5 cans. Approximately 40 test specimens were prepared from each of the wafers.

9.3 Apparatus for Accelerated Life Testing

The electromigration life testing equipment was supplied by British Telecom. Research Labs. and was almost identical to that used by Sim (1979). A full description of the equipment will be given, however, since it has not been described in detail elsewhere.

9.3.1 The Heater Block

The specimens were mounted in anodized heat-sink studs which were screwed into a massive aluminium block. Heat-sink compound was used on the thread to improve thermal contact. Resistive heating elements embedded in the block were thermostatically controlled to provide a constant and uniform temperature over the surface of the block. The specimens were surrounded by "Kaowool" thermal insulation and the whole assembly was placed in a draught-free environment (figure 9.2). Temperature was measured by chromel-alumel thermocouples placed under two of the heat-sinks, one at the centre of the block, and one near the edge. Both gave readings equal to within 0.5 K.

9.3.2 Current and Voltage Measurement

The specimens in the heater block were connected in series to simplify the

monitoring equipment. Direct current was supplied by a Kingshill 60 volt, 1 amp stabilized power supply used in constant current mode with an external reference resistor. The current drifted by less than 0.5% over a period of several hundred hours.

The specimen current was measured by taking the voltage across a 1 Ω resistor in series with the specimens (figure 9.3). A 100 Ω variable resistor connected in parallel was used to trim the resistance to precisely 1 Ω and ensure accurate current measurement. The voltage across any one of the specimens could be monitored using a rotary selector switch, and a changeover switch enabled current and voltage to be displayed on the same DVM.

The voltage across a 0.5 Ω resistor in series with the specimens was used to drive a chart recorder running at 25 mm per hour. The trace provided a continuous record of the specimen current and was used to determine the times at which failures occurred.

The current density in the metallization was calculated from knowledge of the total current and cross sectional area of the track. The latter was not accurately determined, due to the lack of suitable equipment to measure the track width. However, since all the specimens were subjected to the same photolithographic process, the track widths were assumed to be equal and close to the nominal value of 10 μm. The film thicknesses were 1 μm $\pm$ 50 nm, as measured by the quartz crystal microbalance. The cross sectional area is therefore expected to vary by $\pm$ 5% between the four wafers. This is supported by the $\pm$ 5% variation of the track resistances from the mean value of 5.25 Ω . A current of 100 mA, corresponding to a current density of 1.0 ($\pm$ 0.05) x $10^{10} A m^{-2}$ was used for the majority of tests.

It is likely that the film resistivities differed slightly as a result of their different microstructures. Resistivity could not be measured, however, because of

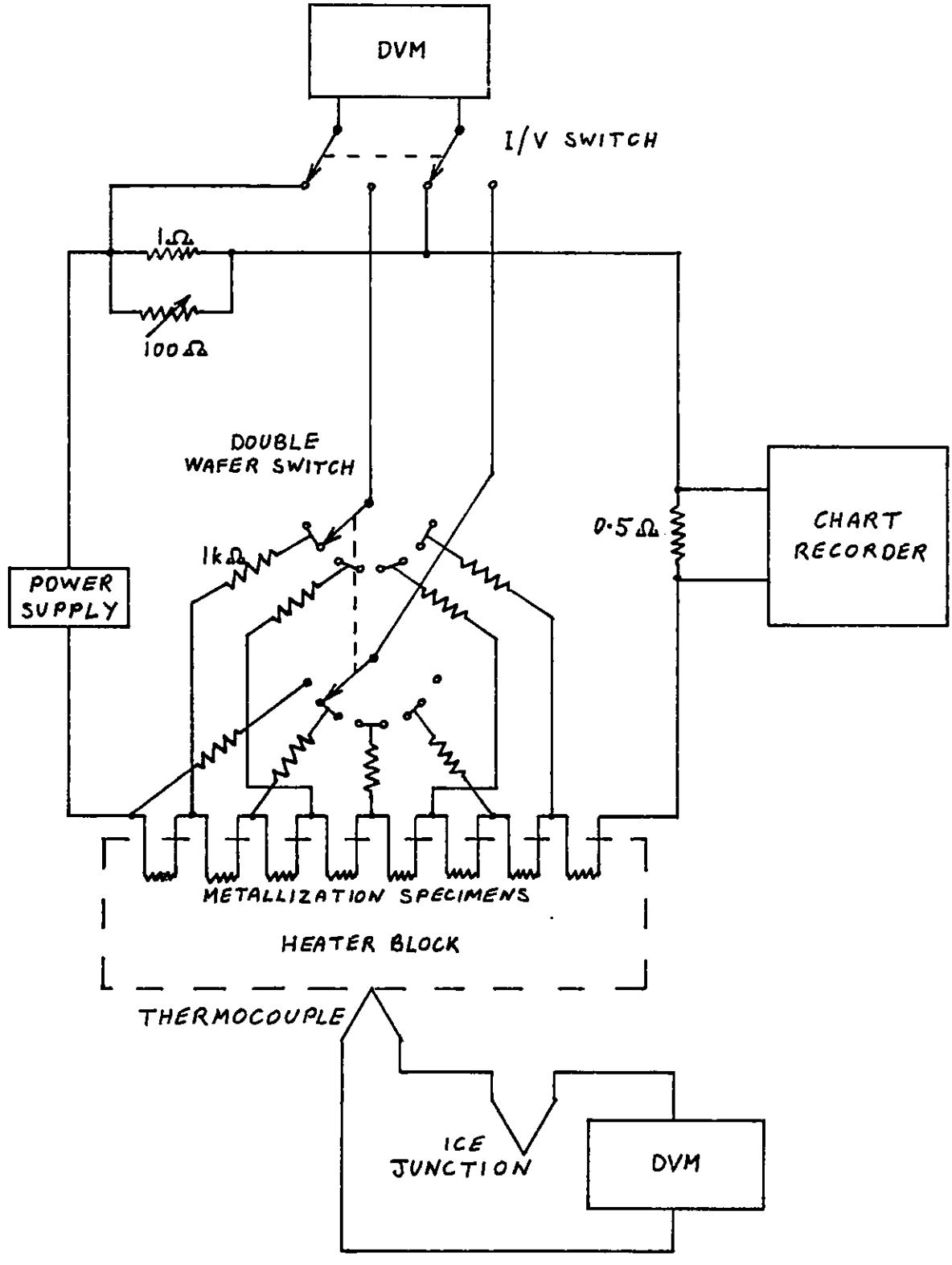

Circuit diagram of the electromigration life test equipment.

FIGURE 9.3

the uncertainties in the track dimensions and the unknown magnitudes of the contact resistances. Ideally a 4-point probe technique should be used (Harper 1970).

9.4 Experimental Method

When passing a current of approximately 100 mA, the temperature of the metallization was found to increase by a significant amount because of Joule heating. Since the track temperature (rather than the ambient temperature) controls the rate of electromigration, this temperature rise had to be determined. This was accomplished as follows.

A current of 1 mA was passed through the specimens at room temperature and the individual voltage drops, and hence track resistances, were determined. (A current of 1 mA did not cause appreciable Joule heating). The heater block temperature was raised to the required value for the test ($\sim$ 453 K), and the resistance measurement was repeated. Now, however, thermally generated emf's, which could be as large as 10% of the voltage drop, had to be taken into account. The thermal emf's were measured with the specimens open-circuit and then subtracted from the voltage drops measured when 1 mA was flowing. The temperature dependence of the track resistance dR/dT was determined for each specimen, assuming a linear increase of R with T. The required test current ($\sim$100 mA) was then applied and the track resistances again measured. (Thermal emf's were negligible compared with the voltage drops at 100 mA). The temperature rise ΔT of each specimen above the ambient (heater block) temperature was calculated using the equation :-

$$\Delta T = \frac{dT}{dR} \Delta R \qquad (9.1)$$

The mean temperature rise was approximately 5 K at 100 mA. Individual specimens in a batch varied by $\pm$ 1.5 K due to differences in track resistance and track-to-ambient thermal resistance. Resistance measurements can only give some

average value of the temperature along the track. However, measurements by Stephens and Sinnadurai (1974) using liquid crystals have shown that the temperature variation along a track carrying 1×10^{10} A m^{-2} is only of the order of 1 K.

The heater block was adjusted so that the mean track temperature was equal to the desired test temperature and the chart recorder monitoring the test current was started. The trace was examined at regular intervals to see if any specimen had failed. When this occurred, the current in all of the specimens fell to zero. This is thought not to affect the failure time distribution, as the maximum possible "down-time" was 14 hours (for a failure occurring overnight) and the total test time was typically 300 hours. The down-times were noted and subtracted from the total test time to give the effective "hours run". Failed specimens were located by resistance measurement and were short-circuited. The current was reapplied gradually to avoid causing failure by thermal shock. The track resistance of some specimens was measured at regular intervals during the test in order to observe the progression of electromigration damage with time.

Each batch was tested until approximately 95% of the specimens had failed. The specimens were allowed to cool and removed from the heater block. The TO5 cans were removed from the headers by careful use of a lathe fitted with a very fine parting tool. The metallizations were examined by optical microscopy (using a Nikon "Labophot") or by scanning electron microscopy (using a JEOL "JSM-35").

9.5 Test Conditions

The 40 specimens from each wafer were tested in 3 batches of 12 to 16 specimens per batch. This gave adequate statistics while enabling a reasonably wide range of test conditions to be investigated. For wafers A, B and D, the batches were tested at 1×10^{10} A m^{-2} and temperatures of 433 K, 453 K and 473 K in order to investigate the

temperature dependence of the MTF and permit extrapolation to lower temperatures. The test conditions were chosen to yield reasonable test times (several hundred hours) without overstressing the specimens.

For wafer C, one batch was tested at $1 \times 10^{10} A\ m^{-2}$ and 453 K, to allow a direct comparison of the MTF with the other three metallizations. The other two batches were tested at 518 K with current densities of $1 \times 10^{10} A\ m^{-2}$ and $3 \times 10^{9} A\ m^{-2}$, in an attempt to reproduce the "annealing" effects reported by Sim (1979) for aluminium metallizations of comparable grain size. (See section 8.6.4).

9.6 Results

9.6.1 Observations on the Failed Specimens

In all of the specimens, the current-carrying track was found to contain randomly distributed hillocks and voids, whereas the areas of metallization not subjected to an electric current were free from visible damage. It was therefore concluded that void and hillock formation resulted from the combined effects of high temperature and high current density (i.e. electromigration). In a given batch, the longest-lived specimens had the highest density of voids and hillocks.

The site of open circuit failure was always readily identifiable. The break in the track was accompanied by melting of the aluminium in about 95% of cases, usually with the formation of a large "droplet" of melted material on the anode side of the break. The electrical resistance of the broken track was effectively infinite in all cases. The distribution of failure sites along the track is shown in figure 9.4. The random nature of the distribution suggests that temperature gradient effects were negligible, except maybe near the bond pads, where the lower temperature might have been responsible for the small number of failures occurring in these regions. The failure sites are thus thought to be associated with structural irregularities in the aluminium

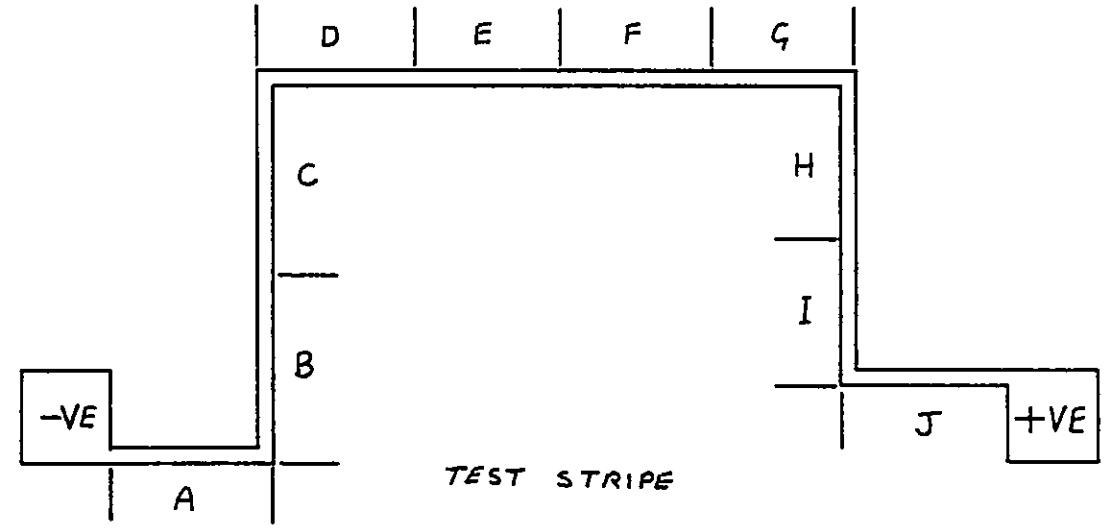

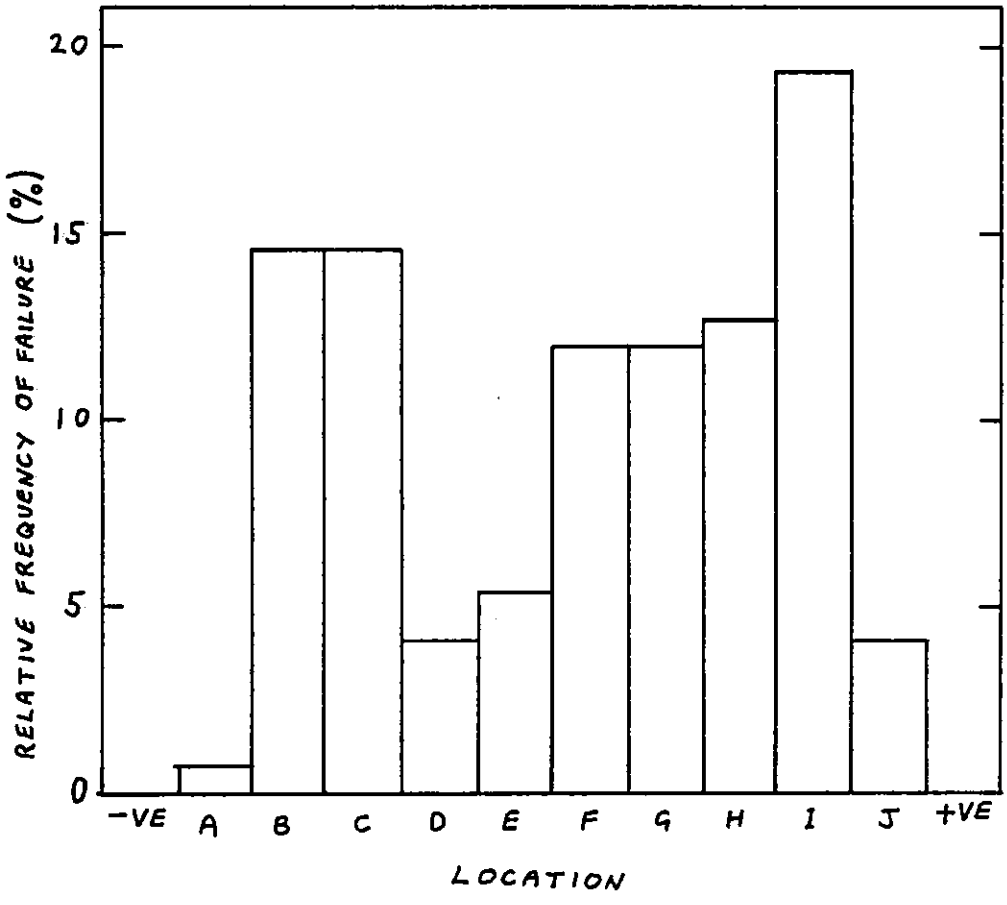

Distribution of failure sites along the test track.

FIGURE 9.4

film. This hypothesis is supported by the observation that in the larger-grained films, the voids were usually seen to follow the grain boundaries.

The smallest-grained (0.5 μm median grain size) metallization specimens suffered the highest density of void and hillock formation during testing, even though they tended to be shorter-lived than the larger grained specimens. Typical optical micrographs (figures 9.5a and b) show the general roughening of the current-carrying track. The scanning electron micrograph in figure 9.5c shows a typical open circuit failure site, while figure 9.5d shows a whisker, approximately 80 μm long and 500 nm in diameter, which grew during testing. Such whiskers were observed in approximately 10% of specimens from wafer A, but were very rare in specimens from the other wafers. The network of voids and small hillocks visible in figure 9.5d is typical of the pattern of electromigration damage in the small-grained films, irrespective of the test conditions.

Specimens from wafer B were of similar appearance, though with fewer hillocks and voids. This is thought to be due to the larger median grain size (1.7 μm) of the aluminium on wafer B, which meant that there were fewer potential damage sites per unit area of the metallization.

The large-grained (2.6 μm) aluminium from wafer C suffered very little overall degradation resulting from electromigration. A typical track contained several large voids, one or two of which almost spanned the track width. Voids were always seen to be associated with the grain boundaries, which were clearly visible in these specimens (see figure 9.6). No difference in the overall damage pattern was detected between specimens in batch C1, tested at 1×10^{10} A m^{-2} and 453 K, and batch C3, tested at 3×10^{9} A m^{-2} and 518 K. However, specimens in batch C2, which were tested at 1×10^{10} A m^{-2} and 518 K and gave a very short (24 hour) MTF, had an exceptionally low level of overall damage.

The metallization of wafer D had a small grain size and contained a high

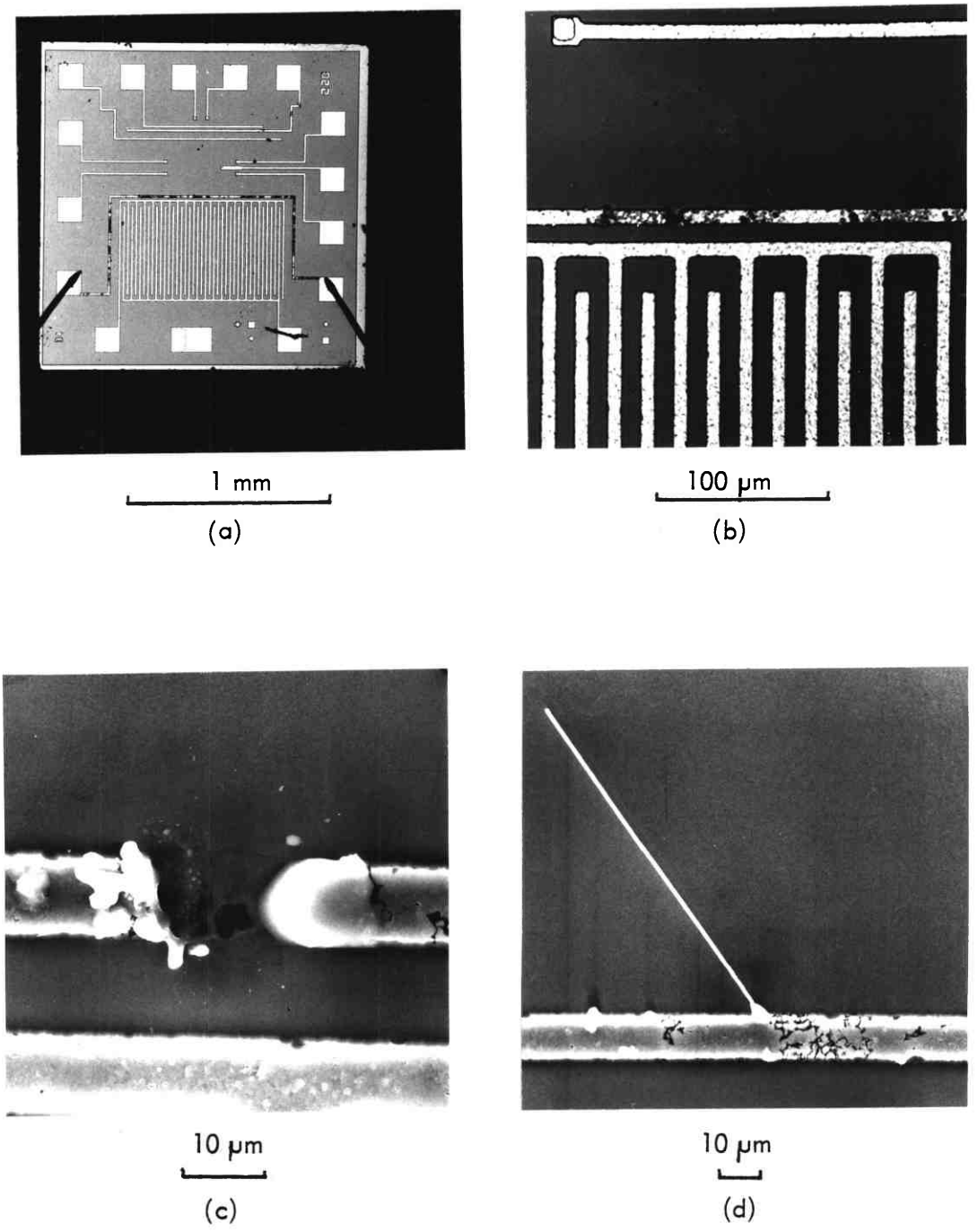

Electromigration damage in metallization A. Optical micrographs (a) and (b) show the general degradation of the current-carrying track and the region around a failure site. Scanning electron micrographs (c) and (d) show details of an open-circuit failure site and a whisker.

FIGURE 9.5

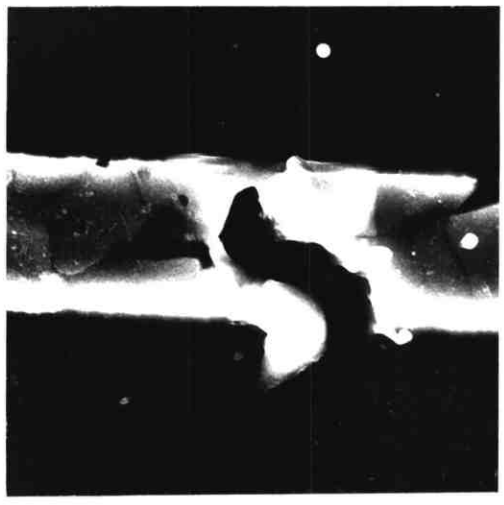

10 um

Scanning electron micrograph of a grain-boundary void in metallization C.

FIGURE 9.6

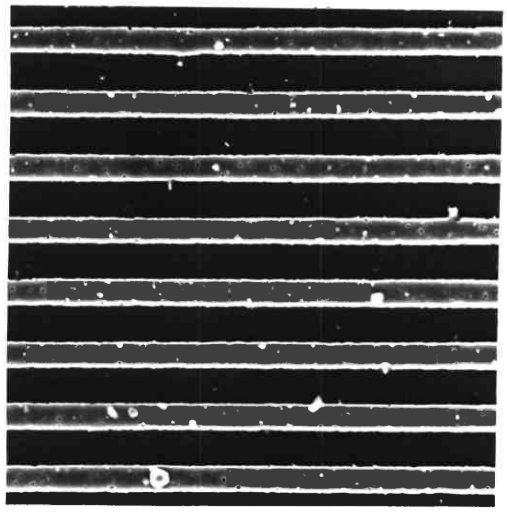

100 um

Scanning electron micrograph showing annealing hillocks in metallization D.

FIGURE 9.7

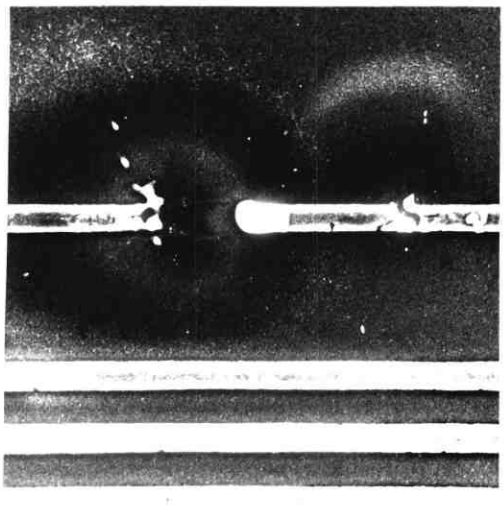

100 um

Scanning electron micrograph showing "halo" around a failure site.

FIGURE 9.8

density of annealing hillocks prior to accelerated life testing. Morphological changes resulting from electromigration were therefore difficult to detect (figure 9.7). As far as could be determined, however, the density of electromigration voids and hillocks in these specimens was similar to that found in specimens from wafer A.

In some specimens, the scanning electron microscope revealed a dark "halo" around the site of open circuit failure (see figure 9.8). The phenomenon was seen in specimens from all four wafers, usually where the failure had been exceptionally violent with severe melting of the aluminium and a large section of the track missing. EDAX failed to detect aluminium or any other element apart from silicon and oxygen in the haloes, so they do not appear to be formed by debris from the vaporized track. The effect may be due to crater formation as a result of local heating around the failure site, but this could not be clearly determined in the SEM.

9.6.2 Thermal Resistance

The thermal resistances of the metallization specimens were determined by dividing the temperature rise above ambient (say 453 K) by the power dissipated in the track due to a current of 100 mA. The results (see table 9.1) show that the mean thermal resistance is not critically dependent upon deposition temperature in the range 475 to 675 K. However, the thermal resistance of specimens from wafer D (which was annealed at 700 K for 2 hours after deposition) was between 10% and 15% lower than that of the other wafers.

9.6.3 Resistance Changes during Testing

Typical resistance versus time curves are shown in figure 9.9. The initial rate of increase of resistance was slow and was approximately the same for all the specimens in a batch. As the test time increased, the rate of resistance change accelerated and marked differences became apparent between various specimens. Where the MTF of the batch was short ($\sim$ 150 hours or less) the track resistance of

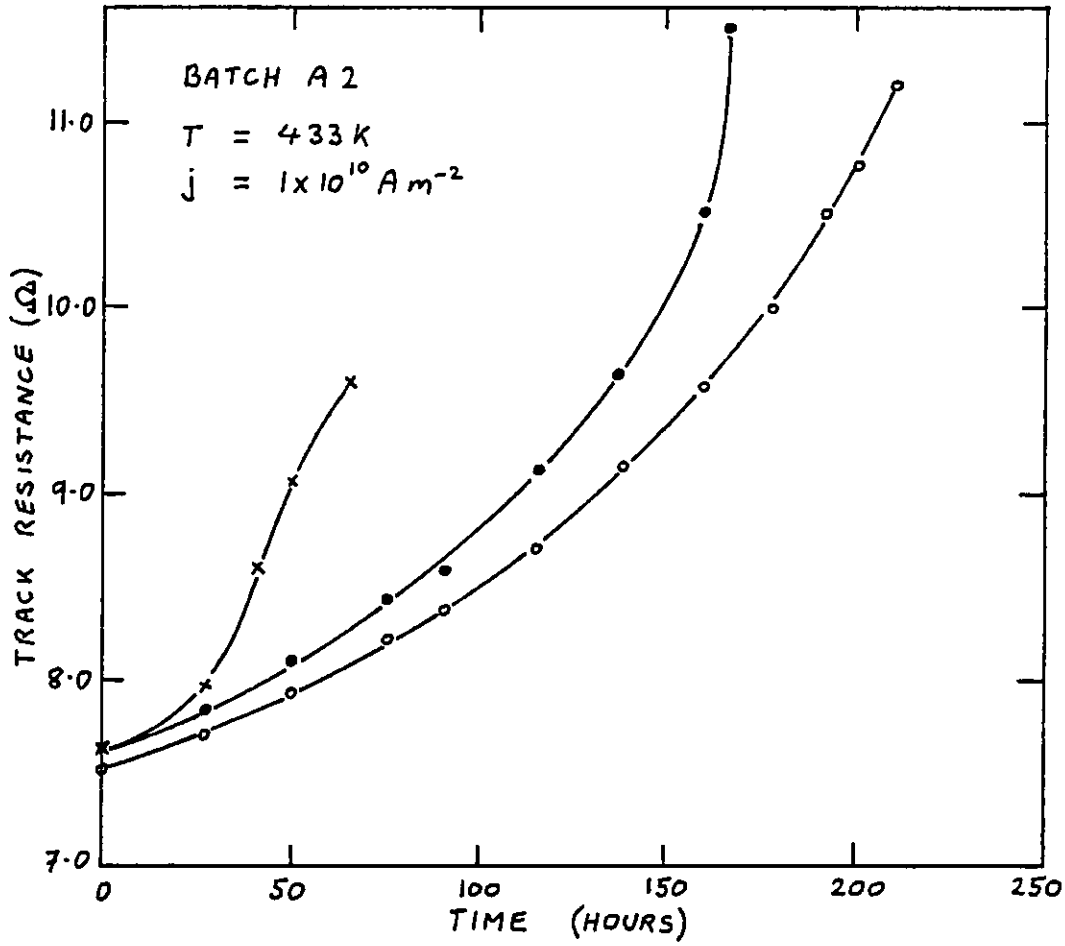

(a)

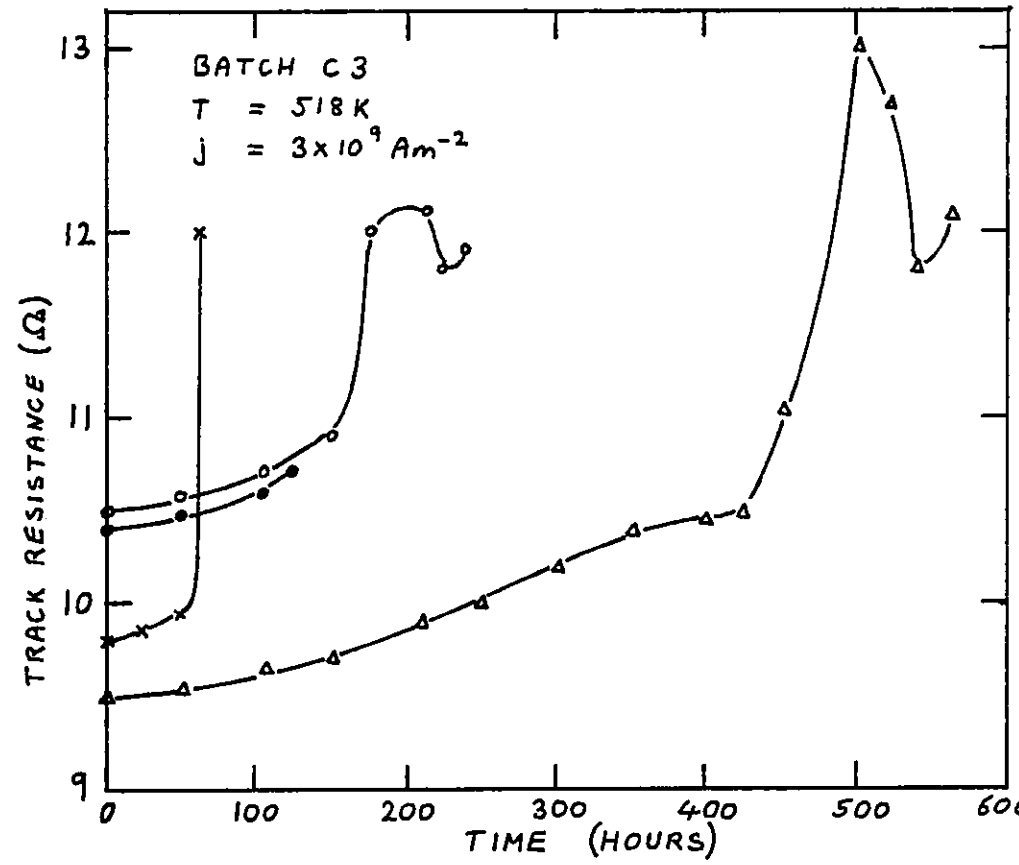

(b)

Variation of track resistance with time for (a) three specimens from batch A2 and (b) four specimens from batch C3.

FIGURE 9.9

each specimen increased steadily until open circuit failure occurred (figure 9.9a). For longer-lived specimens, however, the rate of change of track resistance often fluctuated and in some cases the resistance was seen to decrease with time (figure 9.9b). For these specimens, there was no correlation between the initial rate of change of resistance and the lifetime of the track.

9.6.4 Life Test Results

The failure data from the accelerated life tests were plotted on log-normal probability paper (figures 9.10 to 9.13), and a least squares fit was used to obtain the values of the median time to failure t_{50} and the standard deviation σ_f. The majority of the data was reasonably well represented by a log-normal distribution, although there was considerable scatter, giving rise to errors of up to $\pm$ 15% in t_{50} and $\pm$ 25% in σ_f. Plotting the results on log-extreme value graph paper did not improve the fit. This is not inconsistent with Schoen's model for electromigration failure (1980), since the median grain diameters of all the films tested were considerably smaller than the track width.

For wafers A, B and D, which were tested at $1 \times 10^{10} Am^{-2}$ at temperatures in the range 433 to 473 K, the standard deviations of the failure time distributions were fairly independent of the test conditions. For wafers A and B, σ_f was equal to 0.37 ± 0.07 and for wafer D, σ_f was 0.27 ± 0.07. There was no correlation between σ_f and the test temperature or the MTF. The variation of σ_f is thus thought to be due to random errors.

For wafer C, however, σ_f varied widely with test conditions. The batch tested at 453 K and $1 \times 10^{10} Am^{-2}$ gave a standard deviation of 0.6. This is significantly larger than the corresponding values for wafers A, B and D. This may be due to the larger mean grain size of wafer C, in accordance with Schoen's model. The batch tested at 518 K and $1 \times 10^{10} Am^{-2}$ gave a σ_f of 0.23 and the batch tested at 518 K

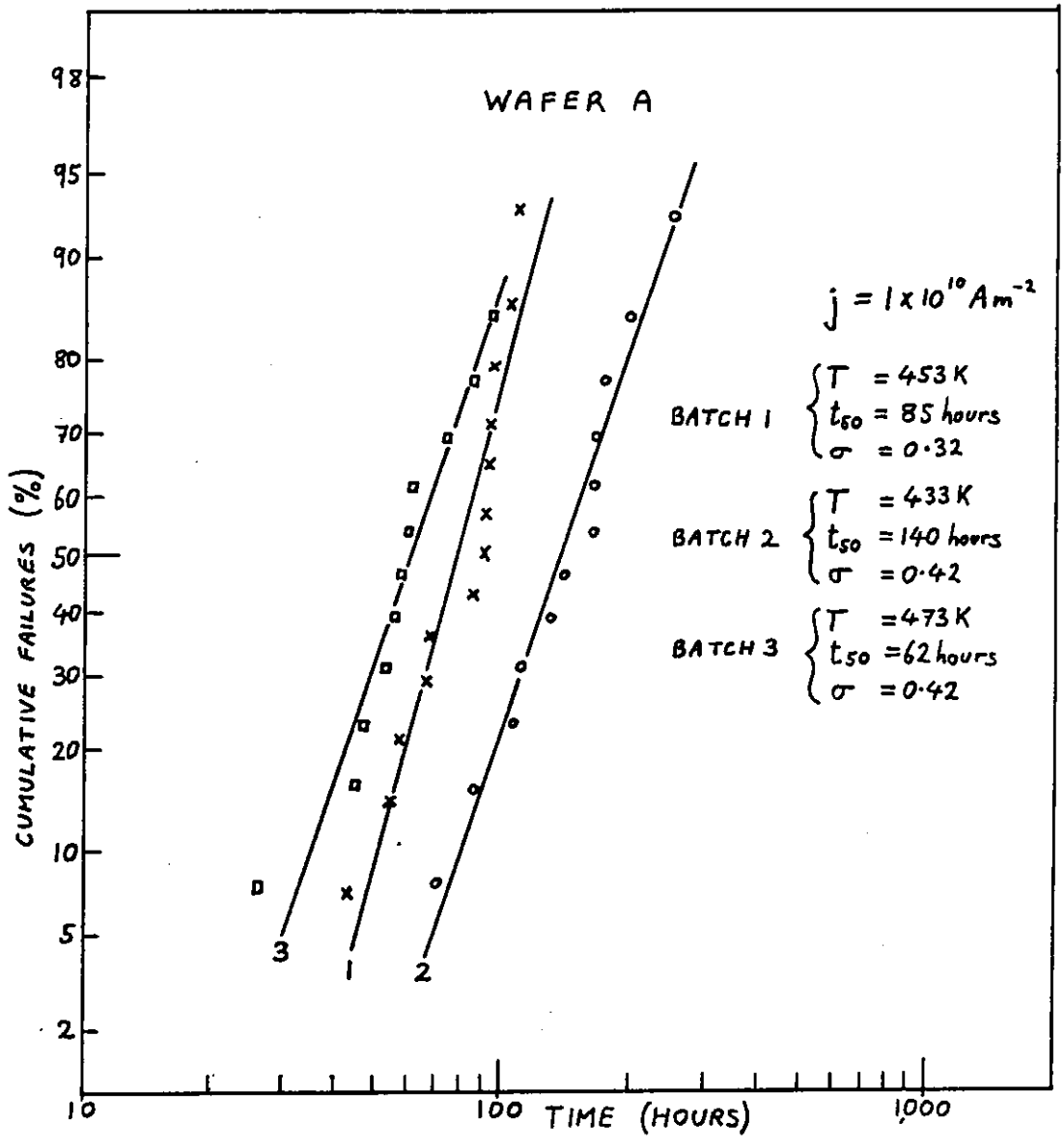

Log-normal plot of the failure time distributions of metallization A.

FIGURE 9.10

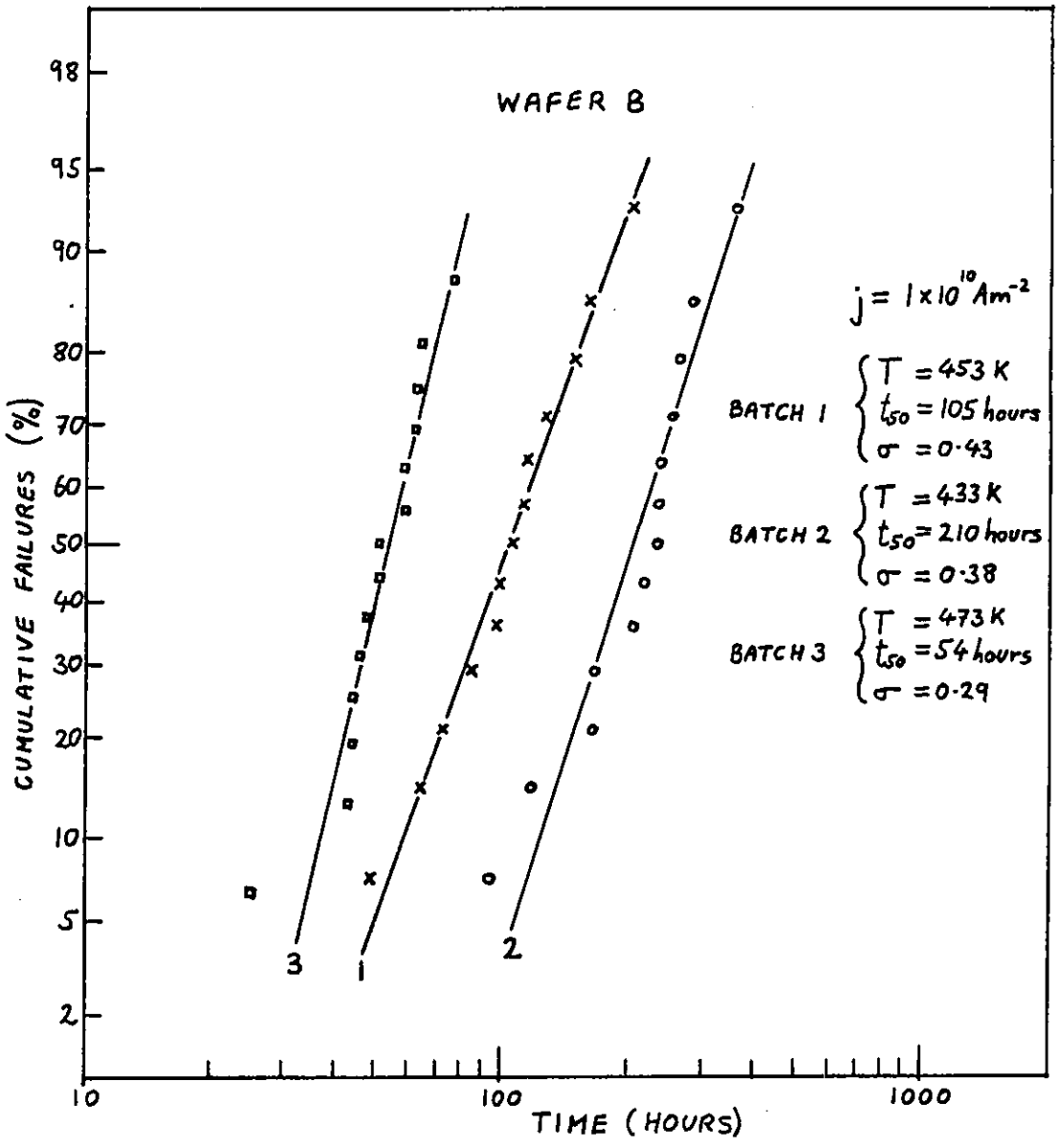

Log-normal plot of the failure time distributions of metallization B.

FIGURE 9.11

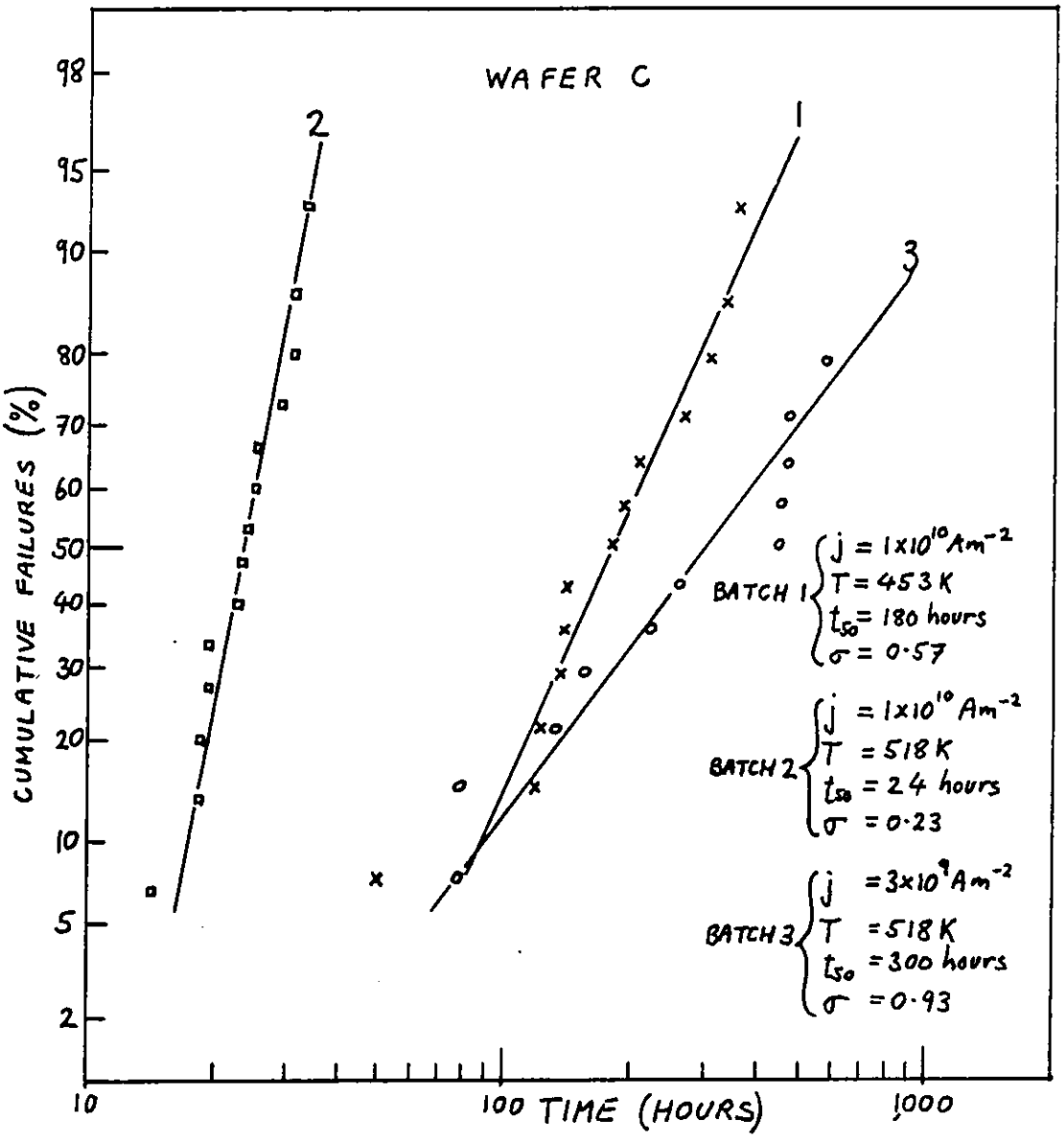

Log-normal plot of the failure time distributions of metallization C.

FIGURE 9.12

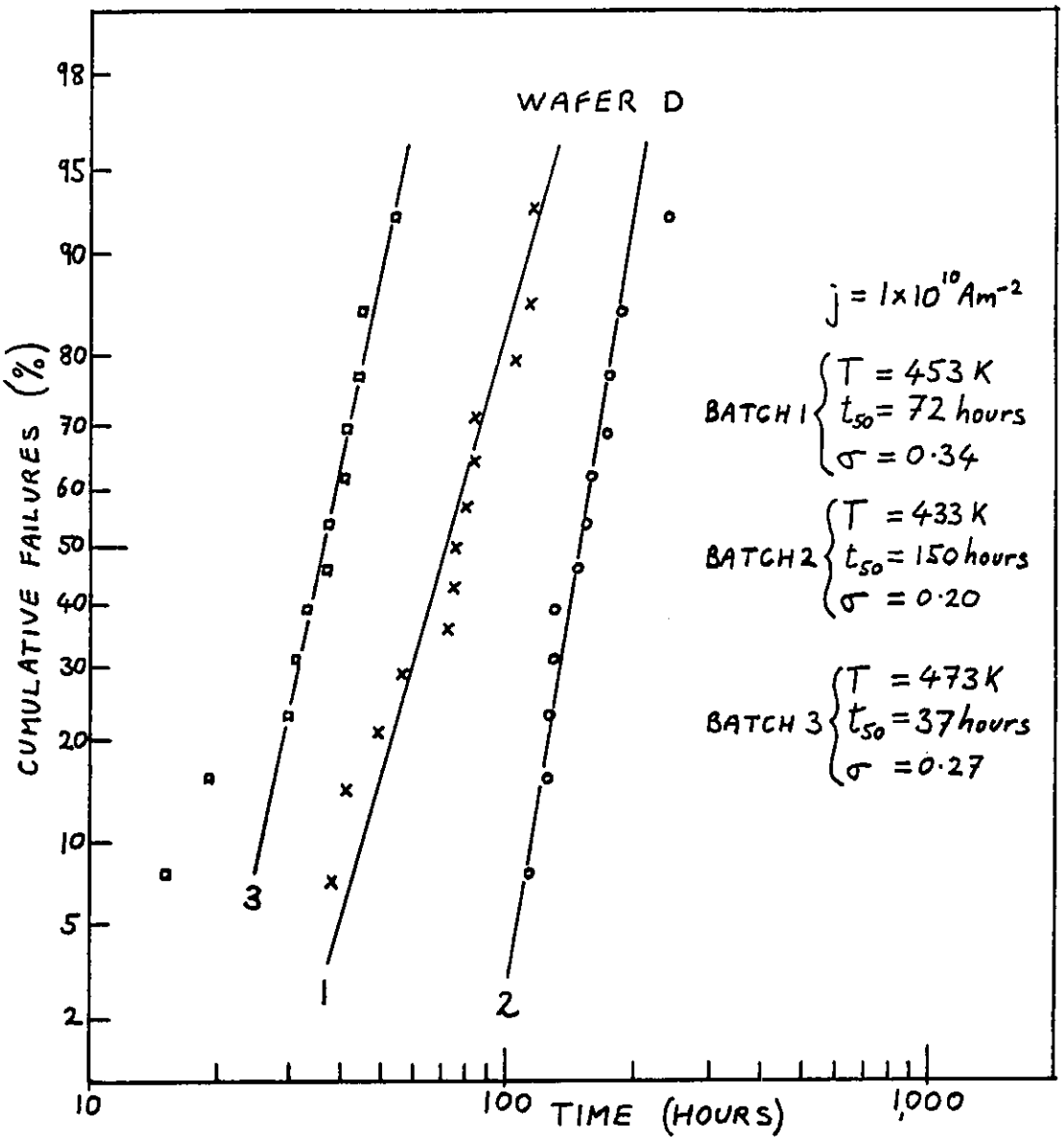

Log-normal plot of the failure time distributions of metallization D.

FIGURE 9.13

and $3 \times 10^9 Am^{-2}$ a σ_f of 0.93. These differences cannot be explained by statistical errors and may indicate a change of failure mode.

For all the metallizations tested, t_{50} decreased with increasing temperature. Arrhenius plots (figure 9.14) yielded an effective activation energy of 0.60 ± 0.05 eV for metallizations B, C and D and 0.35 ± 0.05 eV for metallization A. Because of this difference in ϕ, metallization A had a shorter MTF than metallizations B and D when tested at 433 K, and a longer MTF when tested at 473 K. For metallizations B, C and D, however, the MTF increased with median grain size d_o, regardless of test temperature. The relationship appears to be of the form $t_{50} \propto d_o^m$, with m equal to 1.0 ± 0.2 over the range of grain sizes investigated (see figure 9.15), in agreement with the results of Saito and Hirota (1974).

Extrapolation of the data to a track temperature of 350 K yields MTF's of 1300, 7000, 8500 and 18000 hours for metallizations A, D, B and C respectively. The use of the Venables and Lye model (1972) to predict the MTF's at a current density of 5×10^8 Am^{-2} yields a factor of 100 increase. The MTF's for the four metallizations are therefore approximately 15, 80, 100 and 200 years respectively. The corresponding times for 1% failure are approximately 6, 33, 35 and 55 years.

For wafer C, the current density dependence of the MTF was investigated at a temperature of 518 K. Assuming a relationship of the form $t_{50} \propto j^{-n}$, the results give a value of 2.1 ± 0.2 for n. This is consistent with the results of Sim (1979) and other workers. However, since only 2 data points were obtained from the present experiments, the power law dependence could not be verified.

The life test results are summarized in table 9.2.

9.6.5 Life Test Results from 50 nm-Oxide Specimens

These metallizations were very similar to the ones discussed in the preceding sections, except that the SiO_2 layer had a thickness of only 50 nm (compared with

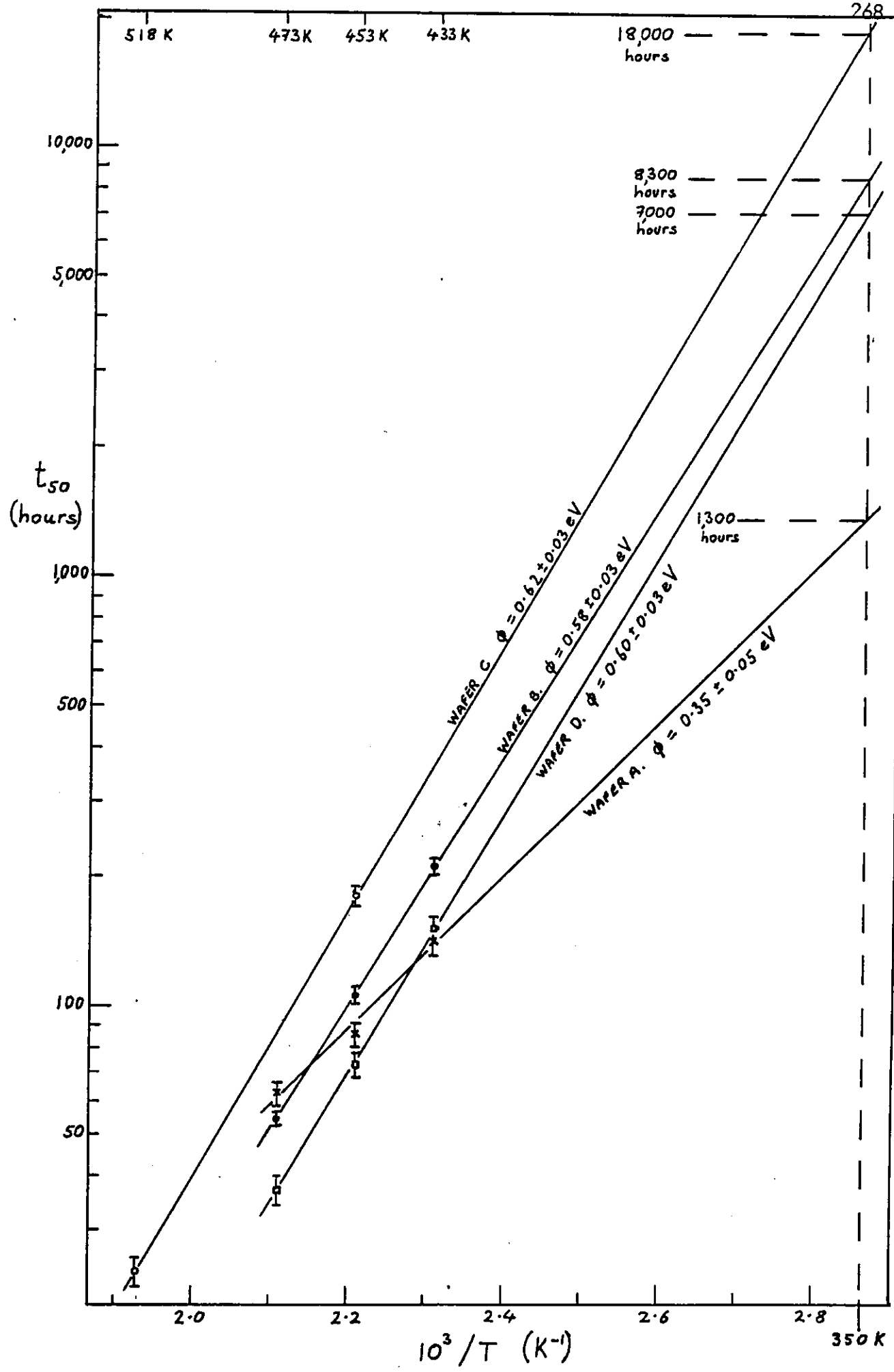

Arrhenius plots (median time to failure versus reciprocal temperature) for the four metallizations.

FIGURE 9.14

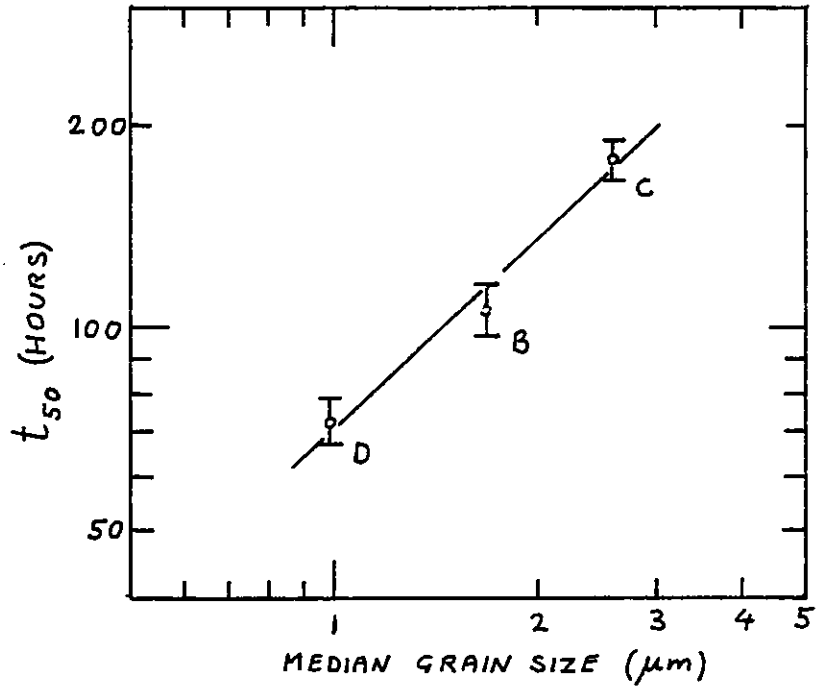

Log-log plot of median time to failure versus median grain size.

FIGURE 9.15

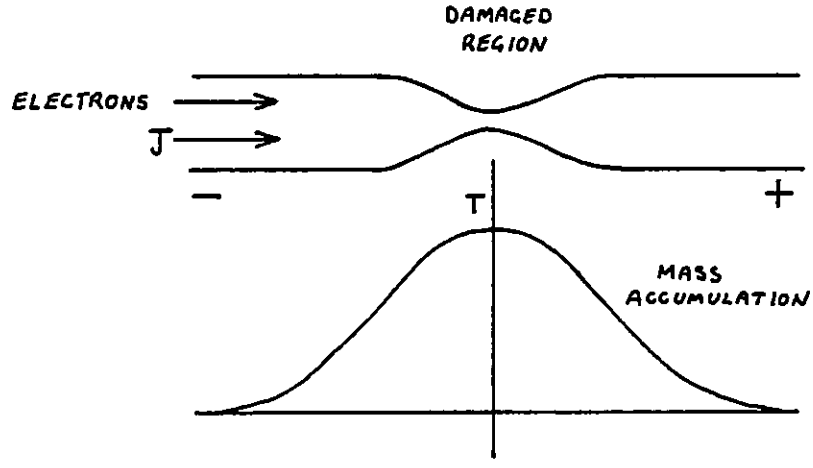

Localized temperature gradients in the region around an open-circuit failure site may cause mass accumulation on the anode side.

FIGURE 9.16

Wafer	Batch	Number of Samples	Temperature (K)	Current Density ($A\ m^{-2}$)	t_{50} (hours)	σ_f
	1	14	453	1×10^{10}	85 ± 5	0·3
A	2	13	433	1×10^{10}	140 ± 10	0·4
	3	13	473	1×10^{10}	62 ± 5	0·4
	1	14	453	1×10^{10}	105 ± 5	0·4
B	2	14	433	1×10^{10}	210 ± 10	0·4
	3	16	473	1×10^{10}	54 ± 5	0·3
	1	14	453	1×10^{10}	180 ± 10	0·6
C	2	15	518	1×10^{10}	24 ± 2	0·2
	3	14	518	3×10^{9}	300 ± 50	0·9
	1	14	453	1×10^{10}	72 ± 5	0·3
D	2	13	433	1×10^{10}	150 ± 10	0·2
	3	13	473	1×10^{10}	37 ± 3	0·3

Accelerated Life Test Data

TABLE 9.2

1 μm). Accelerated life tests were performed using a current density of $1 \times 10^{10} Am^{-2}$ and temperatures of 433 and 453 K. The specimen failure distributions were approximately log-normal, but the MTF's were a factor of 5 smaller than for the corresponding metallizations on 1 μm of SiO_2. Furthermore, when failure occurred, the track resistance did not increase at an accelerating rate, resulting in an open circuit, as for the other specimens. Instead, the resistance increased, then fluctuated with time as failure occurred, and the track never went open circuit. The final resistance was usually of the order of several k Ω and was dependent on the direction of current flow in the track.

Microscopic examination of the failed specimens revealed extensive discoloration of the metallization track and the surrounding substrate area. Often no localized failure site was visible. In view of this evidence and the rectifying nature of the failed track, failure is thought to have occurred by chemical reaction between the aluminium and the thin SiO_2 layer, resulting in an aluminium-silicon contact. The reaction may have been promoted by localized heating caused by incipient electromigration failure. Ionic motion in an electric field may also have been involved in the failure mechanism, as in these specimens one end of the test track was connected to header and was hence in electrical contact with the silicon die. Due to the voltage drop along the track, an electric field of up to $3 \times 10^{7} Vm^{-1}$ existed across the SiO_2 layer. Reversing the polarity of the connections, however, did not appear to change the failure process.

Because these specimens did not fail by the normal mechanisms, further tests were abandoned due to lack of time. Nevertheless, the failure mode involved may be important in certain circumstances and warrants further investigation.

9.7 Discussion

Metallization specimens A, B, C and D (i.e. those on 1 μm of SiO_2) appeared to fail by one of the normal electromigration failure modes, resulting in an open circuit condition. Whether flux divergence at a triple point or an abrupt change in grain size was the major cause of failure could not be determined, but all voids appeared to be associated with the grain boundaries.

The initial steady rise in track resistance during accelerated life testing is attributed to the formation and growth of microscopic voids. No incubation time effect was observed in the behaviour of the track resistance. This is consistent with the calculations of Rosenberg and Ohring (1971), which show that the incubation time for void formation is of the order of several minutes. As the voids grow, current crowding around the voids is thought to give enhanced Joule heating, leading to an accelerated rate of resistance change as observed. In short-lived specimens, this process simply continued until open circuit failure occurred. However, some reversal of the electromigration damage appears to have taken place in specimens which survived for longer than about 150 hours, as evidenced by the fluctuations in track resistance.

The effect may be due either to changes in the Al - SiO_2 interface or to changes in the microstructure of the aluminium. No changes in the overall appearance of the metallization were observed after testing (apart from the presence of voids and hillocks). It therefore seems likely that whatever changes were responsible for the reversal of the damage process were localized to the potential failure site and took place because of the high temperature and high atomic mobility in that region. Enhanced Al - SiO_2 reaction would promote better thermal contact between the metallization and the die (as shown by the thermal resistance measurements on annealed and non-annealed specimens). This would reduce the damage rate, but it is difficult to see how it could reverse the damage process. If the reaction products entered some of the aluminium grain boundaries

in the damaged region, however, a reversal of the flux divergence could result. Another possible explanation is the motion of grain boundaries (i.e. localized grain growth) in the vicinity of the failure site. This could, for example, change the configuration of a triple point so as to reverse the flux divergence. Examination of the damaged regions of a failed specimen by a sensitive analytical technique such as SIMS may reveal any chemical changes that have occurred. However, an in-situ microscope experiment will be necessary in order to detect structural changes in the metallization.

The final stage of open circuit failure appears to have occurred by melting of the aluminium, with a large droplet of metal usually being formed on the anode side of the failure region. This is believed to be due to an accumulation of metal on the anode side of the damaged region as a result of localized temperature gradients in the final stages of failure (see figure 9.16).

The standard deviation of the failure distribution showed some grain size dependence, in that films of 2.6 μm median grain diameter gave a larger σ_f than films of 1.7 μm median grain diameter and less. This is consistent with the statistical models described in section 8.6.2. The dependence of σ_f on the test conditions, observed in the large grained films, has not been investigated theoretically. The results can be qualitatively understood, however, by considering the potential for failure of various structural irregularities in the metallization as a function of test conditions. When the conditions are severe (i.e. high temperature and current density) a larger proportion of the sites of positive flux divergence are expected to be active (i.e. give rise to voids of considerable size) than when the current density and temperature are low. Therefore, the standard deviation of the failure distribution will be smaller for severe test conditions, as observed. An alternative explanation is that under certain extreme conditions, "annealing" of the metallization occurs,

resulting in a change in microstructure (Sim 1979). The large standard deviation obtained using very high test temperature and low current density (to prolong life time) observed in the present work supports Sim's results (see section 8.6.4).

The thermal resistance measurements indicated that high temperature annealing can improve thermal contact between the metallization and the die, though the improvement was only $\sim$ 10% for a 2 hour anneal at 700 K. Apparently, the thermal resistance was independent of deposition temperature in the range 475 - 675 K, suggesting that Al - SiO_2 interface formation at 475 K was adequate for good thermal contact. This result is somewhat surprising in view of the TEM results on the Al - SiO_2 interface (Chapter 4) which showed that crystalline reaction products were only produced at temperatures of 575 K and above. The discrepancy may be due to a greater temperature rise during the deposition of the 1 μm films used for the electromigration experiments than with the 50 nm films used for the interface study. (The temperatures quoted are substrate temperatures at the beginning of the deposition process). Alternatively, the extent of interfacial reaction needed for good thermal contact may be less than the detection limit of the TEM experiment. Another possible explanation is that small differences in the metallization-die thermal resistance between the different metallizations were obscured by variations in the die-header thermal resistance.

All four metallizations were found to have a strong $\langle 111 \rangle$ fibre texture and all had roughly the same grain size standard deviation. Therefore, the possibility of variation in these parameters affecting the electromigration performance was ruled out in the present study. The difference in MTF between the four metallization specimens is therefore attributed mainly to median grain size differences. Variations in Al - SiO_2 interface structure and surface topography, however, could also be important. For example, the presence of growth hillocks in metallization A might affect any surface

diffusion mechanism involved in electromigration failure, and could explain the large discrepancy in effective activation energy between film A and films B, C and D. A smaller Al - SiO_2 interface width, due to the lower deposition temperature of metallization A, may have affected the damage mechanism by reducing interfacial diffusion. These questions are difficult to resolve, however, because of the inter-dependence of deposition temperature, surface topography, grain size and interface structure of thin film metallizations.

9.8 Conclusions

(i) The electromigration MTF of aluminium metallizations shows an approximately linear increase with median grain size.

(ii) The standard deviation of the failure time distribution tends to increase as grain size approaches track width.

(iii) The failure time standard deviation is dependent on the accelerated life test conditions. σ_f is reduced by the use of high temperatures and current densities.

(iv) Metallization-die thermal contact is improved by annealing, but the effect is small.

(v) Metallizations deposited at 575 K and 675 K have an effective activation energy for electromigration failure of 0.6 eV, as do metallizations deposited at 475 K and annealed at 700 K for 2 hours. Metallizations deposited at 475 K without annealing have an effective activation energy of 0.35 eV.

(vi) The MTF varies inversely as the square of the current density in the range 3×10^9 to $1 \times 10^{10} Am^{-2}$ at 518 K.

(vii) "Annealing effects" in the final stages of electromigration failure can reduce the damage rate or even reverse the damage process.

CHAPTER 10

SUMMARY

The effects of deposition conditions and annealing treatments on the internal microstructure and interface structure of evaporated aluminium thin films on thermally oxidized silicon were investigated using a variety of experimental techniques. The electromigration performance of films of different microstructures was then assessed by accelerated life testing. The main conclusions to be drawn from these experiments are summarized in the following.

Aluminium films, deposited onto amorphous SiO_2 by tungsten-filament evaporation in a vacuum of better than 2×10^{-6} mbar, followed an island growth mode. The island size and the mean thickness at which complete coverage was attained increased with substrate temperature in the range 295 K to 675 K. The grain size distributions of 1 μm thick films were found to be log-normal, and the median grain size ranged from 0.5 μm for deposition at 295 K to 2.6 μm at 675 K. Post-deposition annealing resulted in some grain growth, but the process was very slow at temperatures less than 450 K. All the 1 μm thick films had a strong $\langle 111 \rangle$ fibre texture. "Growth hillocks" were observed on the surfaces of some films, but their occurrence was suppressed by the use of deposition temperatures in excess of 475 K, deposition rates of 10 nm s^{-1} and residual gas pressures in the region of 2×10^{-6} mbar.

In aluminium films deposited under normal high vacuum conditions onto "as prepared" thermally oxidized silicon subtrates at 575 K and above, Al - SiO_2 reaction occurred to give an interfacial layer containing polycrystalline silicon and η - Al_2O_3. The thickness of the reaction zone was estimated to be several nanometres. Higher deposition temperatures and post-deposition annealing treatments brought about further interfacial reaction. Aluminium films deposited onto ion-bombarded SiO_2 under ultra high vacuum conditions reacted with the substrate at room temperature over a period of

several hours, to give an interfacial reaction zone of approximately monolayer thickness. Aluminium deposited onto "as prepared" SiO_2 under the same conditions, however, did not react at room temperature. Water vapour adsorbed by the SiO_2 surface is thought to be responsible for the reduced reaction rate of the latter specimens.

Accelerated life tests were carried out on four different metallization specimens with median grain sizes in the range 0.5 μm to 2.6 μm, produced by deposition at different substrate temperatures and in one case by post-deposition annealing. (Aluminium films of smaller grain size, prepared by deposition at 295 K, could not be used for electromigration testing. This was because of poor film-substrate adhesion as a result of lack of interfacial reaction at this temperature). The films tested failed by an open circuit failure mode characterized by the formation of voids at the grain boundaries. The failure sites are believed to be associated with local divergences of the electromigration flux due to structural irregularities in the film.

The failure time distributions were approximately log-normal. The median time to failure increased approximately linearly with median grain size and the standard deviation of the failure time distribution also tended to increase with grain size. This is consistent with the statistical models for electromigration failure of Attardo et al (1971) and Schoen (1980). The MTF of all films had an inverse exponential (Arrhenius type) temperature dependence in the range 433 to 518 K. The three films of larger median grain size (1.0 μm to 2.6 μm) gave an effective activation energy for electromigration failure of 0.60 ± 0.05 eV, in good agreement with most published results. The films of 0.5 μm median grain size, however, gave an activation energy of 0.35 ± 0.05 eV. This result is not fully explicable in terms of any known theory of electromigration failure, but differences in the topography of the free aluminium surface or the structure of the Al - SiO_2 interface due to the relatively low deposition temperature

(475 K) of this metallization may be responsible. The effect of current density acceleration was only investigated for the largest-grained film. The MTF was found to be inversely proportional to the square of the current density between 3×10^9 and 1×10^{10} Am^{-2} at 518 K, in agreement with the majority of published results. The standard deviation of the failure time distribution tended to decrease with increasing severity of test conditions. This effect is thought to be due to an increase in the number of active damage sites under conditions of high temperature and current density.

From the above results it is evident that the deposition conditions have a marked effect on the electromigration performance of aluminium thin film metallizations. For optimum reliability, the following rules for the metallization process should be observed:

(i) The SiO_2 surface should be clean in order to facilitate the Al - SiO_2 interfacial reaction which is essential for good adhesion of the metallization.

(ii) The deposition temperature should be high enough to promote the Al - SiO_2 interfacial reaction ($\gtrsim$ 475 K). In order to produce a large grain size and hence optimise the electromigration MTF, a higher substrate temperature is beneficial. A temperature of 675 K yields a median grain size of approximately 3 μm in 1 μm thick aluminium films and gives high reliability of 10 μm wide tracks.

(iii) High deposition rates ($\sim$ 10 nm s^{-1}) and low residual gas pressures ($\sim 1 \times 10^{-6}$ mbar) promote a large grain size, $\langle 111 \rangle$ fibre texture and smooth aluminium surface, all of which are conducive to high reliability.

(iv) High temperature annealing causes grain growth, which may be desirable for increased electromigration MTF. However, annealing also enhances the Al - SiO_2 reaction and roughens the aluminium surface and may therefore be detrimental to the performance of some MOS devices and multi-level structures. The high temperature 'sintering' process often used to obtain good Al-Si Ohmic contact could thus jeopardize the reliability or performance of certain devices. It may be possible to obviate the need

for "sintering" by chemical cleaning of the contact windows and the use of a high deposition temperature in the metallization process.

The results of the present study apply strictly to 10 μm pure aluminium metallizations on silicon-based devices. For many other types of device, the metallization system has still to be optimized. In the case of VLSI devices using 1 μm wide metallizations, some progress has already been made, but our understanding of electromigration damage in very narrow conductor stripes is far from complete. The reliability of aluminium metallizations has been improved by the addition of copper. Further optimization by the use of a third alloy element seems possible, but will require considerable experimentation.

Devices based on compound semiconductors require different metallization schemes presenting new reliability problems which may be investigated by use of a combination of techniques. For example, XPS and TEM have proved useful in the study of the Al - SiO_2 interfacial reactions and may be applied to other metal-insulator and metal-semiconductor systems. In addition the use of SIMS for the detection of hydrogen is suggested. TEM, in conjunction with a suitable thinning technique (e.g. chemical or ion-beam etching), is a valuable tool for examination of the microstructure of metallizations on "real" substrate materials. For alloy metallizations, the use of STEM with micro-diffraction and micro-EDAX facilities may yield information on the distribution of the various alloy elements within the film.

APPENDIX A

THE PREPARATION OF THE SiO_2 SUBSTRATES

SiO_2 subtrates were prepared by oxidizing polished, single crystal silicon wafers. Two types of wafers were used : 1-inch wafers of {111} - oriented n-type silicon of 4×10^{-2} Ω m resistivity, and 2-inch wafers of {100} -oriented p-type silicon of 6×10^{-2} Ω m resistivity. The first type were all given a 1 μm oxide layer and were used in the XPS experiments. The second type were given either a 50 nm oxide layer (for use in the TEM experiments) or a 1 μm layer (for use in the accelerated life test experiments).

The oxidation procedures were as follows. The polished wafers were cleaned by boiling in nitric acid for 15 minutes, then immersing in a 5% aqueous solution of hydrofluoric acid for 30 seconds. 50 nm SiO_2 layers were grown by heating the wafers in a silica tube at 1148 K for 10 minutes in oxygen, followed by 25 minutes in steam, followed by a further 10 minutes in oxygen. 1 μm SiO_2 layers were grown by heating at 1153 K for 10 minutes in oxygen, followed by 16½ hours in steam and a further 10 minutes in oxygen.

All subtrates were prepared at the British Telecom. Research Labs.

APPENDIX B

CALIBRATION OF THE QUARTZ CRYSTAL MICROBALANCE

The quartz crystal microbalance, used to measure the thickness of evaporated aluminium films, was calibrated using the technique of FECO (fringes of equal chromatic order). The technique has been described in detail by Tolansky (1948) and Scott et al (1950) and only a brief outline is given here.

The aluminium film whose thickness was to be determined was deposited onto a clean glass microscope slide. A channel was scored in the film, using a fine needle, so that the substrate was exposed. A 50 nm (i.e. totally reflecting) aluminium film was then deposited on top of the first film, to give a reflecting surface which followed the contours of the first film (see figure B1). A second glass slide with a 20 nm (i.e. partially reflecting) aluminium film was clamped in front of the first slide, so that the two aluminium surfaces were parallel and in close proximity. Multiple beam interference fringes of equal chromatic order were obtained from the plates using the experimental arrangement shown in figure B2. The spectrum (figure B3) consisted of dark fringes, each of which contained a "step" corresponding to the channel in the film. The channel depth Δt (which was equal to the thickness of the first aluminium film) was determined from measurements of the fringe positions λ and "step heights" $\Delta\lambda$, using the equation :

$$\Delta t = \frac{n}{2} \Delta\lambda_1 \qquad (B1)$$

where

$$n = \frac{\lambda_2}{\lambda_1 - \lambda_2} \qquad (B2)$$

Δt was determined from each visible fringe (of which these were typically 5) and the mean value taken. FECO measurements were performed on 5 films of thicknesses

in the range 30 nm to 1 μm and the results plotted against the corresponding frequency changes of the quartz crystal microbalance. Figure B4 shows the microbalance to be linear in the range of interest with a sensitivity of 19.5 Hz nm^{-1}. These results were obtained using one quartz crystal which was clean when the calibration experiment was started and had a 2 μm coating of aluminium by the end of the experiment. Crystals used in the experiments described in Chapters 4, 7 and 9 were replaced when they had acquired a coating of 2 μm or less, since the accumulation of thicker layers is believed to affect their sensitivity (Heyman and Miller 1978).

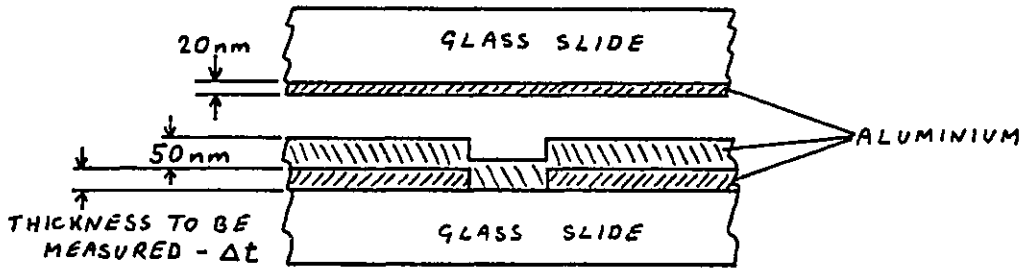

The interference plates.

FIGURE B.1

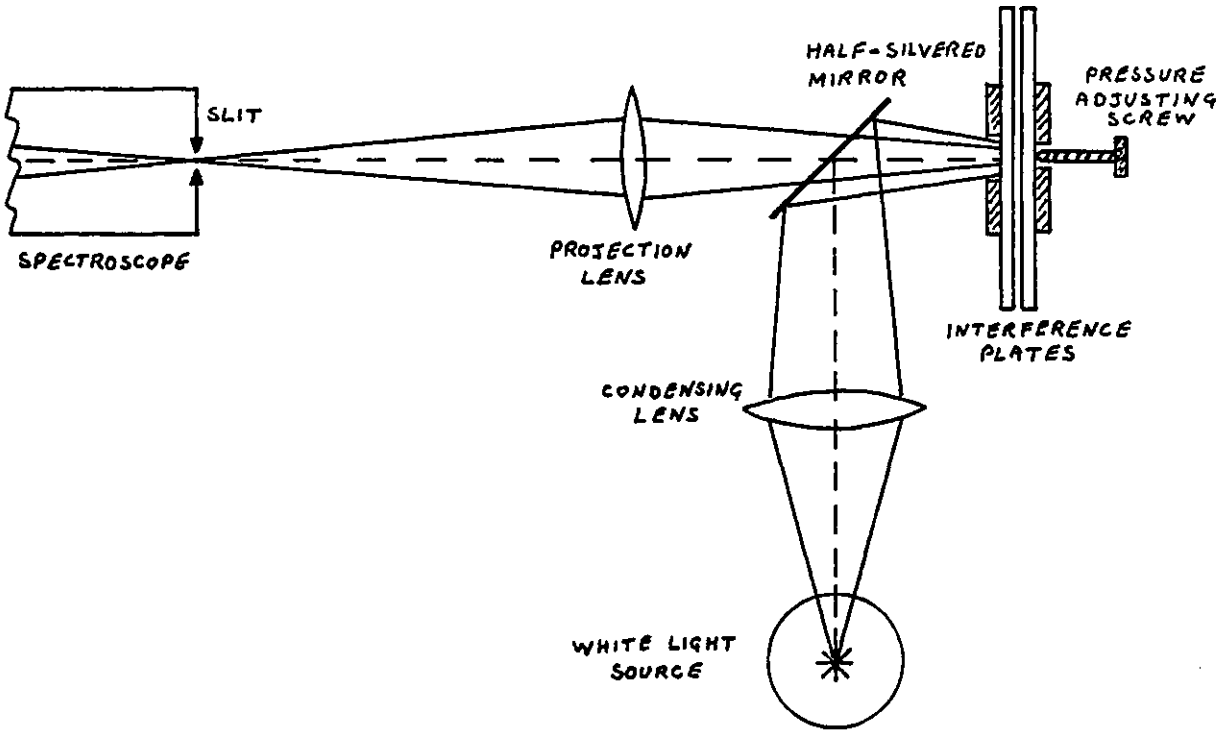

The interferometer.

FIGURE B.2

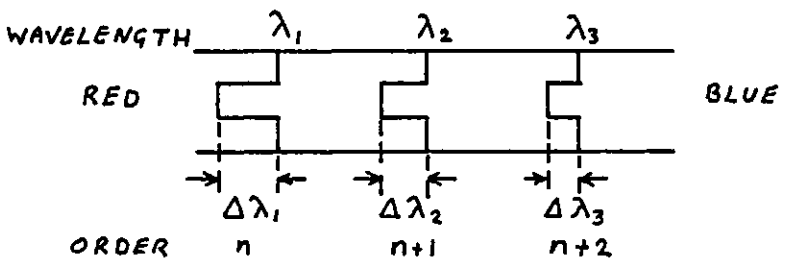

The appearance of the fringes.

FIGURE B.3

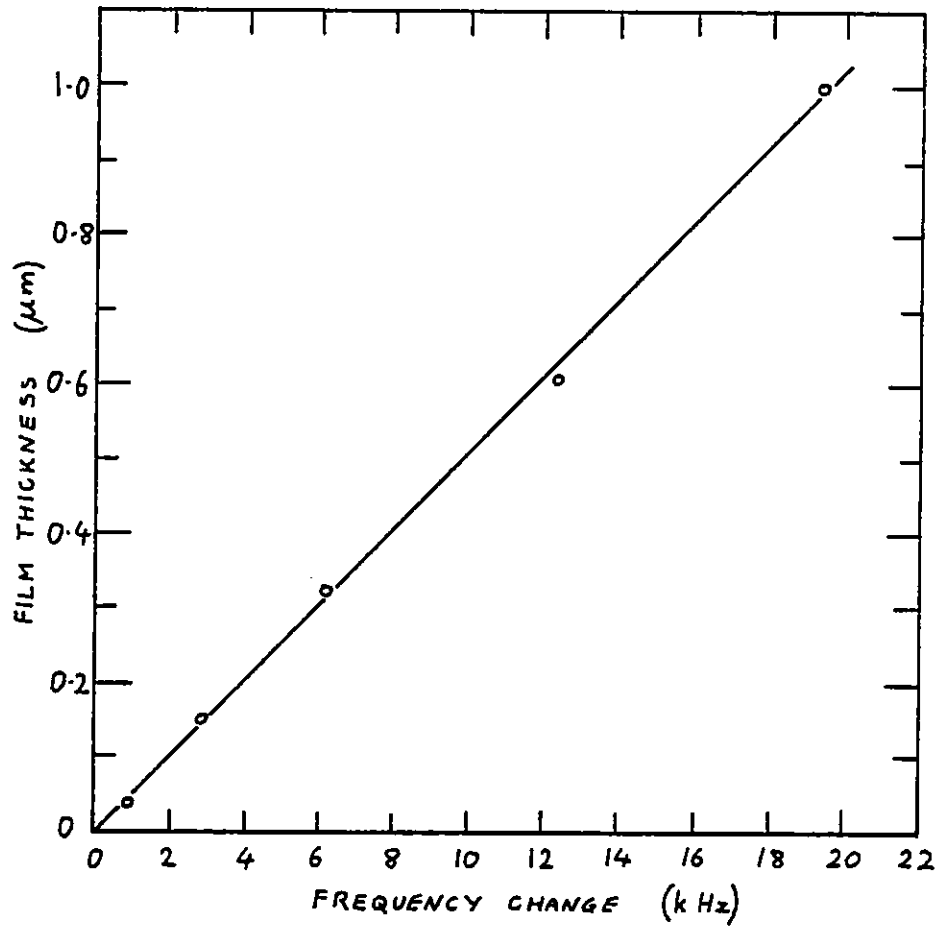

Calibration curve for the quartz crystal microbalance.

FIGURE B.4

APPENDIX C

CALIBRATION OF THE THERMOCOUPLES

The temperature of the oxidized silicon wafer during aluminium deposition was measured by a chromel-alumel thermocouple positioned at the edge of the substrate holder (Chapters 4 and 7). This was calibrated against a chromel-alumel thermocouple embedded in a lead pellet which was placed on the centre of a test wafer. The melting point of the lead, determined from a cooling curve, was used as the calibration point. The calibration curve is shown in figure C1. By use of the thermocouple at the edge of the substrate holder, the temperature at the centre of the substrate could be determined to $\pm$ 5 K. Another thermocouple placed near the edge of the substrate showed that the temperature variation over the substrate surface was less than 10 K.

The chromel-alumel thermocouple used in the in-situ TEM experiments (Chapter 4) was calibrated directly against the melting point of lead. Lead was deposited onto graphite substrates in a vacuum evaporation plant to produce particles of approximately 250 nm diameter. These particles had crystallographic shapes which were clearly visible in the TEM. The specimens were heated in-situ for several minutes at temperatures just below the melting point of lead, as determined by the chromel-alumel thermocouple. The temperature was then allowed to fall by $\sim$ 20 K and the lead particles were examined by TEM to see if melting had occurred (this procedure circumvented the possible effects of electron beam heating). The process was repeated, the temperature being increased in steps of 1 K until melting was observed (i.e. the particles lost their crystallographic shapes and became spherical). The depression of the melting point due to particle size effects is negligible for diameters of the order of 250 nm (Spiller 1979).

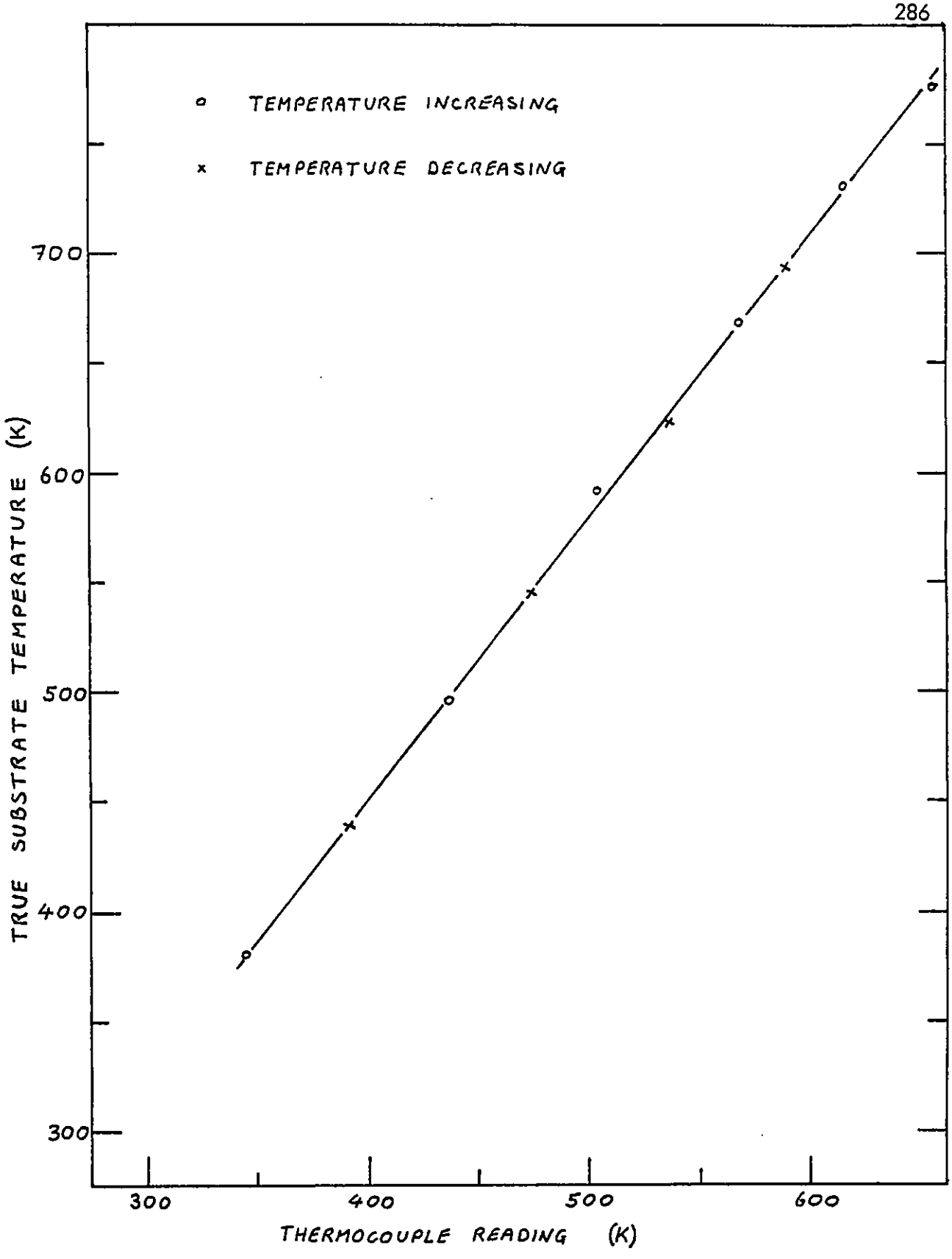

Thermocouple calibration curve.

FIGURE C.1

APPENDIX D

THE CRYSTAL STRUCTURE OF THE ALUMINAS

The properties of all the known forms of alumina have been reviewed by Wefers and Bell (1972). The gamma (γ) and eta (η) phases are two of the "transition aluminas" which exist at temperatures up to $\sim$ 1,100 K. They transform to the stable α-phase (corundum) via the δ- or θ-transition phases. The transition aluminas cannot be formed from α-alumina. They are thought to be thermodynamically unstable states of structural reordering. The transition aluminas are not true polymorphs of Al_2O_3 and are believed to contain hydroxyl ions.

η-alumina has a spinel structure of lattice constant 0.790 nm. The cubic close-packed stacking has a strong 1-dimensional disorder and the spinel lattice is tetragonally deformed.

γ-alumina also has a spinel structure, with a well ordered oxygen sublattice and disordered aluminium sublattice. The octahedral cation sites are believed to be fully occupied, but the tetrahedral sites have numerous vacancies. This gives rise to a strong tetragonal deformation and the unit cell has lattice constants :-

$$a_o = 0.562 \text{ nm} ; \quad c_o = 0.780 \text{ nm}$$

γ-alumina may contain varying amounts of hydroxyl ions.

α-alumina has a rhombohedral structure with the oxygen atoms forming nearly close-packed layers and the aluminium atoms lying in some of the interstices. The close packing results in the higher density of α-alumina (3.9×10^3 kg m^{-3}) compared with η- and γ-alumina ($\sim 3.2 \times 10^3$ kg m^{-3}).

APPENDIX E

STATISTICAL NOTES

E.1 The Log-Normal Distribution

The log-normal distribution represents a random variable whose logarithm follows a normal distribution. The probability density function $p_{LN}(X)$ is given by :-

$$p_{LN}(X) = \frac{1}{\sqrt{2\pi}\,\sigma_{LN}} \frac{1}{X} \exp\left[-\frac{1}{2\sigma_{LN}^2}(\ln X - \mu_{LN})^2\right] \qquad (E.1)$$

where μ_{LN} and σ_{LN} are numerical constants. The form of the distribution is shown in figure E.1. (Eadie et al 1971).

If $Y(= \ln X)$ is used as the variable, the distribution becomes a simple Gaussian :-

$$p_G(Y) = \frac{1}{\sqrt{2\pi}\,\sigma_G} \exp\left[-\frac{1}{2\sigma_G^2}(Y - \mu_G)^2\right] \qquad (E.2)$$

of standard deviation σ_G and mean μ_G. The mean is also equal to the median and mode of the distribution.

The cumulative normal distribution is given by :-

$$P_G(Y) = \int_{Y_{min}}^{Y} p_G(Y')\,dY' \qquad (E.3)$$

where $P_G(Y_{min}) = 0$ and $P_G(Y_{max}) = 1$. The median value of Y, Y_{50} is defined by $P_G(Y_{50}) = 0.5$.

The log-normal plots used in Chapters 7 and 9 are plots of $P_G(Y)$ against Y. The probability that a measurement will lie between $Y_{50} - \sigma_G$ and $Y_{50} + \sigma_G$ is 0.683. Hence σ_G is readily determined from the log-normal plot.

E.2 The Log-Extreme Value Distribution

The log-extreme value distribution represents a random variable X whose

logarithm Y follows the extreme value distribution defined by :-

$$p_{EV}(Y) = \frac{1}{\sigma_{EV}} \exp\left[\pm \frac{\mu_{EV} - Y}{\sigma_{EV}} - e^{\pm(\mu_{EV} - Y)/\sigma_{EV}} \right] \quad \text{(E.4)}$$

The extreme-value distribution gives the limiting distribution for the largest (+ sign) or smallest (- sign) element of a set of independent observation from a distribution of exponential type (e.g. normal). For the case of failure time distributions, the appropriate form of the extreme value distribution is the one containing the negative sign. It is shown graphically in figure E.2 (Eadie et al 1971).

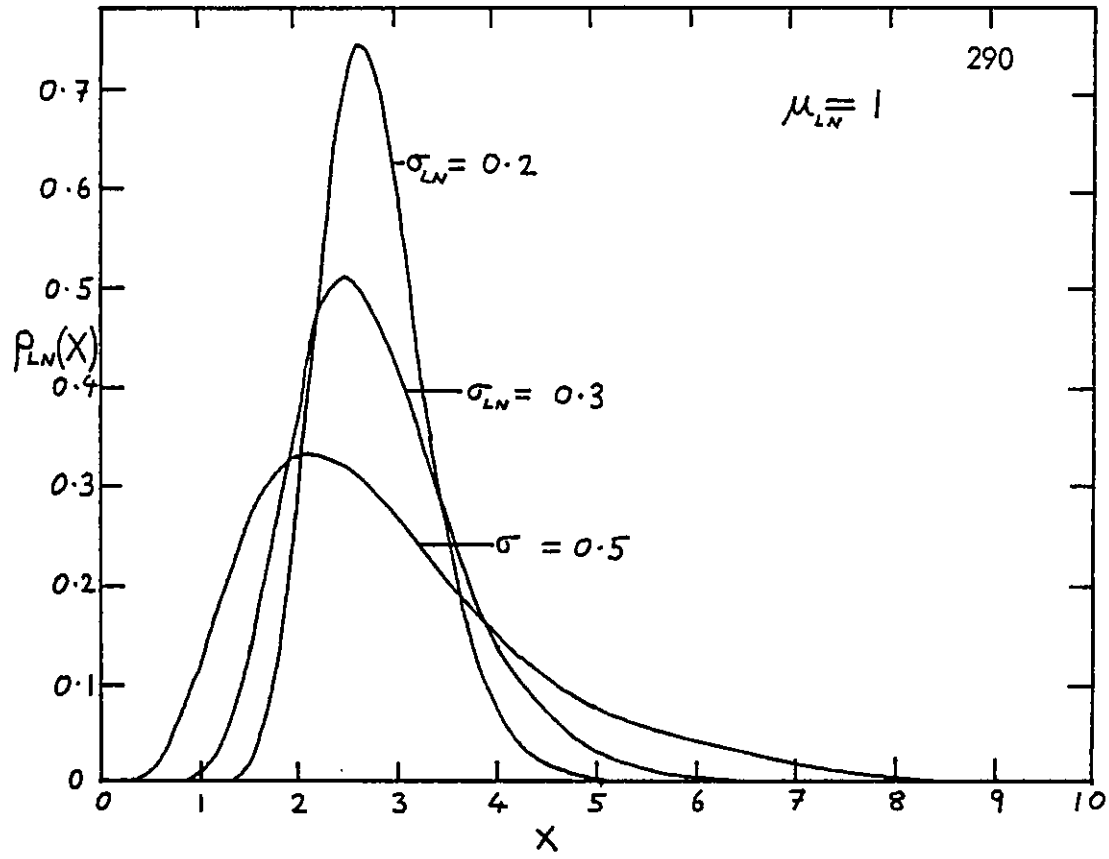

The log-normal distribution

(from Eadie et al 1971)

FIGURE E.1

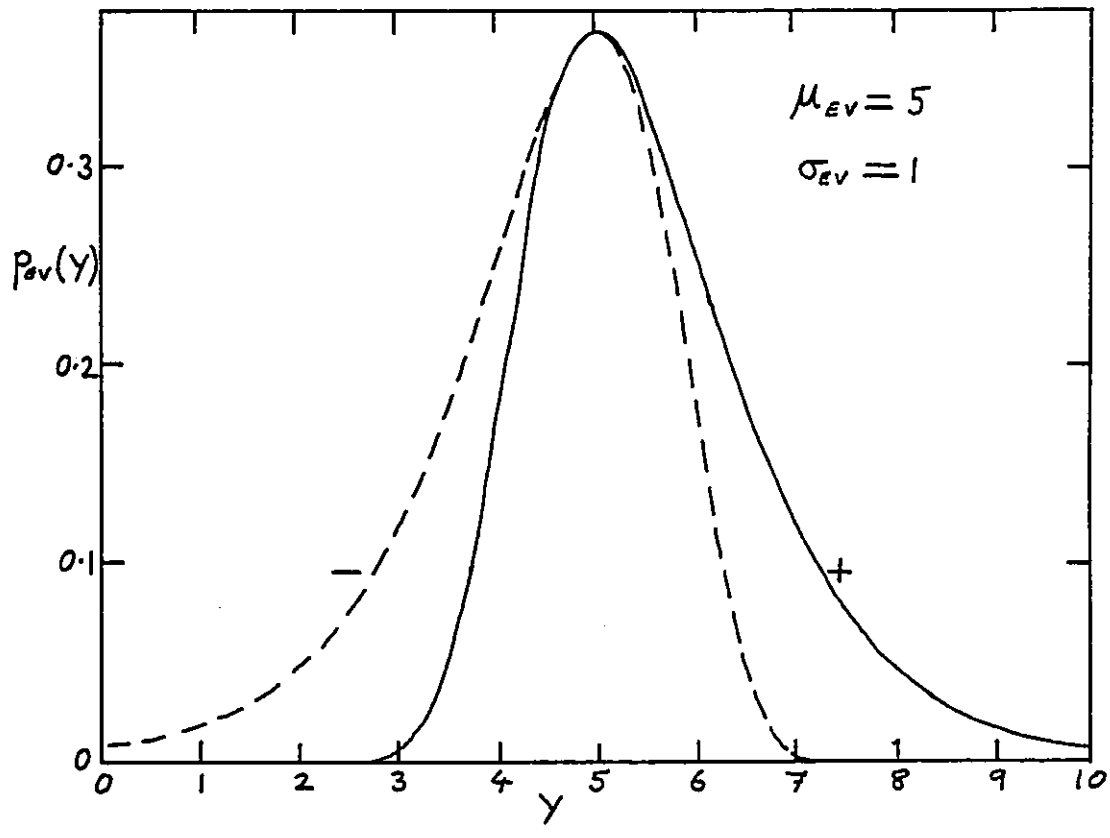

The extreme-value distribution

(from Eadie et al 1971)

FIGURE E.2

ACKNOWLEDGMENTS

I wish to express my sincere thanks to all the people who have helped me during the course of my PhD. I am particularly grateful to Pete Dobson for supervision, advice and encouragement; professor M. Blackman and Dr. N. D. Lisgarten for many useful discussions; Geoff Spiller for invaluable practical guidance and for some of the SEM work; Alun Hughes for use of the ESCALAB and for much help with the XPS work; Chris Pollard for practical advice; Deanne Eastwood for her patience in typing this tome; and last but not least Christine White for practical advice and assistance, proof reading the thesis and moral support.

I am also indebted to Robert Lawson and Steve Sim of British Telecom. Research Labs. for the provision of equipment and materials; John Gowers of Philips Research Labs. for help with the jet-thinning apparatus; Paul Grant of the I.C. Geology Department for most of the SEM work; and the Science Research Council and British Telecom. for the provision of a CASE studentship.

REFERENCES

Agarwala, B.N. et al (1970), J. Appl. Phys. 41, 3954

Agarwala, B.N. et al (1976), Thin Solid Films 34, 165

Ainslie, N.G. et al (1972), Appl. Phys. Lett. 20, 173

Aimes, I. et al (1970), I.B.M. J. Res. Dev. 14, 461

Attardo, M.J. and Rosenberg, R. (1970), J. Appl. Phys. 41, 2381

Attardo, M.J. et al (1971), J. Appl. Phys. 42, 4343

Azzam, R.M.A. and Bashara, N.M. (1977). "Ellipsometry and Polarized Light" (North-Holland)

Bachrach, R.Z. and Bauer, R.S. (1979). J. Vac. Sci. Technol. 16, 1149

Bateson, S. (1952) Vacuum 11, 365

Bauer, E. (1964). "Growth of Oriented Films on Amorphous Substrates". Single Crystal Films. Ed. Francombe and Sato (Pergamon)

Bauer, R.S. et al (1978), Proc. Int. Top. Conf. on SiO_2 and its Interfaces (Ed. Pantelides), 401

Bauer, R.S. et al (1979). Inst. of Phys. Conf. Series 43, 797

Bauer, R.S. et al (1980), Appl. Phys. Lett. 37, 1006

Berenbaum, L. (1971), J. Appl. Phys. 42, 880

Berenbaum, L. and Rosenberg, R. (1969). Thin Solid Films 4, 187

Bicknell, R.W. (1973), J. Phys. D : Appl. Phys. 6, 1991

Black, J.R. (1969). IEEE Trans. Electron Devices ED-16, 338

Blair, J.C. (1970), Appl. Phys. Lett. 17, 281

Blech, I.A. (1970), Thin Solid Films 6, 113

Blech, I.A. (1976), J. Appl. Phys. 47, 1203

Blech, I.A. and Kinsbron, E. (1975), Thin Solid Films 25, 327

Blech, I.A. and Meieran, E.S. (1969), J. Appl. Phys. 40, 485

Blech, I.A. and Sello, H. (1966). Physics of Failure in Electronics 5, 496

Blech, I.A. et al (1975). J. Cryst. Growth 32, 161

Bosvieux, C. and Friedel, J. (1962). J. Phys. Chem. Sol. 23, 123

Bower, R.W. (1973), Appl. Phys. Lett. 23, 99

Bradley, D.E. (1961). "Replica and Shadowing Techniques". Techniques for Electron Microscopy, Ed. Kay (Blackwell)

Brondyke, K.J. (1953), J. Amer. Ceramic Soc. 36, 171

Cardona, M. and Ley, L. (1978). "Photoemission in Solids", Topics in Appl. Phys. 26, 1

Chang, C.C. (1971), Surf. Sci. 25, 53

Chang, C.C. (1974), "Analytical Auger Spectroscopy". Characterization of Solid Surfaces. Ed. Kane and Larrabee (Plenum)

Chapman, B.N. (1974), J. Vac. Sci. Technol. 11, 106

Chaudhari, P. (1974), J. Appl. Phys. 45, 4339

Chaug, Y.S. and Huang, H.L. (1976), J. Appl. Phys. 47, 1775

Chopra, K.L. (1969). "Thin Film Phenomena" (McGraw-Hill)

Chou, N.J. and Eldridge, J.M. (1970), J. Electrochem. Soc. 117, 1287

Chung, M.F. and Jenkins, L.H. (1970), Surf. Sci. 22, 479

Cook, C.F. et al (1980), J. Vac. Sci. Technol. 17, 44

Cratchley, D. and Baker, A.A. (1967), Amer. Ceramic Soc. Bull. 46, 191

Dhere, N.G. et al (1975). Thin Solid Films 30, 267

Dobson, P.J. (1968) "Vapour Deposited Metal Films". Ph.D. Thesis, Univ. of Southampton

Eadie, W.T. et al (1971) "Statistical Methods in Experimental Physics" (North-Holland)

English, A.T. and Melliar-Smith (1978), Ann. Rev. Mat. Sci. 8, 459

English, A.T. et al (1972). Appl. Phys. Lett. 21, 397

Evans, S. et al (1978). J. Electron. Spect. and Rel. Phenomena 14, 341

Fiks, V.B. (1959), Soviet Phy. - Solid State 1, 14

Flodstrom, S.A. et al (1976) Phys. Rev. Lett. 37, 1282

Forsyth, P.J.E. (1963), Acta Met. 11, 703

Fuchs, K. (1938). Proc. Cambridge Phil. Soc. 34, 100

Fuller, C.R. and Ghate, P.B. (1979) Thin Solid Films 64, 25

Gerardin, M. (1861) Compt. Rend. 53, 727

Gifkin, R.C. (1967) Mat. Sci. Eng. 2, 181

Gilder, H.M. and Lazarus, D. (1966), Phys. Rev. 145, 507

Goldstein, B. and Pensak, L. (1959), J. Appl. Phys. 30, 155

Grigorovici, R. et al. (1962), J. Phys. Chem. Sol. 23, 428

Grunthaner, F.J. et al (1979), J. Vac. Sci. Technol. 16, 1443

Gupta, D. (1973). J. Appl. Phys. 44, 4455

van Gurp, G.J. (1971). Appl. Phys. Lett. 19, 476

van Gurp, G.J. (1973). J. Appl. Phys. 44, 2040

Hall, C.E. (1966) "Introduction to Electron Microscopy" (McGraw-Hill)

Harper, C.A. (1970) "Handbook of Materials and Processes for Electronics" (McGraw-Hill)

Hartstein, A. et al (1978). Proc. Int. Top. Conf. on Si O_2 and its Interfaces (Ed. Pantelides), 51

Herman, D.S. et al (1972). J. Vac. Sci. Technol. 9, 515

Hersener, J. and Ricker, Th. (1973). Direktabb. Oberfl. 6, 311

d'Heurle, F.M. and Gangulee, A. (1973). Proc. 10th Ann. Rel. Phys. Symp. 165

d'Heurle, F.M. and Ho, P.S. (1978). Thin Films - Interdiffusion and Reaction (Ed. Poate et al), 243

d'Heurle, F.M. and Rosenberg, R. (1973). Physics of Thin Films (Ed. Haas and Francombe) 7, 257

d'Heurle, F.M. et al (1968) Trans. Met. Soc. AIME 242, 502

Heyman, J.S. and Miller, W.E. (1978) J. Vac. Sci. Technol. 15, 219

Hickmott, T.W. (1980) J. Appl. Phys. 51, 4269

Hirsch, P.B. et al (1965) "Electron Microscopy of Thin Crystals" (Butterworths)

Hirth, J.P. et al (1964) "Theory of Nucleation in Deposition on Substrates". Single Crystal Films, Ed. Francombe and Sato (Pergamon)

Hofmann, S. et al (1977) Thin Solid Films 43, 275

Holland, L. (1956) "Vacuum Deposition of Thin Films" (Chapman and Hall)

Horowitz, S.L. and Blech, I.A. (1972) Mater. Sci. Eng. 10, 169

Howard, J.K. and Ross, R.F. (1968). I.B.M. Tech. Rep. 22, 601

Hughes, A.E. and Phillips, C.C. (1982). Paper submitted to Surf. and Interface Analysis

Hummel, R.E. et al (1976). J. Phys. Chem. Sol. 37, 73

Huntington, H.B. (1975) "Electromigration in Metals". Diffusion in Solids. Ed. Nowick and Burton (Academic Press)

Huntington, H.B. and Grone, A.R. (1961), J. Phys. Chem. Sol. 20, 76

Huntington, H.B. and Ho. S.C. (1963), J. Phys. Soc. Japan 18, Suppl. II, 202

Johnson, O. (1975) Chemica Scripta 8, 162

Johnson, R.P. (1938) Phys. Rev. 54, 459

Kerr, D.R. et al (1964) I.B.M. J. Res. Dev. 8, 376

Kinsbron, E. (1980) Appl. Phys. Lett 36, 968

Krueger, Wm. H. and Pollack, S.R. (1972a) Surf. Sci. 30, 263

Krueger, Wm. H. and Pollack, S.R. (1972b) Surf. Sci. 30, 280

Lahiri, S.K. (1970) J. Appl. Phys. 41, 3172

Learn, A.J. (1973) J. Appl. Phys. 44, 3

Learn, A.J. (1976) J. Electrochem. Soc. 123, 894

Lehman, H.S. (1964) I.B.M. J. Res. Dev. 8, 422

Lowry, R.K. and Hogrefe, A.W. (1980) Solid State Technol. 23, 71

Mattox, D.M. (1973) Thin Solid Films 18, 173

Mayer, O. and Fromm, E. (1977) Z. Metall. 68, 27

Moulson, A.J. and Roberts, J.P. (1960) Trans. Brit. Ceramic Soc. 59, 388

Mullins, W.W. (1957) J. Appl. Phys. 28, 333

Nagasima, N. et al (1974) J. Electrochem. Soc. 121, 434

Nowak, W.B. (1976) Met. Trans. 7A, 1503

Osburn, C.M. and Weitzman, E.J. (1972) J. Electrochem. Soc. 119, 603

Pearmain, K. and Dorey, G. (1967) R.A.E. Tech. Rep. 67060

Penney, R.V. (1964) J. Phys. Chem. Sol. 25, 335

Philofsky, E. and Hall. E.L. (1975). IEEE Trans. on Parts Hybrids and Packaging. PHP-11, 281

Philofsky, E. et al (1971) Proc. 9th Ann. Rel. Phys. Symp., 120

Pinsker, Z.G. (1953) "Electron Diffraction" (Butterworths)

Prabriputaloong, K. and Piggott, M.R. (1973a), J. Amer. Ceramic Soc. 56, 184

Prabriputaloong, K. and Piggott, M.R. (1974), J. Electrochem. Soc. 121, 430

Prabriputaloong, K. and Piggott, M.R. (1974), J. Electrochem. Soc. 121, 430

Presland, A.E.B. et al (1972). Surf. Sci. 29, 424

Prokop, G.S. and Joseph, R.R. (1972), J. Appl. Phys. 43, 2595

Prokop, G.S. et al (1970) Proc. 8th Ann. Rel. Phys. Symp., 121

Reicha, F.M. and Barna, P.B. (1980), Acta. Phys. Sic. Hung. 49, 237

Rhodin, T.N. and Walton, D. (1964). "Nucleation of Oriented Films". Single Crystal Films. Ed. Francombe and Sato (Pergamon)

Ritchie, R.H. (1957). Phys. Rev. 106, 874

Rosenberg, R. (1970), Appl. Phys. Lett. 16, 27

Rosenberg, R. and Berenbaum, L. (1968). Appl. Phys. Lett. 12, 201

Rosenberg, R. and Ohring, M. (1971). J. Appl. Phys. 42, 5671

Saito, M. and Hirota, S. (1974). Rev. Elect. Comms. Labs. 22, 678

Santoro, C.J. (1969). J. Electrochem. Soc. 116, 361

Sato, K. et al (1971). Met. Trans. 2, 691

Schoen, J.M. (1980). J. Appl. Phys. 51, 513

Scofield, J.H. (1976). J. Electron. Spect. and Rel. Phenom. 8, 129

Scoggan, G.A. et al (1975). Proc. 13th Ann. Rel. Phys. Symp., 151

Scott, G.D. et al (1950). J. Appl. Phys. 21, 843

Seah, M.P. and Ench, W.A. (1979). Surf. and Interface Analysis 1, 3

Seith, W. and Wever, H. (1953). Z. Electrochem. 59, 942

Siegbahn, K. (1972). 3rd Int. Conf. on Atomic Phys. (Boulder, Col.)

Sigsbee, R.A. (1973). J. Appl. Phys. 44, 2533

Silverman, R. (1968). J. Electrochem. Soc. 115, 674

Sim, S.P. (1979). Microelectron. Reliab. 19, 207

Sinha, A.K. and Sheng, T.T. (1978). Thin Solid Films 48, 117

Skaupy, F. (1914). Verh. Deut. Phys. Ges. 16, 156

Sondheimer, E.H. (1950). Phys. Rev. 80, 401

Sondheimer, E.H. (1952). Advan. Phys. 1, 1

Sorbello, R.S. (1973). J. Phys. Chem. Sol. 34, 937

Spiller, G.D.T. (1979). Ph.D. Thesis. Univ. of London

Spokas, J.J. and Slichter, C.P. (1959). Phys. Rev. 113, 1462

Springer, R.W. and Catlett, D.S. (1978). J. Vac. Sci. Technol. 15, 210

Standage, A.E. and Gani, M.S. (1967). J. Amer. Ceramic Soc. 50, 101

Stephens, C.E. and Sinnadurai, F.N. (1974). J. Phys. E : Sci. Instr. 7, 641

Strausser, Y.E. and Majumder, K.S. (1978). J. Vac. Sci. Technol. 15, 238

Strausser, Y.E. et al (1978). Thin Solid Films 52, 203

Sun, P.H. and Ohring, M. (1976). J. Appl. Phys. 47, 478

Tai, K.L. and Ohring, M. (1977). J. Appl. Phys. 48, 36

Taylor, G.M. (1980). Solid State Technol. 23, 92

Thomas, J.E. and Young, D.R. (1964). I.B.M. J. Res. Dev. 8, 368

Tolansky, S. (1948). "Multiple Beam Interferometry of Surfaces and Films" (Clarendon)

Totta, P.A. and Sopher, R.P. (1969). I.B.M. J. Res. Dev. 13, 226

Underhill, P.R. and Gallon, T.E. (1981). Vacuum 31, 477

Unvala, B.A. and Censlive, M. (1973). Vacuum 23, 327

Vaidya, S. et al (1980a). Appl. Phys. Lett. 36, 464

Vainshtein, B.K. (1964). "Structure Analysis by Electron Diffraction" (Pergamon)

Venables, J.A. and Price, G.L. (1975). "Epitaxial Growth - Part B" (ed. Matthews), 381 (Academic Press)

Venables, J.D. and Lye, R.G. (1972). Proc. 10th Ann. Rel. Phys. Symp., 159

Verhoeven, J. (1963). Met. Rev. 8, 311

Vossen, J.L. et al (1974). J. Vac. Sci. Technol. 11, 60

Wagner, C. (1933). Z. Physikal. Chem. 164, 231

Wefers, K. and Be,, G.M. (1972). Alcoa Res. Labs. Tech. Paper 19

Weise, J. (1972). Thin Solid Films 13, 169

Wever, H. (1956). Z. Electrochem. 60, 1170

Wever, H. and Seith, W. (1955). Z. Electrochem. 59, 942

Wolters, D.L. (1979). Inst. of Phys. Conf. Series 50, 19

Wyckoff, R.W.G. (1963). "Crystal Structures" 2nd edition (John-Wiley).

J. Phys. D: Appl. Phys., 14 (1981) L17–22. Printed in Great Britain

LETTER TO THE EDITOR

Evidence for reaction at the Al–SiO_2 interface

S Roberts and PJ Dobson
Surface Physics Group, Blackett Laboratory, Imperial College of Science and Technology, Prince Consort Road, London SW7 2BZ, UK

Received 19 December 1980

Abstract. Evidence from x-ray photoelectron spectroscopy (XPS) and transmission electron microscopy (TEM) is presented for a solid state reaction between aluminium and oxidised silicon, which results in the formation of a crystalline oxide phase of aluminium and elemental silicon. The oxide phase has been identified as a mixture of η and γ phases which are less dense and have more 'open' structures than the most stable α–Al_2O_3 phase. We suggest that this reaction which can occur under the conditions used for the manufacture of integrated circuits may be significant for electromigration failure mechanisms.

1. Introduction

The Al–SiO_2 interface is of considerable importance in governing the reliability of integrated circuits, where aluminium contact metallisations run over thermally grown SiO_2 on the device surface and may also be covered by a SiO_2 passivation layer. The properties of the Al–SiO_2 interface affect bonding and thermal contact between the metallisation and the die and may also control the rate of electromigration damage. Electromigration via the Al–SiO_2 interface is expected to be particularly important in the case of narrow (<2 μm) metallisation line widths where a 'bamboo' grain structure has been shown to exist (Vaidya *et al* 1980). Here, the grain boundaries tend to be perpendicular to the direction of electric current flow and the failure mechanisms associated with grain boundary mass transport (Rosenberg and Ohring 1971) are relatively unimportant.

Reactions at the Al–SiO_2 interface are also thought to be responsible for changes in the Al–SiO_2 work function on annealing (Hickmott 1980). Consequently, the performance of metal–oxide–semiconductor (MOS) devices depends on the structure of the Al–SiO_2 interface.

We report here on some investigations into this interface, using a combination of transmission electron microscopy and diffraction and x-ray photoelectron spectroscopy. We have identified conditions under which chemical reaction between aluminium and silicon dioxide occurs, i.e.

$$4Al + 3SiO_2 \rightarrow 2Al_2O_3 + 3Si.$$

For convenience we shall discuss the two techniques separately.

0022-3727/81/030017+06 $01.50

2. X-ray photoelectron spectroscopy (XPS)

All experiments were performed in a V-G Scientific ESCALAB 5 spectrometer. The substrates consisted of 1 μm layers of SiO_2 grown on (111) oriented silicon by heating at 1400 K in steam for 2 h. These were used in two conditions: (i) 'clean as received', which showed some carbon contamination, possibly as high as 20% monolayer coverage, and (ii) argon ion bombarded to remove all traces of carbon from the XPS and Auger spectra. Aluminium (99.995% purity) was deposited at rates between 5×10^{-2} and 2×10^{-1} nm s^{-1} from a tungsten filament evaporator. The deposition rates and film thicknesses were monitored using a calibrated quartz crystal oscillator microbalance. The base pressure was 3×10^{-11} mbar, rising to 7×10^{-10} mbar during evaporation. The substrates were held at room temperature during aluminium depsition.

After 0.5 nm of aluminium had been deposited on the ion-bombarded SiO_2, XPS spectra were obtained, using the Mg Kα line at 1253.6 eV. Electron induced Auger electron spectroscopy could not be performed because of electrostatic charging effects, which probably resulted from the dicontinuous island nature of the aluminium deposit. Figure 1 shows the XPS results. Curves A to D show that even at room temperature changes are occurring. Note in particular the growth of the Al_2O_3 features, this being

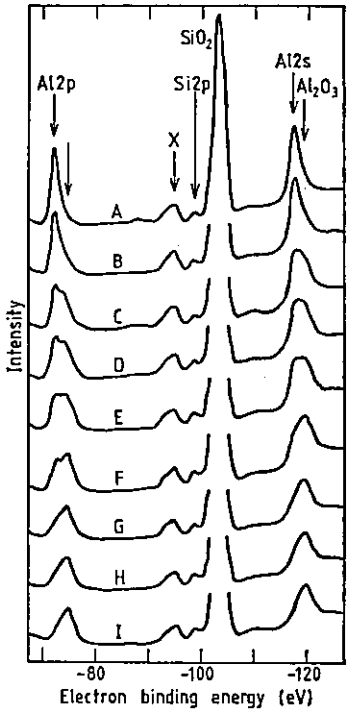

Figure 1. XPS spectra from 0.5 nm of Al on ion-bombarded SiO_2 for different times after deposition at room temperature: A, 30 min; B, 19 h; C, 42 h; D, 91 h; and then subsequent treatment: E, 30 min at 525 K; F, 16 h at 525 K; G, 30 min at 575 K; H, 30 min at 650 K; I, 30 min at 750 K.

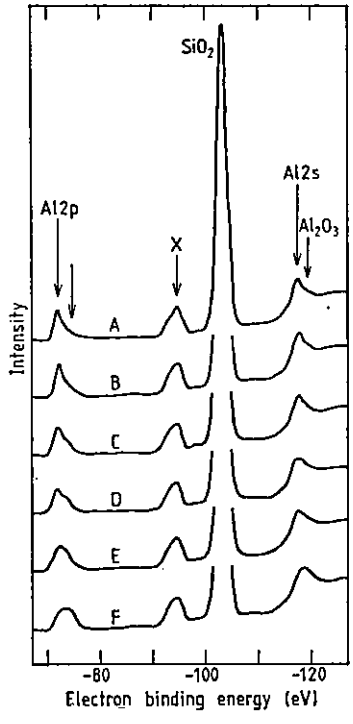

Figure 2. XPS spectra of the 'as received' SiO_2 after deposition of 0.3 nm of Al at room temperature: A, 15 min; B, 5 h; C, 21 h; D, 44 h; E after 30 min further annealing at 650 K; F, 30 min at 750 K.

accompanied by a slight increase in the Si 2p peak. The feature at X is a Mg Kα satellite due to the fact that the x-rays were not monochromated. At elevated temperatures (during which the base pressure was always less than 10^{-1} mbar), the sequence is seen to continue with gradual growth of the Al_2O_3 2p at the expense of the metallic aluminium 2p peak. Changes in the Al 2s peak are not as clear since the Si 2p plasmon loss is superimposed on the Al 2p peak.

With the 'as received' Si O_2 substrates the reaction was not as rapid. Figure 2 illustrates the results for a deposit of 0.3 nm of aluminium. Compare curve C of figure 2 to see how slowly the reaction proceeds on the 'as received' substrate at room temperature However, heating did bring about reaction, although the presence of silicon is less marked in this case.

In order to establish that the oxidation of aluminium was not caused by ambient oxygen in the vacuum chamber, 0.5 nm of aluminium was deposited on to an argon ion bombarded silicon substrate. Even after 160 h at room temperature followed by an anneal at approximately 850 K for 30 min, there was negligible Al_2O_3 formation as detected by XPS. We therefore feel confident that the Al_2O_3 seen in figures 1 and 2 was produced by reaction at the Al–SiO_2 interface.

3. Transmission electron microscopy (TEM)

Two sets of experiments have been performed in which use was made of TEM and diffraction to examine reaction at the Al–SiO_2 interface. In the first set, aluminium was deposited on to oxidised silicon wafers in a 'clean vacuum' coating unit which had a liquid nitrogen trap and used polyphenyl ether pumping fluid. The wafers were of (111) orientation and had approximately 50 nm of thermally grown oxide on the surface. They were used in the 'as received' condition. 50 nm of aluminium was deposited on to the substrates at approximately 1 nm s^{-1} from a tungsten filament evaporator. The substrates were heated to 650 K during deposition, by a tungsten strip radiative heater (Unvala and Censlive 1973) and radiation from the evaporator itself raised the substrate temperature by a further 50 K. The pressure rose from 10^{-7} to 10^{-6} mbar during deposition. After the wafers had cooled to room temperature they were removed from the vacuum chamber and 3 mm discs were prepared by ultrasonically cutting the wafers. The silicon was removed from the centre of each disc by 'jet etching' with HF:HNO_3, 1:2 by vol. (Bicknell 1973) to leave 50 nm of aluminium supported on 50 nm of SiO_2. The specimens were examined on a JEOL 100U TEM using an electron beam of 80 keV energy. Both the direct examination of the specimens and carbon/platinum shadowed replicas of the surface showed the aluminium deposit to consist mainly of islands of approximately 0.5 μm diameter and 0.1 μm height, with some smaller islands of around 50 nm diameter covering much of the area between the larger islands. The electron diffraction pattern yielded rings with the d-spacings as shown in the first column of the table. There was no evidence for any strong preferred orientation, i.e. tilting the specimen did not give rise to 'arcing' of the rings.

There is clear evidence for an oxide phase of aluminium, tentatively identified as polycrystalline η or γ-Al_2O_3 (Wefers and Bell 1972), and polycrystalline elemental silicon. We do not believe that the crystalline oxide could have resulted from reaction with residual oxygen-containing gases during aluminium deposition as the principal gas present during deposition was hydrogen. Transfer of the specimen from the evaporation chamber to the electron microscope must have resulted in atmospheric oxidation of the aluminium surface, but such oxide has been shown to be amorphous (Prabriputaloong and Piggott

1974). The detected silicon can only have resulted from chemical reaction at the interface and is easily distinguished from residual single crystal silicon on the reverse side of the wafer.

Diffraction patterns taken from aluminium films deposited on to identical substrates at temperatures of 575 K and less exhibited only the polycrystalline aluminium rings, but films deposited at room temperature and immediately heated at 675 K for 1 h *in vacuo* were found to contain polycrystalline silicon and Al_2O_3.

In the diffraction data described above, only one feature arising from the aluminium oxide was clearly visible, most of the rings being obscured either by the much stronger aluminium features or by diffuse background from the amorphous SiO_2. A second set of TEM experiments was performed in order to elucidate the structure of the aluminium oxide. The substrates used were again silicon wafers with a 50 nm SiO_2 layer and these were cut into 3 mm discs, jet etched to remove the silicon, then washed in trichloroethylene and acetone, and finally vapour-cleaned in isopropyl alcohol. Aluminium was

Table 1. A comparison of the crystallographic *d*-spacings (in nm) obtained using transmission electron diffraction with x-ray data for η and γ-Al_2O_3 (Wefers and Bell 1972) and the calculated *d*-spacings for aluminium and silicon. The first column is for Al deposited on to amorphous SiO_2 at 650 K; the second column refers to Al and SiO_2 heated in the electron microscope until reaction was complete.

Electron diffraction		Calculated values				X-ray diffraction	
Deposited at 370 K	Fully reacted	Aluminium		Silicon		γ Al_2O_3	η Al_2O_3
		hkl	*d*	*hkl*	*d*		
	0.464						0.46
0.33	0.313			111	0.314		
0.285	0.280					0.27	0.28
	0.238					0.241	0.240
0.233		111	0.233				
	0.227					0.228	0.227
						0.218	
						0.209	
0.202		200	0.202				
	0.196					0.198	0.197
						0.195	
	0.192			220	0.192		
0.164	0.163			311	0.164		
	0.155			222	0.157		
						0.154	0.152
0.143		220	0.143				
	0.140					0.139	0.140
	0.136			400	0.136		
0.126	0.125			331	0.125		
0.122		311	0.122				
	0.121						0.121
0.117		222	0.117				
						0.114	0.114
0.112	0.111			422	0.111		
						0.104	0.103
0.101		400	0.101				

deposited in the TEM, the background pressure being 10^{-6} mbar, rising to 5×10^{-5} mbar (mainly hydrogen) during deposition. The specimens were then heated at 870 K until reaction between the aluminium and SiO_2 was complete, as indicated by the disappearance of the Al diffraction features. The resulting diffraction pattern showed the presence of polycrystalline Si and η-Al_2O_3; the *d*-spacings are listed in the second column of the table.

4. Discussion

The results establish that aluminium and amorphous silicon dioxide undergo a solid state reaction with the formation of polycrystalline Al_2O_3 and elemental silicon. Furthermore, this reaction is likely to occur under the conditions used for the fabrication of integrated circuit metallisations. We shall shortly consider the implications of this interfacial reaction for the performance of semiconductor devices.

Our results compare well with studies reported elsewhere. Bachrach and Bauer (1979) investigated the reaction between thin layers of aluminium and silicon oxidised under controlled UHV conditions, using high resolution XPS. Their results suggested that an intermediate oxidation state of aluminium was formed initially, followed by the formation of Al_2O_3 after several hours at room temperature. Elemental Si was also observed. The reaction has also been reported by Strausser *et al* (1978), who used Auger electron spectroscopy in conjunction with ion sputter profiling to investigate the interface between 50 and 100 nm films of Al sputter-deposited on to thermally oxidised silicon. The reaction products were found to be distributed over a 40 nm layer at the interface, although some mixing may have occurred during depth profiling. The reaction rate for our ion bombarded specimens was comparable to, although slightly less than, that reported by Bachrach and Bauer (1979). The rate for the 'as received' SiO_2 was much lower and suggests that atmospheric exposure of the SiO_2 gives rise to slower reactions.

The TEM experiments, whilst corroborating the above, can also be compared to some studies by Prabriputaloong and Piggott (1974), who used transmission electron microscopy and diffraction as well as x-ray diffraction to measure reaction rates between aluminium films and quartz and vitreous silica substrates in the temperature range 675 to 1125 K. They observed the polycrystalline θ-Al_2O_3 phase with some trace of α-Al_2O_3 and showed that the reaction was more rapid for vitreous silica than for quartz (activation energies of 31 ± 3 and 64 ± 6 kcal mol^{-1} respectively). They also found that contamination of the substrates by water led to a lower reaction rate.

The absence of interfacial reaction in the case of aluminium deposited on to atmospherically exposed SiO_2 at temperatures less than 575 K is a possible cause for the non-adhesion of aluminium metallisations prepared under similar conditions in the microelectronics industry. Such non-adhesion can give rise to local 'hot spots' which result in a higher rate of electromigration damage and early device failure (Rosenberg and Berenbaum 1968).

The phase of Al_2O_3 present at the Al–SiO_2 interfaces may determine the extent to which they contribute to electromigration in the metallisation. The η-phase is less dense than the most stable oxide (α-Al_2O_3) and can be considered to have a relatively open structure; Lippens and de Boer (1964) state that the structure is a tetragonally deformed spinel lattice. It is tempting to suggest that passage of aluminium atoms along the Al–η–Al_2O_3 interface may be facilitated by this open, distorted structure. If electromigration is to be restricted, a close-packed oxide, i.e. α-Al_2O_3, would be desirable. We

are continuing our studies in order to identify the conditions for the formation of different aluminium oxide phases at the interface and we are performing accelerated electromigration life tests on aluminium metallisations prepared under various conditions.

As was mentioned earlier, chemical reaction at the Al–SiO_2 interface has been shown to affect the electrical properties of MOS structures. We suggest that the phase of Al_2O_3 present might also be important. The relationship between the various so-called transition aluminas is very poorly understood, and their electrical properties appear not to have been studied in any systematic fashion.

5. Conclusions

We have established that a solid state reaction between aluminium and oxidised silicon can occur under conditions similar to those used for the manufacture of integrated circuits. This can have two important implications as far as electromigration failure is concerned. Firstly, a reaction should help to provide adhesion and hence good thermal contact between the aluminium film and the substrate, thereby not giving rise to 'hot spots' and enhanced electromigration. Secondly, the open structure of the η (or γ) Al_2O_3 at the Al–Al_2O_3 interface may provide a channel for Al ion migration which will be the most significant path for sub-micron VLSI circuitry. We also highlight the poor understanding of the general occurrence of oxide phases of aluminium and the lack of data regarding the electronic nature of these phases.

Acknowledgments

This work is part of an SRC CASE programme with British Telecom Research Laboratories, and we wish to thank R W Lawson and S P Sim of those laboratories for provision of samples and facilities. We are also very grateful for the provision of XPS facilities by Professor D J Bradley and Dr W Sibbett and record our gratitude to A E Hughes for helpful discussions.

We also acknowledge with gratitude information about the oxide phases of aluminium supplied by Dr A J Dowell of the Chalfont Technological Centre of the British Aluminium Company and assistance with the 'jet thinning' technique given by Dr J Gowers of Philips Research Laboratories, Redhill.

References

Bachrach R Z and Bauer R S 1979 *J. Vac. Sci. Technol.* **16** 1149–53
Bicknell R W 1973 *J. Phys. D: Appl. Phys.* **6** 1991–9
Hickmott T W 1980 *J. Appl. Phys.* **51** 4269–81
Lippens B C and de Boer J H 1964 *J. Electrochem. Soc.* **121** 430–4
Prabriputaloong K and Piggott M R 1974 *J. Electrochem. Soc.* **121** 430–4
Rosenberg R and Berenbaum L 1968 *Appl. Phys. Lett.* **12** 201–4
Rosenberg R and Ohring M 1971 *J. Appl. Phys.* **42** 5671–9
Strausser Y E *et al* 1978 *Thin Solid Films* **52** 203–14
Unvala B A and Censlive M 1973 *Vacuum* **23** 327–9
Vaidya S *et al* 1980 *Appl. Phys. Lett.* **36** 464–6
Wefers K and Bell G M 1972 *Tech. Paper No.* 19, *Alcoa Res. Labs.*